University of Basel

Swiss Nanoscience Institute

SNI SWISS NANOSCIENCE INSTITUTE
EINE INITIATIVE DER UNIVERSITÄT BASEL UND DES KANTONS AARGAU

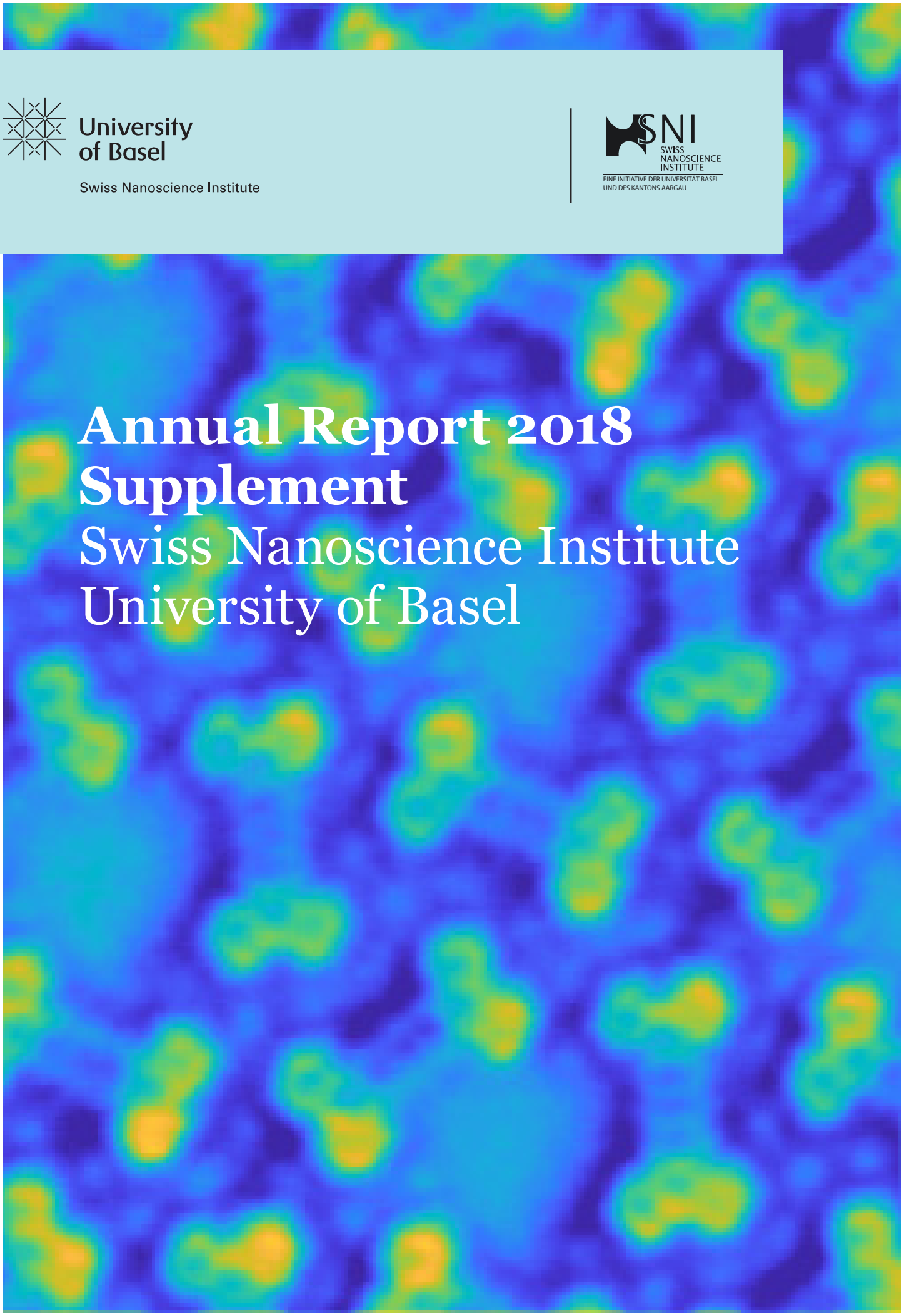

Annual Report 2018 Supplement

Swiss Nanoscience Institute
University of Basel

The Swiss Nanoscience Institute (SNI) is a research initiative of the Canton of Aargau and the University of Basel.

This report summarizes work conducted at the Swiss Nanoscience Institute (SNI) in 2018.

Swiss Nanoscience Institute
Klingelbergstrasse 82
4056 Basel
Switzerland
www.nanoscience.ch

Cover: Atomic force microscopic image of "nano-bone" molecules on a gold surface. The molecule is a building block for the formation of two-dimensional organic topological insulators (Rémy Pawlak, Department of Physics, University of Basel).

Contents

A miniaturised hybrid ion-atom chip trap

Project P1214: An ion-atom hybrid trap on a chip
Project Leader: S. Willitsch and P. Treutlein
Collaborators: I. Rouse (SNI PhD Student), A. Mokhberi, and R. Schmied

Introduction

A single atom can be viewed as the ultimate nanoscale system, and achieving control over a single particle provides the possibility to build quantum computers, probe the fundamental constants of physics, and stringently test the limits of theoretical physics. The first issue to overcome in achieving this goal is to pin a particle in place long enough to be able to perform an experiment. By applying laser light at a precise frequency, certain particles may be decelerated until they reach a temperature less than one-thousandth of a degree above absolute zero, and a host of advanced cooling methods allows the temperature to be reduced even further than can be achieved through laser cooling. Even at these low temperatures, however, the residual motion of the particle limits the amount of time for which it could be observed. Thus, a further tool is required: the ability to remotely apply forces to the particle to ensure that it remains in a single region of space. For neutral particles, this is achieved using magnetic fields, whereas for charged particles (ions) electric fields are typically employed. If these fields are correctly generated, then the atoms can be forced to remain in a single spatial location for periods of time from milliseconds to days. The control over these particles is further enhanced through the use of "chip traps" – miniaturised devices which greatly improve the spatial resolution of the trapping fields, thus allowing for more precise manipulation of the particles.

While confining a single type of matter already allows for a range of experiments to be performed [1], the scope of these experiments is greatly enhanced when multiple different types of particle are confined simultaneously. For example, the collisions between two different species may lead to a simple chemical reaction, opening up the field of ultracold controlled chemistry. The required confinement of multiple species can be achieved through a hybrid trap combining two different types of trapping technology, as has been previously demonstrated world-wide. However, unlike the single-species traps, these hybrid traps have not yet benefited from the miniaturisation, and so precise manipulation of the trapped particles is limited, hindering the scope of possible experiments. Moreover, the interaction between trapped ions and neutral atoms leads to the observation that the ions deviate from thermal equilibrium [2-4], potentially complicating the interpretation of results obtained in hybrid traps.

In this report, we present the outcome of a two-part investigation into these hybrid systems. Firstly, we discuss the design and construction of a prototype hybrid ion-atom chip trap, enabling enhanced control of ultracold systems. Secondly, we present the results of a theoretical investigation into the statistical properties of the ion-atom system in which we explore how and why an ion in contact with co-trapped atoms fails to exhibit the expected thermal equilibrium.

A hybrid ion-atom chip trap

In collaboration with CSEM and FHNW, we have designed and fabricated a miniaturised device for ion-neutral experiments. This device combines elements of the two pre-existing chip-trap architectures and offers more precise control than can be achieved in traditional macroscopic particle traps. The chip consists of a gold-plated laser-cut ceramic wafer attached to a printed circuit board (PCB), with electrical conductivity between the two elements established through wirebonding. By passing electrical currents through the wires of the PCB, precisely shaped magnetic potentials can be generated to provide confinement of neutral particles. Meanwhile, by applying a set of static and time-dependent voltages to the gold electrodes, the motion of ions may be manipulated to ensure that these remain trapped for extended periods of time.

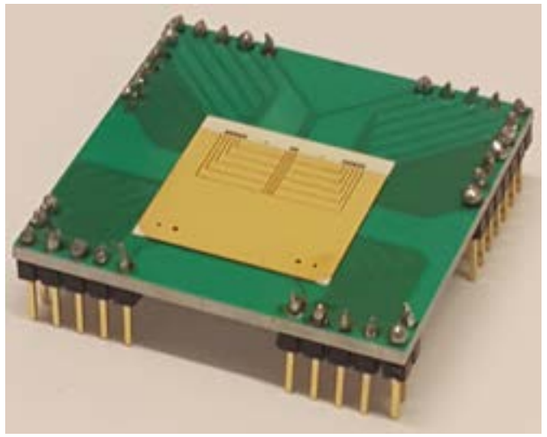

Fig. 1 A photograph of the completed hybrid chip. The gold electrodes produce electric fields for trapping charged particles, while the wires on the printed circuit board generate magnetic fields for the control of neutral atoms.

Although the ion trap is capable of directly capturing particles emitted from a calcium source, the magnetic traps generated by the current carrying wires are too shallow to be able to trap the rubidium atoms until they have been pre-cooled. This initial cooling stage is performed using a magneto-optical trap (MOT), requiring a larger current passed through a thicker copper wire, integrated into a heatsink on the base of the chip. The combination of this magnetic field and laser light reflected from the metallic surface of the chip produces a mirror-MOT, capable of capturing hot rubidium atoms and cooling them to a sufficiently low temperature to be transferred to a magnetic trap generated by the chip. By varying the currents applied to the wires, these atoms are then transported to the location of the ions, such that the particles may interact.

Once trapped and cooled, the particles are highly sensitive to their environment. Indeed, if the particles are not isolated from their surroundings, collisions between the trapped particles and the atmosphere would lead to them heating back to room temperature and becoming lost. Therefore, these experiments must be performed under ultra-high vacuum conditions. We achieve this through constructing a miniaturised vacuum chamber by gluing a quartz cuvette onto the chip and attaching this to a vibration-free ion pump.

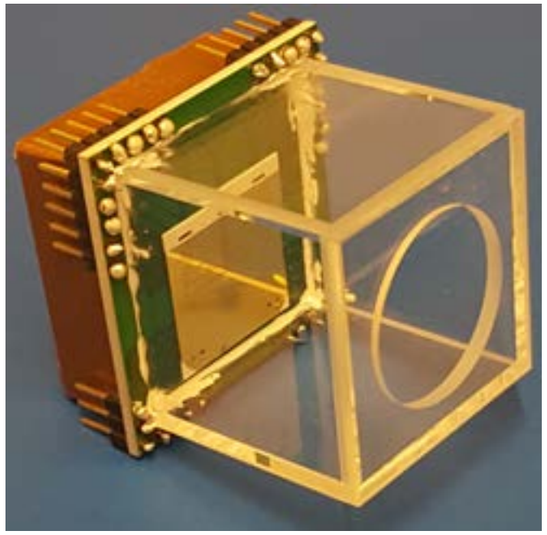

Fig. 2 The hybrid chip attached to a 3cm x 3cm fused silica cell forming a vacuum chamber for experiments. The copper block contains a water-cooling channel and a structure for generating the magnetic field for the initial magneto-optical trap.

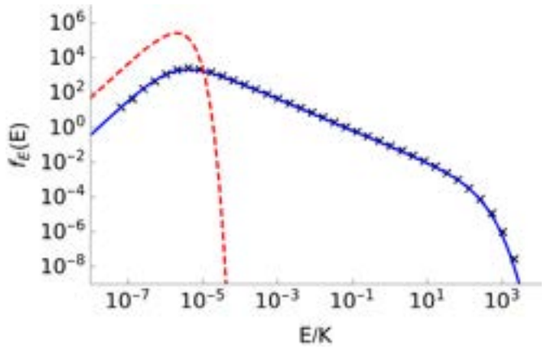

Fig. 3 Double-logarithmic plot of the energy distribution of an ion interacting with an ultracold buffer gas in the hybrid chip trap. The solid blue line indicates the best-fit to the simulated distribution (black crosses), while the red dashed line gives the distribution predicted when thermal equilibrium holds.

Non-equilibrium thermodynamics

Typically, matter can be assumed to exist in a state of thermal equilibrium, meaning that it obeys certain statistical properties and that if two types of particle are allowed to interact they will eventually reach the same temperature. This does not hold if the matter in question is a collection of ions in contact with the environment through residual molecules of background gas [2], or an ion interacting with an ensemble of atoms [3-4]. In the latter case, as a result of the time-dependent trapping fields used to confine the ion the collisions between the ion and atoms which would usually cool the ion to the temperature of the atoms may instead lead to the ion gaining energy overall. As a result of this process, the ion does not reach the temperature of the atoms and exhibits a non-thermal energy distribution. Recently, we have extended our previous investigations into this behaviour [3-4] to include the effect of the trapping potential used to confine the neutral atoms, finding that this further modifies the observed energy distribution. Consequently, we have been able to predict the form of the energy distribution for an ion held in the hybrid chip trap, as well as for the existing hybrid traps used by a number of other groups.

Conclusions

In summary, we have developed a miniaturised architecture to enhance the degree of control over ultracold matter, and analytically derived the expected form of the energy distribution for an ion interacting with a co-trapped buffer gas in this hybrid chip trap. Together, these results pave the way for both an improved control of particles during experiments on ultracold matter, and an increased understanding of the properties of the particles during these experiments.

References

[1] S. Willitsch, *Coulomb-crystallised molecular ions in traps: methods, applications, prospects*, Int. Rev. Phys. Chem. **31**, 175 (2012)

[2] I. Rouse and S. Willitsch, *Superstatistical velocity distributions of cold trapped ions in molecular dynamics simulations*, Phys. Rev. A **92**, 053420 (2015)

[3] I. Rouse and S. Willitsch, *Superstatistical energy distributions of an ion in an ultracold buffer gas*, Phys. Rev. Lett. **118**, 143401 (2017)

[4] I. Rouse and S. Willitsch, *Energy distributions of an ion in a radio-frequency trap immersed in a buffer as under the influence of additional external forces*, Phys. Rev. A **97**, 042712 (2018)

On the energy dissipation of charge density wave systems and topological insulator surfaces

Project P1301: Energy dissipation over structural and electronic phase transitions
Project Leader: E. Meyer and M. Poggio
Collaborators: D. Yildiz (SNI PhD Student), M. Kisiel, U. Gysin, and Th. Glatzel

Current status of the research

Bodies in relative motion separated by few nanometers of vacuum gap experience a tiny friction force [1]. Non-contact form of friction can be measured by cantilever oscillating like a pendulum over the surface. Conventional forms of energy dissipation are phononic friction where tip energy is lost to the creation of surface acoustic phonons and Joule dissipation where the oscillating tip provokes the local electric current [2]. Suppression of Joule dissipation is expected on the surface of topological insulator (TI) due to lack of electrons backscattering [3]. Our aim is to understand the frictional response of Bi_2Te_3 in both the TI phase as well as when the TI phase is suppressed by an external magnetic field. Another, yet elusive form of energy loss is van der Waals dissipation. It occurs where oscillating tip couples to the fluctuating electromagnetic field driven by massive fluctuating electric charge such as charge density wave (CDW) on the surface of TaS_2.

Energy dissipation and image potential states on Bi_2Te_3 surface

We studied the surface of the TI, namely Bi_2Te_3 by means of the pendulum AFM/ STM. Measurements were done at 5K and the same ATEC-NcAu cantilever (k=58 N/m) was used for Scanning Tunneling Spectroscopy (STS) and dissipation measurements.

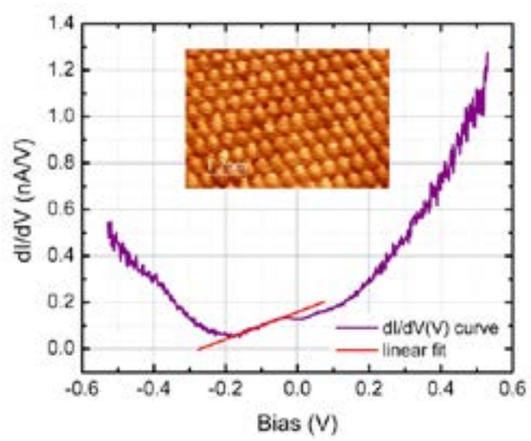

Fig. 1 STM image with atomic resolution (inset) and dI/dV curve. with a PtIr tip. The dI/dV curve showing the Dirac cone localized at Vb=-0.2V was obtained by numerical derivation of the I/V curve measured by STS.

The atomically flat surface of Bi_2Te_3 is shown in figure 1 together with STS spectrum showing a Dirac cone, suggesting that topological character of the surface is preserved.

STS study of IPS were first reported in 1985 and helped to understand the chemical nature of the surface [4]. We reported on IPS on Bi_2Te_3 by means of STS. z-V spectroscopy was performed in constant current mode and with an active feedback. Tip gets retracted by STM feedback while sweeping the bias voltage of the sample. The presence of IPS manifests itself as

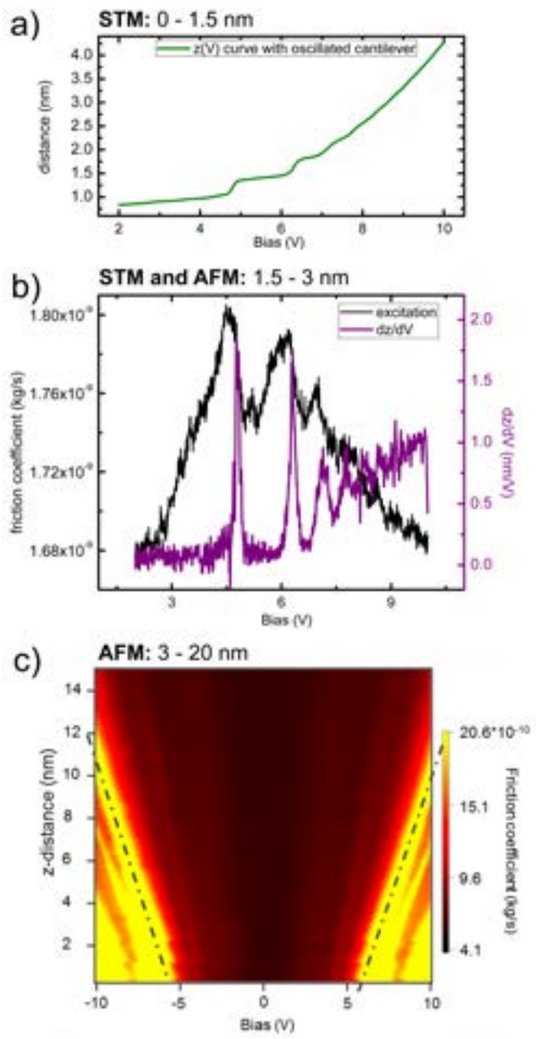

Fig. 2 (a) z-V curve on Bi_2Te_3. Steps represent IPS (>5V) that are measured by STS (b) IPS (first derivative of z-V) measured together with AFM energy dissipation peaks. (c) Energy dissipation peaks observed at far tip sample distances as a function of tip – sample voltage and distance.

a Rydberg series in the STS spectra (Fig. 2a). Combined STM and AFM measurements with oscillating tip sensed series of dissipation peaks correlated with the IPS. Changes in dissipation signal and their correspondence to Rydberg series of IPS provides strong hint that both phenomena are linked together and the field emission resonances affect the mechanical dissipation (Fig. 2b). Mechanical dissipation measurements which nominally operate at large tip-sample distances, thus far from tunneling regime, again sensed a series of dissipation peaks (Fig. 2c). The character of the peaks suggests that the effect is voltage controlled rather than force and confirms the electronic character of energy dissipation. Dissipated power is in the order of tens of meV/cycle indicating single electron tunneling process. The observed dissipation features phenomenology fits to a model of resonance tunneling as follows. For the specific tip-sample voltage and distance the conditions for resonant tunneling are created and the IPS located above the surface gets populated. The resonance tunneling is modulated with the cantilever oscillation frequency due to oscillatory motion of the tip and thus spatial modulation of the barrier. For positive sample bias, electron tunnels from tip to the IPS before it decays into the crystal and dissipation rises due to charge fluctuations in the system during tunneling.

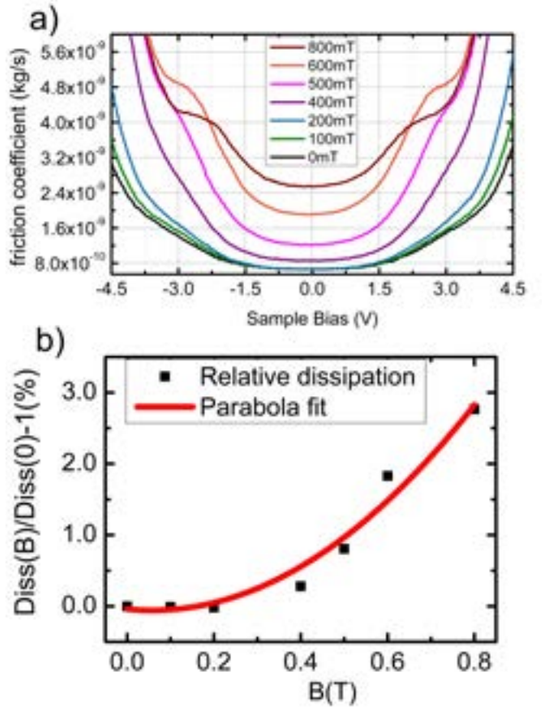

Fig. 3 (a) Dissipation - bias curves for different external magnetic fields measured at 5nm tip-sample distance. (b) Relative energy dissipation (Vb=0V) vs. magnetic field. Behavior of dissipation shows a parabolic dependence, suggesting strong relation to magnetoresistance of Bi_2Te_3.

Dissipation on Bi_2Te_3 for varying B-Field

To further examine the impact of Joule losses and magnetic field on the dissipation and corroborate on the effect of weak-antilocalization, we performed the dissipation measurements under external magnetic field ranging from B = 0–0.8 T oriented perpendicularly to the sample surface.

We noticed the rise of overall dissipation for compensated CPD voltage as shown in figure 3a. Thus, Joule dissipation, connected with electron conduction of the sample in the underlying surface state (the bulk is an insulator), initially low, rises dramatically for magnetic field B > 0.2 T (Fig. 3b), where the spin-momentum locking appears to be destroyed, and backscattering is present.

Fluctuating charge density wave on TaS_2

1T-TaS_2 has rich phase diagram for CDW and even undergoes Mott transition at low temperatures. It is our interest to understand the frictional nature of TaS_2 due to electronic and structural phase transition driven by temperature change. We noticed that dissipation at different temperatures corresponds to the change of sample resistivity and at very low temperature dissipation resembles Joule dissipation. Room temperature measurement however shows that the fluctuation dissipation has certain dynamics (Fig. 4). Character of the noise spectrum changes from 1/f to 1/f2 when the tip approaches to surface. Different than free cantilever case, the power exponent 2 is a signature of Brownian motion process. The measurement indicates van der Waals friction present due to the fluctuations of the weakly pinned CDW. The model for van der Waals dissipation assumes the massive electric charge represented by CDW presents on the surface of TaS_2. Fluctuating CDW at finite temperatures generates fluctuating electric field that can be measured by pendulum AFM.

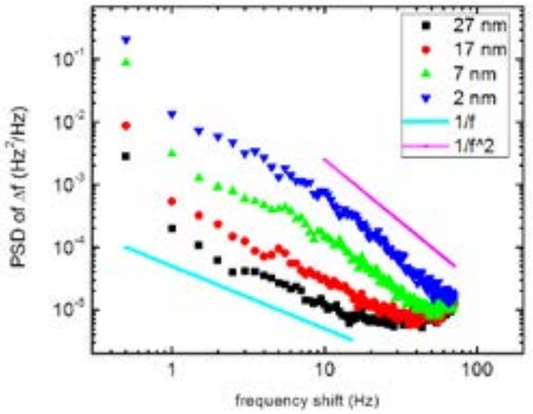

Fig. 4 Noise measurement shows that the fluctuating forces are the source of dissipation on 1T-TaS_2 surface. For a tip positioned far from the surface the noise shows 1/f1 dependence and it changes to 1/f2 for close tip-sample distances indicating Brownian motion process.

References

[1] M. Kisiel, E. Gnecco, U. Gysin, L. Marot, S. Rast, E. Meyer, *Suppression of electronic friction on Nb films in the superconducting state*, Nat. Mat. **10**, 119-122 (2011)

[2] A. Volokitin, B. N. J. Persson, H. Ueba, *Giant enhancement of noncontact friction between closely spaced bodies by dielectric films and two-dimensional systems*, JETP **104**, 96-110 (2007)

[3] M. Z. Hasan and C. L. Kane, *Topological insulators*, Rev. Mod. Phys. **82**, 3045-3067 (2010)

[4] G. Binnig, K. H. Frank, H. Fuchs, N. Garcia, B. Reihl, H. Rohrer, F. Salvan, A. R. Williams, *Tunneling Spectroscopy and Inverse Photo-emission: Image and Field States*, PRL **55**, 991-994 (1985)

Hydrodynamic force generation of predivisional bacterial cells

Project P1302: Dynamics and molecular principles of surface-based cell motility and mechanosensation
Project Leader: T. Pfohl and U. Jenal
Collaborators: N. Sauter (SNI PhD Student) and M. Sangermani

C. crescentus cells divide asymmetrically, in which a stalked mother cell produces a motile daughter cell that is equipped with pili and a single rotating flagellum. The flagellum does not only allow swimming of the daughter cell, the flagellar motor also seems to be essential for cell division and surface sensing [1, 2].

The beating of the flagellum starts about 3 – 4 min before cell separation is completed. The flagellum has an immediate onset of the rotation and is already fully assembled before the beating starts. The flagellum of the predivisional daughter cell switches its rotation direction regularly at a time scale of seconds [3].

Hydrodynamics of the flagellum – the loaded swimmer cell
For a better analysis of the duration of the clockwise (CW) and counterclockwise (CCW) rotation sequences of the flagellum and characterization of the hydrodynamic conditions, we developed a method which is also directly sensitive to flagellum-induced forces [3]. Predivisional cells attached onto micrometer-sized polystyrene beads ("loaded swimmers"), were recorded and we analyzed the duration and magnitude of the flagellum induced motion.

C. crescentus cells attach easily and quickly onto micrometer-sized polystyrene beads of differently functionalized surfaces – "non-functionalized" (polystyrene), carboxylate or amino functionalized. However, the attachment efficiency for permanent attachment, depends on the surface properties of the bead. Cells showed the highest attachment rate for carboxy-coated beads, followed by non-functionalized polystyrene beads and amino-coated beads (Fig. 1). The number of cells per bead increased over time. First attachment of cells on beads was already observed within minutes after addition of the beads to the cell suspension. The number of cells attached to a bead was not only determined by the surface coating and the incubation time, but also by the size of the bead. Larger beads accommodate more cells.

Swimming behavior of the loaded swimmer
Surprisingly, cells attached to a bead and reaching the late predivisional stage started to swim, dragging the attached bead with them. A sequence of bright field images of a swimming cell attached via a stalk and a holdfast to a colloidal bead is shown in figure 2.

The flagellum is located at the free pole of the daughter cell. This condition simplifies the determination of the swimming direction and therefore the rotation direction of the flagellum to a large extent. When the flagellum is rotating CW, it generates a pushing movement and the cell swims forward. When the flagellum is rotating CCW, it generates a pulling movement and the cell swims backwards. We are able to track the position of the bead over time. When swimming backwards (CCW rotation of the flagellum), the cell swam slightly faster than forward (CW rotation of the flagellum). Forward swimming speed was on average about 13 µm/s and backward swimming speed was on average about 18 µm/s. The loaded cell spent about 2/3 of its swimming time swimming forward and about 1/3 swimming backwards. The distribution of swimming forward and backwards respectively CCW and CW rotation of the flagellum is in good agreement with what we have found for cells attached to a solid surface and published data for the free swimming swarmer cell [4].

Determining the hydrodynamic forces
To determine and compare the forces that are generated when the flagellum is propelling a loaded predivisional cell, we characterized the cell trajectories in more detail. Therefore, we analyzed the swimming speed of predivisional cells attached to small polystyrene beads (as shown in Fig. 2) and compared it with the speed of swarmer cells and predivisional cells. With the calculated friction factor γ for the different cell shapes and sizes, we were able to determine the average force F using the measured average swimming speed.

The swimming speeds, friction factors and generated forces for swarmer cells, predivisional cells, and loaded predivisional cells are shown in figure 3.

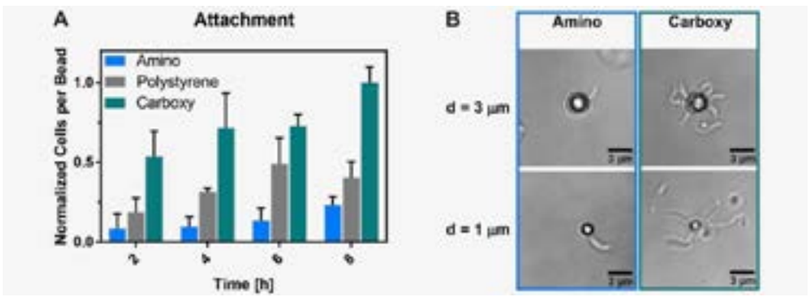

Fig. 1 Surface attachment efficiency. A: Normalized numbers of attached cells per bead. B: The number of cells attached to a bead depends on the size and the surface coating of the bead. Shown are amino- and carboxy-coated beads, with a diameter of 3 µm (top) and 1 µm (bottom) [3].

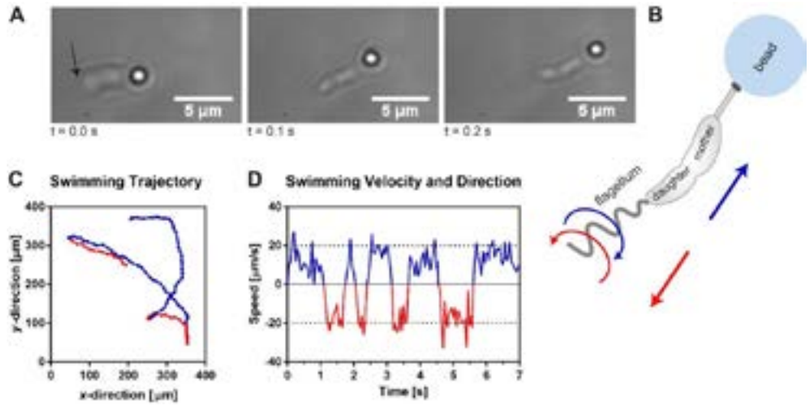

Fig. 2 Example of a swimming predivisional cell attached to a small bead. A: Consecutive bright field images of a swimming predivisional WT cell attached to a polystyrene bead with diameter 1 µm in PYE. The arrow indicates the flagellated pole. B: Scheme of the predivisional cell attached to the bead (CW rotation of flagellum, causing forward swimming: blue. CCW rotation of flagellum, causing backward swimming: red) C: Example trajectory of the swimming cell. Forward swimming: blue, backward swimming: red. D: Swimming velocity of the cell attached to the bead. Forward swimming: blue, backward swimming: red [3].

The effectively generated hydrodynamic force of a loaded predivisional cell is about 67 % of the hydrodynamic force which can be generated by a free swimming swarmer cell. This reduction of the net hydrodynamic force might be attributed to a more disadvantageous friction behavior due to the attached load.

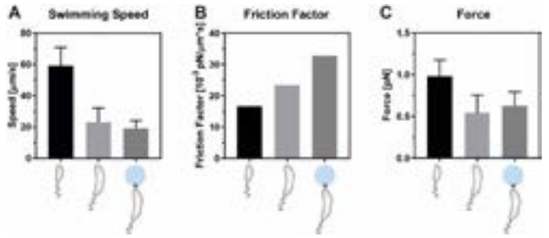

Fig. 3 Forces generated by the flagellum. A: Average swimming speed of a swarmer cell, a predivisional cell and a predivisional cell attached to a bead (from left to right). B: Friction factor of the corresponding cell shapes and sizes. C: Net force generated by the flagellum to propel the indicated cell shapes and sizes forward at the average swimming speed [3].

Conclusions
In this project, we developed a method to characterize the beating properties of the flagellum of predivisional *C. crescentus* cells and in addition to measure the flagellum-induced hydrodynamic forces. We found that the flagellum of predivisional daughter cells starts beating several minutes before the cell is released and already shows the same switching frequency of the rotation direction as free-swimming swarmer cells. In case that these predivisional cells are loaded with colloidal micro-particles, the cells swim, dragging the attached bead with them, due to the rotating flagellum. A CW rotating flagellum generates thereby a pushing movement, whereas a CCW rotating flagellum generates a pulling motion with net hydrodynamic forces of about 1 pN.

References

[1] I. Hug, S. Deshpande, K. S. Sprecher, T. Pfohl, U. Jenal, *Second messenger-mediated tactile response by a bacterial rotary motor*, Science **358**, 531-534 (2017)

[2] M. Sangermani, PhD thesis: *Pili: the microbes' Swiss army knifes*., University of Basel (2018)

[3] N. Sauter, PhD thesis: *Dynamics and Force Generation of Flagellum and Pili in Caulobacter Crescentus*, University of Basel (2018)

[4] B. Liu, M. Gulino, M. Morse, J. X. Tang, T. R. Powers, K. S. Breuer, *Helical motion of the cell body enhances Caulobacter crescentus motility*, PNAS **111**, 11252-11256 (2014)

Assembly of rotaxanes and daisy chains

Project P1303: Assembly and investigation of electrochemically triggered molecular muscles
Project Leader: M. Mayor and M. Calame
Collaborators: Y. Aeschi (SNI PhD Student), Laurent Jucker, and S. Drayss-Orth

Introduction
The rotaxane structural motif is fundamental in the realm of mechanically interlocked Molecules (MIMs)[1]. Modern syntheses of rotaxanes most frequently rely on template directed assembly, starting form pseudorotaxane host-guest complexes [1]. Control over association thermodynamics and kinetics is required to design and synthesis MIMs in a modular fashion. This has led to the evolution of more complex topologies such as molecular knots, sheafs or daisy chains. Not only extension of topological complexity but also the synthesis of inter-locked, functional molecules was achieved. As a result, a multitude of molecular shuttles, muscles and elevators are known to date [2].

Within Project P1303, the use of a hydrophobic driving force for the synthesis of MIMs was examined. In particular the optimization of daisy chain synthesis was a key goal. For this purpose, a recognition motif with a high binding strength and synthetic extensibility was chosen. Diederich-type cyclophanes were identified as ideal receptors, while a multitude of suitable guest components are strongly complexed by this type of host. Based on Cyclophane **1**, syntheses of (pseudo) rotaxanes and daisy chains were realized within the project. Three publications have resulted from these investigations, which are presented herein.

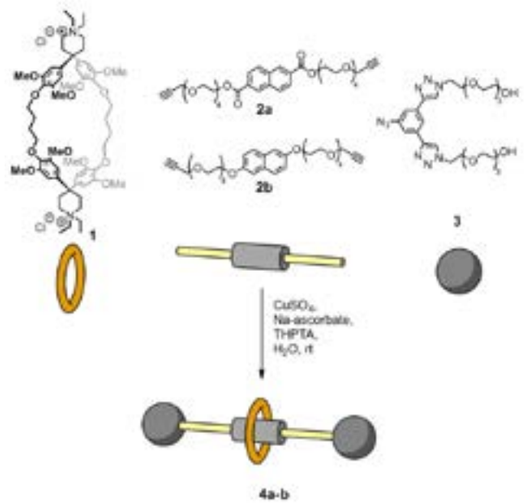

Fig. 1 Assembly of [2] rotaxanes from cyclophane **1**, *tetra-ethylene glycol substituted naphthalenes* **2a/b** *and stopper* **3**.

Aqueous Assembly of [2]Rotaxanes [3]
Naphthalene guests substituted with tetraethylene glycol chains in the 2,6-positions (**2a/b**) show high association constants (10^4-10^5 M^{-1}) with cyclophane **1** in water.

The alkyne termini of **2a/b** were introduced as reactive sites for Copper-catalyzed azide-alkyne cyclo-addition (CuAAC). Azide-functionalized stopper **3** allowed to obtain interlock the pseudorotaxane complex formed between **1** and **2a/b**, furnishing **4a/b** in 59 and 19 % yield respectively.

Aqueous Assembly of Zwitterionic Daisy Chains[4]
A descendant of cyclophane **1** was synthesized, to which a dianionic OPE-rod was tethered, furnishing a daisy chain monomer. Driven by a hydrophobic effect combined with coulombic interaction, this monomer aggregates strongly in aqueous media, forming interlinked structures.

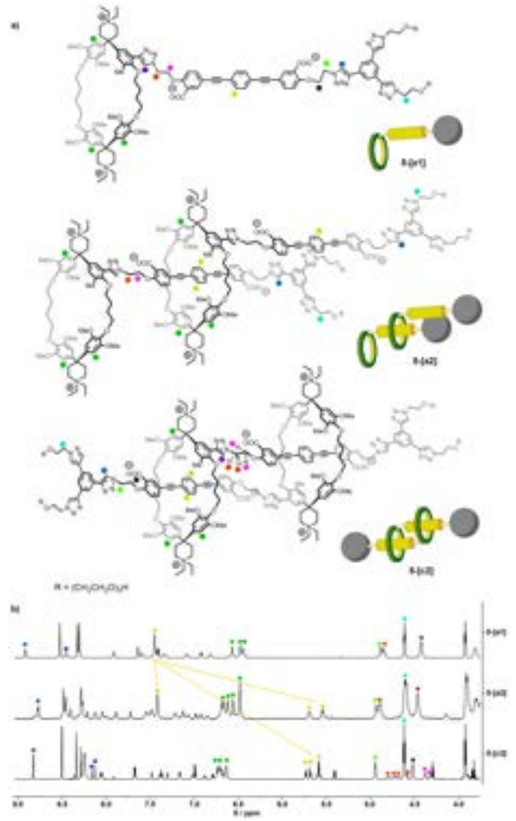

Fig. 2 a) Molecular structures and graphic representations of the molecular daisy chains. b) Partial 1H-NMR-pectra of the daisy chains, including structural assignments (colored dots)

In analogy to the rotaxane synthesis, interlocked daisy chains were obtained by reacting the inter-linked structures with a bulky stopper in a CuAAC reaction. A mixture of compounds was obtained, which was separated by consecutive preparative HPLC. Three major products were isolated (Fig. 2a), which were identified as stoppered monomer (**5-[a1]**; 7.3 %), acyclic dimer (**5-[a2]**; 3.0 %) and cyclic dimer (**5-[c2]**; 30 %). Cyclic dimers are typically obtained as the major product as formation of smaller aggregates is entropically favored [5]. The compounds were subsequently characterized by 1H-NMR (Fig. 2b), where

the presence of complexed OPE-phenylene protons results in the resonances between 5.5 and 5.8 ppm. Due to the unsymmetric nature of the subunits, **5-[c2]** consist of a mixture of diastereomers. This can be concluded from the occurrence of two separate sets of resonances of the OPE phenylene protons at ~5.6 ppm.

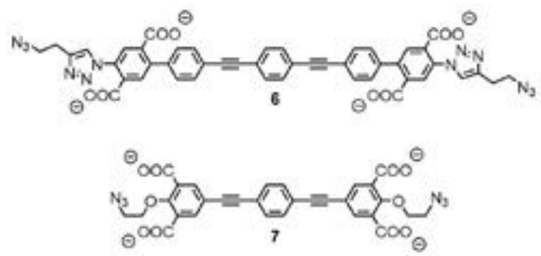

Fig. 3 Molecular structures of **6** *and 7. Sodium counterions are omitted for clarity.*

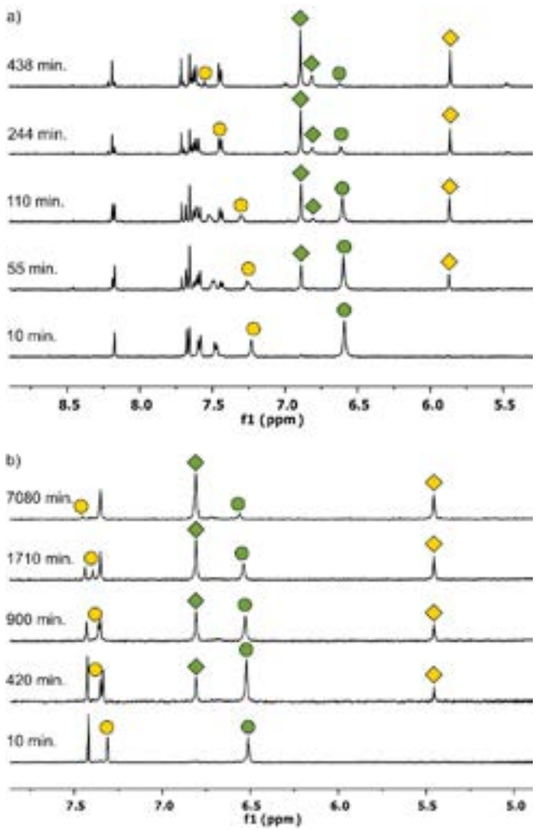

Fig. 4. Time-dependent 1H-NMR data for the complexation of a) 6 and b) 7 1. Circles denote signals with decreasing intensity during the time course of measurement, diamonds denote signals with increasing intensity. The green color denotes cyclophane aryl protons, The yellow color denotes phenylene protons of **6** *and 7.*

Slow Formation of Pseudorotaxanes in Water
The beneficial effect of electrostatically complementary host and guest components was expanded to tetraanionic OPE rods with terephthalic and salicylic acid termini (Fig. 3). The tetraanionic character not only improves solubility in water, but also slows down the association process to form pseudorotaxanes with **1**.

Monitoring by 1H-NMR revealed half-lives of several hours for the reactions (Fig. 4). The pseudorotaxane complexes become apparent by the phenylene proton resonances, which are shifted to ~5-6 ppm. The slow association process is a result of the steric demand of phthalate termini, posing an activation barrier to overcome. Furthermore, the terminal azide functionality of these compounds enables the integration of such OPE rods into more complex rotaxane systems.

Conclusion
Aqueous-based recognition based on Diederich-type cyclophanes and conjugated guests as a valuable tool for constructing MIMs due to their strong interaction and synthetic versatility. The developed CuAAC stoppering strategy with **3** or its derivatives allows to obtain mechanically interlocked species. The synthesis of rigid daisy chains in aqueous media represents is rarely achieved, particularly due to the difficulty of balancing hydrophilic and hydrophobic properties. Finally, the phthalate solubilizers have shown their potential for controlling host-guest association kinetics while providing a high affinity towards **1**. Integration of terephthalate termini into daisy chain structures may result in daisy chains with kinetically controllable association modes.

References

[1] C. J. Bruns, J. F. Stoddart, *The Nature of the Mechanical Bond*, Wiley, (2016)

[2] S. Erbas-Cakmak, D. A. Leigh, C. T. McTernan, A. L. Nussbaumer, *Artificial Molecular Machines*, Chem. Rev, **115**, 10081 (2015)

[3] Y. Aeschi, S. Drayss-Orth, M. Valášek, F. Raps, D. Häussinger, M. Mayor, *Assembly of [2]-Rotaxanes in water*, Eur. J. Org. Chem, **28**, 4091 (2017)

[4] Y. Aeschi, S. Drayss-Orth, M. Valášek, D. Häussinger, M. Mayor, *Aqueous Assembly of Zwitterionic Daisy Chains*, Chem. Eur. J, **25**, doi.org/10.1002/chem.201803944 (2019)

[5] J. Rotzler and M. Mayor, *Molecular daisy chains*, Chem. Soc. Rev, **42**, 44 (2013)

Monitoring β-barrel membrane protein folding

Project P1304: Folding mechanisms of β-barrel outer membrane proteins and their catalysis by natural holdases and foldases
Project Leader: S. Hiller and D. J. Müller
Collaborators: N. Ritzmann (SNI PhD Student), P. Rios Flores, T. Raschle, and J. Thoma

The biogenesis of outer membrane proteins (Omps) poses a complex biophysical challenge to the pro- and eukaryotic cell, because the Omps are synthesized at locations distant from their target membrane. Essential parts of Omp biogenesis are accomplished by molecular chaperones that pass the unfolded substrates from the ribosome to the destination membrane [1]. In the Gram-negative bacterium E. coli, periplasmic chaperones SurA and Skp transport the substrate to the Bam complex, which folds and inserts them into the outer membrane [2]. The in vitro and the in vivo folding mechanisms of β-barrel Omps from mitochondria or Gram-negative bacteria are so far not understood. In this project, we employ structural biological and nanotechnological approaches to characterize the folding process of complex Omps at molecular detail. In the following we report several papers, which we published since starting our project and thereafter provide an overview of the following challenges in this project.

Monitoring Backbone Hydrogen Bond Formation

The three-dimensional structure of a β-barrel membrane protein is defined by backbone hydrogen bonds between adjacent strands. The biogenesis pathways of β-barrel membrane proteins are essential, but the underlying mechanism is still unclear. To obtain insight into this process, we used the 8-stranded OmpX from E. coli as a model system. At the onset of the experiment, OmpX (148 aa) was solubilized in chaotropic denaturant solution, where the polypeptide was fully unfolded and adopted a random coil conformation without residual structure. By studying how this coil folds, we found that the residue-specific kinetics of interstrand hydrogen-bond formation are uniform in the entire β-barrel and synchronized to formation of the tertiary structure. OmpX folding propagates via a long-lived conformational ensemble state in which all backbone amide protons engage in hydrogen bonds only transiently. Stable formation of the entire OmpX hydrogen bond network occurs downhill of the rate-limiting transition state and appears cooperative on the overall folding time scale.

Chaperone Assisted Insertion and Folding

The correct insertion and folding of membrane proteins is essential for living cells. Whereas in living cells molecular chaperones increase the folding yields of soluble proteins by suppressing misfolding and aggregation, it is not understood how they modulate the insertion and folding of integral membrane proteins into membranes. To study this process, we used single-molecule force spectroscopy (SMFS) and NMR spectroscopy to characterize how periplasmic holdase chaperones SurA and Skp shape the folding trajectory of the large β-barrel Omp FhuA from E. coli [4]. After having unfolded and extracted a single FhuA from the lipid membrane by SMFS, we monitored how the unfolded polypeptide inserts and folds into the membrane. The unfolded FhuA polypeptide is prone to misfolding and cannot insert into the membrane (Fig. 1). However, the presence of either of the two periplasmic chaperones SurA or Skp prevented misfolding by stabilizing a dynamic, unfolded state. Thereby SurA allowed the unfolded substrate to stepwise insert and fold the unfolded FhuA polypeptide towards its native structure.

Maltoporin Unfolding Pathways

The next challenge in this project was to study whether Omps generally unfold and fold similarly to FhuA. We hence first unfolded maltoporin LamB from E. coli by SMFS [5]. It was observed that also maltoporin stepwise unfolds β-hairpins until the β-barrel has been completely unfolded and extracted from the membrane. Thereby the folding probability of a β-hairpin was found to be correlated to its mechanical stability. The study was fundamental to characterize at later stage the insertion and folding of other Omps by BAM.

Characterizing the β-barrel assembly factor BAM

The core component BamA of the β-barrel assembly machinery (BAM) adopts several conformations, which are thought to facilitate the insertion and folding of β barrel proteins into the bacterial outer membrane. Which factors alter the stability of these conformations remains to be quantified. We thus applied SMFS to characterize the mechanical properties of BamA from E. coli (Fig. 2) [6]. In contrast to the N-terminal periplasmic polypeptide-transport-associated (POTRA) domains, the C-terminal transmembrane β-barrel domain of BamA is mechanically much more stable. Exposed to mechanical stress this β-barrel stepwise unfolds β-hairpins until unfolding has been completed. Thereby, the mechanical stabilities of β-barrel and β-hairpins are modulated by the POTRA domains, the membrane composition and the extracellular lid closing the β-barrel. We anticipate that these differences in stability, which are caused by factors contributing to BAM function, promote conformations of the BamA β-barrel required to insert and fold outer membrane proteins.

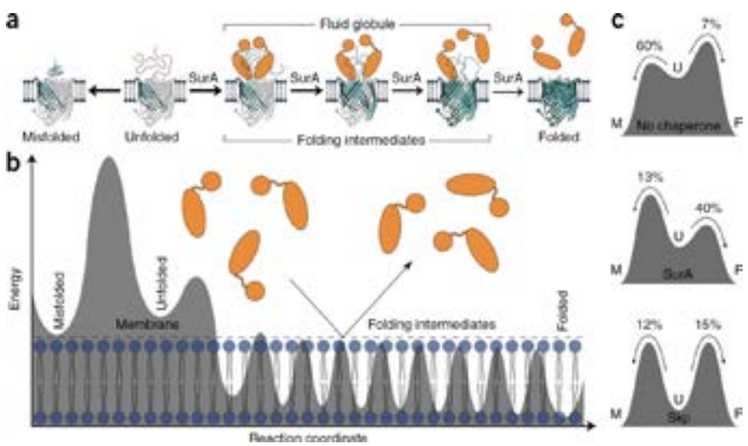

Fig. 1 Folding of FhuA receptors. a) Insertion and folding pathways of FhuA in the absence and in the presence of the SurA chaperone (orange). Without SurA, the majority of unfolded FhuA receptors misfold. SurA stabilizes the unfolded state of FhuA and promotes step-wise insertion and folding of β-hairpins in the lipid membrane until the receptor completed folding. b) Hypothetical folding free-energy landscape of FhuA in the presence of SurA. SurA is excluded from the membrane (blue). Each β-hairpin inserted into the membrane is stabilized by a free-energy well. c) Modulation of the folding free-energy landscape by SurA and Skp chaperones. Free-energy barriers separate the unfolded (U) from the misfolded (M) and folded (F) states. Image taken from ref [4].

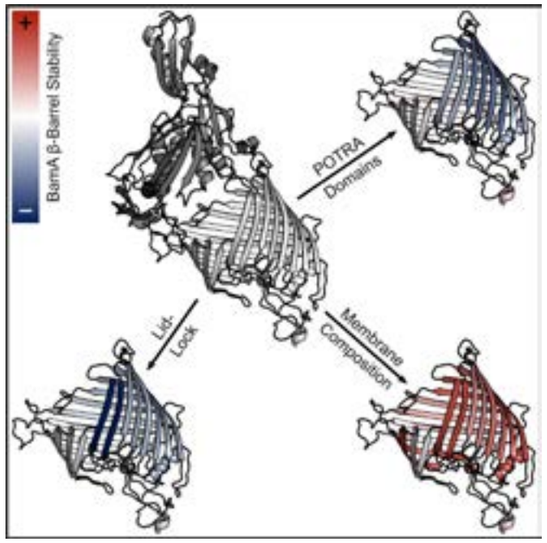

Fig. 2 Factors influencing the stability of BamA. Image taken from ref [6].

Directed Insertion of Membrane Proteins

In an attempt to study how whether we could already apply the knowledge gained in this proposal and guide the insertion of membrane proteins, we engineered light-driven proton pumps having either a red (RFP) or green (GFP) fluorescent protein fused to its N- or C-terminus [7]. The hydrophilic fluorescent proteins allowed the directed insertion of proton pumps into liposomes and to select the liposomes depending on fluorescence. The thus manufactured nanoreactors were used to generate proton gradients by light, which is a prerequisite to power a broad variety biomolecular processes. In the future, this side project will enable to supply nanoscopic factories with energy and to translocate polypeptides or other molecules across membranes.

Latest progress and Challenges Ahead

Within the last year, we could achieve considerable progress in preparing outer membrane vesicles (OMVs) from E. coli [8] and begun to characterize the Bam insertion machinery at close to native conditions. Currently we are in the process of gathering enough SMFS and NMR data to understand how the Bam complex facilitates the insertion and folding of complex Omps. Given the complexity of the insertion and folding process and the multiple molecular machines involved in this process (BamA, -B, -C, -D, -E and SurA, Skp, etc), the systematic study of all details of this exciting process will require substantial additional efforts. Encouraged by our substantial results so far, with all these years of hard work we have made a big step towards understanding how the periplasmic chaperones SurA and Skp transport the Omp substrate to the Bam complex, and how they together fold and insert the substrates into functional Omp structure. It may be only a matter of time until we can then use these insights to assemble nanomachines in membranes.

References

[1] T. J. Knowles, A. Scott-Tucker, M. Overduin, I. R. Henderson, *Membrane protein architects: the role of the BAM complex in outer membrane protein assembly*, Nat Rev Microbiol **7**, 206 (2009)

[2] J. G. Sklar, T. Wu, D. Kahne, T. J. Silhavy, *Defining the roles of the periplasmic chaperones SurA, Skp, and DegP in Escherichia coli*, Genes Dev **21**, 2473 (2007)

[3] T. Raschle, P. Rios Flores, C. Opitz, D. J. Müller, S. Hiller, *Monitoring backbone hydrogen bond formation in β-barrel membrane protein folding*, Angew Chem Int Ed **55**, 5952 (2016)

[4] J. Thoma, B. M. Burmann, S. Hiller, D. J. Müller, *Impact of holdase chaperones Skp and SurA on the folding of β-barrel outer membrane proteins*, Nat Struct Mol Biol **22**, 795 (2015)

[5] J. Thoma, N. Ritzmann, D. Wolf, E. Mulvihill, S. Hiller, D. J. Müller, *Maltoporin LamB unfolds beta-hairpins along mechanical stress-dependent unfolding pathways*, Structure **25**, 1139 (2017)

[6] J. Thoma, Y. Sun, N. Ritzmann, D. J. Müller, *POTRA domains, extracellular lid, and membrane composition modulate the conformational stability of the β barrel assembly factor BamA*, Structure **26**, 987 (2018)

[7] N. Ritzmann, J. Thoma, S. Hirschi, D. Kalbermatter, D. Fotiadis, D. J. Müller, *Fusion domains guide the oriented insertion of light-driven proton pumps into liposomes*, Biophys J **113**, 1181 (2017)

[8] J. Thoma, S. Manioglu, D. Kalbermatter, P. D. Bosshart, D. Fotiadis, D. J. Müller, *Protein-enriched outer membrane vesicles as a native platform for outer membrane protein studies*, Commun Biol **1**, 23 (2018)

Solid supports for serial protein crystallography: From silicon to polymer technology

Project P1305: X-FEL based dynamic studies on 2D and 3D nanocrystals of membrane proteins on solid supports
Project Leader: C. Padeste and H. Stahlberg
Collaborators: N. Opara (SNI PhD Student), T. Braun, X.-D. Li, I. Martiel, and A. Karpik

In 2018, commissioning and pilot experiments have been carried out at SwissFEL, the new X-ray Free Electron Laser (XFEL) facility located at PSI. In the field of protein crystallography, such ultra-high brightness X-ray sources provide new possibilities to determine the 3-dimensional atomic structure of micro- and nano-crystals based on X-ray diffraction, which is often difficult to achieve with synchrotron X-ray sources. One of the important characteristics of XFEL-based crystallography, however, is the destruction of the crystals by the extremely intense femtosecond X-ray pulses. In order to obtain com-plete data sets, large numbers of crystals need to be sequentially delivered at a high frequency to the probing X-ray beam. This serial crystallography approach has been demonstrated by applying protein crystal handling methods such as liquid jet and lipidic cubic phase injection technologies, as well as the so-called fixed target technology [1]. In the latter, the crystalline sample is deposited on a thin film support, which is mounted on a stage and scanned through the beam, thus sequentially probing the individual crystals with the focused X-rays.

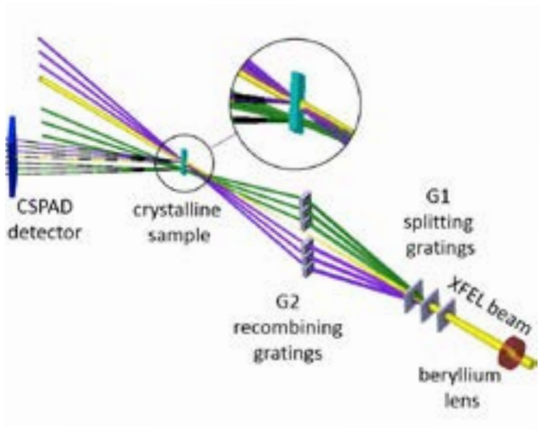

Fig. 1 Scheme of the used X-ray optics set-up used for X-ray pump/ x-ray probe experiments at LCLS (adapted from [3]): a set of diffraction gratings is used to couple a fan of beams from the primary X-FEL pulse. A second set of gratings redirects the beams back to the sample, where they arrive with defined time delays (19-213 fs). The crystal is first hit by the intense pump beam (yellow) followed by probing pulses (purple) with defined time delays. A second set of delayed beams (green, reference) is hitting the crystal in an unpumped region. Pump, probe and reference beams are diffracted at the same Bragg plane of the protein crystal result in a set of spatially separated peaks on the detector. The dashed lines (- - -) indicate diffracted beams from the crystals collected on a CSPAD detector. For control measurements, the pumping beam can be blocked with an attenuator.

In this project, we focused on novel concepts and optimization of supports for specific applications in serial protein crystallography. In the first part, we developed a silicon/silicon nitride-based system for X-ray pump/X-ray probe experiments [2]. To address the time dependence of X-ray radiation damage to lysozyme crystals, a split-and-delay line based on diffractive X-ray optics was used (Fig. 1), which was designed by the X-ray optics group of PSI (led by Dr. Christian David), and temporarily built up at the LCLS, the Linac Coherent Light Source at Stanford University. Lysozyme microcrystals were grown directly on in-house fabricated silicon chips with arrays of silicon nitride windows, which were sealed with second chip to prevent the crystals from dehydration [2]. The samples were then mounted on a scanning stage that allowed addressing the individual windows at a frequency of up to 1 Hz [3].

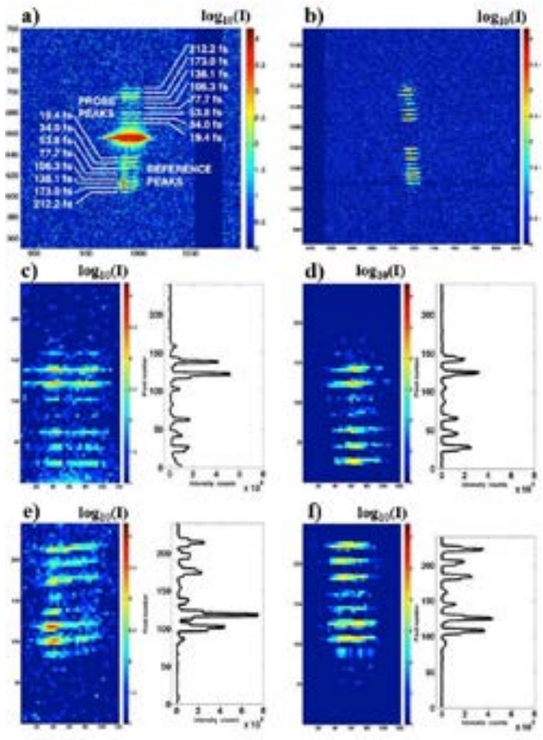

Fig. 2 Examples of registered diffraction signals of (a) a pumped shot and (b) an unpumped shot. c) - f) Regions of interest selected for intensity integration (logarithmic scale) and delayed peaks' intensity profiles (linear scale) representing values of counts registered on the detector after integration in x direction. c) and d) probe and e) and f) reference part of the signal of a) and b) respectively [3].

The experimental set-up allowed covering time-scales relevant for serial femtosecond crystallography by providing probe signals at eight different delay times between 19 and 213 femtoseconds after each X-ray pump event (Fig. 2). The obtained results were summarized as follows [3]: "Even though significant impact on the crystals was observed at long time scales after exposure with single X-ray pulses, the collected diffraction data showed no significant signal reduction that could be assigned to beam damage on the crystals in the sampled time window and resolution range. This observation is in agreement with estimations of the applied radiation dose, which in these experiments was below the values expected to cause damage on the femtosecond time scale. Nonetheless, the experiments demonstrated the feasibility of time-resolved pump-multiprobe X–ray diffraction experiments on protein crystals."

More recently we concentrated on polymer-based supports for application at SwissMX, the fixed target endstation implemented at SwissFEL. This endstation is equipped with an automated sample changer and a uniquely fast and precise scanning stage to collect data on randomly dispersed micro-crystals at a rate of up to 100 Hz. To take full advantage of the precious XFEL beamtime, hit rate enhancing techniques are being developed, such as crystal prelocation using microscopic techniques or crystal prepositioning in specially designed supports. Furthermore, the background of the supports needs to be minimized to allow extracting high-resolution data from the challenging, weakly diffracting microcrystalline samples. Reliable, but simple sample preparation and large-scale availability of low-background supports are crucial for efficient data collection, since hundreds to thousands of samples need to be measured during one beam-time slot. To meet these needs, we started the development of polymer-based supports, optimized for low background by minimizing the thickness of the support membrane and by providing the ability for efficient blotting of the protein crystallization solution (Fig. 3).

Fig. 3 Functionality of the polymer supports: The crystal suspension is deposited on an ultrathin perforated polymer film suspended in a polymer frame; using blotting paper the solution is blotted from the backside of the support, immediately before shock-freezing of the sample.

For the commissioning of SwissMX in November 2018 we provided several hundred supports, consisting of a 2 µm thick polymer film with periodic perforations of 2 µm in diameter and 4 µm distance, suspended in a polymer frame (Fig. 4). The efficiency of the blotting was confirmed in synchrotron and XFEL-based measurements, which showed diffraction patterns from crystals of different proteins on a very low, diffuse background. Furthermore, the ultrathin polymer membrane provided enough stability for multiple probing by unattenuated XFEL pulses at distances below 100 µm, thus enabling efficient probing of the deposited samples.

Even though originally motivated by XFEL applications, the serial diffraction data collection approach is gaining increasingly more importance also for synchrotron-based protein crystallography. Due to faster high-sensitivity detectors, improved indexing and structure determination routines, as well as higher brilliance and lower focal spot sizes achieved in most recently built or upgraded synchrotron sources, collection of data sets from a series of microcrystals rather than from one or a few large single crystals has become an interesting alternative, especially for challenging targets such as membrane proteins [4]. The experience in the fabrication of dedicated supports gained during this SNI project will be valuable for further developments of supports for serial diffraction experiments on protein crystals at both, synchrotron and free electron laser X-ray sources.

Fig. 4 Polymer supports mounted on pins fitting to the sample-changing robot. The area of the perforated 2 µm thick polymer film is 2x2 mm2 in size, suspended in a 5x5 mm2 sized frame.

References

[1] M. S. Hunter et al., *Fixed-target protein serial microcystallography with an x-ray free electron laser*, Sci. Rep. **4**, 6026 (2014)

[2] N. Opara, I. Martiel, S. A. Arnold, T. Braun, H. Stahlberg, M. Makita, C. David, C. Padeste, *Direct protein crystallization on ultrathin membranes for diffraction measurements at X-ray free electron lasers*, J. Appl. Cryst. **50**, 909-918 (2017)

[3] N. L. Opara et al., *Demonstration of femtosecond X-ray pump X-ray probe diffraction on protein crystals*, Structural Dynamics **5**, 054303 (2018)

[4] T. Weinert et al., *Serial millisecond crystallography for routine room-temperature structure determination at synchrotrons*, Nat. Commun. **8**, 542 (2017)

Optoelectronic characterization of graphene-based nanojunctions

Project P1307: Optoelectronic nanojunctions
Project Leader: M. Calame and M. Mayor
Collaborators: J. Overbeck (SNI PhD Student), O. Braun, M. Perrin, G. Borin Barin, Q. Sun, R. Darawish, R. Fasel, C. Daniels, and V. Meunier

Introduction

In this project, we investigate transport phenomena in nanojunctions, adding optical measurement techniques to better characterize the materials and interfaces involved. Starting with mechanically controlled break junction (MCBJ) measurements on small molecules [1] we extended this technique to the investigation of strain effects in suspended graphene membranes by combined transport measurements and Raman spectroscopy, see report of 2017 for details. That technique has been used to investigate a variety of nanomaterials for electronic devices as detailed below.

Longitudinal Modes in Graphene Nanoribbons

Graphene Nanoribbons (GNR) are thin stipes of graphene that exhibit an electronic bandgap due to lateral confinement of charge carriers and edge effects [2]. Our collaborators at Empa synthesize these ribbons from molecular precursors under UHV conditions. Their atomically well-defined structure makes them promising candidates for novel electronic device architectures. Through the choice of molecular precursor, the width of armchair-edge AGNR can be precisely controlled. The length, which is crucial for device-integration, varies greatly as a function of process parameters. We characterized these ribbons with Raman spectroscopy to gain insights into their vibrational properties and assess the transfer process from growth to device substrates. Figure 1 shows low energy Raman spectra for several AGNRs, all exhibiting a low-energy mode that we attribute to a longitudinal compressive mode (LCM). Samples with a large number of short ribbon segments (verified by STM) exhibit spectrally separated peaks at low energy. Comparison with DFT simulation allow us to clearly identify these modes as signatures of GNR formed by the polymerization of 2 or 3 precursor molecules.

Substrate Interaction & GNR-alignment

The long vibrational wavelength of the newly identified LCM makes it more sensitive to substrate interactions than other Raman active modes. We have designed an optimized sample structure that leads to an interference-enhanced Raman signal with low substrate related background. In combination with added capabilities to measure at low temperatures, this allows us to investigate the interaction of GNRs with device substrates. This study is key for understanding nanojunctions formed by different materials. A manuscript is in preparation. Furthermore, modelling the film of GNR as an ensemble of scattering dipoles has allowed us to extract the degree of alignment of GNRs on growth and device substrates (Fig. 2). This has led to a new study on the influence of ribbon density on GNR alignment by R. Fasel et al. Moreover, polarization dependent measurements are an additional tool for understanding the properties of low energy modes and verifying their ribbon-origin.

Extension to non-armchair GNR

GNR with zigzag-edge structure are more reactive under ambient conditions, which limited their use for devices so far. Recently, we investigated a new type of GNR with a mixed armchair and zigzag edge structure by Raman spectroscopy in vacuum and confirm its stability after transferring to devices. The corresponding transport measurements are shown in figure 3 below.

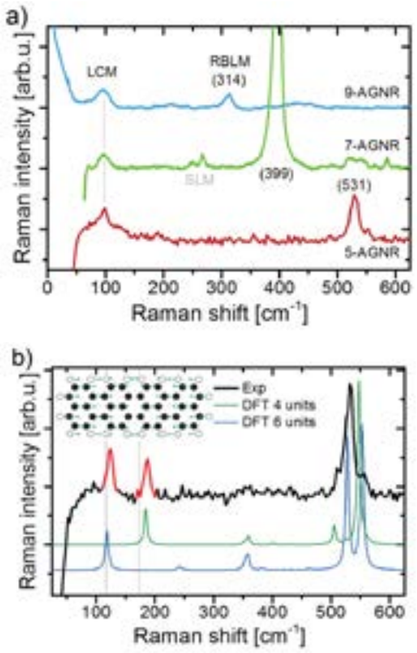

Fig. 1 a) Low-energy Raman spectra of 5-, 7-, and 9-atom wide AGNR. b) Spectrum of a sample with exceptionally short ribbons showing two spectrally separated low-energy peaks and simulated Raman spectra for short ribbon segments (inset).

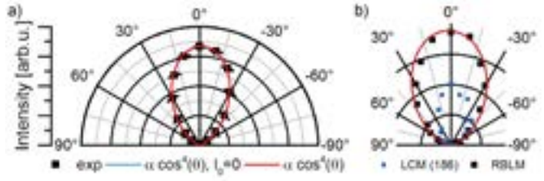

Fig. 2 a) Polar plots of Raman intensity fitted with different dipole models. b) Comparison of polarization dependent intensities for RBLM an LCM.

Transport Experiments on Graphene Nanoribbons

In parallel with the optimization of the growth & transfer processes of the ribbons we expanded the fabrication and characterization of GNR-devices in a field-effect transistor geometry. Building on previous work with electrodes fabricated by an electrical breakdown technique [3], we are currently preparing a manuscript reporting the transport properties of aligned metallic GNR. Furthermore, we established the fabrication of top-down patterned graphene electrodes allowing us to reach more than 1000 devices per chip. Figure 3 shows IV-curves and a stability diagram measured on a sample with randomly oriented GNRs showing Coulomb blockade. Over the course of a project work by Nanoscience student Silvan Käser, we improved the electrical characterization methods so that hundreds of devices could be tested. This approach is now being applied to the above-mentioned types of GNR and extended to structures with local gates to selectively gate electrodes and nanoribbons.

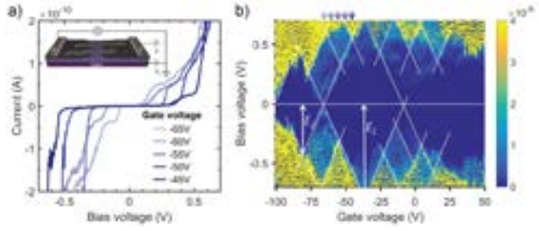

Fig. 3 a) Current-voltage traces at various gate voltages (corresponding positions in panel b) indicated with arrows) for GNR contacted by graphene electrodes. The inset shows the schematic of the device and measurement set-up. b) dI/dV-map as a function of the applied bias voltage and gate voltage. White dotted lines are guides to the eye. Measurements at 9K.

Organic Thermoelectric Materials

In a collaboration with a second group at Empa and TU Munich, we used Raman spectroscopy to investigate the electronic properties of molecular thin-films of PEDOT:PSS upon the introduction of inorganic salts [4]. The increase in intensity and up-shift of the band at roughly 1500 cm^{-1} indicates a change of the PEDOT towards its benzoid form, accompanied by a reduced conductivity and lower thermoelectric power factor (Fig. 4). This study extends the use of Raman spectroscopy in our lab from sp2-carbon materials to the optimization of thin films relevant for electronic applications.

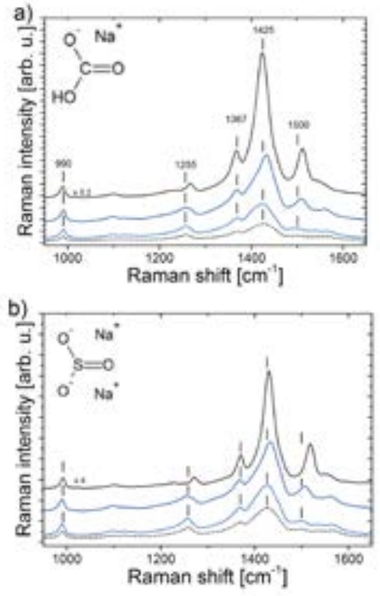

Fig. 4 Raman spectra on PEDOT:PSS de-doped with the inorganic salts shown as inset. Increasing salt concentration from bottom (reference) to top.

Summary and Outlook

We have established measurement strategies that allow us to use Raman spectroscopy for the characterization of various nanostructured materials, in particular, graphene nanoribbons. We have identified a new vibrational signature in GNR that is sensitive to the weak interactions of sp2-carbon materials with device substrates, which will advance our understanding of graphene-GNR junction formation. Moreover, we have established Raman spectroscopy as a tool to monitor the fabrication process of GNR-based devices. This increased the reliability in sample fabrication and allows us to achieve device yields that make statistical data analysis approaches similar to those of the MCBJ approach feasible for the future.

Acknowledgements

We thank Roman Furrer for help with CVD-Graphene growth, Silvan Käser for help with GNR Transport Measurements and Marta de Luca for fruitful discussions.

References

[1] A.Vladyka, M. Perrin, J. Overbeck, R. R. Ferradas, V Garcia- Suarez, M. Gantenbein, J. Brunner, M. Mayor, J. Ferrer, M. Calame, *In-situ formation of one-dimensional coordination polymers in molecular junctions,* Nature Communications 10, 262 (2019)

[2] J. Cai et al. *Atomically precise bottom-up fabrication of graphene nanoribbons*, Nature **466**, 470 (2010)

[3] M. El Abbassi, L. Pósa, P. Makk, C. Nef, K. Thodkar, A. Halbritter, M. Calame, *From electroburning to sublimation. Substrate and environmental effects in the electrical breakdown process of monolayer graphene*, Nanoscale **9**, 17312 (2017)

[4] N. Saxena, J. Keilhofer, A. K. Maurya, G. Fortunato, J. Overbeck, P. Müller-Buschbaum, *Facile optimization of thermoelectric properties in PEDOT:PSS thin films through acido-base and redox dedoping using readily available salts,* ACS Applied Energy Materials **1**, 336 (2018)

Crystalline and free-standing calixarene-based monolayers and bilayers

Project P1308: Supramolecular charge and spin architectures produced by chemical clipping
Project Leader: P. Shahgaldian and T. Jung
Collaborator: M. Moradi (SNI PhD Student)

Introduction

The possibility to fabricate materials with a meticulous control over the organization of molecular building blocks has, for decades, mobilized the attention and efforts of chemists and material scientists. This control was anticipated to allow for the production of advanced materials with tunable physicochemical properties and functionalities. With major progresses crystal engineering has undergone over the past few decades, this major scientific aspiration turned out to become reality. A fact that strongly substantiates this statement is the emergence of metal- or covalent-organic frameworks (MOFs and COFs). It is, however, challenging to apply those design strategies to two-dimensional systems.

This PhD project aimed at developing a novel approach for the design of supramolecular layers with an atomically precise architecture and thickness on solid surfaces. It stems from findings achieved by the project partners on the stabilization of Langmuir-Blodgett (LB) films through a self-assembly process using supramolecular clips [1].

In the frame of this project, we have focused our efforts on the self-assembly of calixarenes to form organized monolayers using either supramolecular or coordination bonds. Calixarene are macrocyclic molecules produced by the base-catalyzed reaction of substituted phenols and formaldehyde. When suitably modified, they exhibit amphiphilic properties and have been extensively studied for their self-assembly properties. In order to produce crystalline calixarene-based monolayers, we produced a series of derivatives bearing short alkyl chains at the lower rim and polar functions at the upper rim (i.e. carboxylate, methyl-carboxylate and cyano) (Fig. 1).

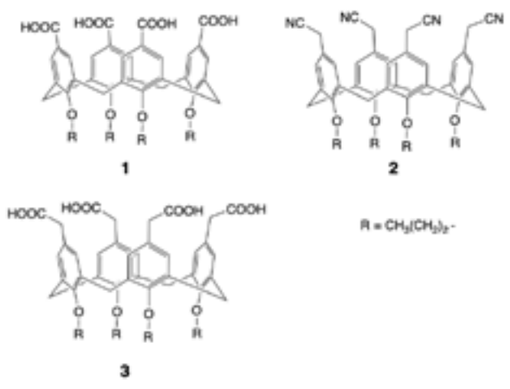

Fig. 1 Chemical structure of O-propyl calixarene derivatives

Results

The parent calix[4]arene was first alkylated via a Williamson reaction in basic conditions. Carried out at room temperature, the alkylated derivative is locked in the cone conformation. The calix[4]arenetetracarboxylic acid **1** was obtained by oxidation of the tetraformyl derivative produced by reacting the alkylated calixarene with hexamethylenetetramine. The study of the self-assembly properties of **1**, in the presence of transition metal ions, allowed producing the first example of a metal–organic coordination network based on a complex three-dimensional amphiphile. The method developed allows for the fabrication of extended crystalline layers at the air–water interface and on solid surfaces [2].

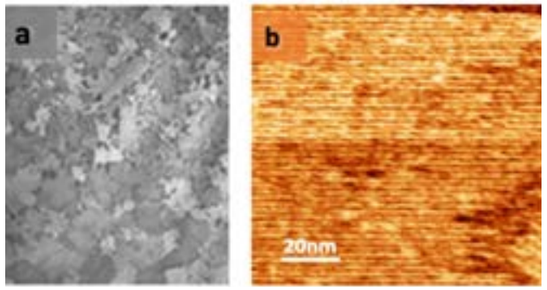

Fig. 2 Brewster angle (a) and atomic force (b) micrographs of 1-based self-assembled monolayers.

Crystallization of **2** yielded crystals suitable for X-ray diffraction studies with synchrotron radiation. The resulting structure showed that **2** is in the pinched-cone conformation and that cyano functions point away from the calixarene cavities. This amphiphile packs in a bi-layer fashion with hydrophobic layers alternating within the extended structure.

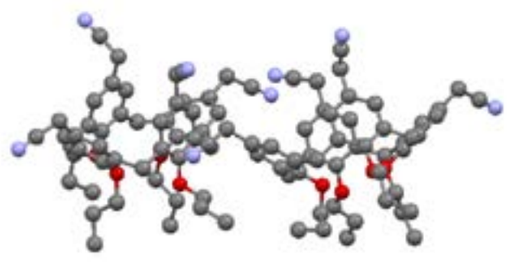

Fig. 3 Extended structure found in the crystal structure of 1 showing methyl-cyano functionalities pointing away from macrocycle cavities. Color code: C – grey, N – blue, O – red. Hydrogen atoms are omitted for clarity.

The study of the self-assembly properties of the cyano-modified derivative, **2**, revealed a behavior drastically different from that of **1**. Indeed, we demonstrated that even in the presence of coordination metal ions, the self-assembly of the amphiphile is mainly driven by dipole-dipole (-CN· · ·NC-) interactions. Acting in a synergistic fashion, these interactions allow for a remarkable monolayer stability. It is an accepted paradigm that strong and directional interactions are needed for the design of stable supramolecular architectures. The present, first example of a stable free-standing monolayer predominantly stabilized via dipole-dipole, i.e. non covalent and slightly directional, interactions provides a first violation of this paradigm. Combining Langmuir isotherm results, XPS, NEXAFS and AFM, we established a molecular model of the packing of 2-based monolayers (Fig. 3). Even more remarkably, the free-standing layers produced have been demonstrated to be stable when submitted to photon, photoelectron and electron irradiations.

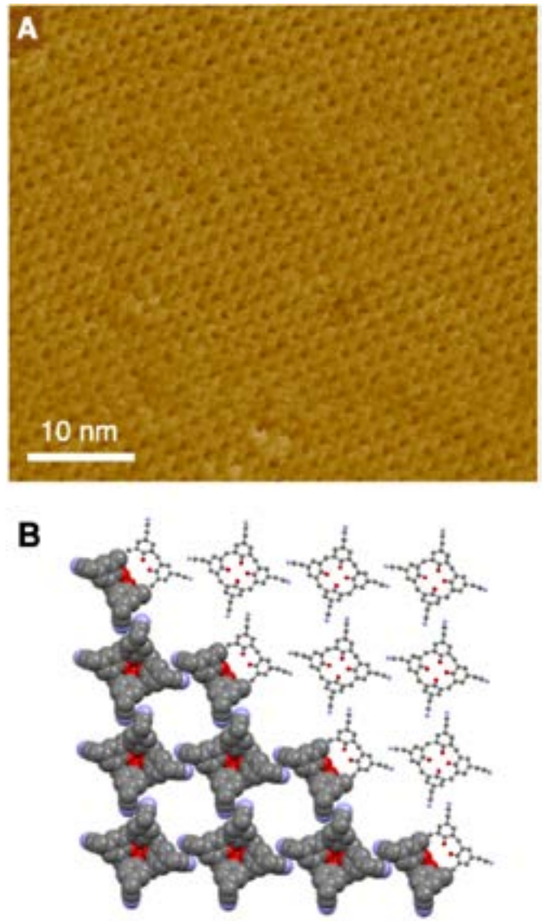

Fig. 4 Molecular resolution AFM micrograph (A) and molecular model (B) of 2-based Langmuir monolayer.

The study of the self-assembly properties of **3** revealed a different behavior. The methylene bridge linking the COOH groups with the calixarene body of 5,11,17,23-tetra-methylcarboxy-25,26,27,28-tetrapropoxy calix[4]arene provides the conformational flexibility for the COOH functions to coordinate to ionic centers with different coordination geometries. Monolayers and bi-layers of **3** were formed by coordination via Cu^{2+} or Ni^{2+} ions, respectively, at the air-liquid interface. The assembled layers were transferred from the air-water interface onto solid substrates using the Langmuir-Schaeffer method where they – still – exhibited a 2D periodic molecular structure in AFM.

This work established a molecular design strategy for the fabrication of metal-organic coordination networks (MOCN) of calix[4]arene macrocycles upon changing the transition metal ions. The designed building block **3**, with flexible methyl carboxy linkers, coordinates Cu^{2+} ions and forms bilayers of MOCNs. Thereby we present the first example of a MOCN with a controllable degree of bilayer formation. The same calix[4]arene forms crystalline monolayers of MOCN's by octahedral coordination with Ni^{2+} ions. This well-tunable molecular-design system paves the way towards the fabrication of non-trivial 2D self-assembled networks.

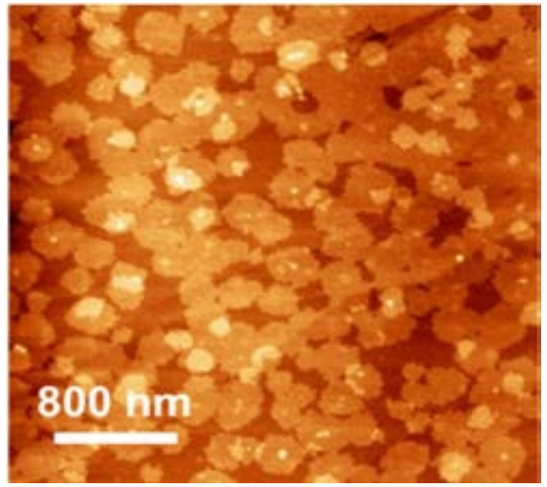

Fig. 5 AFM micrographs of 3-based layers showing bilayered structures formed at the surface of the Langmuir monolayer.

Conclusion

The work carried out in the frame of this PhD project allowed establishing a set of molecular design rules for the fabrication of stable and crystalline 2D networks based on calixarenes. Our findings pave the way towards the design of robust 2D layers with molecularly precise architectures and controllable physicochemical properties.

References

[1] N. Moridi, C. Wäckerlin, V. Rullaud, R. Schelldorfer, T.A. Jung, P. Shahgaldian, *Langmuir–Blodgett monolayer stabilization using supramolecular clips*, Chem. Commun. **49**, 367 (2013)

[2] M. Moradi, L.G. Tulli, J. Nowakowski, M. Baljozovic, T.A. Jung, P. Shahgaldian, *Two-dimensional Calix[4]arene-based metal-organic coordination networks of tunable crystallinity*, Angew. Chem., Int. Ed. **56**, 14395 (2017)

Interfacing a nanomechanical membrane and atomic spins with laser light

Project P1309: Cooling and control of a nanomechanical membrane with cold atoms
Project Leader: P. Treutlein and P. Maletinsky
Collaborators: T. Karg (SNI PhD Student), B. Gouraud, and C. T. Ngai

Light is a powerful carrier of quantum information and a versatile tool that allows to remotely couple different quantum systems. In this project, we explore the use of laser light to interface ultracold atoms and a nanomechanical membrane oscillator [1]. The resulting hybrid atom-optomechanical system offers new possibilities for quantum control of mechanical vibrations, precision sensing, and quantum-level signal transduction [2]. Our group reported the first experiments along these lines, demonstrating sympathetic cooling of a nanomechanical membrane by coupling to ultracold atoms [3]. In these experiments, the mechanical oscillator was coupled to the atomic motion in a trap. More versatile couplings and a higher level of control can be achieved by coupling the mechanical oscillator to the atomic spin. We conceived and implemented a scheme that uses laser light to realize such a coupling between a nanomechanical membrane and an ensemble of ultracold atoms in a dipole trap. We developed a quantum description of the light-mediated spin-membrane interactions and observed first signatures of spin-membrane and membrane-spin coupling in our experiment.

Theory of light-mediated interactions

In the past year we developed a general method to engineer light-mediated Hamiltonian interactions between cascaded quantum systems interconnected by an optical field. Our approach is entirely general and applies to a wide range of physical systems, including mechanical oscillators, cold atoms and solid-state spins. So far, cascaded quantum systems have only been discussed in the context of unidirectional couplings that allow one-way quantum communication, e.g. emission of a photon from the first system and subsequent absorption by the second system. However, coherent interaction is impossible in such a unidirectional scheme because of decoherence and quantum noise induced by the light-matter interaction. In our work we show that this problem can be overcome in a looped geometry where one or several of the cascaded quantum systems couple to the optical field twice. In this way one can achieve destructive interference of the light-induced quantum noise while at the same time realizing strong bidirectional Hamiltonian coupling. Provided that optical losses are small, the strong coupling regime can be reached, thus enabling coherent quantum dynamics such as state swaps or two-mode-squeezing [4].

Experimental setup

Our experimental setup to realize such a coherent Hamiltonian coupling between a collective atomic spin and a nanomechanical membrane oscillator is depicted in figure 1. A linearly polarized laser beam first probes the atomic spin precession about a transverse magnetic field via Faraday rotation such that the spin component Xa parallel to the laser axis modulates the light polarization. Using suitable polarization optics we convert this into an optical amplitude modulation between the two arms of a Mach-Zehnder interferometer. By coupling one interferometer arm to the optomechanical cavity the membrane oscillator experiences a force proportional to Xa, resulting in atom-membrane coupling. Oscillations of the membrane position Xm generate a phase modulation of the cavity output field. Recombination of the interferometer arms translates this into a modulation of the laser's circular polarization. The laser beam is directed back at the atomic ensemble with a small angle to spatially separate it from the input beam. The circular polarization modulation proportional to Xm now produces an effective magnetic field that drives Rabi oscillations of the spins, thus generating membrane-atom coupling. As both directions of the light-mediated interaction act simultaneously, mechanical and spin excitations are exchanged in a coherent fashion. Optical quantum noise driving the atomic spin is canceled by destructive interference between the first and second atom-light interaction.

Observation of spin-membrane and membrane-spin coupling

Recently we observed first signatures of unidirectional coupling from atomic spins to membrane (Fig. 2) and from membrane to atomic spins (Fig. 3, 4). The membrane mode

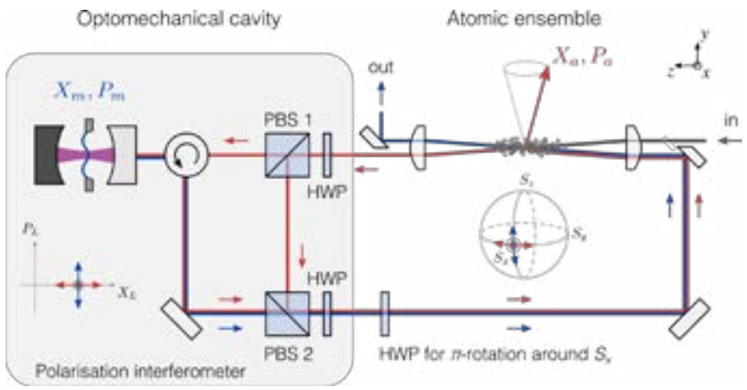

Fig. 1 Sketch of the experimental setup for bidirectional coupling of a collective atomic spin to a membrane oscillator inside an optical cavity. PBS: polarizing beam splitter, HWP: half-wave plate.

frequency is 1.96 MHz and the spin Larmor frequency can be tuned with the magnetic field. Experiments are performed with the membrane at room temperature and a cavity of 115 MHz linewidth.

In the atoms-to-membrane experiment (Fig. 2) we detect the light directly at the output of the polarization interferometer before it goes back to the atoms. The sequence starts with an external radio-frequency pulse that rotates all atomic spins into the plane orthogonal to the magnetic field where they start to precess. Their Larmor frequency is tuned to the mechanical resonance. The coupling laser beam is then switched on and carries the spin signal to the membrane, exciting it to a large oscillation amplitude about 20 dB above the thermal noise floor. After the spin signal has decayed the membrane motion decays and reaches thermal equilibrium after about 100 ms.

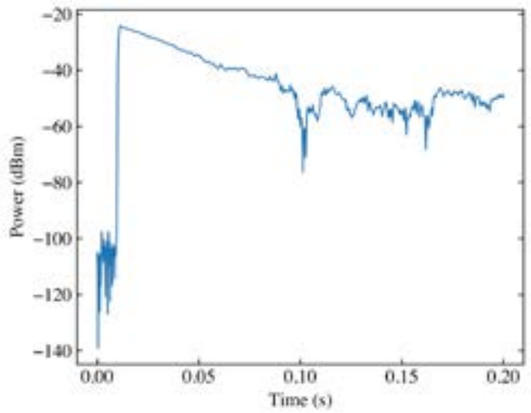

Fig. 2 Resonant excitation of the membrane oscillator by the Larmor precession of the atomic spins. The power of the detected optical signal is proportional to the mean square amplitude of the membrane.

For the membrane-to-atoms experiment we skip the first atom-light interaction and directly input the coupling laser into the polarization interferometer. After excitation of the membrane vibrations with an additional laser, we switch on the coupling beam for 200 µs. Afterwards an auxiliary laser beam probes only the atoms to provide an independent measurement of the spin precession. A typical detector time trace is shown in figure 3. The coupling beam signal (red) shows fast spin precession at 1.96 MHz modulated by a slow envelope of about 200 µs period, showing the Rabi oscillations of the spins induced by the membrane. The membrane signal itself is not detected because it is in an optical quadrature orthogonal to the one being measured. During the probe window (blue) the spin precession decays in the absence of the interaction.

In order to verify the resonant character of the interaction we tune the spin Larmor frequency via the external magnetic field (Fig. 4). We observe the peak excitation amplitude at a field of 2.77 G where the mechanical and spin frequencies are equal. The line shape corresponds to the susceptibility of the atoms as the mechanical oscillator has a much narrower linewidth. The large error bars represent thermal fluctuations of the mechanical oscillator.

In conclusion, we demonstrated the basic building blocks of a coherent optical interface between a mechanical oscillator and the atomic spin. Given the strong one-way interactions presented here we anticipate the observation of normal-mode splitting in the bidirectional coupling scheme. Our experiment allows to explore a variety of different dynamics by manipulating the optical field on its way between the systems. Finally we aim to realize sympathetic ground state cooling of the membrane and coherent dynamics in the quantum regime.

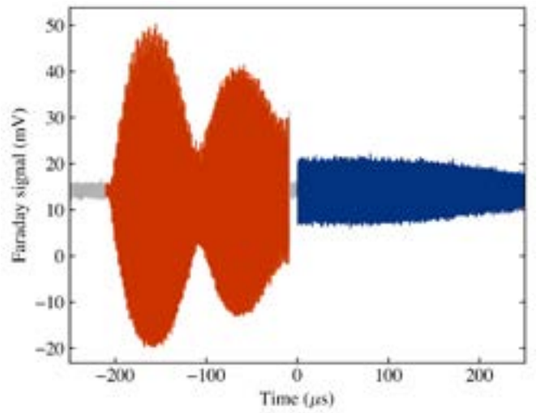

Fig. 3 Photodetector time trace of a typical experiment where the membrane drives the atomic spin. The red trace is the measurement of the coupling beam, showing Rabi oscillations of the spin driven by the membrane. The blue trace is the probe beam signal (coupling beam turned off).

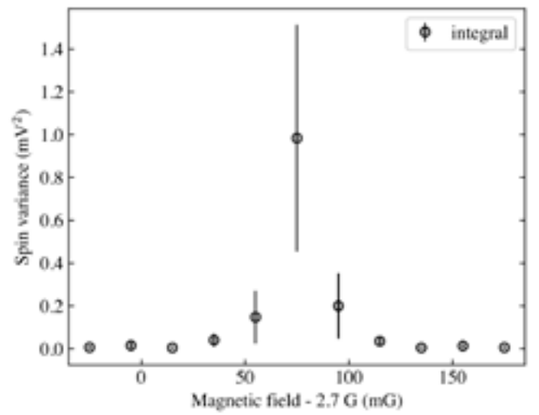

Fig. 4 Measured spin response to the membrane drive as a function of the external magnetic field that tunes the spin Larmor frequency across the mechanical resonance.

References

[1] M. Aspelmeyer, P. Meystre, and K. Schwab, *Quantum optomechanics*, Phys. Today **65**, 29 (2012)

[2] P. Treutlein, C. Genes, K. Hammerer, M. Poggio, and P. Rabl, *Hybrid Mechanical Systems*, in "Cavity Optomechanics" (eds M. Aspelmeyer, T. Kippenberg, and F. Marquardt) 327–351 (Springer, 2014)

[3] A. Jöckel, A. Faber, T. Kampschulte, M. Korppi, M. T. Rakher, and P. Treutlein, *Sympathetic cooling of a membrane oscillator in a hybrid mechanical–atomic system*, Nat. Nanotechnol., **10**, 55–59 (2015)

Nanofluidic devices for particle trapping and molecular sensing

Project P1310: Plasmonic sensing in biomimetic nanopores
Project Leader: Y. Ekinci and R. Y. H. Lim
Collaborator: D. Sharma (SNI PhD Student)

Introduction

Microfluidic devices have been used in various applications and fields of research in past decades ranging from biology [1, 2], fluid dynamics, material science [3, 4, 5] to diagnostics [6]. Combining microfluidic devices with nanoscale channels and nanofeatures provides a platform for molecular dynamic, intermolecular interactions studies and molecular sensing for nanoscale molecules at low concentration. In various applications micro- and nanofluidic devices have been used for molecule separation [7], sorting [2] and trapping [8].

In our previous work, we have developed integrated micro/nanofluidic devices for high-throughput single nanoparticle trapping, where particle trapping inside the device relies on the electrostatic interaction between the device surface and the particle surface [3, 4, 9, 10]. Detection of trapped particles was performed using interferometric scattering (iSCAT) [11]. The device provides a controlled fluidic environment for the high-throughput and contact free confinement of nanoparticles in the range of 150 nm to 10 nm, which is useful for molecular dynamic study as well as molecular detection [3, 4, 11]. However, due to electric field screening in the presence of the high salt concentration of the buffer solution such as blood, the electrostatic trapping inside these devices is not effective. Thus, to enable molecular detection at very small concentrations (~10 pg/ml) in presence of blood, urine etc., a robust method is required. To provide such method we developed a lab-on-a-chip platform that allows particle separation, sorting and trapping at specific locations in the device for molecular sensing in the range of nano- to picomolar concentration. In combination with optical detection using surface-enhanced Raman spectroscopy (SERS) and localized surface plasmon resonance (LSPR), a highly sensitive (~10 pg/ml) molecular detection can be achieved [12].

The lab-on-a-chip (LoC) platform was developed using state-of-the-art lithography processes and replica molding. A negative master was developed on a Si wafer using electron-beam lithography. Later the device pattern was transferred to PDMS mold using replica molding as shown in figure 1. For replica molding UV curable PDMS base and resin mixture (ShinEtsu Chemical Co. Ltd.) was used in 1:1 weight ratio, and cured for 4 min under UV exposure at 30 mW/cm^2 and then baked at 509°C in an oven at atmospheric pressure. Patterned PDMS mold was further prepared for final device assembly by punching holes at in/out-port locations. Immediately before final device assembly, a cleaned cover glass and a prepared PDMS mold were processed with air plasma for the activation of glass and PDMS surface for effective covalent binding.

The device was specifically designed to use functionalized nanoparticles for early disease diagnosis, where nanoparticles can be functionalized with disease-specific antibodies. A blood sample was mixed with antibody-functionalized nanoparticles before the experiments to detect disease specific biomarker presence and concentration. The LoC platform had areas specifically designed for passive separation of micromolecules from the sample solution and size-based trapping of nanoparticles at detection area, enabling multi-particle detection on a single device as shown in figure 2. In combination with gold nanoparticles functionalized with antibodies related to

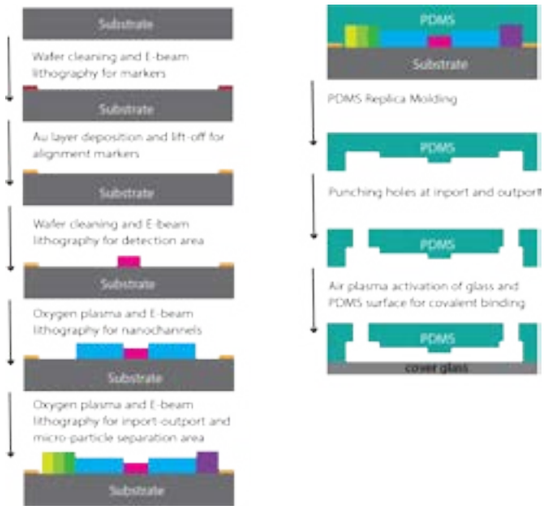

Fig. 1 Fabrication and development of lab-on-a-chip platform using state of art lithography processes on a Si wafer and replica molding using polydimethylsiloxane (PDMS). The final integrated micro/nanofluidic device was developed using air plasma activation of patterned PDMS and a cover glass.

Fig. 2 Schematics of a lab-on-a-chip platform for early disease detection using antibody-functionalized nanoparticles. The blood sample is injected at the in-port area in combination with functionalized nanoparticles allowing antibody-antigen binding on the nanoparticle surface, and detection of bound antibodies at the detection area.

the biomolecule of interest, the device provides a means to detect biomarkers using surface-enhanced Raman spectroscopy (SERS). By performing optical measurement on trapped nanoparticles one can get both qualitative and quantitative information of the disease-specific biomarkers.

The device was specifically designed to use functionalized nanoparticles for early disease diagnosis, where nanoparticles can be functionalized with disease-specific antibodies. A blood sample was mixed with antibody-functionalized nanoparticles before the experiments to detect disease specific biomarker presence and concentration. The LoC platform had areas specifically designed for passive separation of micromolecules from the sample solution and size-based trapping of nanoparticles at detection area, enabling multi-particle detection on a single device as shown in figure 2. In combination with gold nanoparticles functionalized with antibodies related to

the biomolecule of interest, the device provides a means to detect biomarkers using surface-enhanced Raman spectroscopy (SERS). By performing optical measurement on trapped nanoparticles one can get both qualitative and quantitative information of the disease-specific biomarkers.

To optimize the device design, we performed preliminary experiments for molecular detection, size-based nanoparticle sorting and trapping, and micro-particle separation. Passive sorting of nanoparticles was achieved by deterministic lateral displacement (DLD) [13] using different micro-structured arrays integrated on the LoC platform as shown in figure 3. DLD arrays support both size-based particle separation as well as the directional displacement of nanoparticles. Further optimization of the DLD array will lead to location-specific trapping of nanoparticles based on their sizes in the detection area as shown in figure 2, which would allow multiplexable detection on a single LoC platform.

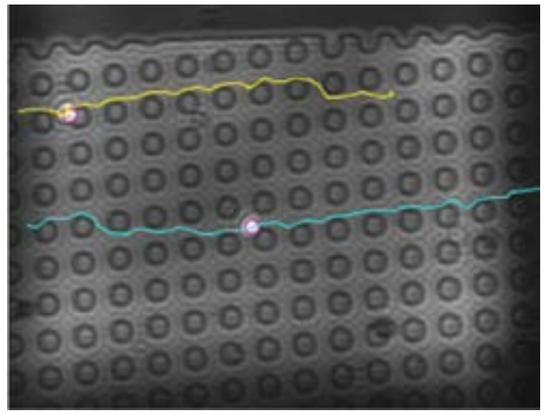

Fig. 3 Microarray inside the integrated micro/nanofluidic device for size-based sorting of nanoparticle and directional motion of the particles of interest. Presence of deterministic lateral displacement arrays assists directional motion of nanoparticles of 200 nm diameter.

Preliminary sensing experiments were performed in different buffer solutions using 80 nm diameter gold nanoparticles which consist of -COOH group on the particle surface. The presence of gold nanoparticles enhances the electric field coupled with the particles leading to both SERS signal as well as nanoparticle agglomeration and melting due to overheating and plasmon coupling. Thus, further optimization in both detection settings and method is required for precise detection of SERS signal from the molecules attached on the nanoparticle surface.

We believe further optimization of device design and SERS measurement procedure can lead to a multiplexable LoC platform that would allow multi-biomarker detection on a single chip.

References

[1] C. Zhang, J. Xu, W. Ma, W. Zheng, *PCR microfluidic devices for DNA amplification*. Biotechnol Adv, **24(3)**, 243-284 (2006)

[2] M. Krishnan, I. Monch, P. Schwille, *Spontaneous stretching of DNA in a two-dimensional nanoslit*, Nano Letters, **7(5)**, 1270-1275 (2007)

[3] M. A. Gerspach, N. Mojarad, D. Sharma, T. Pfohl, Y. Ekinci, *Nanofluidic lab-on-a-chip trapping devices for screening electrostatics in concentration gradients*, Microelectronic Engineering, **175**, 17-22 (2017)

[4] D. Sharma, M. A. Gerspach, T. Pfohl, R. Y. H. Lim, Y. Ekinci, *Single positively charged particle trapping in nanofluidic systems*, Microelectronic Engineering, **175**, 43-49 (2017)

[5] N. Mojarad, V. Sandoghdar, M. Krishnan, *Measuring three-dimensional interaction potentials using optical interference*, Opt Express, **21(8)**, 9377-9389 (2013)

[6] M. Soler, A. Belushkin, A. Cavallini, C. Kebbi-Beghdadi, G. Greub, H. Altug, *Multiplexed nanoplasmonic biosensor for one-step simultaneous detection of Chlamydia trachomatis and Neisseria gonorrhoeae in urine*, Biosens Bioelectron, **94**, 560-567 (2017)

[7] J. Fu, R. B. Schoch, A. L. Stevens, S. R. Tannenbaum, J. Han, *A patterned anisotropic nanofluidic sieving structure for continuous-flow separation of DNA and proteins*, Nat Nanotechnol **2(2)**, 121-128 (2007)

[8] M. Krishnan, N. Mojarad, P. Kukura, V. Sandoghdar, *Geometry-induced electrostatic trapping of nanometric objects in a fluid*, Nature, **467(7316)**, 692-695 (2010)

[9] M. A. Gerspach, N. Mojarad, D. Sharma, Y. Ekinci, T. Pfohl, P*neumatically Controlled Nanofluidic Devices for Contact-Free Trapping and Manipulation of Nanoparticles*, Part. Part. Syst. Charact. **35(12)**, 1800161 (2018)

[10] M. A. Gerspach, N. Mojarad, D. Sharma, Y. Ekinci, T. Pfohl, *Soft electrostatic trapping in nanofluidics*, Microsystems & Nanoengineering, **3**, 17051 (2017)

[11] M. A. Gerspach, N.Mojarad, T. Pfohl, Y. Ekinci, *Glass-based geometry-induced electrostatic trapping devices for improved scattering contrast imaging of nano-objects*, Microelectronic Engineering, **145**, 43-48 (2015)

[12] R. Wang, H. Chon, S. Lee, Z. Cheng, S. H. Hong, Y. H. Yoon, et al. *Highly Sensitive Detection of Hormone Estradiol E2 Using Surface-Enhanced Raman Scattering Based Immunoassays for the Clinical Diagnosis of Precocious Puberty*, ACS Appl Mater Interfaces, **8(17)**, 10665-10672 (2016)

[13] D. W. Inglis, J.A. Davis, R. H. Austin, J. C. Sturm, *Critical particle size for fractionation by deterministic lateral displacement*, Lab Chip, **6(5)**, 655-658 (2006)

Single-cell visual proteomics to study the prion-like spreading of α-synuclein

Project P1401: Targeted single cell proteomics using magnetic nanoparticles to study prion-like spreading of amyloid nanoparticles
Project Leader: T. Braun and H. Stahlberg
Collaborators: C. Schmidli (SNI PhD Student), A. Bieri, C. Leu, R. Sütterlin, A. Syntychaki, A. Hierlemann, M. Leist, S. Gutbier, U. Pieles, and A. Fränkl

Introduction
Neurodegenerative disorders such as Parkinson's disease (PD) and Alzheimer's disease (AD) mainly affect the elderly, and due to demographic shifts, they afflict an increasing number of people. To develop effective strategies for preventing or postponing neurodegenerative disorders, the causative factors must be identified, and the pathomechanisms must be understood.

Unusual intra- and extracellular aggregates are closely associated with PD and AD. These 'plaques' are related to disease-specific, misfolded proteins. In PD, the plaques are intracellular Lewy bodies containing α-synuclein (α-syn), and in AD, the plaques are extracellular amyloid-β aggregates and intracellular tau-protein tangles. A stereotypic spreading of these plaques throughout the brain is typical for these disorders. The model of prion-like spreading of aggregates containing misfolded proteins provides an elegant explanation for this phenomenon. However, the detailed mechanism for this spreading is unknown, and different pathways have been suggested. The pathomechanisms that trigger the misfolding of these proteins are mysterious.

This project aims to study the prion-like progression of PD by combining classical and novel methods. We use well-characterized neuronal cell systems, grown in microfluidic structures, and expose them to synthetic amyloid fibrils. Subsequently, the reaction of the cells, the fate of the seeds in the cell, and the spreading of the misfolding to 'healthy' cells are characterized. We use a unique combination of standard and new analysis nano-tools, providing comprehensive orthogonal and correlative information on the single-cell level.

'Seeding' of dopaminergic neuronal cells
Figure 1 shows differentiated, dopaminergic Lund human mesencephalic (LUHMES) cells, which were incubated with fluorescently labeled α-syn nanoparticles. Confocal microscopy revealed that the dopaminergic neuron-like cells internalized the nanoparticles. Interestingly, comparable tau nanoparticles (AD) were not taken up at all (data not shown). The light microscopy also reveals that the seeds are clustering in the cells. However, the resolution is not high enough for an interpretation of the potential mechanism. Therefore, electron microscopy (EM) was employed to study further the fate of the internalized seeds using (i) untargeted single-cell visual proteomics [1-3], and (ii) targeted visual proteomics [4].

(i) Single cell visual proteomics
The principles of the single-cell visual proteomics approach are shown in figure 2. Cells with internalized α-syn are identified using a fluorescence light-microscope. An individual selected cell is targeted with a platin coated micro-capillary, and the cell structure is destabilized using five short electro-pulses. Simultaneously, the cell lysate is aspirate in the microcapillary in a volume of approx. three nL. In the end, the cell lysate is conditioned with heavy metal salts and dispensed on an EM-grid. Subsequent analysis in the EM allows for the detection of the seeds and associated structures. The seed sizes and structure are identical to the used particles for the cell

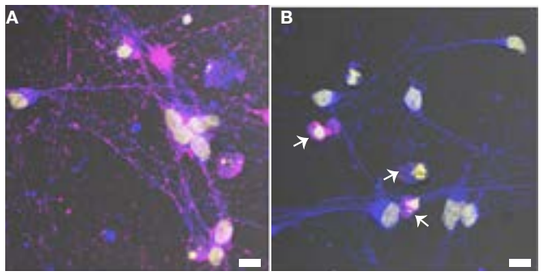

Fig. 1 Seeding of dopaminergic neuronal cells with PD-related α-syn (A) and AD-related tau (B). The seeds were applied to dopaminergic LUHMES -cells as demonstrated by the tyrosine hydroxylase labeling shown in blue. Seeds are shown in magenta, and the nuclei are visualized by DAPI staining (yellow). Whereas α-syn is taken up readily into the cells, tau seeds are only associated with dead cells identified by the fragmented nuclei (arrows). Courtesy Cedric Leu and Rosmarie Sütterlin, C-CINA. Scale bars: 10 µm.

seeding. Interestingly, the observed seeds from in single-cell are clustered. This observation is in good agreement with our findings using confocal light microscopy. Furthermore, proteins are attached to the seeds, and membrane-like structures are associated with the seed clusters. This membrane association was recently observed in Lewy bodies [6].

Whereas the preliminary interpretation of the seed-structures is possible, many questions remain open. We are now investigating the attached proteins to the seeds using a method we called 'interaction labeling' [5] (see section (ii)). However, we also expect changes in the structural proteomics visible as small particles in the background of figure 2B. We developed new image processing algorithms, directly comparing a negative control (untreated cells) with a positive control (seeded cells). The principles of this 'differential visual proteomics' approach are explained in figure 3.

(ii) Targeted visual proteomics from single cells
To study the processing of internalized seeds by the dopaminergic neuronal cells, we developed a method for the isolation of the seeds taken up by an individual cell. We used biotin-functionalized seeds for our experiments, which bind to streptavidin-coated magnetic beads. These beads can be trapped using magnetic field gradients generated by electromagnets (see the report of the ARGOVIA MiPIS project). After the washing, the trap is deactivated, and the 'fished' seeds are eluted, stained and directly written onto an EM-grid for visualization (data not shown). This protein isolation opens new ways for future sample analysis, e.g. by a so-called 'interaction labeling' we developed recently [4].

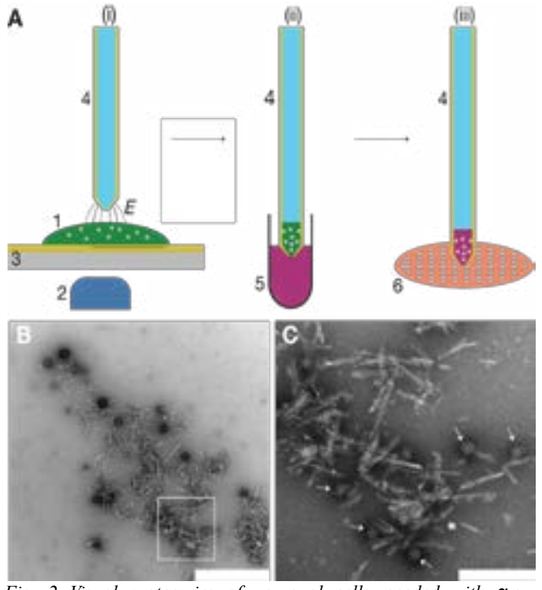

Fig. 2 Visual proteomics of neuronal cells, seeded with α-syn nanoparticles. A) Visual proteomics work-flow. (i) An individual cell (1) with fluorescently labeled α-syn nanoparticles is selected in the fluorescence light microscope (2). The cell is lysed by electroporation (E) [5] and by the simultaneous aspiration of a 3 nL volume, collecting the cell lysate in the capillary (4). Note that for the electrical connectivity, the cells are grown on an electrically conducting, grounded, ITO-coated glass slide (3) and that the microcapillary is Pt coated (yellow) for the electrical connectivity. (ii) Conditioning of the sample by a diffusion-driven process [1], removing sample salts and complementing the cell lysate with heavy metal stain. This is performed merely by immersing the apex of the micro-capillary (4) into a heavy metal salt vial (5). (iii) Writing of the conditioned 3 nL volumes onto an EM-grid (6). B) Seed-cluster from a single cell. Fibril fragments are found in the same dimension and inner structure as the in vitro seeds. Scale bar: 1 µm. C) Higher magnification of the indicated region in (B). Compared to the seeds before, the seeds are clustered, covered by proteins, and supposed membrane structures (arrows) are associated with the seed-clusters. Scale bar: 200 nm.

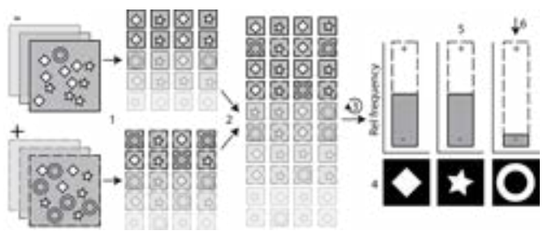

Fig. 3 Principles of 'differential visual proteomics' algorithm. Pulse-chase like experiments are performed as positive (+) and negative control (-). Single-cell lysates are prepared for imaging in the EM from both trials resulting in two stacks of projections of cell lysate constituents (dotted frame for positive control). Three different proteins are shown in white. For analysis, all particles are "picked" (1) resulting in two galleries of protein projections. Subsequently, the particle galleries are pooled (2). For every particle, the origin (positive or negative control) is known. The combined particle gallery is now subjected to a maximum-likelihood-based alignment and classification algorithm (3). The classification and averaging results in class-averages of higher signal to noise ratio compared to the original projections of single molecules (4). Since we know the origin of every particle contributing to a given class (5), we can screen for classes with significant differences between the positive and negative control (arrow, 6). These classes are likely responsible for the biological reaction upon the pulse-chase disturbance.

References

[1] S. A. Arnold, S. Albiez, N. Opara, M. Chami, C. Schmidli, A. Bieri, H. Stahlberg, C. Padeste, T. Braun, *Total sample conditioning and preparation of nanoliter volumes for electron microscopy*, ACS Nano, **10**(5): 4981-4988 (2016)

[2] S. A. Arnold, S. Albiez, A. Bieri, A. Syntychaki, R. Adaixo, R. A. McLeod, K. N. Goldie, H. Stahlberg, T. Braun, *Blotting-free and lossless cryo-electron microscopy grid preparation from nanoliter-sized protein samples and single-cell extracts*, J. S. B. **197**, 3 (2017)

[3] C. Schmidli, L. Rima, S. A. Arnold, T. Stohler, A. Syntychaki, A. Bieri, S. Albiez, K. N. Goldie, M. Chami, H. Stahlberg, T. Braun, *Miniaturized sample preparation for transmission electron microscopy*, JoVE; e57310 (2018)

[4] D. Giss, S. Kemmerling, V. Dandey, S. Stahlberg, T. Braun, *Exploring the inter-actome: microfluidic isolation of proteins and interacting partners for quantitative analysis by electron microscopy*, Anal. Chem., **86**, 4680–4687 (2014)

[5] S. Kemmerling, S. A. Arnold, B. A. Bircher, N. Sauter, C. Escobedo, G. Dernick, A. Hierlemann, H. Stahlberg, T. Braun, *Single-cell lysis for visual analysis by electron microscopy*, J. S. B., **183**, 467-73 (2013)

[6] S. H. Shahmoradian, et al., *Lewy pathology in Parkinson's disease consists of a crowded organellar membranous medley*, bioRxiv; 10.1101/137976 (2018)

Pushing the limits of lightweight materials

Project P1402: Lightweight structures based on hierarchical composites
Project Leader: C. Dransfeld and C. Schönenberger
Collaborators: W. Szmyt (SNI PhD Student) and C. Padeste

Context
Modern high-performance structural parts are often made of carbon fibre (CF)-reinforced plastics due to their excellent mechanical properties and remarkably low weight. The potential of these materials is however limited by a significant drawback. The mechanical properties of these materials are only well-pronounced in the fibre direction, dominated by the properties of the CF. However, in the direction perpendicular to the fibre the mechanical performance is significantly weaker, governed by the properties of the polymer matrix and fibre-matrix interface in particular.

In this project we aim to significantly enhance the fibre-matrix interface by controlled growth of carbon nanotubes (CNTs) directly on the surface of the CF. The CNTs exhibit extraordinary mechanical properties, which makes them a great choice for the nanoscale reinforcement. We are aiming for a direct synthesis of CNTs on the surface of CF in an aligned and dense manner (Fig. 1). This approach results in the higher load and alignment of CNTs in the matrix between the fibres as compared to other approaches, e.g. CNT dispersion in the matrix or grafting of CNTs onto CF using electrophoresis [1]. Moreover, owing to the outstanding heat- and current conductivity of the CNTs, the incorporation of CNTs in the matrix results in a significant increase in the conductivities of the composite [1], which is also desirable in many applications.

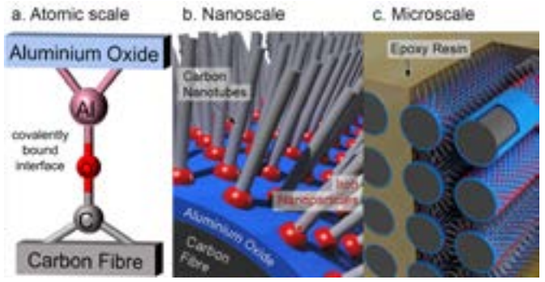

Fig. 1 Schematic illustration of the considered scales of the hierarchical composite; a. atomic scale - atomic bonds need to be ensured; b. nanoscale – the CNT synthesis and nano-reinforcement takes place, c. microscale – multiple fibres pack together in a bulk composite.

There are many challenges in the development of the hierarchical composite. It has been shown [2], that in the chemical vapor deposition (CVD) process of CNT synthesis, the CF mechanical properties are severely deteriorated. We have identified that the diffusion of the iron catalyst into CF in is a phenomenon significantly contributing to this process. We have also established that a 12 nm thick aluminum oxide film provides a sufficient diffusion barrier, ensuring the protection of the CF in the harsh CVD conditions [3, 4]. We have however found that the adhesion of the alumina to the CF – measured as interface shear strength (IFSS) – diminishes completely at the high-temperature CNT synthesis conditions [3] (Fig. 2), which is an issue that we are currently solving. The other challenge is the optimization of the CNT length. We are aiming for a length that is a fraction of the CF diameter (~7 µm), so that the volume of CNTs does not hinder the fibre compaction and still provides a significant interface reinforcement.

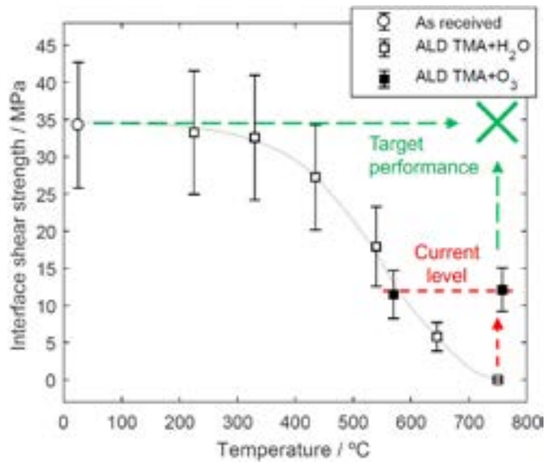

Fig. 2 The IFSS of the CF-alumina interface with respect to the heat treatment temperature [5]. The currently achieved and target performance is indicated. The grey line guides along the declining trend of the IFSS.

Experimental and results
To ensure a good adhesion of the protective alumina film to the CF, we are developing a process that results in a covalent bonding between the film and the fibre. For this purpose, we are modifying the atomic layer deposition (ALD) process, which is used to coat the CF with alumina. In the classic alumina film synthesis, one alternately exposes the substrates to water and trimethylaluminum vapors, gradually building an extremely uniform layer of aluminium oxide with atomic precision control of thickness. In the new approach, we are introducing a pre-treatment of CF with ozone and entirely replacing water with ozone in the process in order to promote the covalent bonding not only at defect sites of the graphitic CF surface, but also uniformly over its entire surface. Our latest results indicate that the IFSS can be retained significantly [5], but more experiments are needed to reach further improvement (Fig. 2).

So far, we have been testing the IFSS between alumina and CF by means of single fibre fragmentation tests as described in [3, 5]. A different micromechanical testing approach is the single fibre pullout test. We have found it to be vastly more efficient with large sample sets when a commercial embedding and testing system (FIMATEST by Textechno Herbert Stein GmbH & Co. KG, Germany) is employed, like in [6]. The method relies on a precise embedding of a fibre in a droplet of the matrix and a subsequent fibre pullout once the matrix is cured. In the process, the force and displacement data is recorded from which the IFSS can be deduced (Fig. 3).

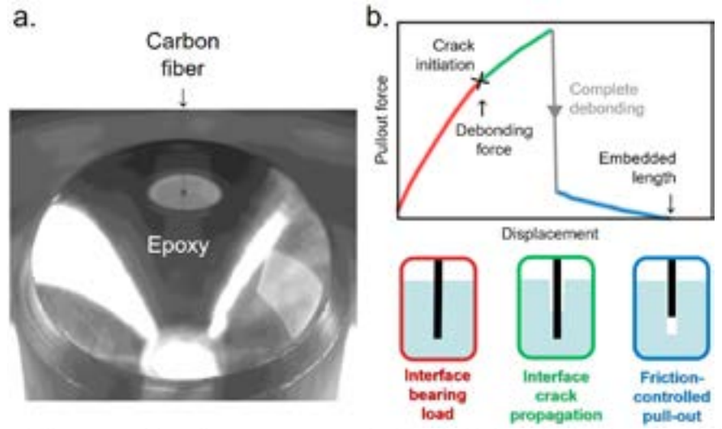

Fig. 3 Illustration of the pullout test; a. picture of a CF embedded in a droplet of epoxy ready for a pullout test; b. schematic graph of a force-displacement curve as recorded during a test with color-coded illustrations below.

Another important aspect of this study is the development of the CVD process to obtain CNTs of desired morphology. The CNTs need to be of high quality, high surface density and of a desired length. Moreover, the process needs to be applicable to complex substrate surfaces such as CF. As it has been stated [7] and as we have confirmed, the factor that predominantly influences the CNT density, alignment and uniformity is the homogeneous catalyst deposition. We are currently developing a method of catalyst deposition in which the coating homogeneity is promoted by functionalisation of the alumina surface prior to the dipcoating in an iron salt solution. We are obtaining much more uniform results with the surface functionalisation as compared to dipcoating only as it has been done previously [3] (Fig. 4). The CNT length is controlled by the time of exposure to the hydrocarbon gas in the CVD process and by the growth temperature.

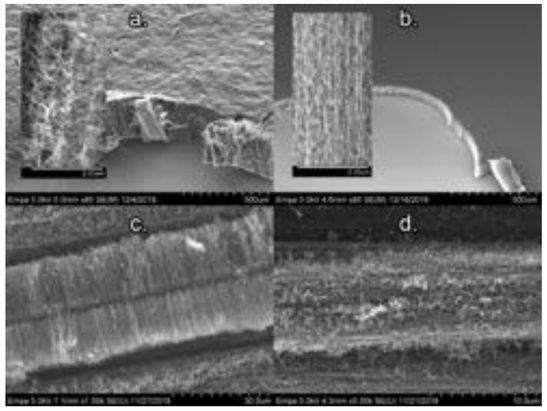

Fig. 4 a, b SEM images of CNTs on flat Al_2O_3/SiO_2 substrate, two different catalyst deposition methods. a. dip-coating in iron salt solution only; b. surface functionalization prior to the dip-coating. Magnifications in the insets show the degree of CNT alignment. c, d SEM of CNTs on Al_2O_3/CF: c CNTs too long, but of high density, d. CNTs of too low density, but of a desirable length.

Summary and conclusion
The current results show a new perspective on achieving supreme control of the CNT synthesis on the CF while successfully mitigating detrimental effects on the fibre mechanical properties. Therefore, this study constitutes a significant step towards the close investigation of hierarchical fibres in the polymer matrix.

References

[1] H. Qian, E. S. Greenhalgh, M. S. P. Shaffer, A. Bismarck, *Carbon nanotube-based hierarchical composites: a review*, J. Mater. Chem. **20**, 4751 (2010)

[2] Q. Zhang, J. Liu, R. Sager, L. Dai, J. Baur, *Hierarchical composites of carbon nanotubes on carbon fiber: Influence of growth condition on fiber tensile properties*, Compos. Sci. Technol. **69**, 594–601 (2009)

[3] S. Vogel, C. Dransfeld, B. Fiedler, J. Gobrecht, *Protective effect of thin alumina layer on carbon fibre to preserve tensile strength during CNT growth by CVD*, Proceedings of ECCM16 - 16th European Conference on Composite Materials, Seville, Spain, June 22nd-26th (2014)

[4] W. Szmyt, et al. *Protective effect of ultrathin alumina film against diffusion of iron into carbon fiber during growth of carbon nanotubes for hierarchical composites investigated by ptychographic X-ray computed tomography*, Carbon **115**, 347–362 (2017)

[5] W. Szmyt, L. Marot, M. Calame, C. Padeste, C. Dransfeld, *Carbon fibre-carbon nanotube multiscale composites - nanoengineering of the fibre surface for protection in extreme processing conditions*, Proceedings of ECCM18 - 18th European Conference on Composite Materials, Athens, Greece, June 24th-28th (2018)

[6] S. Zhandarov, et al., *Investigation of interfacial strength parameters in polymer matrix composites: Compatibility and reproducibility*, Adv. Ind. Eng. Polym. Res. **1**, 82–92 (2018)

[7] P. Agnihotri, S. Basu, K. K. Kar, *Effect of carbon nanotube length and density on the properties of carbon nanotube-coated carbon fiber/polyester composites*, Carbon **49**, 3098–3106 (2011)

Launch and detection of neutral biomolecules in high vacuum

Project P1403: Tailor-made proteins and peptides for quantum interference experiments
Project Leader: V. Köhler and M. Mayor
Collaborators: J. Schätti (SNI PhD Student), M. Debiossac, M. Kriegleder, P. Geyer, A. Shayeghi, P. Rieser, U. Sezer, G. Richter, G. G. Rondina, D. Häussinger, and M. Arndt

Neutral biomolecules in the gas phase

Investigations on charge neutral biomolecules in the gas phase are limited, despite potential rewards and insights associated with their study. These include e.g. the validation of theoretical models to determine the folding behaviour of oligopeptides and the influence of charge on protein-protein interactions. Two fundamental difficulties contribute to the lack of their exploration: i) complex biomolecules are notoriously difficult to volatilize due to their fragility and abundant intermolecular interactions, ii) once neutrals are formed, they become invisible for common detectors used in mass spectrometry, i.e. a convenient read-out for the experiments is lacking. Fragmentation-free post-ionization of biomolecules in high vacuum was so far limited to constructs of around 2 kDa, the cut-off likely caused by an increase incompetitive fragmentation channels and electron recapture processes. We present here two complimentary approaches to address these challenges: i) the selective photocleavage of peptides decorated with tailored photo-active tags [1] and ii) the femtosecond laser desorption of especially designed large peptide constructs which are rich in chromophores and carry a high number of perfluoroalkyl chains to reduce intermolecular interactions [2, 3].

Photocleavable tags for charge reduction of electrosprayed oligopeptides

Inspired by an initial study on signal depletion based on photocleavage of laser desorbed model compounds by M. Mayor, M. Arndt and coworkers [4], we investigated charge reduction of electrosprayed oligopeptides with a range of photoactive groups derived from ortho-nitroarylethers.

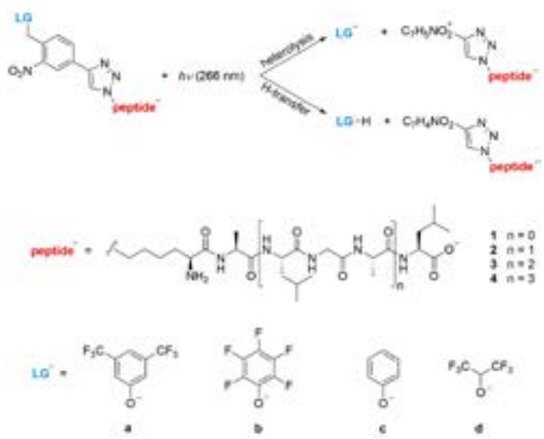

Fig. 1 Peptides equipped with a set of photocleavable tags and observed cleavage mechanisms [1]. LG = leaving group.

Electrospray ionization is the most widely employed ionization technique in mass spectrometry applications for life sciences and it enables the launch of charged biomolecules under mild and fragmentation-free conditions. The combination of launch by electrospray and charge removal by photocleavage appealed to us also for the following reasons: i) charged species resulting from the electrospray process can be mass selected and controlled by electric and magnetic fields, ii) photocleavage of especially designed tags can be selective as well as time and spatially resolved. Parameters such as peptide length and leaving group quality have been identified that steer the cleavage mechanism, namely bond heterolysis or cleavage under H-transfer (Fig. 1).

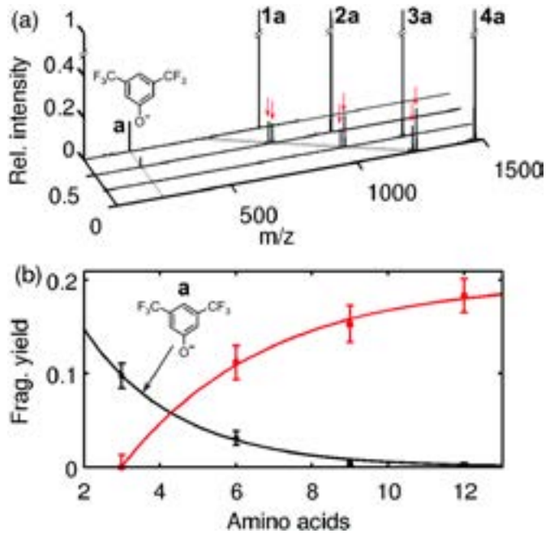

Fig. 2 UV photocleavage experiments on a set of modified peptides in high vacuum carried out inside a modified TOF-MS by our collaborating partners in Vienna. a) Mass spectra for peptides 1a-4a upon irradiation. b) Fragment yield for LG^- (dark circles) and fragments formed under H-transfer (red circles) in dependence of the peptide length [1].

While short peptides cleaved upon irradiation under bond heterolysis, longer peptides cleaved preferentially under H-transfer (Fig. 2). Heterolysis was also observed for collision induced dissociation pointing to a thermal nature of the process. Although the heterolytic process permitted charge removal from the peptide fragment when the experiments were carried out in negative ion mode, alternative constructs are needed to apply the methodology to higher mass regimes. First results in this respect are very promising. The formation of neutral peptides has so far only been confirmed indirectly, i.e. by the depletion of the parent peptide signal and the appearance of the leaving group signal. Further efforts are required to detect the neutrals after formation.

Neutral launch of large peptide constructs – design considerations

In an alternative approach we sought to launch neutral peptides directly instead of neutralizing charged species in the gas phase. To reduce intermolecular interactions such as H-bonds and electrostatic interactions, basic nitrogen atoms were amidated with fluoroalkylchains. A high tryptophan content of the peptides – required for efficient photoionization – was realized by alternating lysine with tryptophan residues. The alternating motif provided additionally good solubility of the unmodified peptides, a prerequiste for successful synthesis. The accessiblity of simple tryptophan oligomers such as 5 was limited to 10 residues and the constructs could not be obtained in high purity. Global amidation of the peptides was carried out after cleavage from the resin. Constructs with up to 50 amino acids and a molecular weight exceeding 20 kDa as in 7 were prepared and tested. The long fluorous tails contribute substantially to the molecular weight.

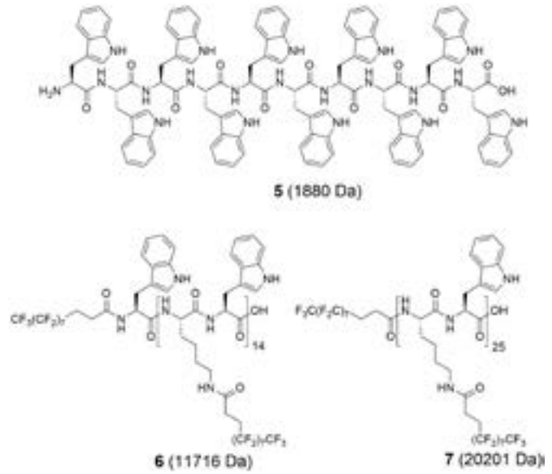

Fig. 3 Selected constructs studied in neutral launch and UV-postionization experiments [2].

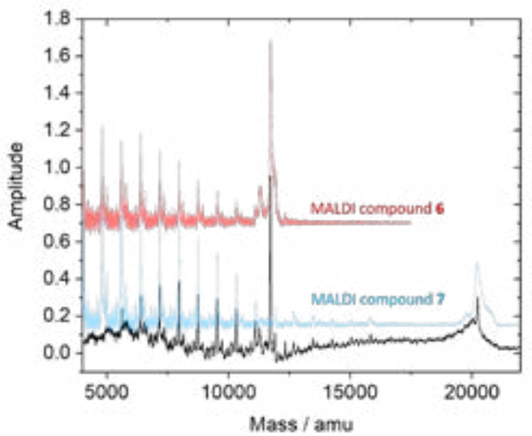

Fig. 4 TOF-MS of a laser desorbed and photoionized mixture of compound 6 and 7 (black line) and comparison with independently calibrated MALDI-TOF-MS spectra of compound 6 (red line) and 7 (blue line), respectively [2].

Laser desorption and photoionization

Previous launch studies under thermal heating in an oven with related constructs were limited to tripeptides and the attempted launch and detection of a nonapeptide resulted in extensive fragmentation [3]. Laser desorption on the other hand enabled efficient transfer of large species into the gas phase. Detailed studies carried out by our collaborating partners in Vienna revealed that very short laser pulses (300 fs) for desorption allow for a substantially improved material economy in the experiments. To our great delight could the largest construct (7) be launched and photoionized under optimized conditions. A comparison of the experimental data with independently calibrated MALDI spectra recorded at the University of Basel led to unambiguous confirmation, that construct 7 could indeed be launched in neutral form and subsequently photoionized under observation of intact molecules thereby increasing the mass limit for photoionization by one order of magnitude (Fig. 4).

References

[1] M. Debiossac#, J. Schätti#, M. Kriegleder, P. Geyer, A. Shayeghi, M. Mayor, M. Arndt, V. Köhler, *Tailored photocleavable peptides: fragmentation and neutralization pathways in high vacuum*, Phys. Chem. Chem. Phys. **20**, 11412 (2018) #Equal contribution. Published by the PCCP Owner Societies.

[2] J. Schätti, P. Rieser, U. Sezer, G. Richter, P. Geyer, G. G. Rondina, D. Häussinger, M. Mayor, A. Shayeghi, V. Köhler, M. Arndt, *Pushing the mass limit for intact launch and photoionization of large neutral biopolymers*, Commun. Chem. **1**, 93 (2018)

[3] J. Schätti, U. Sezer, S. Pedalino, J. P. Cotter, M. Arndt, M. Mayor, V. Köhler, *Tailoring the volatility and stability of oligopeptides*, J. Mass. Spectrom. **52**, 550 (2017)

[4] U. Sezer, P. Geyer, M. Kriegleder, M. Debossiac, A. Shayeghi, M. Arndt, L. Felix, M. Mayor, *Selective photodissociation of tailored molecular tags as a tool for quantum optics*, Beilstein J. Nanotechnol. **8**, 325 (2017)

Delivering polymer vesicles into cell nuclei

Project P1404: Selective transport of funtionalized nanocarriers into biomimetic and natural nuclear pore complexes
Project Leader: R.Y. H. Lim and C. G. Palivan
Collaborator: C. Zelmer (SNI PhD Student)

Introduction
The cell nucleus is the ultimate target for many therapeutic treatments including cancer, brain disorders and heart dysfunction [1]. However, little is known about how synthetic nanocarriers (NC) infiltrate into the cell nucleus [2, 3]. In particular it remains unresolved how large cargoes are transported through nuclear pore complexes (NPCs) that manifest a key cellular barrier in eukaryotes [4].

Here, we have developed functional polymer NCs that are selectively internalized in the cell nucleus. A key advance of our study includes resolving individual NCs that infiltrate NPCs at the single event level. This follows from developing a transmission electron microscope (TEM) method for characterizing soft matter-based nano-objects, which remains challenging in crowded cellular environments.. This requires special conditions, such as Ruthenium Red (RR) encapsulation inside NCs and a regressive EDTA post-treatment. This provided snapshots of NCs inside cells and was complemented by time-lapse fluorescence microscopy. Analyzing the time-dependent nuclear NC accumulation intensity serves as a measure of actual carrier mobility and calculate kinetic import rates. Our findings underscore the potential applications of polymersome NCs to encapsulate, target and release therapeutic payloads into cell nuclei.

Engineering nuclear targeting nanocarriers
Biocompatible polymersomes were prepared using a mixture of PMOXA4-PDMS44-PMOXA4 (95 wt%) and maleimide end-group functionalized derivative (5 wt%) via a solvent-free rehydration method. Polymersome NCs stand out for their enhanced membrane stability compared to liposomes and bio-chemical functionalization at their extralumenal interface to facilitate targeting approaches [5, 6]. To induce the essential nuclear targeting specificity, we functionalized nuclear localization signals (NLSs) to the maleimide linking sites presented at the NC. Furthermore, we co-encapsulated RR inside the cavities and Bodipy 630/650 into the membranes of functionalized polymersomes. Extrusion through 50 nm filters yielded NLS-nanocarriers that are 44 ± 17 nm as determined by TEM (Fig. 1). In parallel, similar sized polymersomes lacking NLSs were prepared to serve as non-specific controls.

Polymersome nanocarriers infiltrate living cell nuclei via NPCs
By using TEM and a regressive EDTA staining, we identified intact polymersomes within thin-sections prepared from HeLa cells [7]. Those featured a closed 71 ± 13 nm spanning circular membrane and a bright inner cavity. Indeed, NLS-NCs bypassed the nuclear envelope (NE) via NPCs (Fig. 2A) and populated the cell nucleus (Fig. 2B). As expected, blank NCs that lacked NLS were less likely to enter the nucleus and aligned predominantly along the cytoplasmic side of the NE (Fig. 2C). In sum, we found that 52% of all identified NLS-NCs populated the nuclear interior. In addition, 31% were found in NPCs while 17% remained in the cytoplasm. In comparison, 80% of blank NCs were found in the cytoplasm. These results are indicative for highly selective and hence efficient NLS-NC import.

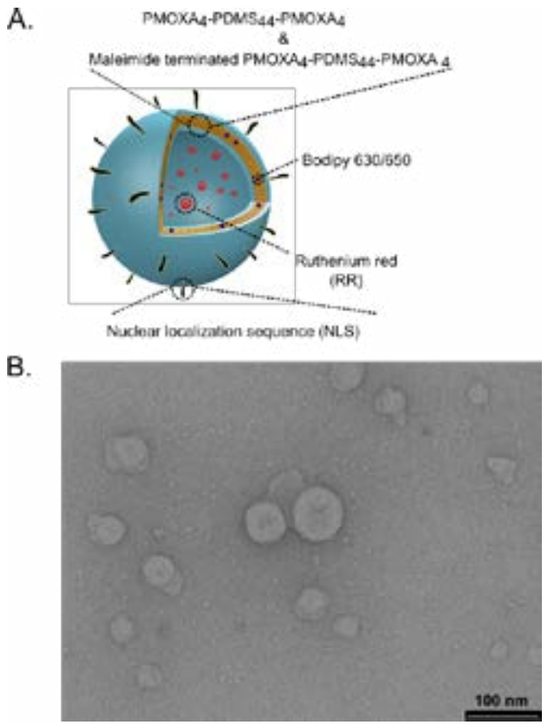

Fig. 1 Functional polymersome NCs A. NCs are constructed of amphiphilic PMOXA4-PDMS44-PMOXA4 block-copolymers and surface functionalized with NLS tags, B. and show a characteristic rounded morphology in TEM.

Thereafter, we evaluated the nuclear targeting efficacy of NLS-NCs vs. blanks in HeLa cells by laser scanning confocal microscopy (Fig. 3A, 3B.). While both nanocarriers infiltrated into the cells, only NLS-NCs showed strong nuclear import. Further our time-dependent measurements revealed that the efficiency and kinetics of import was enhanced for NLS-NCs as compared to the blank controls (Fig. 3C).

Summary
In a collaborative effort of the Lim and the Palivan labs, we have developed a novel polymer based nanocarrier system for selective nuclear delivery. We were able to localize intact polymer vesicles in the cellular context and currently continue our research with the in situ release of nuclei active cargo entities.

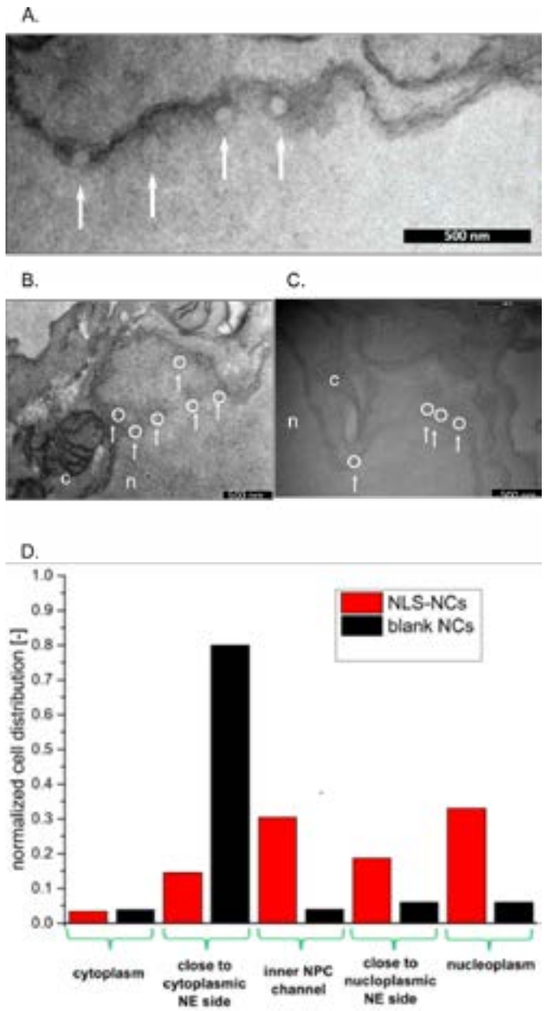

Fig. 2 Nuclear import of functional NLS-NCs A. is facilitated by NPC translocation B. and fosters their accumulation within cell nuclei. C. Blank NCs are rejected from nuclear entry and align along the NE. D. NLS-NCs shows a homogenous spatial distribution across the nuclear envelope whilst blank NCs are mostly retained in the cytoplasm.

References
[1] S. Tammam, H. Azzazy, A. Lamprecht, *How successful is nuclear targeting by nanocarriers?*, J. Control. Release **229**, 140-153 (2016)

[2] M. Stewart, *Molecular mechanism of the nuclear protein import cycle*, Nat. Rev. Mol. Cell Biol. **8(3)**, 195-208 (2007)

[3] S. Vujica, C. Zelmer, R. Panatala, R. Y. H. Lim, *Nucleocytoplasmic transport: a paradigm for molecular logistic in artificial systems*, CHIMIA **70(6)**, 413-417, (2016)

[4] A. Hoelz, E. W. Debler, G. Blobel, *The structure of the nuclear pore complex*, Ann. Rev. Biochem. **80**, 613-643 (2011)

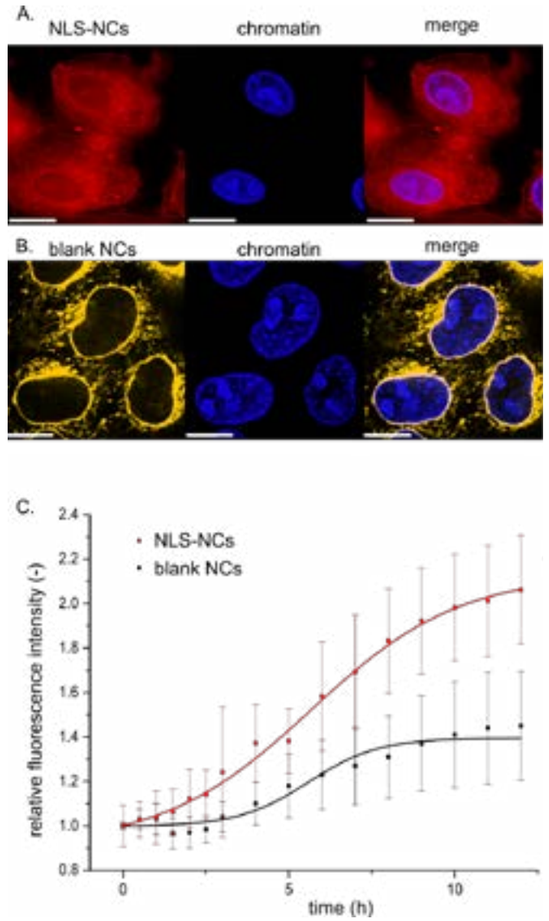

Fig. 3 HeLa cells after 12h incubation with A. functional NLS-NCs compared to B. blank NCs. Scale bar = 10 µm. C. Time dependent import evolution of NLS-NCs vs. blank NCs.

[5] C. G. Palivan, R. Goers, A. Najer, X. Zhang, W. Meier, *Bioinspired polymer vesicles and membranes for biological and medical applications*, Chem. Soc. Rev, **45(2)**, 377-411 (2016)

[6] V. Mikhalevich, C. Zelmer, A. Car, C. G. Palivan, W. Meier, *Bioinspired membranes*, RSC Polymer Chemistry Series, **22**, 221-258 (2017)

[7] P. Tanner, V. Balasubramanian, C. Palivan, *Adding Nature's organelles: Artificial peroxisomes play their role* Nano Letters, **13(6)**, 2875-2883 (2013)

Surface functionalization and nano-photonics for diamond quantum sensing

Project P1405: Surface-functionalization of diamond nano-magnetometers for applications in nano- and life-sciences
Project Leader: U. Pieles and P. Maletinsky
Collaborators: M. Batzer (SNI PhD Student), M. Grimau, B. Shields, L Thiel, and S. Saxer

Introduction

This project aims at enhancing the performance of spins in diamond as quantum sensors in the material- and life-sciences. Over the last years, such spins have been established as highly attractive platforms to perform nanoscale quantum sensing with highest spatial resolution and sensitivity [1]. Various architectures are being pursued [2], from scanning probe tips [3], over diamond mechanical oscillators to "wide-field imaging" geometries [4] containing spin ensembles for magnetometry. Common to all these approaches is the fact that the spins in question need to be placed to within few nanometers of the diamond surface to maximize sensing performance. Such proximity, however, is also known to negatively affect the spin's quantum coherence properties through ubiquitous, but poorly understood noise sources (creating fluctuating electric-, magnetic- or strain-fields). The goal of this project is to overcome these key limitations for diamond-based sensing technologies by devising and implementing suitable strategies to passivate diamonds noisy surface. Furthermore, we explore novel spin systems in diamond and innovative approaches in nanophotonics to further enhance sensing performance.

Experimental results

1. Novel photonic nanostructures results

We have explored novel approaches for efficient light extraction from fluorescent color centers in diamond. Our conventional and established approach consists in placing such emitters into diamond nanopillars, which we fabricate in-house using advanced nanofabrication tools, including plasma etching of diamond. Such nanopillars enhance light-extraction efficiencies from spins in diamond by at least one order of magnitude and we employ the resulting cylinders as scanning probes for nanoscale magnetometry. One downside of such cylindrical nanopillars (with typical diameters ~200 nm) is that the proximity of the spins to the scanned surface is only poorly controlled – small misalignments in the angle of the pillar with respect to a scanned surface can lead to a significant increase of this distance.

We have developed a new approach which may overcome this issue by a radical change of the geometry of the diamond nanostructure from cylindrical to pyramidal. The diamond nanopyramids are formed by overgrowth of our diamond nanopillars using chemical vapor deposition (CVD) of ultrapure diamond, which is performed at a partner lab at the Fraunhofer Institute in Freiburg. Such CVD growth is highly anisotropic with respect to diamond's crystalline axes, in that growth along the [111] axes is much faster than growth along [001]. Such overgrowth therefore continuously converts a [001]-oriented diamond nanopillar into a pyramid with [111]-facets. Overgrowth of just few microns of diamond material then yields the near-perfect pyramids shown in figure 1a, with tip-apex radii on the order of 10 nm.

After fabrication of these structures, we have successfully incorporated color center spins (in form of both, Silicon-Vacancy (SiV) and Nitrogen-Vacancy (NV) centers) into the pyramids by ion implantation. We subsequently conducted systematic studies of the fluorescence properties of these centers, which were located close to the pyramid apex. We have observed optically detected electron spin resonance (not shown) and, more importantly, a highly directed fluorescence emission from the pyramids. In particular, we have demonstrated directional emission towards the pyramid base by back-focal plane imaging, which represents a measurement of the angular emission characteristics of the device. Figures 1b and 1c show a comparison of such BFP images taken for upward (away from the diamond tip) and downward (towards the pyramid base) emission. A clear directional emission and a narrowing of the exit cone aperture (the effective "numerical aperture" of the device) in the downward direction was shown.

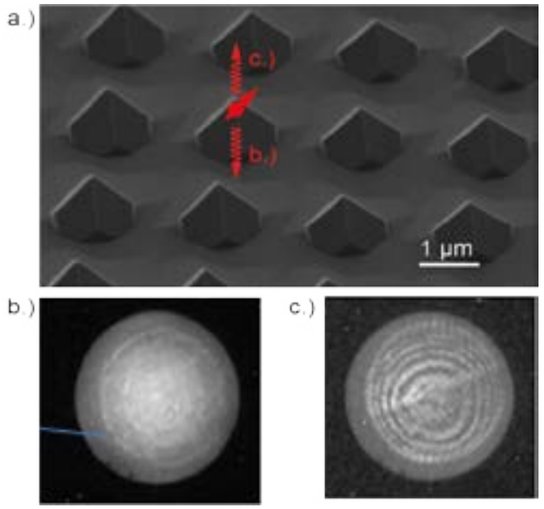

Fig. 1 (a) Single-crystalline diamond nanostructures in form of nanoscale pyramids. The pyramids were created by overgrowth of diamond nanopillars with high-purity diamond material. (b) and (c) show back-focal plane emission patterns of SiV center emission from the pyramids in the downward (b) and upward (c) direction. A clear narrowing of the emission cone, together with an increase of overall emission intensity is observed in the downward direction as compared to the upward direction. The perimeter of the circular image in both cases corresponds to a numerical aperture of 0.8 in air.

2. New color centers in H-terminated diamond

Last year, we have demonstrated the successful termination of diamond surfaces with Hydrogen, using annealing in a Hydrogen atmosphere. This approach was developed in collaboration with members of the Schönenberger group, in whose furnace the functionalization was performed. Next to terminating dangling bonds on the diamond, such H-terminated surfaces result in a band-bending within the diamond, which typically leads to de-ionization (from negative to neutral or positive) of color centers [5]. While this charge conversion is undesired in the case of NV centers, recent results [6] showed the contrary for SiV centers. Remarkably, such neutral Silicon-Vacancy centers (SiV^0) have recently been shown to exhibit excellent coherence properties and could therefore be very well suited for quantum sensing [6]. A key difficulty there, however, is the required charge state control to favor SiV^0 over the normally prevalent SiV^- state.

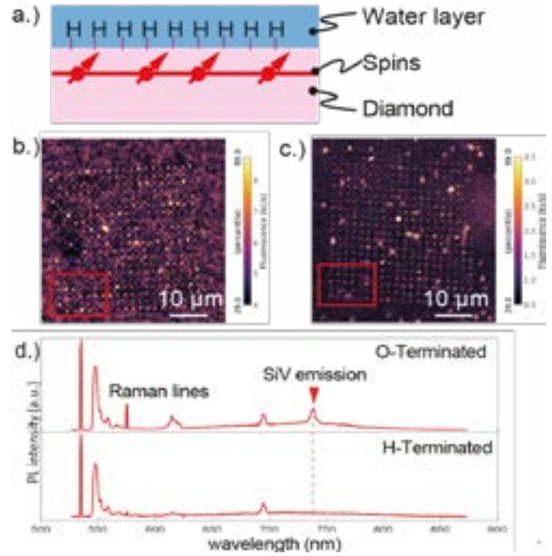

Fig. 2 (top) Schematics illustrating the diamond hydrogen termination used to control emitter charge state and to passivate diamond dangling bonds. b.) and c.) Confocal fluorescence maps of ordered arrays of SiV centers with Oxygen (b) and Hydrogen (c) terminated diamond. A clear difference in SiV emission is observed (see, e.g. region highlighted in red. D.) fluorescence spectra recorded on an SiV location for Oxygen and Hydrogen terminated diamond. A complete disappearance of the SiV^0 emission after Hydrogen termination is observed, indicating a transition into another charge state (not visible in the spectral range shown). The transition between O-termination and H-Termination is completely reversible.

We addressed this issue by combining our ability to faithfully hydrogen-terminate diamond, with our recently developed know-how in implanting and characterizing SiV centers in diamond. Figure 2b-d shows the key results of our study so far. We were able to create shallow (~20 nm deep) SiV- centers in regular arrays using Si ion implantation and annealing, followed by suitable patterning of the diamond surface. For O-terminated diamond, we saw clear and stable fluorescence, which we could spectroscopically assign to SiV- emission (Fig. 2d). Upon Hydrogen termination, all SiV–emission disappeared (Fig. 2c, d), indicating a transition to an SiV^0 or SiV^+ charge state. Importantly, the process is fully reversible, i.e. upon renewed O-termination, all SiV locations showed SiV^0 emission again.

We are currently investigating the fluorescence and charge properties of the color centers after H-termination. Given that both SiV^0 and SiV^+ emit in the infrared range, for which our setups are currently ill-equipped, we perform these measurements with a partner lab at the Ludwig-Maximilians University in Munich, and concise results are still pending.

Outlook

The main goals for the coming year will be to finalise the characterization of our pyramidal diamond photonic nanostructures and definitely determine the charge state of SiV emitters after H-termination. Furthermore, we still aim at capping a H-terminated diamond surface with hBN to expel water and, thereby stabilise negatively charged colour centres near the surface.

These achievements, which we hope to write up into separate publications in the spring, will form the end of SNI school project P1405 and its candidate, Marietta Batzer, will defend her thesis in the summer 2019.

References

[1] J. M. Taylor, P. Cappellaro, L. Childress, L. Jiang, D. Budker, P. R. Hemmer, A. Yacoby, R. Walsworth, M. D. Lukin, *High-sensitivity diamond magnetometer with nanoscale resolution*, Nature Physics **4**, 482 (2008)

[2] L. Rondin, J.-P. Tetienne, T. Hingant, J.-F. Roch, P. Maletinsky, V. Jacques, *Magneto-metry with nitrogen-vacancy defects in diamond*, Rep. Prog. Phys. **77**, 056503 (2014)

[3] P. Appel, E. Neu, M. Ganzhorn, A. Barfuss, M. Batzer, M. Gratz, A. Tschoepe, P. Maletinsky, *Fabrication of all diamond scanning probes for nanoscale magnetometry*, Rev. Sci. Instrum. **87**, 063703 (2016)

[4] A. Horsley, P. Appel, J. Wolters, J. Achard, A. Tallaire, P. Maletinsky, P. Treutlein, *Microwave device characterisation using a widefield diamond microscope*, Phys. Rev. Applied **10**, 044039 (2018)

[5] M. V. Hauf, B. Grotz, B. Naydenov, S. Pezzagna, J. Meijer, F. Jelezko, J. Wrachtrup, M. Stutzmann, F. Reinhard, J.A. Garrido, *Chemical control of the charge state of nitrogen-vacancy centers in diamond*, PRB **83**, 081304 (2011)

[6] B. C. Rose et al., *Observation of an environmentally insensitive solid-state spin defect in diamond*, Science **361**, 60-63 (2018)

Different distance depencences of electron transfer rates for low and high driving-forces

Project P1406: Charge transfer versus charge transport in molecular systems
Project Leader: O. S. Wenger and M. Calame
Collaborators: S. Neumann (SNI PhD Student) and J. Overbeck (SNI PhD Student)

Introduction

The rates of electron transfer reactions (k_{ET}) usually decrease with increasing donor-acceptor distance, and the conductivity of a molecular wire typically decreases upon elongation. Whilst so-called hopping processes can lead to very shallow distance dependences, it is very rare that electron transfer rates or conductivities increase upon distance elongation. However, early theoretical work predicted such phenomena for systems in which the driving-force for electron transfer is sufficiently large [1]. Surprisingly, there had been no unambiguous experimental observations confirming these theoretical predictions until we reported increasing electron transfer with increasing donor-acceptor distance (r_{DA}) a few years back [2, 3].

In this SNI-funded project, we set out to explore how the magnitude of this unusual phenomenon correlates with the driving-force of the electron transfer reaction, aiming to get more quantitative insight than in our initial studies. Toward this end, we synthesized rigid rod-like donor-photosensitizer-acceptor compounds, so-called molecular triads, in which the kinetics of photo-triggered electron transfer events are not limited by diffusion. We then explored these compounds with spectro-electrochemical methods and nanosecond transient absorption spectroscopy. In the past year of the funding period, we have been able to obtain a nearly complete picture of how the distance dependence of k_{ET} varies as a function of driving-force.

A complete series of molecular triads

We have now completely synthesized and characterized the three series of donor-photosensitizer-acceptor compounds shown in figure 1, comprised of a total of 7 molecules, 3 of which were available from prior studies [2, 3]. The typical synthetic protocol for such compounds involves 7-12 synthetic steps hence this is a very time-consuming task, requiring very careful molecular design ahead of time. In all these molecular triads, excitation of the central transition-metal-based photosensitizer with visible light triggers electron transfer, leading to an oxidized donor on the one hand and a reduced acceptor on the other hand. The subsequent thermal charge-recombination process between the donor-localized hole and the acceptor-localized electron is then the key process of interest. This charge-recombination event is associated with driving-forces (Δ-G_{ET}^0) of ca. 1.2 eV, 1.6 eV or 2.0 eV depending on triad series (Fig. 1).

For the TAA-ph_n-Ru-ph_n-NDI compound (displayed at the top of Fig. 1), we find a normal distance dependence, i. e. a decrease of k_{ET} with increasing r_{DA} (red squares in Fig. 2). For this compound, the driving-force for charge recombination is relatively low, only ca. 1.2 eV. At the other extreme, for the TPA-phn-Ir-phn-AQ triads (bottom of Fig. 1) the driving-force is very large, ca. 2.0 eV. In that case, the distance dependence of k_{ET} is abnormal, exhibiting an increase upon distance elongation (green triangles in Fig. 2), similar to what we previously reported for the TAA-ph_n-Ru-ph_n-AQ compound series (middle of Fig. 1, blue circles in Fig. 2).

We learn from the data in figure 2 that for relatively low-driving-forces (red) the distance dependence of electron transfer

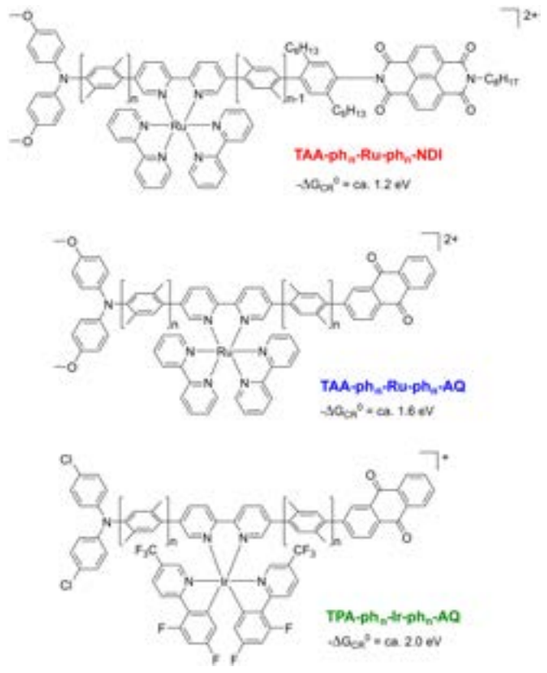

Fig. 1 Molecular triads synthesized and investigated in this work. Driving-forces (Δ-G_{ET}^0) for thermal charge recombination between oxidized triarylamine donors and reduced acceptors are as indicated.

rates is fundamentally different than for high driving-forces (blue, green) [4]. In fact, in order to observe the unusual distance dependences very high driving-forces of 1.6 eV and above are required, and we speculate that this is the key reason why this effect had not been observed earlier. It seems that most prior investigations focused on systems with lower driving-forces.

Ongoing further work

Due to the high driving-force of our new TPA-phn-Ir-phn-AQ triad remarkable 2.0 eV of energy can be stored in the charge separated state by absorption of a single photon. Recently, an energy storage of 1.7 eV for a single photon absorption and 2.0 eV for a two photon process were reported for molecular systems [5, 6]. However, we wondered if we can increase the amount of stored energy and set out to explore a Z-Scheme like approach where two light-absorbing units build up a high energy charge-separated state after the absorption of two photons. Unlike as the system reported by the groups of Hammarström and Odobel, [6] our Z-Scheme approach is purely organic and should store ca. 2.8 eV after double photoexcitation (Fig. 3). Our system uses optical charge transfer processes instead of the more commonly used photoinduced electron transfer reactions. This circumstance makes an exact structural planning and study of the different units of our system essential. We are currently synthesizing four reference compounds to test the design of our target system and to collect important

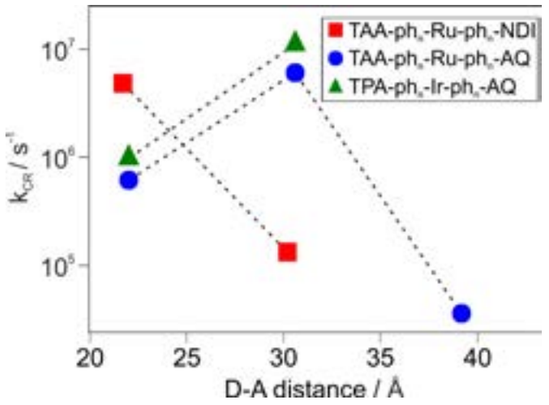

Fig. 2 Distance-dependence of the rate for thermal charge recombination in the molecular triads from Fig. 1.

information for the overall design. In a next step we will then set out to synthesize our target system.

Conclusion

Electron transfer rates do not always decrease with increasing reactant separation. Our systematic studies demonstrate for the first time that for highly exergonic processes the reaction rates can actually increase with increasing distance. This could have important implications for solar energy conversion, where undesired highly exergonic charge-recombination events are usually in competition with desired photo-induced charge-separation processes that are more weakly exergonic. Furthermore, we anticipate that our fundamental findings will be of relevance in the greater context of molecular electronics, for example with regard to precise control of charge transfer rates.

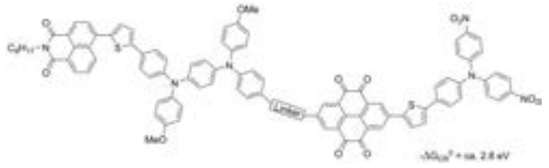

Fig. 3 Molecular approach for a Z-Scheme analogue storing ca. 2.8 eV.

References

[1] B. S. Brunschwig, S. Ehrenson, N. Sutin, *Distances Dependence of Electron Transfer Reactions – Rate Maxima and Rapid Rates at Large Reactant Separations*, J. Am. Chem. Soc. **106**, 6858 (1984)

[2] M. Kuss-Petermann, O. S. Wenger, *Increasing Electron-Transfer Rates with Increasing Donor-Acceptor Distance*, Angew. Chem. Int. Ed. **55**, 815 (2016)

[3] M. Kuss-Petermann, O. S. Wenger, Electron Transfer Rate Maxima at Large Donor-Acceptor Distances, J. Am. Chem. Soc. **138**, 1349 (2016)

[4] S. Neumann, O. S. Wenger, *Fundamentally Different Distance Dependences of Electron Transfer Rates for Low and High Driving-Forces*, Inorg. Chem. doi: 10.1021/acs.inorgchem.8b02973.

[5] G. N. Lim, C. O. Obondi, F. D'Souza, *A High-Energy Charge-Separated State of 1.70 eV from a High-Potential Donor-Acceptor Dyad : A Catalyst for Energy-Demanding Photochemical Reactions*, Angew. Chem. Int. Ed. **55**, 11517 (2016)

[6] L. Favereau, A. Makhal, Y. Pellegrin, E. Blart, J. Petersson, E. Göransson, L. Hammarström, F. Odobel, *A Molecular Tetrad That Generates a High-Energy Charge-Separated State by Mimicking the Photosynthetic Z-Scheme,* J. Am. Chem. Soc. **138, 11**, 3752 - 3760 (2016)

Coupling an ultracold ion to a metallic nanowire

Project P1407: Coupling a single ion to a nanomechanical oscillator
Project Leader: S. Willitsch and M. Poggio
Collaborator: P. Fountas (SNI PhD Student)

Introduction

At present, considerable efforts are undertaken towards creating hybrid quantum systems for the development of quantum technologies. The motivation for a solid state-atomic interface emerges from the possibility to combine the advantages of both platforms. Trapped ultracold atoms offer excellent coherence properties. One of the most promising candidates for an atomic system is an ultracold ion which can be isolated from the environment by being trapped with radiofrequency electric fields in ultra-high vacuum [1]. By laser cooling the ion to its motional ground state, one can manipulate its motional and spin degrees of freedom with high accuracy. Conversely, nanowires are nanomechanical systems that are highly scalable and integrable and can be interfaced with diverse quantum devices [2, 3]. A great challenge is the coupling of the two systems while maintaining good coherence properties [4]. In order to combine the aforementioned advantages, one has to be able to transfer quantum states between them.

Here, we report progress towards the implementation of an interface between an ultracold ion and a metallic nanowire in a miniaturized segmented-layer ion trap (Fig. 1) in order to study the coupling between these two systems mediated by electric fields [4]. We have shown in previous reports possibilities of driving the nanowire and creating Gaussian and non-Gaussian quantum states on the ion at room temperature. In parallel to the completion of the experimental setup (Fig. 1), we present theoretical results on the dynamics of both oscillators when both can be described in the quantum regime, and the limits of their coupling strength. Our immediate aim is to study experimentally the coupling mechanisms underlying this new interface. At a later stage of the project, we envisage the realization of the aforementioned state engineering schemes.

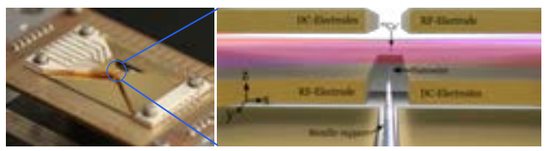

Fig. 1 Left figure: Miniaturized segmented-layer ion trap consisting of a stack of gold-coated alumina wafers clamped together on a printed circuit board. Right figure: Schematic representation of the experiment in the trapping region, showing a trapped $^{40}Ca^{+}$ ion, the corresponding laser beams for cooling the ion to its ground state, the RF and DC electrodes that generate the trapping fields and a conductive nanowire with its support located at a specific distance below the ion.

Quantum dynamics of the coupled nanowire-ion system

To assess the feasibility and potential of such experiments, we have carried out a detailed modelling of the quantum dynamics of the system [4]. We consider the case in which both the ion and the nanooscillator operate in the quantum regime, as would be the case in a cryogenic experiment in which the nanowire is cooled close to the quantum-mechanical ground state of one of its modes. The quantized Hamiltonian of the coupling between the nanowire and the ultracold $^{40}Ca^{+}$ ion reads

$$\hat{\mathcal{H}}_{coupling} = g(\hat{a}^\dagger + \hat{a})(\hat{b}^\dagger + \hat{b})$$

$$with\ g = \frac{\hbar\epsilon}{2d^3}\frac{1}{\sqrt{mM}}\sqrt{\frac{1}{\omega_{ion}\,\omega_{nw}}}$$

Here, â†, â, and b̂†, b̂, are the ladder operators of the ion and the nanowire respectively, g is the coupling strength, $\epsilon = k_c Q_1 Q_2$, where k_c is the Coulomb constant, Q_1 and Q_2 is the charge of the ion and the nanowire respectively and d is the relative distance between the tip of the nanowire and the ion. m,ω and M,ω_{nw} are the mass and the oscillation frequency of the ion and the nanowire respectively. It can be seen that the coupling strength is inversely proportional to the product of the masses of those two systems. Conventional metallic nanowires exhibit very high masses ($M \approx 10^{-14}$ kg) compared to ions which renders the coupling between the two systems very small. This can be mitigated using carbon nanotubes instead ($M \approx 10^{-20}$ - 10^{-23} kg), which are very good conductors in specific configurations. The other dominant limitation towards achieving strong coupling is the mechanical decoherence rate of the nanowire caused by its coupling to the bath which was realistically included in the modelling. With these assumptions, the Lindblad master equation of the coupled system

$$\frac{d\hat{\rho}}{dt} = -\frac{i}{\hbar}[\hat{\mathcal{H}}_{eff}, \hat{\rho}] + \gamma_{ion}^{heating}\,\hat{\mathcal{L}}[\hat{a}^\dagger]\hat{\rho} + \gamma_{ion}^{cooling}\,\hat{\mathcal{L}}[\hat{a}]\hat{\rho} + \gamma_{nw}(N_{nw}+1)\,\hat{\mathcal{L}}[\hat{b}]\hat{\rho} + \gamma_{nw}N_{nw}\,\hat{\mathcal{L}}[\hat{b}^\dagger]\hat{\rho}$$

was solved numerically. Here, $\gamma_{ion}^{heating}$ is the heating rate of the ion in the trap $\gamma_{ion}^{cooling}$ is the cooling rate of the ion from the interaction with the cooling laser. The total effective Hamiltonian of the system is

$$\hat{\mathcal{H}}_{eff} = \hbar\omega_{ion}(\hat{a}^\dagger\hat{a} + \frac{1}{2}) + \hbar\omega_{nw}(\hat{b}^\dagger\hat{b} + \frac{1}{2}) + g(\hat{a}^\dagger + \hat{a})(\hat{b}^\dagger + \hat{b})$$

Choosing typical parameters $m = 6.6 \times 10^{-26}$ kg, a conservative value of $M = 6.6 \times 10^{-20}$ kg, $\omega_{ion}/2\pi = \omega_{nw}/2\pi = 600$ kHz, $d = 50$ µm and a voltage of $V_{nw} = 100$ mV on the nanowire, the coupling strength between the ion and the nanowire is $g/2\pi =$ 37 Hz. Under these conditions, back action of the ion on the nanowire and coherent dynamics cannot be realized at 4.2 K bath temperatures achieved in typical He cryostats due to large thermal excitations. We find that at temperatures above 500 µK, the nanowire essentially behaves like a classical object vis-à-vis the ion. This behaviour changes at lower temperatures which may become technically achievable in the imminent future.

Figure 2 shows the coherent phonon dynamics of the hybrid system with and without continuous sideband cooling of the ion and a nanowire under these conditions.

It can be seen from figure 2a that the nanowire is sympathetically cooled from a single ultracold Ca^{+} ion. Figure 2b shows the energy swap between the nanowire and the ion. In the absence of an ion cooling mechanism, the coherent dynamics is more clearly manifested. Eventually both systems equilibrate with the bath. Moreover, every time that the system undergoes an energy swap, there is a transfer of the quantum state between the ion and the nanowire as is shown in figure 3.

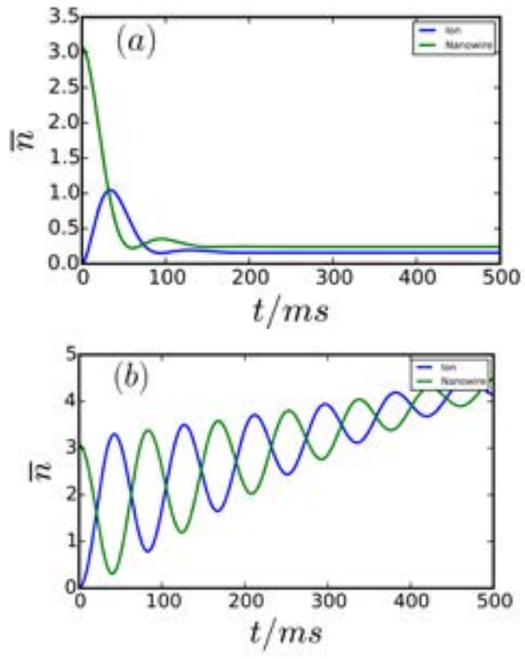

Fig. 2 Phonon dynamics for (a) an ion-nanowire system with continuous cooling of the ion and (b) the same with no ion cooling in the quantum regime. See text for details.

Figures 3a and b show the initial Wigner functions of an ultracold ion and a nanowire in the zeroth and fourth Fock states, respectively. Figures 3c and d show the relevant Wigner functions after a specific interaction time at which one cycle of energy swap has occurred according to figure 2b. It can be seen that the states of the ion and the nanowire have been exchanged. The different intensities of the Wigner functions and the slightly larger spread of the vacuum state of the nanowire compared to the initial states are attributed to the thermal decoherence of the hybrid system. We have seen the same behavior for various initial quantum states for both systems including Fock, coherent, squeezed and thermal states. Therefore, this interaction allows to create specific quantum state in one of these systems and read it out from the other. This might be an interesting approach for studying decoherence mechanisms or creating quantum gates between solid-state and ionic systems, opening up possibilities for new quantum devices.

Outlook

The experimental setup is completed and currently being commissioned. Based on our theoretical results, we believe that this system will prove promising for fundamental studies on the borders of classical and quantum mechanics, and also as a probe of decoherence processes of quantum and macroscopic bodies. Finally, our setup might prove fruitful for various applications in spectroscopy, quantum sensing and quantum technologies.

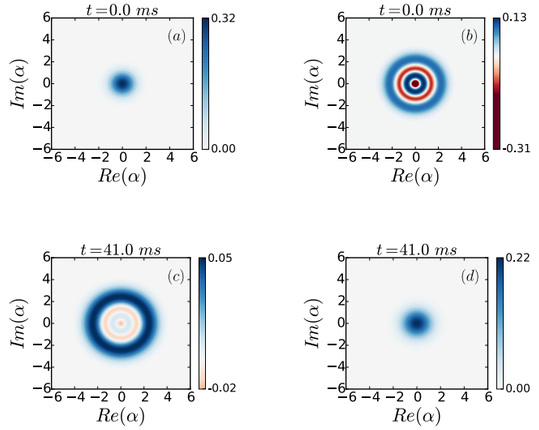

Fig. 3 a, b Wigner functions of the initial states of a ground-state cooled ion, i.e., n=0, and a nanowire in the fourth Fock state n=3, respectively. c, d Wigner functions of the swapped states of the ion and the nanowire respectively after 41 ms of interaction at 100 µK bath temperature and 37 Hz coupling strength. The two systems have swapped their initial quantum states at this point of time.

References

[1] S. Willitsch, *Coulomb-crystallised molecular ions in traps: methods, applications, prospects*, International Reviews in Physical Chemistry **31(2)**, 175 (2012)

[2] M. Montinaro, G. Wüst, M. Munsch, E. Fontana, E. Russo-Averchi, M. Heiss, A. Fortcumberta, I. Morral, R. J. Warburton, M. Poggio, *Quantum dot opto-mechanics in a fully self-assembled nanowire*, Nano Letters **14(8)**, 4454 (2014)

[3] J. M. Pirkkalainen, S. Cho, F. Massel, J. Tuorila, T. Heikkilä, P. Hakonen, M. A. Sillanpää, *Hybrid circuit cavity quantum electrodynamics with a micromechanical resonator*, Nature Communications **6**, 6981 (2015)

[4] P. Fountas, M. Poggio and S. Willitsch, *Classical and quantum dynamics of a trapped ion coupled to a charged nanowire*, New J. Phys **21**, 013030 (2019)

Characterization of hydrogen plasma defined graphene edges

Project P1408: Clean zigzag and armchair graphene nanoribbons
Project Leader: D. Zumbühl and D. Loss
Collaborators: M. Rehmann (SNI PhD Student), Y. B. Kalyoncu, F. Froning, and F. Braakman

Hydrogen Plasma Defined Graphene Edges

Graphene has attracted a lot of interest as an extraordinary material for fundamental research and applications. Graphene nanoribbons are of particular interest as a playground for novel quantum states: in ribbons with crystallographic zigzag (zz) edge termination, ferromagnetic order of electron spins localized on the edge has been predicted [1]. High quality zz edges are required to observe the predicted physical effects. We use a technique employing a cold remote hydrogen (H) plasma [2] which exhibits highly anisotropic etching yielding hexagonal shaped etch pits with edges pointing along the zz direction. To investigate the edge quality of H plasma defined graphene edges, we use Raman spectroscopy. It is known, that a pure zz edge does not show any D-peak in the Raman spectrum, whereas edge disorder in form of point defects and armchair (ac) segments activates the D-peak [3].

Graphite vs Graphene

Figure 1a and b show AFM images of a graphite surface and a graphene on hBN sample, respectively. In both cases, exposure to a remote H plasma creates hexagonal shaped etch pits. To compare the edge qualities of hexagon edges formed on graphite with the ones formed on graphene/hBN, we acquire Raman spectra on both sample types (Fig. 1c). The Raman spectrum measured on graphite exhibits no D-peak which indicates high quality zz edges. In contrast, the Raman spectrum recorded on the graphene/hBN sample shows a substantial D-peak which points towards the presence of edge disorder.

To get further insight into the nature of this edge disorder, polarized Raman measurements are carried out. Thereby, linearly polarized light is focused at the edge and Raman spectra are recorded for different angles of the polarization with respect to the graphene edge. The data is fitted to a theory proposed by Xu et al. [4] which allows to deduce the relative abundance of point defects to ac-30° segments, both of which are possibly present at a zz edge and would give rise to a D-peak. The fit indicates a very low amount of point defects and suggests that the disorder essentially exists of ac-30° segments only. A second theory [3] allows to extract a ratio of zz/ac segments which yields 60% zz and 40% ac segments.

The differences in edge quality between edges on graphite and edges on graphene/hBN could originate from the different substrates, i.e. the lattice mismatch between graphene and hBN possibly leads to Moiré super-lattice effects which might influence the quality of the H plasma etching process and hence the quality of the created edges. Further investigations are required to pinpoint this conjecture and eventually find a way to create more pure zz edges in single layer graphene.

Hole Spins in Ge/Si Core/Shell Nanowires

Single hole spins confined in quantum dots (QDs) in Ge/Si core/shell nanowires (NWs) combine several advantageous properties which make them potentially very powerful quantum bits [5]. The natural abundance of non-zero nuclear spins in both silicon and germanium is relatively small and can be further reduced to a negligible amount by isotopic purification. Furthermore, hole spins have no contact hyperfine interaction due to their p-type wavefunction. These properties make hole spin qubits in silicon and germanium resilient against dephasing via interaction with nuclear spins. A particularly promising feature of hole spins in Ge/Si core/shell NWs is the nature of spin-orbit interaction (SOI) in this system. Confinement to one dimension gives rise to an effective SOI in the valence band, which is predicted to be both strong and tunable [6], enabling fast all-electrical spin manipulation. An external electric field can be used to set the strength of this SOI. This promises the capability of electrical gating of the SOI, allowing to switch to a large SOI for high interaction strengths and fast quantum operations, or to turn off SOI for increased qubit coherence.

We electrostatically tune hole QDs of variable length to very low hole occupation numbers and study their excited state spectrum, allowing us to make comparisons to theoretical predictions on the nature and strength of the SOI [7].

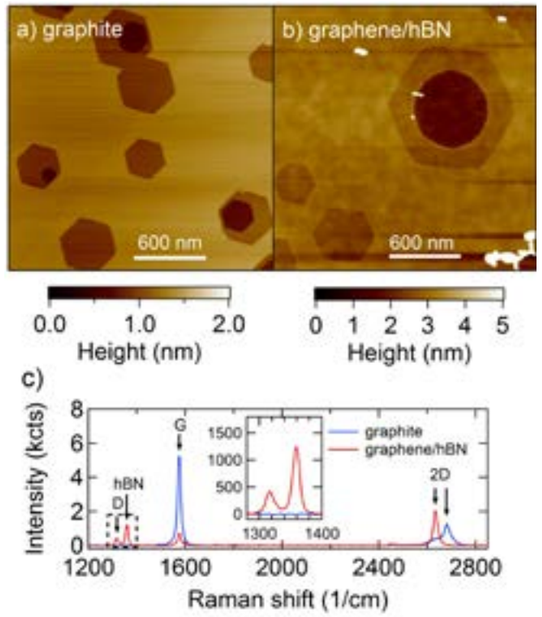

Fig. 1 AFM topography image of a graphite surface a) and a graphene on hBN surface b) after exposure to a remote H plasma which creates hexagonal etch pits on the surfaces due to an anisotropic etching effect. c) Raman spectra recorded on the graphite surface (blue) and the graphene/hBN sample (red). The D-peak is absent on graphite but present on the graphene/hBN sample. The Raman spectra were recorded with a red laser (λ = 633 nm), circularly polarized light, an intensity of 1.5 mW and an integration time of 60 s with one accumulation.

Experimental Setup

We use a Ge/Si NW with an estimated Ge core radius of 10 nm and Si shell thickness of 2.5 nm. Five Ti/Pd bottom gate electrodes are lithographically defined on a p++-doped Si substrate covered with 290 nm thermal oxide. The bottom gates have a thickness of 15 nm, a width of 20 nm, and are equally spaced with a pitch of 50 nm. On either side of these gates, a plateau gate is defined, which serves to prevent bending of the NW. The bottom gates are subsequently covered by a layer of Al_2O_3 of thickness 20 nm through atomic layer deposition at 225°C. In a next step, the NW is placed deterministically on top of the bottom gates using a micromanipulator setup. Electrical contact to the NW is made through two Ti/Pd (0.5/60 nm) contact pads, which are lithographically defined and metallized after a brief HF dip to strip the NWs native oxide.

We perform transport measurements by applying a dc source-drain bias V_{SD} over the NW and measuring the differential conductance using standard lock-in techniques.

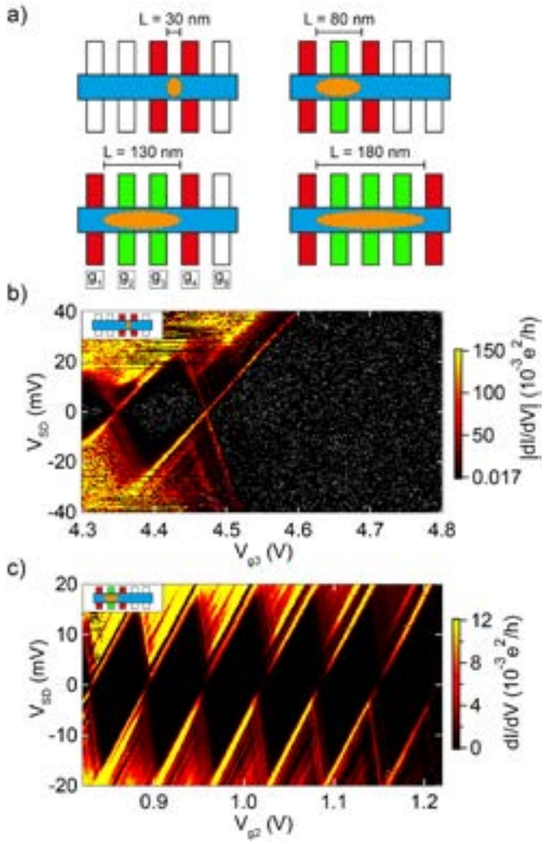

Fig. 2 Schematic picture of the gate configurations used to form QDs (orange) of different lengths using 2, 3, 4, and 5 gates, respectively. (b) Lock-in signal dI/dV versus VSD and Vg3 of QD formed by two gates. To enhance contrast, values below the colorscale were given a grey color. Here, Vg4=1700 mV. (c) Lock-in signal dI/dV versus VSD and Vg2 of QD formed by three gates. Here, Vg1=2000 mV and Vg3=4000 mV. Insets in (b) and (c) schematically show used gate configurations.

Quantum Dots of Different Sizes

Figure 2 a) shows schematically how the bottom gates can be used to form QDs of different sizes, ranging from 30 nm for the smallest dot, to 180 nm for the largest dot. Exemplarily the charge stability diagrams for the smallest dot and the dot over 3 gates are shown in figure 2b and c, respectively. In general, many regular Coulomb diamonds are observed for the dots over 3, 4 and 5 gates. The smallest dot, however, is formed between 2 gates which both act as tunnel barriers (red) and no separate plunger gate (green) is available for this configuration. Thus, tuning the potential on the dot also affects the tunnel couplings to the reservoirs and consequently only a few Coulomb diamonds can be observed for this dot.

Several indications suggest that single-hole occupation is reached in the smallest QD. First, the last Coulomb diamond edge increases linearly up to at least $[V_{SD}] = 40$ mV (see Fig. 2b). Second, even at high V_{SD}, no features involving tunneling of multiple holes are observed for the last visible Coulomb diamond. Third, the energy of the first excited state in the second Coulomb diamond appears to be significantly reduced with respect to that found in the last diamond, consistent with an exchange energy appearing for two-hole states.

Future experiments will incorporate additional sidegates to investigate the tunability of the SOI in these systems and to further exploit the potential use of Ge/Si NWs as hosts for spin-qubits.

References

[1] Y. Son, M. L. Cohen, S. G. Louie, *Half-metallic graphene nanoribbons*, Nature **444**, 347 (2006)

[2] D. Hug, S. Zihlmann, M. K. Rehmann, Y. B. Kalyoncu, T. N. Camenzind, L. Marot, K. Watanabe, T. Taniguchi, D. M. Zumbühl, *Anisotropic etching of graphite and graphene in a remote hydrogen plasma*, npj 2D Materials and Applications **1**, 21 (2017)

[3] C. Casiraghi, A. Hartschuh, H. Qian, S. Piscanec, C. Georgi, A. Fasoli, K. S. Novoselov, D. M. Basko, A. C. Ferrari, *Raman Spectroscopy of Graphene Edges*, Nano Lett. **9**, 1433 (2009)

[4] N. Y. Xu, *Thermal Dynamics of Graphene Edges Investigated by Polarized Raman Spectroscopy*, ACS Nano **5**, 147 (2011)

[5] C. Kloeffel, D. Loss, *Prospects for Spin-Based Quantum Computing in Qunatum Dots*, Annu. Rev. Condens. Matter Phys. **4**, 51 (2013)

[6] C. Kloeffel, M. Trif, D. Loss, *Strong spin-orbit interaction and helical hole states in Ge/Si nanowires*, Phys. Rev. B **84**, 195314 (2011)

[7] F. N. M. Froning, M. K. Rehmann, J. Ridderbos, M. Brauns, F. A. Zwanenburg, A. Li, E. P. A. M. Bakkers, D. M. Zumbühl, F. M. Braakman, *Single, double, and triple quantum dots in Ge/Si nanowires*, Appl. Phys. Lett. **113**, 073102 (2018)

Nano-mechanical membranes for fast viscosity and liquid density measurements

Project P1501: Nanomechanical mass and viscosity measurement-platform for cell imaging
Project Leader: T. Braun and E. Meyer
Collaborators: P. Oliva (SNI PhD Student), B. Bircher, C.-A. Schönenberger, F. Huber, and H. P. Lang

Introduction
To date, most methods used to determine the viscosity and mass density of liquids have several drawbacks: (i) long measurement time (in the range of minutes), (ii) high sample consumption (in the range of milliliters), (iii) the liquid-density and viscosity cannot be measured simultaneously, and, (iv) the measurements cannot be multiplexed. Nano-mechanical transducers promise to overcome these limitations.

We modified a previously developed high-throughput micro-viscometer [1]. These components allow the liquid characterization using fully clamped, and gold coated silicon-nitride membranes with a thickness of 200 nm. These Si_3N_4 membranes on a silica wafer form a well for sample deposition. The sample can be loaded from the top using a micro-capillary coupled to a high-precision pump (Fig. 1a). The instrument is geared to measure viscosity and liquid density values of small aqueous droplets (V=1 µL). Additionally, real-time measurements that characterize the polymerization of G-actin to F-actin filaments in a label-free manner were performed.

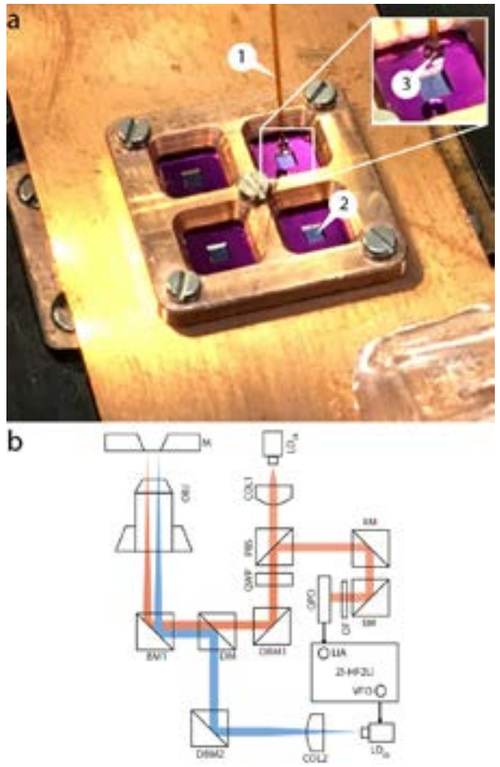

Fig. 1 Mounting of membrane transducer, sample priming and schematic set-up representation. (a) Array of four membrane transducers allowing multiplexed measurements. (1) Fused silica capillary used for sample deposition on (2) the silicon-nitride membrane; (3) Sample droplet. (b) Schematic view of the electronics and optical components.

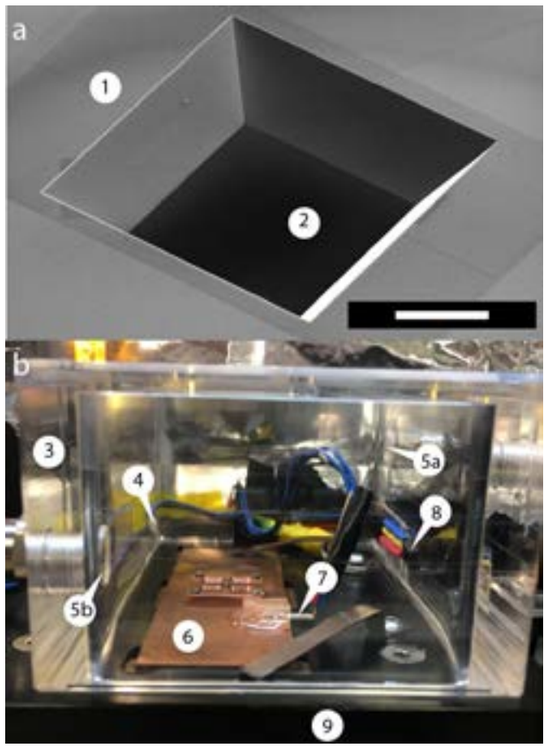

Fig. 2 Membrane transducer and environment control. (a) SEM-image of a single membrane transducer: silicon-frame (1) and the silicon-nitride membrane form a well that can be filled with the test sample. Scale bar: 400 µL. (b) Temperature and humidity-controlled chamber: (3) Humidity chamber mounted on a movable XY-stage; (4) Temperature sensor monitoring the temperature of the humidity chamber; (5a) Inlet and (5b) outlet of the humid air; (6) Temperature-controlled copper plate; (7) Temperature sensor controlling the temperature of the plate; (8) Humidity sensor monitoring the humidity of the chamber; (9) Movable XY-stage.

Micro-viscometer using nano-mechanical membranes
Figure 2 shows the membrane transducer, the liquid handling system and its integration in the set-up. Figure 1b depicts a schematic representation of the photo-thermal excitation, the optical beam deflection system, and the electronic components.

The set-up consists of a detection- and an excitation part, which are mechanically separated from the measurement chamber. A laser beam (LDDE) with a wavelength of 785.4 nm sequentially passes through a collimator (COL1) and an optical isolator (ISO). For monitoring the intensity of the detection laser, a beam-splitter (8:92) with a photo-diode (PD1) has been mounted after the optical isolator. To obtain circularly polarized light, a polarizing beam-splitter (PBS) and a quarter wave-plate (QWP) have been inserted in the optical pathway. The

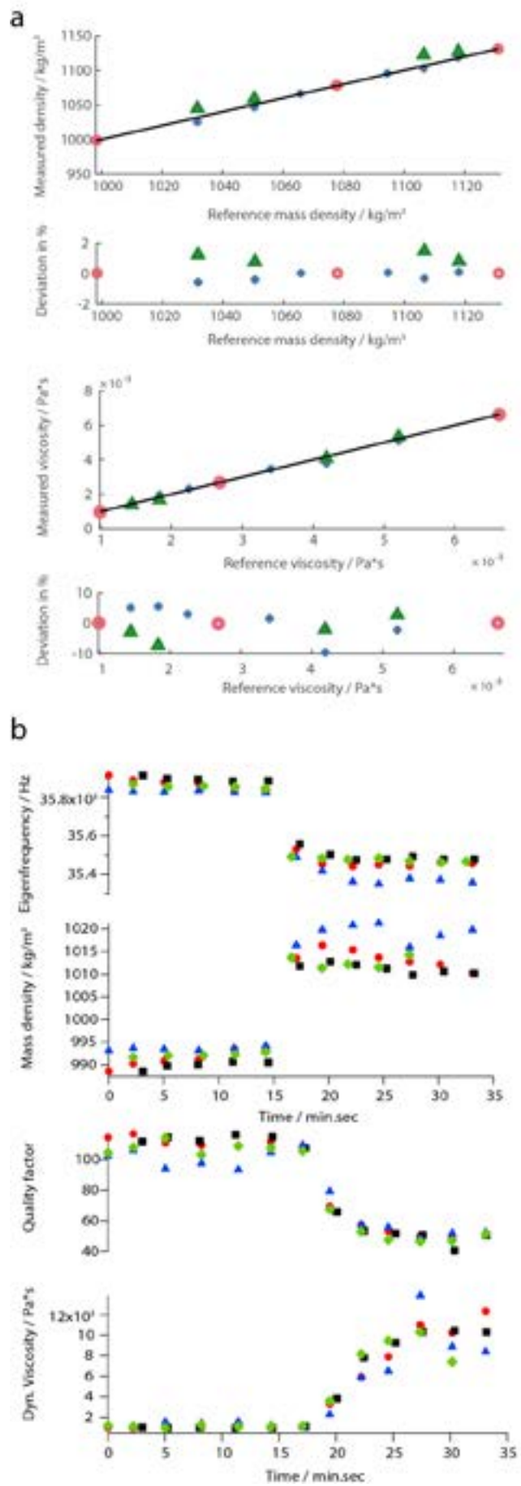

Fig. 3 Liquid density and viscosity measurements of (a) diluted glycerol solutions and (b) polymerization of monomeric actin.

laser beam finally reflects at a broadband mirror (BM1) and is focused using a microscope objective (OBJ). The beam reflects off the gold-coated surface of the silicon nitride membrane and follows the same optical pathway ending on a quadrant

photodiode (QPD), which is placed after the PBS. The QPD was designed to achieve a bandwidth of 3.5MHz.

The excitation part of the setup is composed of a laser beam (LDEX) with a wavelength of 405 nm, which passes through a collimator (COL2), a beam-splitter (8:92), a dichroic mirror (DM), and a broadband mirror (BM1), and is finally focused on the gold-coated membrane using the same objective (OBJ).

Using the internal variable oscillator integrated with Zurich Instruments HF2LI (ZI-HF2LI), amplitude and phase spectra of different modes were recorded. These were used to determine the eigenfrequency and the quality factor. A reduced order model (ROM) allows the calculation of the mass density and viscosity after a three-point calibration [2].

Performed experiments
i.Viscosity and mass density measurements of Newtonian fluids
For the liquid viscosity and density measurements the sensor was first calibrated using three reference solutions. After the calibration the liquid-samples were placed on the membrane, and the amplitude and phase spectra were recorded. From these spectra the eigenfrequencies and quality factors were extracted, and the reduced order model allowed the determination of the liquid density and viscosity. Fig. 3a shows a typical measurement.

ii.Real-time characterization of G-actin polymerization
As biological experiments, we performed a real-time characterization of the polymerization of G-actin to F-actin (Fig. 3a). After loading of the protein in the monomeric form into the measurement well, the eigenfrequency shifts to lower values. After 20min an equilibrium state of the eigenfrequency was obtained. Subsequently, a polymerization-inducing buffer was added. Growing fibrils are expected to shift the viscosity to higher values. Indeed, the Q-factor decreases, due to higher damping, which is related to an increase of the viscosity (Fig. 3b). The growing length of the filaments results in an increasing mass density. Note, that in control experiments without triggering the aggregation, no changes in the mass density and liquid viscosity were observed (data not shown).

Summary and outlook
The instrument and the corresponding control software are now completed, and biological experiments are ongoing.

References

[1] B. A. Bircher, R. Krenger T. Braun, *Automated high-throughput viscosity and density sensor using nanomechanical resonators*, Sens. Actuators, B, **223**(C), 784–90 (2016)

[2] M. Heinisch, T. Voglhuber-Brunnmaier, E. K. Reichel, I. Dufour, B. Jakoby, *Reduced order models for resonant viscosity and mass density sensors*, Sens. Actuators, B, **220**(C), 76–84 (2014)

Towards reconstructing the spin axis of individual CoO nanoparticles

Project P1502: Investigating individual multiferroic and oxidic nanoparticles
Project Leader: A. Kleibert and M. Poggio
Collaborators: D. Bracher (SNI PhD Student), T. M. Savchenko, M. Testa Anta, M. Wyss, F. Nolting, and V. Salgueiriño

Introduction

Antiferromagnetic materials become increasingly important for modern spintronics devices such as spin valves and magnetic random access memories and for the development of novel ultra-hard magnetic materials [1]. While the properties of many antiferromagnetic materials in their respective bulk form have been thoroughly investigated, antiferromagnetic order phenomena at the nanoscale are still poorly understood. For instance, the Neel temperature or the spin axes of nanoscaled antiferromagnetic systems may significantly deviate from their known bulk counterparts due to size and shape effects, or microstructural defects. Knowledge about these properties is crucial for the design of nano-scaled devices, but the absence of a magnetic stray field makes exploring nano-sized systems with antiferromagnetic order very challenging. In this project, we aim to correlate magnetic, electronic and chemical properties of individual CoO nanoparticles with their morphology by combining spatially resolved X-ray absorption (XA) and X-ray magnetic linear dichroism (XMLD) spectroscopy using X-ray photoemission electron microscopy (X-PEEM) with scanning electron microscopy (SEM).

In our earlier report (P1502 2017) temperature dependent XMLD measurements on individual CoO/Co_3O_4core-shell nanooctahedra (referred to as CoO nanooctahedra in the following) with sizes of about 100 nm have been presented. The data revealed a reversible change of the XMLD signal across the bulk materials Néel temperature of CoO TN=285 K. This observation suggests a phase transition from the antiferromagnetically ordered phase to the paramagnetic phase around the bulk Néel temperature. In this report, we present angular-dependent measurements performed below and above the ordering temperature TN, with the goal to uncover anisotropic properties in these particles; in particular we aim to determine the orientation of their spin axes.

Experimental

The CoO nanooctahedra are dispersed by means of drop casting onto silicon substrates with lithographically made gold marker structures. The gold marker structures are used to identify the very same nanoparticles in X-PEEM and SEM measurements. X-PEEM experiments are performed at the Surface/Interface Microscopy (SIM) beamline of the Swiss Light Source. Figure 1a shows a schematics of the X-PEEM setup with the X-ray propagation direction (k), the horizontal (E_h), and vertical (E_v) polarization vector, the spin axis (S) of a nanoparticle, and the azimuthal sample orientation (φ) indicated. Spatially resolved XA spectra with linear horizontally and vertically polarized X-rays are recorded in order to probe the XMLD effect at the Co *L3* edge.

Results

Figure 1b shows an isotropic XA spectrum of an individual CoO nanoparticle. The isotropic spectrum is obtained by averaging XA spectra recorded with circularly left and right polarized X-rays and contains only chemical information. The inset shows a transmission electron microscopy (TEM) image of a reference sample showing the well-defined CoO nanooctahedra under investigation [1]. Depending on their orientation the particle projections appear as hexagons, rhombi, or squares. Figure 1c and d display an SEM image and an X-PEEM elemental contrast map recorded at the Co *L3* edge of the same area on the sample. The elemental contrast map is obtained by dividing an image recorded at a resonant energy (E_1) by an image acquired at a non-resonant photon energy (E_0) as indicated in figure 1b. The white solid circles highlight the very same nanoparticles as seen in the SEM and X-PEEM images.

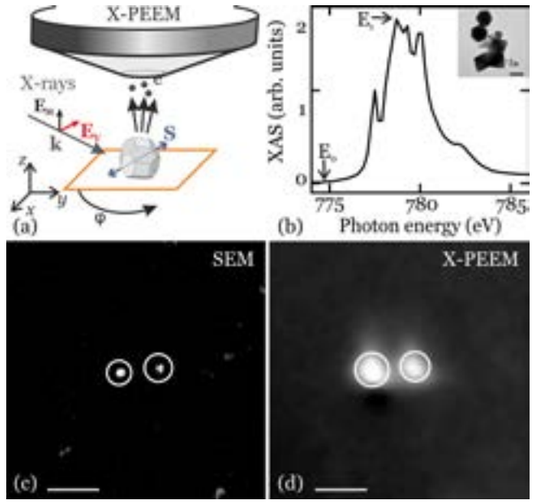

Fig. 1 (a) Schematics of the experimental setup with the X-ray propagation direction (k), the polarization vectors Eh and Ev, the spin axis (S), and the angle φ for the azimuthal sample orientation. (b) Isotropic XA spectrum recorded at the Co L3 edge (below TN). The displayed data represents an average over ten individual CoO nanooctahedra. The inset shows a TEM image of a reference sample with CoO nanooctahedra (scale bar: 100 nm). (c) SEM and (d) X-PEEM image recorded at the Co L3 edge of the same area of the sample. The white circles indicate the same CoO nanooctahedra (scale bar: 1 μm).

Figure 2a displays a high resolution SEM image of an individual CoO nanooctehedra. Crystal facets are indicated by dashed lines. The top {111} facet is oriented almost parallel to the substrate surface (dashed triangle). The orientation of the respective crystal axes [100], [010], and [001] is indicated accordingly. Figure 2b shows the isotropic XA spectrum of this nanooctahedron measured below TN at 110 K. The shape of the XA spectrum is dominated by the typical features of pure CoO and similar to the averaged isotropic XA spectrum shown in Figure 1b [4]. A more detailed analysis will be carried out by means of multiplet calculations. Figure 2c-f display the evolution of the XMLD signal when stepwise varying the azimuthal sample orientation φ from 0° to 110°.

The data reveal a clear azimuthal dependence of the XMLD signal. As a guide to the eye three photon energies (A=776.5 eV, B=777.7 eV and C=779.1 eV) are highlighted by the dashed vertical lines. While the XMLD signal at A and C changes its sign upon a rotation from 0° to 90° the magnitude of the signal at B reduces from a finite positive value to almost zero at 90°, and is eventually inverted if the sample is further rotated to 110°.

The anisotropy of the XMLD signal with respect to the azimuthal orientation of the nanoparticle suggests antiferromagnetic order within the nanoparticle, and likely indicates a single domain state with the its spin axis oriented in the sample plane, but further analysis is required for a final assessment. Our results indicate the possibility of determining the spin axis of individual randomly oriented CoO nanoparticles by means of XMLD spectromicroscopy.

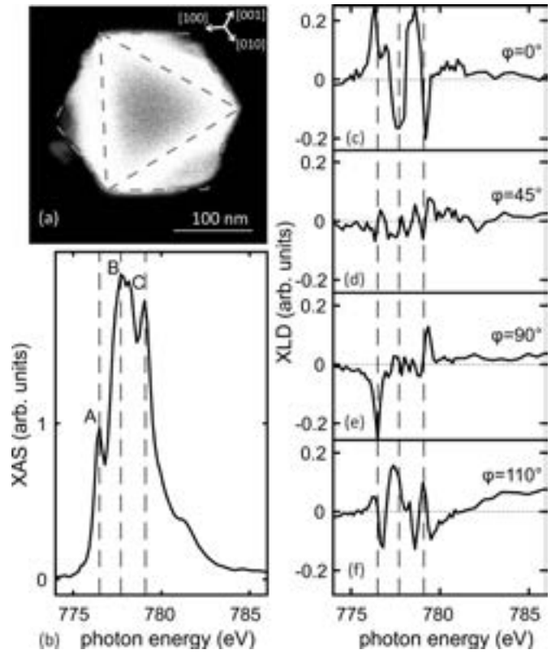

Fig. 2 (a) SEM image of a selected CoO nanoparticle. The white arrows the crystal directions. (c)-(f) show the XMLD spectra for a azimuthal rotation from 0° to 110°.

Summary and Outlook

We measured XA and XMLD spectra of individual CoO/Co_3O_4 core–shell nanooctahedra at azimuthal orientations by means of X-PEEM. SEM images of the very same nanoparticles reveal information on the morphological features of the nanoparticles, such as surface facets, which allow us to correlate the XMLD spectra with the structure and crystal axes of the particles. The azimuthal dependent XMLD spectroscopy indicates the possibility of reconstructing the antiferromagnetic spin axis of individual CoO/Co_3O_4 nanoparticles. Next, we plan to extend the study also to smaller nanoparticles in order to reveal possible size-dependent effects. At present the acquisition of XMLD spectra at several azimuthal orientations and temperatures is quite time-consuming, thus, we plan to acquire and analyze instead XMLD contrast images in the coming measurement campaigns. This would further allow us to probe the particles also with gradually varied X-ray polarization orientation between E_h and E_v, which might allow us to determine the spin axis without prior knowledge of the sign of the features in the XMLD spectra [5].

References

[1] N. Fontaíña-Troitiño, S. Liebana-Vinas, B. Rodriguez-Gonzalez, Z. A. Li, M. Spasova, M. Farle, V. Salgueirino, *Room-temperature ferromagnetism in antiferromagnetic cobalt oxide nanoocta-hedra*, Nano Lett. **14**, 640 (2014)

[2] T.-J. Park, G. C. Papaefthymiou, A. J. Viescas, A. R. Moodenbaugh, S. S. Wong, *Size-dependent magnetic properties of single-crystalline multiferroic $BiFeO_3$ nanoparticles*, Nano Lett. **7**, 766 (2007)

[3] Q. He, Y. et al., *Electrically controllable spontaneous magnetism in nanoscale mixed phase multi-ferroics*, Nat. Commun. **2**, 225 (2011)

[4] A. M. Hibberd, H. Q. Doan, E. N. Glass, F. M. F de Groot, C. L. Hill, T. Cuk, *Co Polyoxometalates and Co_3O_4 thin film investigated by L-edge x-ray absorption spectroscopy*, J. Phys. Chem. C **119**, 4173 (2015)

[5] S. Czekaj, F. Nolting, L. J. Heyderman, P. R. Willmott, G. van der Laan, *Sign dependence of x-ray magnetic linear dichroism on the antiferromagnetic spin axis in $LaFeO_3$ thin films*, Phys. Rev. B **73**, 020401 (2006)

Filming biological factories

Project P1503: Watching giant multienzymes at work using high-speed AFM
Project Leader: T. Maier and R. H. Y. Lim
Collaborators: S. Singh (SNI PhD Student), Y. Sakiyama, and F. Benning

Multienzymes are biological assembly lines
The synthesis and degradation of chemical compounds required to fuel and replicate cells and to form tissues, organs and entire organisms is an essential characteristic of life and is referred to as metabolism. Many metabolic reactions require protein catalysts, the enzymes, for efficient turnover under the moderate and aqueous environment required for life. The majority of enzymes catalyzes specifically a single chemical reaction before releasing the reaction products into the cellular environment. However, important classes of biomolecules require more elaborate production systems, because the biological routes for their synthesis involve reactive or poorly soluble intermediates or require strictly ordered and coordinated reaction steps. Multienzymes integrate several catalytic activities at different sites into giant polypeptides and often employ specific transfer mechanisms to guide intermediates to the next in a series of active sites. The most versatile mechanism for substrate transfer is the use of flexibly tethered carrier proteins, which carry covalently linked intermediates between active sites. Most multienzymes are highly dynamic, however, the contribution of their conformational dynamics to emergent properties of these giant protein assembly lines, e.g. in substrate transfer and allosteric regulation, remains poorly understood.

In this project, we (i) develop novel tools and methods for analyzing and visualizing multienzyme dynamics at the single molecule level and (ii) apply these tools to study key multienzymes in human metabolism and microbial secondary metabolism.

We aim to establish two complimentary methods towards applications for the quantitative and single-molecule-level analysis of multienzyme dynamics. First, High Speed Atomic Force Microscopy (HS-AFM) enables visualization of single-multienzyme dynamics, however, with limited time- and spatial resolution. The moderate resolution of HS-AFM together with the inherent convoluted surface-only representation are critical limitations for interpreting HS-AFM data in terms of atomic-scale motions. Second, single molecule (sm) fluorescence methods, in particular those based on Förster resonance energy transfer (FRET) permit highest temporal and spatial resolution, but require complex labeling, and provide only indirect information on attached fluorescent labels, not the entire molecule of interest.

Our biological studies are focused on mammalian fatty acid biosynthesis and microbial polyketide production. Fatty acid biosynthesis is an essential process and is critically linked to human health. Upregulated fatty acid biosynthesis is associated with metabolic disorders, including non-alcoholic fatty liver disease or type II diabetes, as well as cancer formation and malignancy. Two key multienzyme carry out the nine individual reaction types and more than 40 reaction steps for the synthesis of palmitate. First, acetyl-CoA carboxylase (ACC) catalyzes the two-step carboxylation of acetyl-CoA to malonyl-CoA. Second, fatty acid synthase (FAS) produces palmitate from one molecule of acetyl-CoA and seven molecules of malonyl-CoA in iterative cycles of precursor elongation by decarboxylative condensation with malonyl-CoA followed by multistep modification at the β-carbon position.

With seven different functional protein domains FAS is arguably the most complex multienzyme in humans. Our hallmark studies have revealed the structure and dynamic organization of FAS [1]. ACC catalyzes the committed step of fatty acid and lipid biosynthesis and acts as a hub for short-term regulation by directly integrating regulation via allostery, post-translational modification and direct protein-protein interaction. The upregulation of human ACC activity is directly linked to polymerization into micrometer-size filaments. However, the architecture of human ACC and the structural basis for regulation via filament formation remained enigmatic for more than 50 years. Most recently, we have solved this mystery by cryo electron microscopy of human ACC filaments combined with biochemical analysis (Fig. 1) [2]. However, the dynamic properties of filamentous ACC mostly remain unexplored.

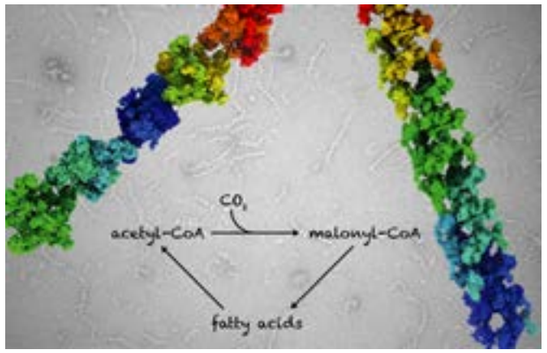

Fig. 1 Structural analysis of ACC filaments. Citrate-induced filaments (left and background) lock ACC into an active conformation, while the C-terminal domain of the BRCA1 protein polymerizes ACC in inactive state (right).

Microbial polyketide synthases (PKS) utilize the same chemical logic as FAS for stepwise precursor elongation, but extent product diversity by chaining individual and varied elongation modules into giant modular assembly lines. Our structural analysis of a single-module PKS [3] and substrate-loading in PKS [4] revealed related but distinct architectures of FAS and PKS, and specific relevance of the unique linker-based domain interactions and the resulting conformational coupling and dynamics in PKS. On the basis of our high-resolution structural data we and others are now able to tackle the analysis of transient states, as well as kinetics and dynamics of substrate transfer in PKS.

High-speed AFM analysis of multienzymes
Atomic Force Microscopy (AFM) is a high resolution (sub-nanometer) surface topography imaging technique, which uses a microscopic cantilever tip to probe a sample surface. High Speed AFM uses low imaging forces and high scanning rates and can be performed on samples in aqueous environment; it is thus uniquely suited to study biomolecules.

We have established HS-AFM as a technique for studying multienzyme dynamics based on reference-free classification of AFM movie series frames and the identification of corresponding molecular states using FAS as an initial sample [5]. Currently, we are attempting to extend this work to filamentous structures for studies of ACC and PKS assembly lines.

A toolkit for multienzyme labelling for sm-FRET
smFRET is very well suited for studies of protein dynamics because of its high temporal (ns time scale) and spatial resolution in resolving distances between fluorophores in a limited distance range (1-10 nm). smFRET uses diluted fluorescently labeled protein samples in a small confocal excitation volume to measure signals from single molecules. A prerequisite for smFRET studies is labeling of proteins with donor and acceptor fluorophores. For proteins, this is most commonly achieved via selective chemical labeling e.g. of cysteine residues. However, simple chemical labeling is not suited for site-specific labelling of giant multienzymes with many reactive side chains required for integrity and catalysis. Incorporation of bio-orthogonal handles via introduction of unnatural amino acids by genetic code expansion (GCE) is a promising alternative. GCE is well established in bacterial systems for single-site labelling. However, dual or multi-site labelling and GCE in eukaryotic expression systems required for efficient multienzyme production are still present substantial challenges.

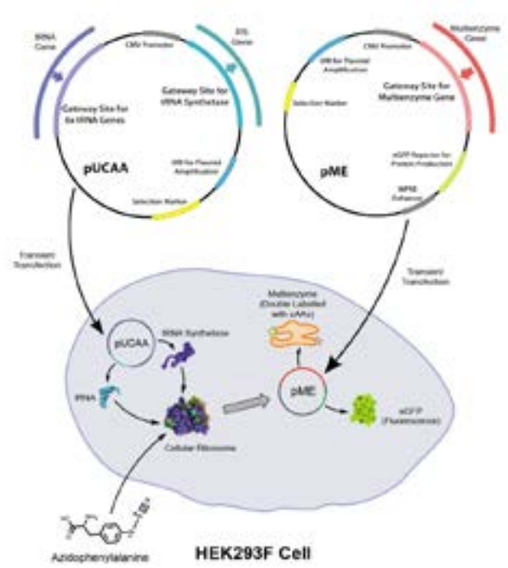

Fig. 2 Constructs and strategy for versatile multi-site labeling of multienzymes in eukaryotic cells by genetic code expansion.

In this project, we are developing a versatile toolkit for multisite labeling of large proteins in eukaryotic cells, e.g. HEK293 cells. We have designed and engineered vector systems for efficiently combining different orthogonal tRNA synthetase/tRNA systems with vectors for multienzyme expression based based on compatible sets of recombination sites and selection systems (Fig. 2). As a next step we are now beginning to test this system in medium throughput transient expression in HEK293 suspension cells. For this purpose, we have specifically optimized cell culture and transfection protocols for obtaining the material- and time-efficiency required for screening large numbers of labelling-site combinations for comprehensive analysis of large multienzymes.

Overall, we have established HS-AFM for filming multienzymes conformational dynamics. We are currently developing a versatile toolkit for multi-site labeling of giant multienzymes in eukaryotic expression to enable complementary smFRET-based analysis. Our work shall ultimately provide blueprints for the engineering of novel, efficient bio-inspired molecular factories.

References

[1] T. Maier, M. Leibundgut, N. Ban, *The crystal structure of a mammalian fatty acid synthase*, Science **321**, 1315 (2008)

[2] M. Hunkeler, A. Hagmann, E. Stuttfeld, M. Chami, Y. Guri, H. Stahlberg, T. Maier, *Structural basis for regulation of human acetyl-CoA carboxylase*, Nature **558**, 470 (2018)

[3] D. A. Herbst, R. P. Jakob, F. Zähringer, T. Maier, *Mycocerosic acid synthase exemplifies the architecture of reducing polyketide synthases*, Nature **531** 533 (2016)

[4] D. A. Herbst, C. R. Huitt-Roehl, R. P. Jakob, J. M. Kravetz, P. A. Storm, J. R. Alley, C.A. Townsend, T. Maier, *The structural organization of substrate loading in iterative polyketide synthases*, Nature Chem Biol **14**, 474 (2018)

[5] F. M. C. Benning, Y. Sakiyama, A. Mazur, H. S. T. Bukhari, R. Y. H. Lim, T. Maier, *High-Speed Atomic Force Microscopy Visualization of the Dynamics of the Multienzyme Fatty Acid Synthase*, ACS Nano **11** 10852 (2017)

Three-layer moiré superlattice and strain engineering in encapsulated graphene

Project P1504: Valleytronics in strain-engineered graphene
Project Leader: C. Schönenberger and M. Calame
Collaborators: L. Wang (SNI PhD Student), A. Baumgartner, P. Makk, S. Zihlmann, and J. Overbeck

Three-layer moiré superlattice in hBN/Gr/hBN

Moiré superlattices (MSLs) can be utilized to tailor the band structure of graphene and have been realized on single interfaces, such as graphene/hBN [1] and graphene/graphene [2]. Here we show that by using both the top and bottom interface of graphene encapsulated in hBN, a new generation of moiré superlattices can be engineered.

Figure 1a illustrates the formation of the MSLs when both hBN layers are considered. On the right side of the illustration, only the top hBN (blue) and the graphene (black) are present, which form the top two-layer MSL (2L-MSL) with superlattice period λ_1. On the left side, only the bottom hBN (red) with the graphene layers are present, forming the bottom 2L-MSL with period λ_2. In the middle of the illustration all three layers are present and a new MSL (3L-MSL) forms with a longer period λ_3. The influence of the MSL can be modeled as an effective periodic potential with the same symmetry. The periodic potentials for the top 2L-MSL and the bottom 2L-MSL are calculated following the model introduced in Ref [1], shown as insets in figure 1a. To calculate the potentials for the 3L-MSL, we sum over the periodic potentials of the top 2L-MSL and the bottom 2L-MSL. The period of the 3L-MSL from the potential calculation matches very well the one of the lattice structure in the illustration.

We have fabricated devices with both the top and the bottom hBN (nearly) aligned to the graphene layer. The two-terminal electrical conductance of one device (inset of Fig. 2b) is plotted as a function of charge carrier density in figure 2b. In addition to the main Dirac point (MDP) at electron density $n_s = 0$, we find two pairs of conductance minima symmetrically around the MDP at higher doping, labeled A and C, which we attribute to two MSLs. Superlattice Dirac points (SDPs) are expected to occur at $n_s = 4\pi/(\sqrt{3}\lambda)$. The pair A of conductance minima at $n_{sA} \approx \pm 2.4 \times 10^{12}$ cm^{-2} can be explained by a graphene/hBN 2L-MSL with a period of 13.2 nm. However, the pair C of conductance minima at $n_{sC} \approx \pm 1.4 \times 10^{12}$ cm^{-2} corresponds to a superlattice period of about 17.3 nm, which is beyond the largest possible period (14 nm) for graphene/hBN systems given by the lattice mismatch between graphene and hBN. In the quantum Hall regime (Fig. 1c), we observe two lines to fan out from $n_{sC} \approx -1.4 \times 10^{12}$ cm^{-2}, corresponding to filling factors $\upsilon = \pm 2$ consistent with a Dirac spectrum. We attribute this feature to a new MSL that is formed by the three layers together: top hBN, graphene and bottom hBN. This is supported by a third fan that originates from $n_{sC} \approx -5 \times 10^{12}$ cm^{-2} and corresponds to the third MSL labeled B. The newly found 3L-MSL can have a period considerably larger than 14 nm. We explain our observation with a simple model, where the overlay of the top 2L-MSL and the bottom 2L-MSL form a third superlattice. This new type of band structure engineering allows one to artificially create an even wider spectrum of the electronic properties of two-dimensional materials.

These results have recently been published [3].

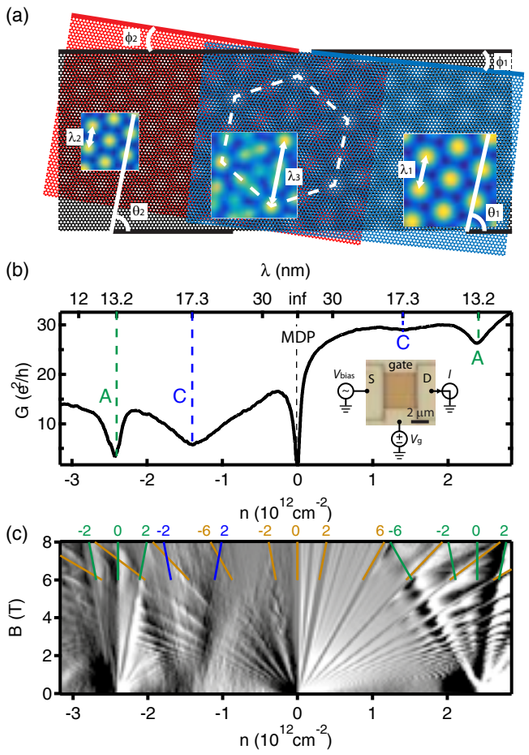

Fig. 1 (a) Illustration of three different MSLs formed in a hBN/graphene/hBN heterostructure. Blue, black and red hexagonal lattices represent top hBN, graphene and bottom hBN lattices, respectively. $\phi 1$ ($\phi 2$) is the twist angle between top (bottom) hBN and graphene. $\theta 1$ ($\theta 2$) indicates the orientation of the corresponding MSL with respect to graphene. The resulting moiré periods are labeled as $\lambda_{1,2,3}$. Insets: moiré potential calculations (b) Two-terminal differential conductance G as a function of charge carrier density n. Inset: micrograph of the measured device. (c) dG/dn as a function of n and B of the same device. Filling factors are indicated at the top of the diagram. Measurements were performed at 4.2K.

Strain engineering in encapsulated graphene

The valley degree of freedom (VDoF) in graphene stems from energetically degenerate, but nonequivalent local minima (maxima) of the conduction (valence) band at the corners of the Brillouin zone. Since the two valleys are far away from each other in momentum space, intervalley scattering is strongly suppressed, suggesting a potential use of the VDoF for electronic applications, referred to as valleytronics.

It has been predicted that non-uniform strain can generate a pseudo-magnetic field in graphene which acts on the two different valleys with opposite sign [4]. We make use of graphene encapsulated by hBN to obtain clean graphene, thereby avoiding valley mixing due to disorder. To strain graphene, the stack is clamped on to a flexible support, which is bent using the break-junction (BJ) technique. Compared to suspended graphene, a significant advantage of substrate clamped devices is that the gate capacitance is not affected by bending, which is crucial for high-resolution transport measurements.

The mechanism of a BJ is illustrated schematically in figure 2. Encapsulated devices are fabricated in the center of a bendable substrate. Controllable strain can then be generated in graphene by bending the substrate, which is described by the push-up distance Δz. Raman spectroscopy is used to characterize the strain in graphene. Here we focus on the 2D peak position of the Raman spectrum, which red-shifts with increasing strain [5].

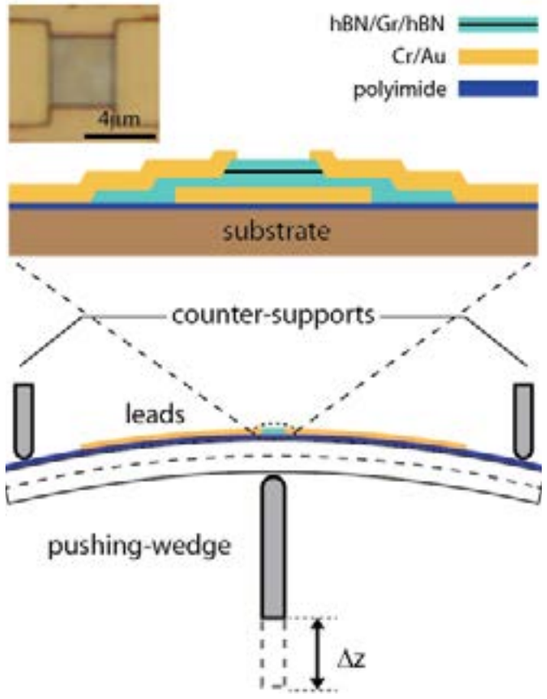

Fig. 2 Schematics of the BJ setup and the cross section of our device. The inset is the micrograph of a typical encapsulated graphene device.

We scan the whole device area and acquire Raman spectra for each pixel at different bending of the substrate. The bending is first increased from $\Delta z = 0$ to $\Delta z = 400$ µm and then decreased back to $\Delta z = 0$. The position of the Raman 2D peak for each pixel is extracted by fitting a Lorentzian to the peak and plotted as a function of the position on the device in figure 3. The Raman 2D peak position shifts to lower values with increasing Δz for the whole device and is reversible with decreasing Δz, indicating a good level of control of the strain in encapsulated graphene by the BJ technique. For this device, an average strain of about 0.15% is achieved at $\Delta z = 400$ µm.

First electrical measurements do show effects that can be assigned to both a strain-induced scalar and pseudo-magnetic potential. To conclude, we have developed a method to generate strain in encapsulated graphene. The next step is to engineer non-uniform strain by modifying the device geometry and study the strain effects in low temperature transport measurements.

We thank Ming-Hao Liu for fruitful collaboration, F. Guinea for fruitful discussions and K. Watanabe and T. Taniguchi for providing high-quality hBN.

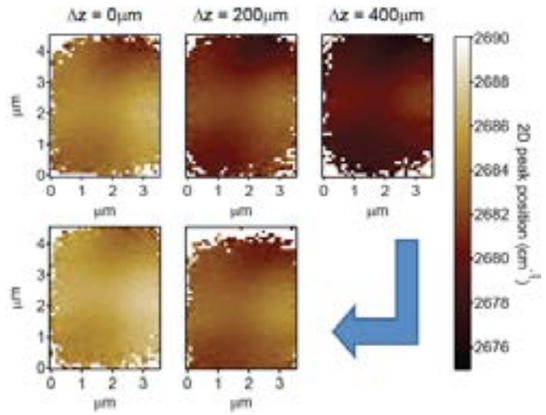

Fig. 3 Raman 2D peak position plotted as a function of locations on the device at different bending of the substrate. The bending is first increased from $\Delta z = 0$ to $\Delta z = 400$ µm and then decreased back to $\Delta z = 0$.

References

[1] M. Yankowitz, J. Xue, D. Cormode, J. D. Sanchez-Yamagishi, K. Watanabe, T. Taniguchi, P. Jarillo-Herrero, P. Jacquod, B. J. LeRoy, *Emergence of superlattice Dirac points in graphene on hexagonal boron nitride*, Nature Physics **8**, 382 (2012)

[2] Y. Cao, J. Y. Luo, V. Fatemi, S. Fang, J. D. Sanchez-Yamagishi, K. Watanabe, T. Taniguchi, E. Kaxiras, P. Jarillo-Herrero, *Superlattice-Induced Insulating States and Valley-Protected Orbits in Twisted Bilayer Graphene*, Phys. Rev. Lett. **117**, 116804 (2016)

[3] L. Wang, S. Zihlmann, M.-H. Liu, P. Makk, K. Watanabe, T. Taniguchi, A. Baumgartner, C. Schönenberger, *New generation of moiré superlattices in doubly aligned hBN/Gr/hBN heterostructures*, arxiv 1812.10031 (2018)

[4] F. Guinea, A. K. Geim, M. I. Katsnelson and K. S. Novoselov, *Generating quantizing pseudo-magnetic fields by bending graphene ribbons*, Phys. Rev. B **81**, 035408 (2010)

[5] T. M. G. Mohiuddin et al., *Uniaxial strain in graphene by Raman spectroscopy: G peak splitting, Grüneisen parameters, and sample orientation*, Phys. Rev. B **79**, 205433 (2009)

Near-field diffraction of coherent electron beam through semi-transparent nano-apertures

Project P1505: A programmable e-beam shaper for diffractive imaging of biological structures at Å resolution
Project Leader: S. Tsujino and J. P. Abrahams
Collaborator: P. Thakkar (SNI PhD Student)

Introduction

The superposition of matter waves and their interference are the backbone of quantum mechanics to understand some of the phenomena such as wave-particle duality. Various experimental investigations using electrons have been repeatedly conducted in the past revealing interesting physical aspects of electron-matter interaction. With the help of existing nano-fabrication techniques, it is feasible to fabricate nanostructures that are well within the spatial transverse coherence length of electron beam. This offers an interesting opportunity to engineer electron wavefront to study the behavior of high-energy electron beam as has been demonstrated by the creation of electron vortex beams [1, 2]. We use electron beam lithography (EBL) based method to fabricate nano-aperture pairs in a silicon nitride membrane and study the interference of high-energy electron beams through them using transmission electron microscopy (TEM).

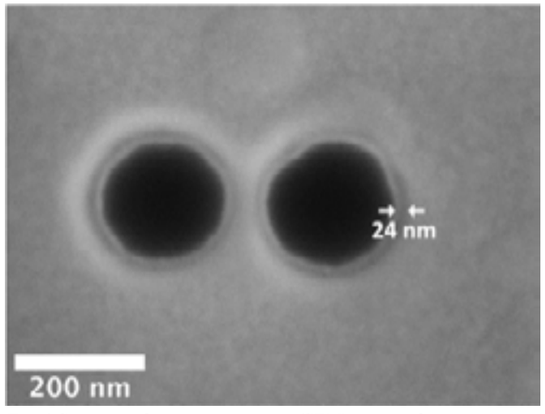

Fig. 1 Scanning electron microscope (SEM) image of a nano-apertue pair. A thin rim of ~24 nm around the aperture indicates that the top and bottom surfaces of the membrane have different aperture diameters. The sample is positioned such that the Cr side is facing the electron source during imaging.

Fabrication and Experiment

We fabricate nano-aperture pairs in low stress silicon nitride membrane. A 30 nm thick Cr layer is deposited on a 200 nm thick silicon nitride membrane using electron beam evaporation. The Cr layer is structured using 100 nm thick 950K PMMA resist patterned using EBL. The pattern is transferred to underlying Cr layer and successively to the membrane using reactive ion etching based on Cl_2 and CHF_3 chemistry respectively. An array of 16 x 10 nano-aperture pairs is fabricated on a single membrane with varying aperture diameter (D) and separation. The aperture diameter D is varied from 120 nm and 1.02 µm with an increment of 60 nm across one dimension. For each aperture-pair, the edge-to-edge aperture separation (g) is varied between D/2 and 5D with an increment of D/2 across the second dimension. The sample preparation with different sizes is crucial to optimize the fabrication parameters with minimal trials and to facilitate detailed analysis of the transmission experiment. A Scanning electron microscope (SEM) image of a nano-aperture with D - 190 nm and g - 60 nm is shown in figure 1. A close inspection of the SEM image shows the presence of a 24 nm wide rim around the aperture resulting in an outer diameter of ~235 nm. The significance of the geometry of closely spaced aperture pairs is discussed in the following section. We observed near-filed diffraction through the nano-aperture pairs using a transmission electron microscope (JEOL JEM 2200FS).

The presence of non-vertical sidewalls is also visualized in near-focus transmission electron microscope (TEM) images as gradually decreasing contrast outside the focused aperture edges (Fig. 2a). In order to observe the interference of the electron beams traversing through individual aperture pairs, we defocused the objective lens in overfocusing direction. The resulting image at a defocus distance of 85 µm is shown in Figure 2b where diffraction from individual apertures can be observed. From the ratio of the defocusing distance and electron wavelength, the diffraction is ascribed as Fresnel diffraction of the incident electron beam by the edge of the nano-apertures. This indicates that the incident electron beam is highly coherent over the aperture area. Furthermore, we observe a bright interference between the two apertures which signifies a two-beam interference. The intensity at the center of the separation between the two apertures is an order of magnitude higher than the transmitted intensity through individual apertures. This is unexpected, considering that the beam intensity at the tail of Fresnel diffracted beams are normally decreasing rapidly [3].

Result and Discussion

In order to compare our experimental results with theory, we performed Fourier optics simulations [3] of transmission and interference of coherent electron beam traversing nano-apertures by identifying the experimental defocusing value as the propagation distance from the sample.

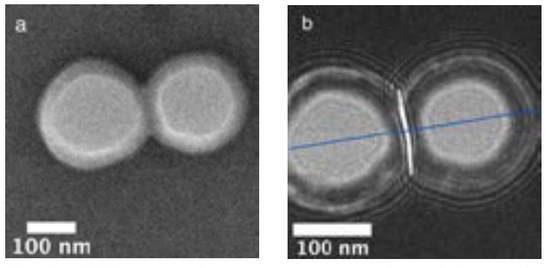

Fig. 2 a TEM images of a nano-aperture pair focused close to the bottom surface (opposite to the top Cr surface) with a diameter D of 150 nm. (b) Overfocused TEM image of the same aperture pair with a defocus value of 85 µm. Brightness and contrast of both images are altered for better visibility. The blue line represents the path across the nano-aperture pair whose intensity profile is depicted in figure 3.

For simplicity, we neglected the partial transmission of electron beam though the sample and assume that the apertures have vertical sidewalls. We found that the simulations are in agreement with the Fresnel diffraction except for the edge diffraction and constructive two-beam interference between two apertures. The diffraction pattern in figure 4a is similar to the diffraction fringes that are observed experimentally in figure 2b inside the aperture. The presence of a constructive interference of Fresnel diffracted beams for large propagation distance of 850 µm is found as shown in figure 4b. However, due to large propagation distance, the period of the Fresnel diffraction fringes inside the apertures are much larger than those observed in the experiment.

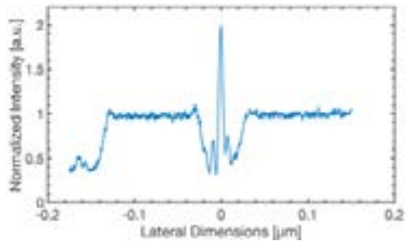

Fig. 3 The plot shows the electron beam intensity profile recorded with a defocusing distance of 85 µm and is averaged over a 50 nm window rough the center of nano-apertures, as represented by a blue line in figure 2b. The intensity is normalized through the intensity through the aperture.

We assert that the discrepancy between the experimental and the simulation results originates from partial transmission of the electron beam through the sample and the slope of the aperture sidewalls. To clarify the influence of the electron transmission through the sloped sidewall, we compared the edge diffraction of the nano-aperture and that of the condenser aperture with opaque vertical straight sidewall imaged at a defocus value of ~197 µm.

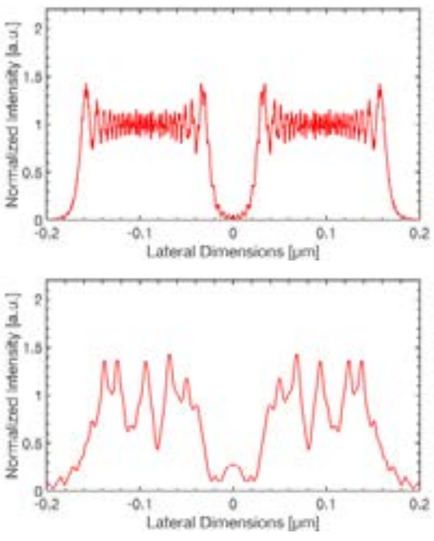

Fig. 4 Fourier optic simulation of Fresnel diffracted beams of circular nano-aperture pairs with D - 150 nm and g - 40 nm after a propagation distance of (a) 85 µm and (b) 850 µm.

The top aperture is seen to be shadowed by the condenser aperture of the microscope and experiences edge diffraction (TEM image not shown here!). The intensity profiles of transmitted electron beam averaged over ~7 nm are shown in figure 5, with green curve showing the diffraction profile from the condenser edge and blue curve from the nano-aperture edge. The comparison of these two curves indicates that the extended and oscillating Fresnel diffraction tail outside the nano-aperture edge is absent in Fresnel diffraction of opaque condenser aperture edge. The details about the experiment and theoretical analysis is submitted in Microelectronic Engineering for publication.

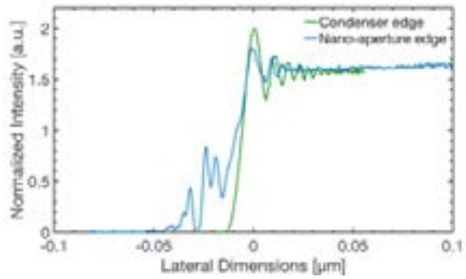

Fig. 5 Comparison of Fresnel diffraction fringes of opaque condenser aperture edge (green) with nano-aperture edge (blue).

References

[1] J. Verbeeck, H. Tian, P. Schattschneider, *Production and application of electron vortex beams*, Nature **467**, 301 (2010)

[2] B. J. McMorran, A. Agrawal, I. M. Anderson, A. A. Herzing, H. J. Lezec, J. J. McClelland, J. Unguris, *Electron vortex beams with high quanta of orbital angular momentum*, Science **331(6014)**, 192–195 (2011)

[3] J. Goodman, *Introduction to Fourier optics* (McGraw-hill, 2008)

Plasmon-enhanced water splitting in hematite

Project P1601: Optical plasmonic nanostructures for enhanced photochemistry
Project Leader: E. C. Constable and S. Fricke
Collaborators: L. Driencourt (SNI PhD Student), B. Gallinet, A. Luu-Dinh, and C. E. Housecroft

Introduction

Electricity can be produced from hydrogen gas using a fuel cell, which only emits water. However, industrial dihydrogen is currently mainly produced in a non-sustainable way, by using natural gas. Water splitting using sunlight is a promising technique for clean dihydrogen production. In this project, a metal oxide semiconductor electrode is immersed in an aqueous electrolyte and used both as a light harvester and a catalyst. The confinement of the electromagnetic field by plasmonic nanostructures is studied for increasing the quantity of light absorbed in the electrode.

A two electrodes photoelectrochemical (PEC) cell using an n-type semiconductor electrode is shown schematically in figure 1a. Incident light generates mobile charge carriers in the semiconductor electrode which can be used to split water to hydrogen and oxygen gas, depending on their energy. An idealized geometry of a hybrid structure including metallic nanoparticles in a metal oxide matrix is shown in figure 1b. Hematite (α-Fe_2O_3) is chosen as metal oxide material, because its small bandgap (2 eV) offers interesting possibilities for plasmonic enhancement through near-field effects.

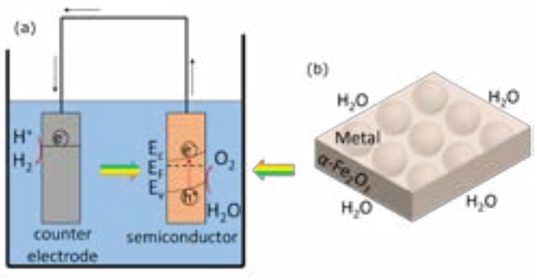

Fig. 1 Principle of water splitting enhanced with plasmonic nanoparticles. (a) Scheme of a two electrode PEC cell. (b) Idealized geometry of a hybrid photoanode with hematite (α-Fe_2O_3) as a semiconductor material and embedded metallic nanospheres as near-field plasmonic enhancers.

Theoretical study

A comparative study of the different plasmonic materials in combination with hematite is first conducted with a simplified model. For an isolated sphere of radius r<<λ and permittivity ε_m in a non-absorbing surrounding medium of permittivity ε, the scattering efficiency can be expressed as [1]:

$$Q_{scat}(\lambda) = \frac{8}{3}k^4r^4\left|\frac{\varepsilon_m(\lambda)-\varepsilon(\lambda)}{\varepsilon_m(\lambda)+2\varepsilon(\lambda)}\right|^2$$

The imaginary part of the surrounding medium permittivity (hematite) has to be set to zero for calculating the electromagnetic response, but is used to extract the absorbance of hematite (Fig. 2a). The computed scattering efficiency spectrum for Ag, Au and Al (Fig. 2b) show that the amplitude of the plasmonic peak is the highest for silver. A necessary condition to increase the light absorption with near-field plasmonic enhancers is that the plasmon resonance overlaps with the spectral region where the surrounding material is absorbing. This effect is considered by multiplying the previous scattering efficiency with the normalized absorbance of hematite computed for a flat layer (Fig. 2a). A general comparison of plasmonic materials is conducted by expressing the permittivity of metals due to intraband transitions with the Drude model:

$$\epsilon(\omega) = 1 - \frac{\omega_p^2}{\omega(\omega - i\gamma)}$$

The amplitude of the plasmonic peak in the effective scattering efficiency spectrum is computed for every couple of parameters (ω_p,γ). The result is shown in figure 2c. Gold and silver are found to give a higher efficiency at their plasmon resonance than aluminum.

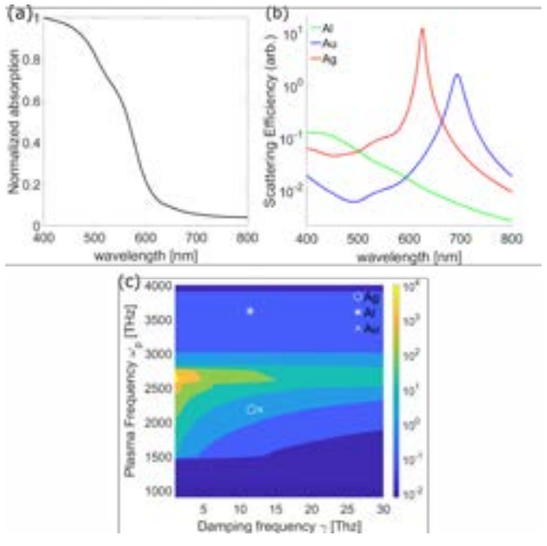

Fig. 2 Influence of the choice of the plasmonic material. (a) Normalized absorbance spectrum of a flat layer of hematite in vacuum (b) Scattering efficiency spectrum in hematite for a sphere made with different metals (c) Maximum value of the effective scattering efficiency as a function of the two parameters of the Drude model. The markers show the value of these parameters for gold, silver and aluminum [2].

Then the effect of considering the optical coupling between neighboring nanoparticles in a periodic system is studied with surface integral equation (SIE) simulations [3]. The considered geometry consist in metallic spheres periodically distributed and embedded in a thin film of hematite. For each configuration, the absorption efficiency in the hematite part of the geometry is computed in one unit cell:

$$\eta_{Abs} = 2Z_{H_2O}\frac{Im(\epsilon_H)ck}{\sigma|E_0|^2}\int_{V_H}|\boldsymbol{E}(\boldsymbol{r})|^2\,\boldsymbol{dr}$$

where Z_{H2O} is the wave impedance in water, $\varepsilon_H = \varepsilon_0 n_H^2$ is the permittivity of hematite, σ is the cross section of the unit cell in the direction transverse to the light propagation and V_H is the volume of hematite in the unit cell.

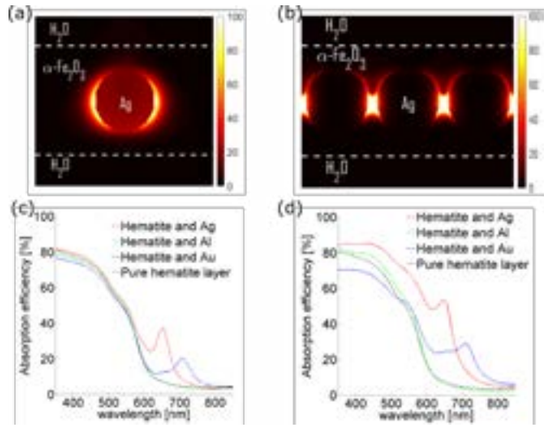

Fig. 3 Collective effects in a periodic system. (a, b) Electric field intensity in a cross section of the simulated geometry for (a) an isolated silver nanosphere and (b) periodically distributed scatterers. (c, d) Absorbed electric field in the hematite part of the geometry when different plasmonic metals are used as (c) an isolated metallic sphere and (d) periodically distributed scatterers. The reference structure is a pure hematite film of the same thickness than the full hybrid structure.

Collective effects are found to increase significantly the absorption of light in hematite, especially when silver is used as a plasmonic material (Fig. 3b, 3d). Moreover, the results for the case of isolated scatterers (Fig. 3a, 3c) agree well with the conclusions of the semi-analytic approach based on the Drude model and Mie scattering.

Hybrid structure hematite/silver nanoparticles

On the basis of these insights, a hybrid structure with hematite as semiconductor and silver nanoparticles is fabricated and optically characterized. A commercial Ag ink (60-80 nm nanoparticles) is spin coated on fluorine-doped tin oxide (FTO) coated glass (Fig. 4a). An electrochemical deposition of iron from an iron precursor in aqueous solution is then performed on top of the nanoparticles [4]. The iron is converted to hematite by annealing the sample in air at 550°C. The fabricated layer shows a high porosity and surface area (Fig. 4b).

The light absorption in the hybrid structure is increased compared to a pure hematite sample (Fig. 4c). In particular the silver nanoparticles show a plasmon resonance centered at 585 nm, blue-shifted compared to the simulations. The difference can be explained by the porosity of the fabricated hematite which results in a decrease of the effective refractive index for the medium surrounding the nanoparticles.

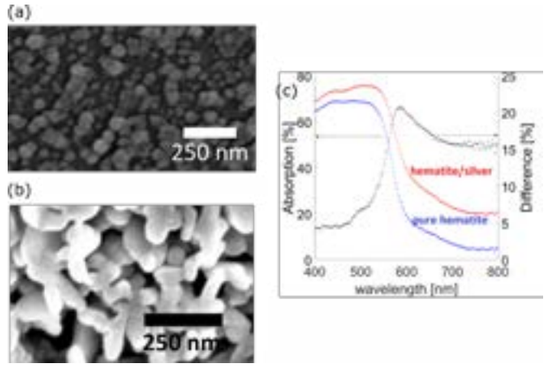

Fig. 4 Fabricated hybrid structure hematite/silver nanoparticles. (a) SEM picture showing silver nanoparticles coated on a glass substrate. (b) SEM picture of a hematite layer made with electrodeposition. (c) Absorbance of the hybrid structure hematite/silver compared to pure hematite.

Conclusion & Outlook

A comparative study of three different metals in both an isolated and a periodic configuration was conducted theoretically to increase the absorption of light in hematite with plasmonic nanoparticles. Silver was found as the most promising plasmonic material and the fabrication of hybrid hematite/silver nanoparticles samples was demonstrated. Further developments in the project include performance assessment for H_2 production and development of cost effective methods for producing efficient electrodes for water splitting.

References

[1] S. A. Maier, Plasmonics: Fundamentals and Applications. Springer US (2007)

[2] A. Rakić, A. B. Djurisic, J. M. Elazar, M. L. Majewski, *Optical properties of metallic films for vertical-cavity optoelectronic devices*, App. Opt. **37**, 5271 (1998)

[3] B. Gallinet, A. M. Kern, O. J. Martin, *Accurate and versatile modeling of electromagnetic scattering on periodic nanostructures with a surface integral approach*, J. Opt. Soc. Am. A, **27**, 2261 (2010)

[4] P. S. Shinde, A. Annamalai, J. Y. Kim, S. H. Choi, J. S. Lee, J. S. Jang, *Fine-Tuning Pulse Reverse Electrodeposition for Enhanced Photoelectrochemical Water Oxidation Performance of α-Fe_2O_3 Photoanodes*, J. Phys. Chem. C **119**, 5281 (2015)

Self-assembly and magnetic order of 2D spin lattices on surfaces

Project P1602: Self-assembly and magnetic order of 2D spin lattices on surfaces
Project Leader: T. A. Jung and J. Dreiser
Collaborators: M. Heydari (SNI PhD Student), M. Baljozovic, A. Ahsan, O. Popova, S. F. Mousavi, M. Moradi, N. Ballav, S.-X. Liu, and S. Decurtins

Introduction

Magnetism at the nanoscale and especially the magnetism of square-planar metallo-porphyrins and –phthalocyanines adsorbed on magnetic and non-magnetic substrates has recently attracted considerable attention. Several groups reported exchange-induced magnetic moments for such molecules upon adsorption on ferromagnetic substrates. On non-magnetic substrates, on the other hand, square-planar molecules provide a rich platform for studying fundamental exchange interactions with and via conduction electrons such as Kondo screening and Ruderman-Kittel-Kasuya-Yosida (RKKY) [1] interaction, respectively. In our recent work we have shown that the interplay of these two phenomena induces long-range ferrimagnetic ordering in a 2D checkerboard layer [2]. Here we investigate the self-assembly of triply-fused and singly bonded porphyrin molecules on atomically clean Au(111) substrates for their potential to provide an anisotropic 2D array comprising two different, pairwise exchange coupled spin bearing systems. In our first experiments, we start to study the on-surface supramolecular assembly of singly-bonded/triply fused porphyrin and the magnetic properties of homo-metallic, metal centered triply fused porphyrins in the powder form and in the mono layer regime by STM and XMCD/XMLD.

Results

Scanning Tunneling Microscopy (STM) reveals supramolecular monolayer islands exhibiting a compact zigzag assembly for both, the singly fused and triply fused bis-porphyrin (Fig. 1b and d).

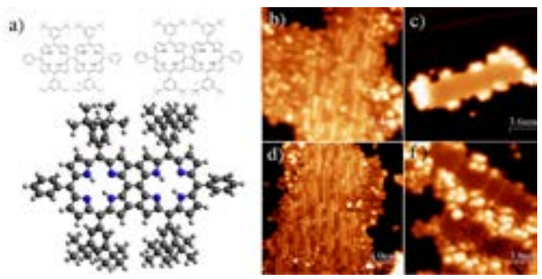

Fig. 1 a) Schematic of tbut- singly-bonded and triply fused porphyrin (top) and tf-porphyrin in a ball and stick representation (bottom); b,d) molecular resolution micrographs of Self-assembly patterns of tb-Singly bonded and triply fused porphyrin molecules c,f) molecular resolution micrographs of the same samples after annealing up to 400°C.

The molecular contrast in STM is dominated by the di-tertiary-butyl-phenyl moieties, which are flexibly attached to the porphyrin backbone of the molecule and flex in response to the molecule-substrate interaction [3]. Already after the initial sublimation, but even more pronounced after annealing to 400°C, we observe patches covered with parallel lines. We tentatively assign these assemblies to a chemical decomposition and reorganization process, possibly the formation of graphene-like platelets. This assessment is consistent with the established chemical experience that at above 300°C the carbon atoms bridging the pyrrole groups release their hydrogens and create C - C bonds [4].

X-ray absorption spectroscopy and X-ray magnetic circular dichroism (XMCD) and X-ray magnetic Linear Dichroism (XMLD) have been used to investigate the chemical composition of metal centered tbut-tf-porphyrin (in particular the case, of tbut-tf-MnMnCl2-porphyrin) in powder form and to determine the temperature and magnetic field dependent magnetic moment (Fig. 2).

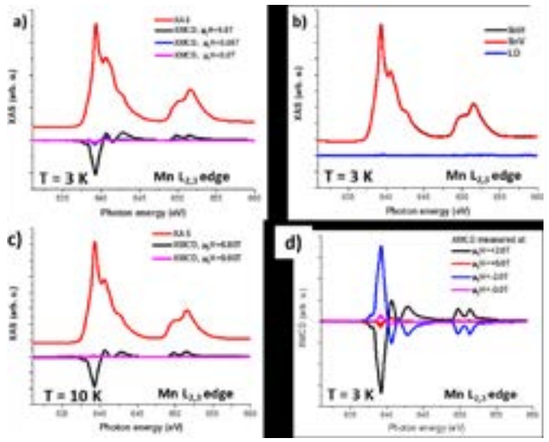

Fig. 2 XAS/XMCD and XMLD spectra of Mn-L edges for tbut-tf-MnMnCl2- porphyrin in normal sample geometry at T = 3K (a,b,d) and 10K (c).

Surprisingly, the XAS spectra suggest the presence of two-oxidation states of Mn atoms. According to the literature [2, 3], porphyrins containing one metal atom only show the Mn3+ oxidation state while in our sample we detect Mn2+ and Mn3+ states. Another important option is partial Cl loss from Mn, as reported earlier [5]. In the case of XMLD, as we expected, there is no detectable dichroism for the powder sample. At T=3K and μBH=6.80T, one considerable XMCD peak is observed at 639.3 eV which significantly weakens with decreasing magnetic field but remains visible in a tiny form at μBH=0 T. In addition, the sign of the remanent magnetization is reversed depending on the preceding magnetic field direction (Fig. 2d). The remanent peak is disappearing above T=10K and is characteristic for weak magnetic exchange. The observed remanence, however, is rather unexpected, for a magnetic molecule with such bulky substituents hindering inter-molecular exchange interaction. Intermolecular exchange could, in principle, occur via interstitial agents or ligands and induce magnetization in the 3D solid phase. This hypothetic assignment would be consistent with both Mn2+ and Mn3+ being observed in the porphyrin crystal i.e. if ligands (like Cl, O, CO, or NO) are bound. To investigate this, spectroscopic and chemical analytical investigations of these interesting samples are needed.

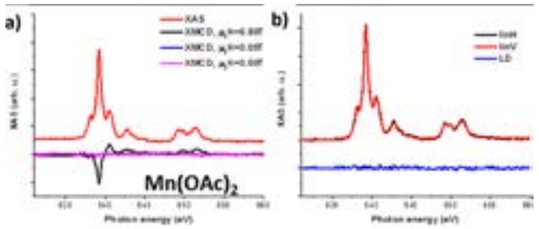

Fig. 3 Mn L-edges XAS/XMCD-XMLD spectra at T=3K and μBH=0, 0.05 and 6.80T of $Mn(oAc)_2$.

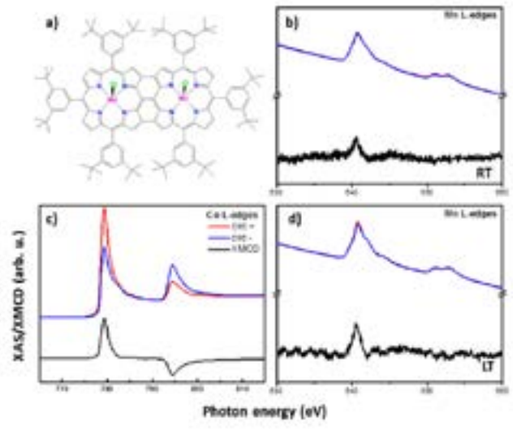

Fig. 4 Schematic of the tbut-tf-MnMnCl2-P (a) XAS/XMCD spectra of the Mn L-edges (b,d) and the Co L-edges (c) for tbut-tf-MnMn-Cl_2-porphyrin on Co substrate in grazing x-ray incidence. These spectra have been taken after initial magnetization of the Co thin film bottom layer substrate along the easy magnetization direction.

As we used $Mn(oAc)_2$ as the source of Mn ions, it is possible that some of these ligands are transferred during sublimation and we see XAS/XMCD contributions of $Mn(oAc)_2$ and/or oAc modified fused porphyrins. Figure 3a,b shows the XAS/XMCD and XMLD of $Mn(oAc)_2$ in the powder form and at normal incidence. Importantly, we cannot identify any signs of remanent magnetization in this sample; even if we had some Mn-acetate ($Mn(oAc)_2$) leftover, it cannot be responsible for the remanence in the fused bis-porphyrin powder. Another possible configuration, is that remanence emerges by the intermolecular coupling via Cl; Linking Mn ions under possible involvement of the Cl atoms and coordinating them in an octahedral ligand field. A further in-depth assessment of possible ligands – for example by providing more or less of the former and detecting the Mn2+/Mn3+ ratio in conjunction with DFT+U simulations would be needed to understand the source of the magnetic coupling and its tenability. With respect to the interesting behavior of this molecule, we also moved forward and investigated its magnetic behavior on surfaces. We successfully deposited fused porphyrins on a ferromagnetic Co substrate in the monolayer regime as revealed by XAS and XPS analysis and are currently in the process to study their magnetic interaction with the substrate. The sample is probed at grazing incidence of the X-ray beam and after initial magnetization along the easy magnetization direction at room temperature (RT) and around 20k (LT). The XAS/XMCD spectra of the Mn L-edges in the powder form agree very well with the published spectra of MnTPPCl [5] porphyrins deposited on Co substrate. XMCD evidences that the molecules are FM exchange coupled to the Co substrate. In addition, the XMCD signal is increasing with decreasing temperature, as expected.

Conclusion

We have investigated the self-assembly of bis-porphyrin molecules in monolayer islands on Au(111). A chemical conversion occurs in a thermally activated process and creates strongly modified, possibly graphene-like layers on the sample. Also the magnetic properties of tbut-tf-MnMnCl2-P in bulk powder form and in the monolayer regime on a ferromagnetic Co substrate have been investigated. In our STM study, we observe a compact zigzag assembly for both triply fused and singly bonded molecules. Remarkably, we find a weak magnetic remanence in our temperature dependent magnetisation of tbut-tf-MnMncl2-P powder samples. Also, we have started to investigate the molecules in monolayer arrangement on Co thin films. Here, the exchange coupling is, expectedly in view of the earlier work of the group, strong enough to be detected up to room temperature and beyond. All these findings indicate that these molecules provide a new class of spin bearing molecular building blocks which can be equipped with two spin centers. Thus, these interesting systems may provide a bridge compound between the fundamentally most exiting multiple spin containing molecular magnets and the simple, single spin containing magnetic molecules.

References

[1] N. Tsukahara, S. Shiraki, S. Itou, N. Otha, N. Takagi, M. Kawai, *Evolution of Kondo Resonance from a Single Impurity Molecule to the Two-Dimensional Lattice*, Phys. Rev. Letters **106**, (2011)

[2] J. Girovsky, et al. *Antiferromagnetic coupling of Cr-porphyrin to a bare Co substrate*, Phys. Rev. B **90**, 220404 (2014)

[3] T. A. Jung, R. R. Schlittler, J. K. Gimzewski, *Conformational identification of individual adsorbed molecules with the STM*, Nature **386**, 696–698 (1997)

[4] J. Cai, et al. *Atomically precise bottom-up fabrication of graphene nanoribbons*, Nature **466**, 470–473 (2010)

[5] D. Chylarecka, et al. *Indirect Magnetic Coupling of Manganese Porphyrin to a Ferromagnetic Cobalt Substrate*, J. Phys. Chem. C **115**, 1295–1301 (2011)

Characterization of nuclear pore membrane proteins and FG nucleoporins by high-speed AFM

Project P1603: A mechano-optical microscope for studying force transduction in living cells
Project Leader: R. H.Y. Lim and E. Meyer
Collaborator: T. Kozai (SNI PhD Student)

Introduction

Nuclear pore complexes (NPCs) mediate the selective transport of biomolecules between the cytoplasm and nucleus in eukaryotic cells. However, its molecular mechanism remains disputed. This is because the NPC barrier is comprised of numerous intrinsically disordered phenylalanine-glycine nucleoporins (FG Nups) that are extremely difficult to visualize, not least at transport-relevant timescales (~10 ms). Recently, we used high-speed atomic force microscopy (HS-AFM) to resolve the dynamic behavior of FG Nups inside NPCs at ~200 ms timescales [1]. Meanwhile, structural changes of FG Nups under transporting conditions are still unclear.

Here, we have used HS-AFM to characterize the dynamic behavior of different FG Nups tethered to a lipid bilayer. We observe that the FG Nups form extended conformations that fluctuate rapidly on a lipid membrane. In parallel, we have successfully reconstituted "pre-NPCs" from two NPC-associated transmembrane nucleoporins (TM Nups; i.e., Pom121 and Ndc1) in lipid bilayers as resolved by HS-AFM. Besides providing insight as to how TM Nups self-assemble to form the NPC channel, we envisage that pre-NPCs may be used as templates to build on other NPC components. Further, their function as an NPC mimic is the subject of ongoing work.

FG Nups tethered to a lipid bilayer

To visualize FG Nups tethered to a lipid bilayer, we first prepared supported lipid bilayers (SLBs) with varying fractions of metal ion chelator (DGS NTA(Ni)) containing lipids (DOPC) on chemically functionalized mica with 3-aminopropyltriethoxy silane (APTES-mica). In this work, a cysteine-modified FG domain construct of histidine-tagged Nup62 (aa 1-240; full length FxFG domain) that is the homolog of yeast Nsp1 is used. The His-tagged Nup62 was bound to the lipid membrane and we conducted HS-AFM observation (Fig. 1).

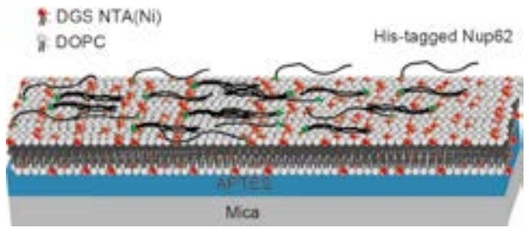

Fig. 1 His-tagged Nup62 is tethered onto a lipid bilayer exposing Ni-NTA binding sites.

In the HS-AFM observation, we have observed that the Nup62 forms extended conformations that fluctuate rapidly on the lipid membrane (Fig. 2). Moreover, the height measured by HS-AFM experiment is 11.1 ± 1.0 nm. This is not consistent with the persistence length of an individual FG Nup [2]. However, there are some reports about multi-protein bundles of FG-Nups observed by molecular dynamics (MD) simulations [3, 4]. The simulations showed that Nsp1, formed brush-like structures with bristles made of bundles 2-27 nups. Therefore, the extended conformation may be a bundle formed by several Nup62 strands.

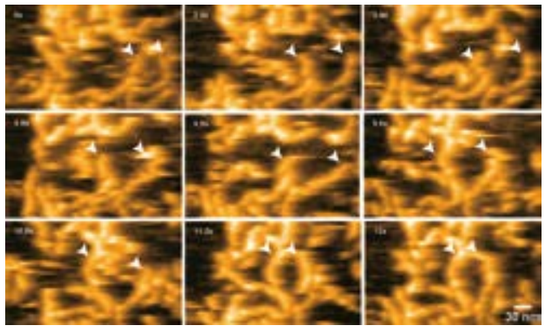

Fig. 2 Extended conformations formed by Nup62. White arrow heads indicate diffusion of Nup62 tethered to the lipid membrane. Frame rate, 5 fps.

Formation of NPC-like pore by Pom121 and Ndc1

TM Nups are localized at the equator of the NPC and clamp the NPC framework [5]. However, it has been unclear that TM Nups could initiate pore formation in vitro conditions and its topological features.

In order to resolve the topological features of pore complexes formed by Pom121 and Ndc1, we reconstituted the two TM Nups into asolectin membranes. HS-AFM then revealed numerous pore-like perforations in the Pom121-Ndc1-lipid membrane [6] (Fig. 3).

Each pore is enclosed by a ring-like structure above the membrane surface. Moreover neighboring pores seem to co-join as elongated slits (Fig. 4). These pores and slits suggest that individual Pom121-Ndc1 sub-complexes are assembling. Their average pore dimensions are 5.8 ± 1.4 nm, 3.2 ± 1.4 nm, 2.5 ± 0.6 nm, 19.5 ± 3.7 nm and 37.3 ± 6.1 nm for height (H_{pore}), ring height (H_{rim}), height of the surrounding membrane (H_{mem}), inner diameter and outer diameter, respectively. Moreover, values of H_{pore}, H_{rim} and H_{mem} for the slits are similar to those of the pores; H_{pore}, H_{rim} and H_{mem} for the slits are 5.7 ± 1.1 nm, 3.2 ± 0.9 nm and 2.8 ± 0.9 nm, respectively.

Our study provides the implication that the Pom121-Ndc1 pores may be used as templates to build on other NPC components that interact with Pom121 and Ndc1.

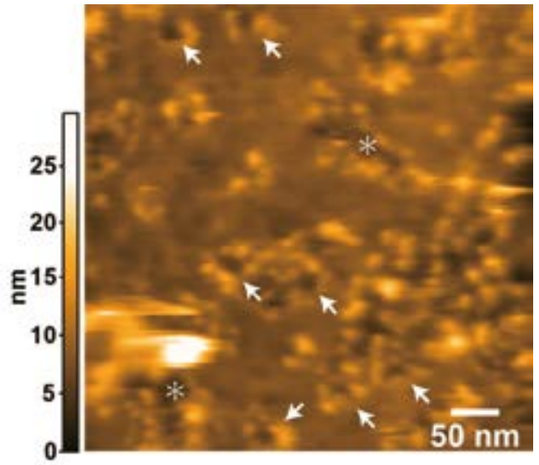

Fig. 3 Lipid membrane including Pom121 and Ndc1 perforated with several pores (white arrows). Asterisks denote elongated pores (slits)

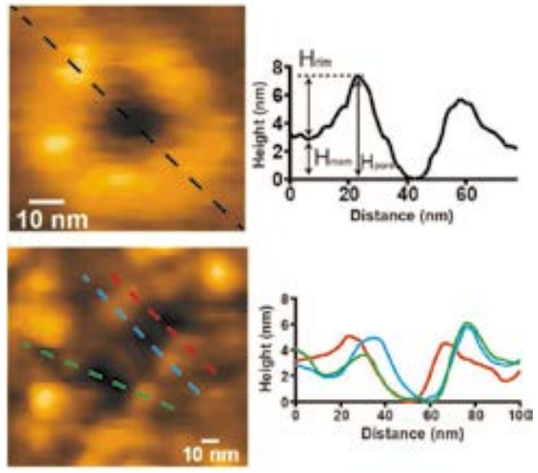

Fig. 4 Height profiles of a pore and slit. Pore height, the ring height and the height of the surrounding membrane are given by H_{pore}, H_{rim} and H_{mem}, respectively as shown in the cross-sectional profile.

Summary

We have successfully visualized Nup62 bundles, and reconstituted the Pom121-Ndc1 pore and determined its topological features. Next, we want to visualize how cargo transport proceeds through FG Nups in vitro and within NPCs.

References

[1] Y. Sakiyama, A. Mazur, L. E. Kapinos, R. Y. H. Lim, *Spatiotemporal dynamics of the nuclear pore complex transport barrier resolved by high-speed atomic force microscopy*, Nature Nano. **11**, 719-724 (2016)

[2] R. Y. H. Lim, et al. *Flexible phenylalanine-glycine nucleoporins as entropic barriers to nucleocytoplasmic transport*, Proc. Natl. Acad. Sci. USA **103**, 9512-9517 (2006)

[3] L. Miao, and K. Schulten, *Transport-Related Structures and Processes of the Nuclear Pore Complex Studied Through Molecular Dynamics*, Structure **17(3)**, 449-459 (2009)

[4] R. Gamini, W. Han, J. E. Stone, K. Schulten, *Assembly of Nsp1 Nucleoporins Provides Insight into Nuclear Pore Complex Gating*, PLOS Comput. Biol. **10(3)**, e1003488 (2014)

[5] H. K. Bui et al., *Integrated structural analysis of the human nuclear pore complex scaffold*, Cell **155**, 1233–1243 (2013)

[6] R. Panatala et al., *Nuclear Pore Membrane Proteins Self-Assemble into Nanopores*, Biochemistry (2019) DOI: 10.1021/acs.biochem.8b01179

Development of hybrid platforms equipped with biomolecules

Project P1604: Selective reconstitution of biomolecules in polymer-lipid membranes
Project Leader: W. Meier and U. Pieles
Collaborator: S. Di Leone (SNI PhD Student)

Introduction

Amphiphilic block copolymers are interesting candidates to create distinct model systems such as polymersomes or planar membranes. They can self-assemble in aqueous media into polymersomes with superior membrane stability and properties that can be further optimized by varying hydrophilic-to-hydrophobic block length ratio. Mixtures of the amphiphilic block copolymers with phopsholipids form the membranes with distinct domains due to physical properties of lipids (membrane thickness of 3-5 nm and copolymers (membrane thickness of 5- 20 nm). The domains formed by amphiphilic block copolymers enhance stability of the whole system and furthermore improve the lateral mobility together with the lipid domains [1, 2]. The presence of the polymer and lipid domains significantly influences the insertion of membrane proteins in a controllable manner. In this project, we planned to use functionalized amphiphilic block copolymers to modulate the polymer-lipid hybrid membrane properties for selective insertion of more than one type of biomolecule. We more specifically selected poly(dimethylsiloxane)-block-poly(2-methyl-2-oxazoline) (PDMS-b-PMOXA) diblock copolymers and saturated lipids (e.g. 1,2-dipalmitoyl-sn-glycero- 3-phosphocholine) or charged lipids (e.g. 1,2- dilinoleoyl-sn-glycero-3-phospho-1'-rac-glycerol) to form hybrid membranes [3]. As model proteins, the inner membrane protein cytochrome c was selected. The cytochrome c was attached to hybrid membranes through either covalent attachment or physical adsorption strategies. With this, we aimed to test the versatility of those polymers and the functionality of the membranes. Furthermore, we planned to insert the channel protein mellitin into different domains in the presence of a polymeric hydrogel spacer, in order to increase membrane's mobility and versatility (Fig. 1). The desired selective distribution and function of the two types of biomolecules in the polymer-lipid membranes will be evaluated.

Material and Methods

In the first part, we focus on the preparation of a suitable hybrid solid-supported bilayer membrane. The polymer used is a PDMS-PMOXA with a carboxylic end group functionalization. The end group was attached to the PMOXA and made it possible to subsequently conjugate with a biomolecule via EDC/NHS coupling.

The obtained hybrid membrane was characterised with Brewster Angle Microscopy and Langmuir isotherm. In order to create a double layer, Langmuir-Blodgett technique was used.

A silica wafer was submerged two times (down-up and down-up approach) into a monolayer at the air-water interface. Laser Scanning Microscopy (LSM) and the polymer-lipid molar ratio was optimized for achieving specific dimension of domains and stability over time (Fig. 2).

To determine the combination of the model protein with the membrane, we performed Quartz Crystal Microbalance with dissipation (QCM-D) measurements (Fig. 3). The flow rate was 50 uL/min and the solution of cytochrome c in phosphate buffer (PB) was injected for 30 minutes. As for the EDC/NHS conjugation, the activators dissolved in PB buffer were separately injected for 20 minutes each. Afterwards PB washing was also

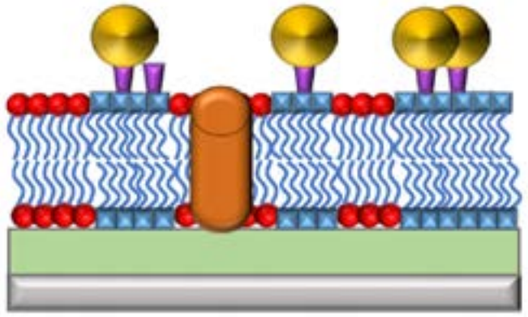

Fig. 1 Scheme for hybrid platform equipped with biomolecules: silica support (grey), spacer (green), lipid (red), polymer (blue), mellitin (brown), RGD sequence (violet) and cells (yellow).

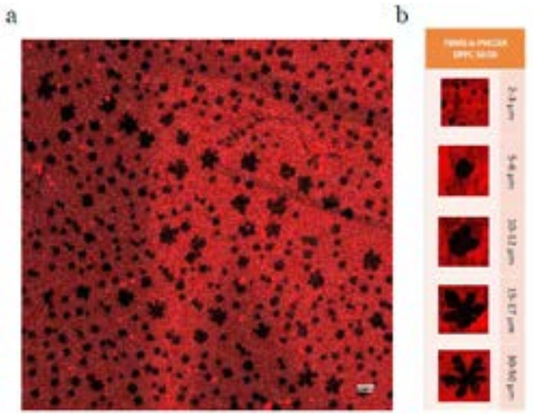

Fig. 2 (a) LSM image of hybrid membrane made of DPPC:PDMS-b-PMOXA-COOH at 50:50 molar ratio (lipid domains in black, polymer domains in red); (b) shape and dimensions of lipid domains.

performed for 45-60 minutes for removing the excess of the protein. Each measurement was replicated. In order to determine defect freeness of membrane Bovine Serum Albumin (BSA) was added to the membranes. BSA did not adsorb on the membrane, compared to the bare silica chip. This control measurement was useful to confirm that we had homogenous membranes with no defects and thus the increasing of mass belongs to the attachment of the desired protein of interest directly to the membrane.

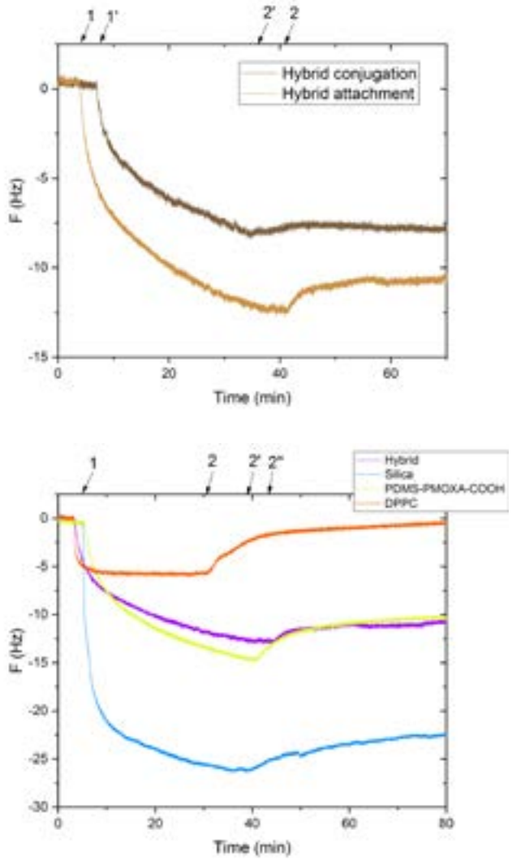

Fig. 3 QCM-D graphs of chemisorption of cytochrome c onto different membranes and silica chip: Comparison between (a) EDC/NHS conjugation and spontaneous attachment onto hybrid membrane; (b) spontaneous attachment onto hybrid, polymer and lipid membrane and silica (1, 1' = cytochrome c 500 µg/mL; 2, 2' = PB buffer).

	[ng / cm²]		
Membrane type	***Attachment***	***Conjugation***	***BSA test***
PDMS-PMOXA-COOH membrane	142 ± 16	265	49
Hybrid membrane	132 ± 37	88	71
DPPC membrane	41 ± 40	/	102
Silica	289 ± 103	/	/

Table 1: Quantification of the cytochrome c (ng/cm²) attached to the different membrane.

Results and discussion

As reported in Table 1, cytochrome c was adsorbed to the polymer membrane and the hybrid membranes, whereas it did not adsorb to the lipid membranes. The driving forces of cytochrome c adsorption are hydrophilic/hydrophobic interactions: the big hydrophilic part of the cytochrome interacted with the outer membrane, through its reactive centre outside and its hydrophobic domain promoted its insertion into the membrane. The stiffness of the DPPC lipid probably hindered the lateral mobility of membrane, resulting into a detachment of cytochrome c from the lipid membrane. The conjugation consisted of a peptidic bond between the lysines residual (Lys27 and Lys73) of the protein and the end group of the polymer via EDC/NHS, resulting in a greater value for the polymer membrane than the hybrid membranes. The obtained results are promising, but still require further investigation.

Outlook

The aim of this project is building a complex, stable and flexible system, in which the biomolecules can be inserted into different domains of a membrane while retaining their functions. This project will create a model membrane platform to host different types of membrane proteins to support high industrial and medical interests.

References

[1] J. Kowal, D. Wu, V. Mikhalevich, C. G. Palivan, W. Meier, *Hybrid Polymer–Lipid Films as Platforms for Directed Membrane Protein Insertion*; Langmuir, **31**, 4868–4877, (2015)

[2] F. Itel, M. Chami, A. Najer, S. Lörcher, D. Wu, I. A. Dinu and W. Meier, *Molecular Organization and Dynamics in Polymersome Membranes: A Lateral Diffusion Study*, Macromolecules **47**, 7588–7596 (2014)

[3] X. Zhang, W. Fu, C. Palivan, W. Meier, *Natural channel protein inserts and functions in a completely artificial, solid-supported bilayer membrane*, Scientific Reports, **3**, 2196, (2013)

Tuning the electronic structure of a metal-organic network

Project P1605: Topological electronic states in metal-coordinated organic networks
Project Leader: M. Muntwiler and T. A. Jung
Collaborators: D. Sostina (SNI PhD Student) and N. Bachellier

Introduction
In addition to their inorganic counterparts and graphene-based architectures, two-dimensional (2D) metal-organic networks have been recently proposed as a new class of materials for realizing exotic quantum phases including topological and anomalous quantum Hall insulators [1-4]. However, while topological effects are predicted by these theoretical studies, their experimental demonstration is still pending.

Goals
Here, we report on an experimental investigation of possible non-trivial topology in a Kagome lattice assembly of 9,10-dicyano-anthracene ($C_{16}H_2N_2$, DCA) molecules and Cu adatoms on a Cu(111) substrate. Theoretical calculations predict that a free-standing layer of metal-coordinated DCA exhibits an array of states around the Fermi level, consisting of one Kagome flat band (FB) with a bandwidth of 3.0 meV above two Dirac bands (DB) derived from molecular pz orbitals [4]. In contrast to the theoretical model, the experimental realization of the Cu-DCA network requires the presence of a metal substrate, which may perturb the 2D electronic structure of the layer and render a direct observation of the intrinsic Dirac cone difficult.

Our goals are to look for predicted flat bands and Dirac bands in the interior and at the edges of the Cu-DCA network using scanning tunneling spectroscopy (STS) and angle-resolved photoelectron spectroscopy (ARPES). STS provides a local probe of edge states of the DCA network and is also capable of probing unoccupied states. ARPES, on the other hand, easily distinguishes localized and dispersive band formation in reciprocal space.

Results
The project started in August 2017. So far, we have investigated the electronic structure of DCA in the two-dimensional network, at the (one-dimensional) edges as well as in unique zero-dimensional formations consisting of one copper adatom and three molecules arranged around it. Figure 1 (a) shows an STM topography image of the network on the Cu(111) substrate. While in the interior, either cyano side group of a molecule is coordinated to a Cu adatom, at the edge, only one side is. In order to understand the difference in the electronic states, we measured STS (Fig. 1b). The peak of the unoccupied LUMO state is significantly shifted compared to the interior, thereby reducing the absolute gap value from 1.47 eV to 1.32 eV. In the case of the isolated trimer (Fig. 1c), the dI/dV curve measured in the middle of one of the trimer molecules shows that the peak of the occupied states is shifted as well as the peak of the unoccupied states, minimizing the absolute gap to 1.21 eV. A decreasing electronic gap is a common observation when molecules are adsorbed on a metal due to the screening of charge. Correspondingly, it should not be mistaken for a dimensional or topological effect in the present case.

Our previous ARPES studies of the DCA-Cu valence band on Cu (111) showed one FB near the Fermi level. In order to confirm the molecular origin of this band, we attempted electron and hole doping with oxygen and potassium. Doping by gas adsorption and deposition of alkaloid metals has proven to be effective in other systems like graphene [5, 6].

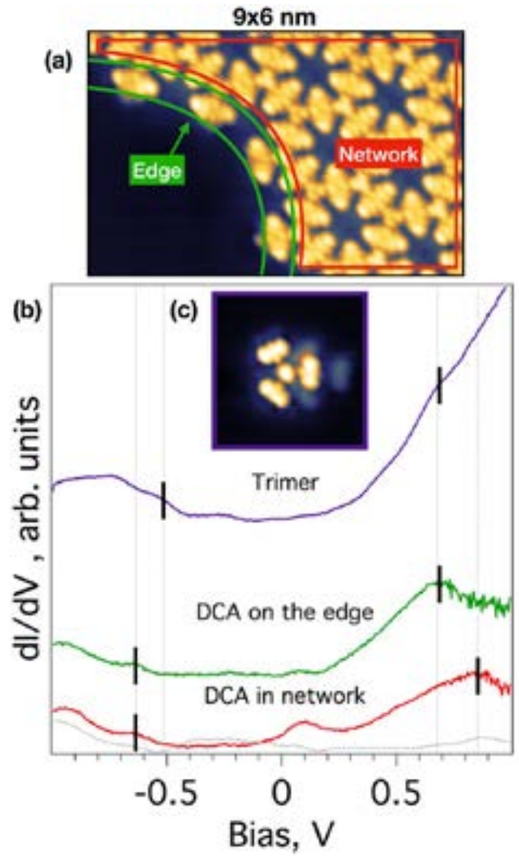

Fig. 1 (a) STM topography of DCA network on Cu (111) substrate (-0.8 V, 100 pA). (b) STM spectroscopy of DCA in different locations with respect to the network. Negative (positive) bias corresponds to the region of occupied (unoccupied) states, respectively. (c) STM topography of an isolated trimer (-0.8 V, 100 pA, 3.5 x 3.5 nm).

Figure 2 shows that the HOMO-derived FB shifts towards lower binding energy after deposition of molecular oxygen due to increased positive charge on the molecules. By analogy with graphene, potassium increases negative charge and leads to a shift to higher binding energy. However, the shifts are much smaller than in graphene (1.3 eV [5]) and not sufficient to bring either occupied (oxygen doping) or unoccupied (alkali doping) states close to the Fermi level.

In figure 3a and b one can see the influence of oxygen adsorption on the network topography measured by means of STM. In addition to the formation of an oxygen top layer which leads to p-doping, measurements show new structures inside the pores of the network formed by oxygen in the shape of rings.

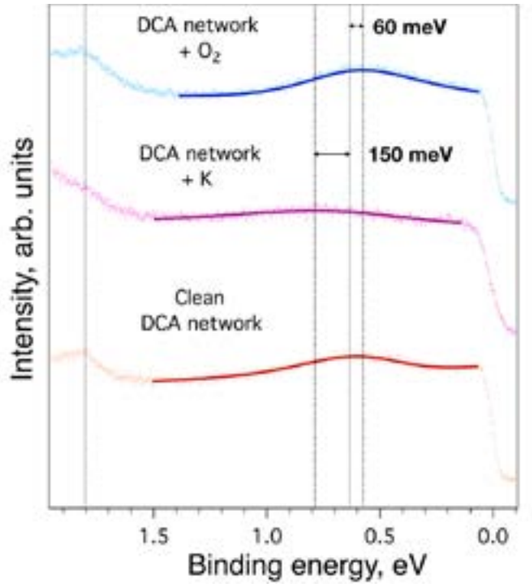

Fig. 2 Valence band XPS spectra of DCA network measured with 62 eV of photon energy. The red line represents the position of molecular electronic states in the pristine DCA network. The purple line is measured after doping with potassium, the blue line after oxygen deposition.

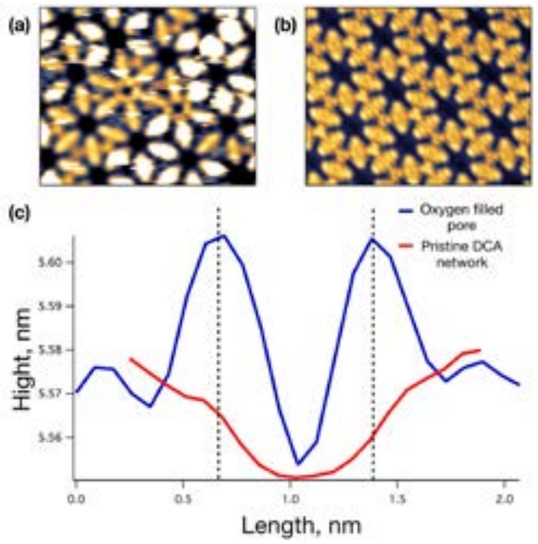

Fig. 3 (a, b) STM topography of the DCA network after and before oxygen deposition (-0.5 V, 20 pA and -0.8, 100 pA respectively, 8x8 nm). (c) STM line profiles through a network pore before and after oxygen deposition.

Outlook
While the presented measurements show flat bands compatible with the theoretical predictions, other evidence like the Dirac bands have not been observed. It is, at the moment, unclear whether their absence is intrinsic, a consequence of the metallic substrate, or due to a lack of experimental resolution. Further experiments in different configurations are planned.

References

[1] Z. Wang, Z. Liu, F. Liu, *Organic topological insulators in organometallic lattices*, Nat. Commun. **4**, 1471 (2013)

[2] Z. F. Wang, N. Su, F. Liu, *Prediction of a Two-Dimensional Organic Topological Insulator*, Nano Lett. **13**, 2842 (2013)

[3] J. Cui, Z. Hu, *An electroactive porous network from covalent metal-dithiolene links*, Chem. Commun. **50**, 3986-3988 (2014)

[4] L. Z. Zhang, Z. F. Wang, B. Huang, B. Cui, Z. Wang, S. X. Du, H.-J. Gao, F. Liu, *Inrinsic Two-Dimentional Organic Topological Insulators in Metal-Dycyanoanthracene Lattices*, Nano Lett. **16**, 2072-2075 (2016)

[5] C. Struzzi et al., *Controlled thermodynamics for tunable electron doping of graphene on Ir(111)*, Phys. Rev. B **94**, 085427 (2016)

[6] A. Piazza et al., *Substrate and atmosphere influence on oxygen p-doping graphene*, Carbon **107**, 696-704 (2016)

Smart peptide nanoparticles for efficient and safe gene therapy

Project P1606: Smart peptide nanoparticles for efficient and safe gene therapy
Project Leader: C. G. Palivan and J. Benenson
Collaborator: S. Tarvidirpour (SNI PhD Student)

Introduction

Gene therapy is of particular significance in the treatment of inherited diseases, neurological disorders and cancer. Maximizing the potential benefits of gene therapy requires efficient and sustained therapeutic gene expression in the target cells, low toxicity, and a high safety profile. Viral or non-viral delivery systems are used to introduce exogenous nucleic acids into host cells. Non-viral gene delivery systems (nVGDS) have several advantages over viral delivery including lower immunogenicity and toxicity, better cell specificity, better modifiability, and lower production cost [1]. Peptides as gene delivery vectors are particularly attractive as they are able to achieve all of these goals along with a higher biocompatibility and biodegradability [2]. The aim of this project is to develop amphiphilic peptide-based nanoparticles able to condense DNA through electrostatic interactions for gene therapy. The high flexibility in peptide design allows for synthesizing purely peptidic amphiphiles that self-assemble into multi-compartment micellar nanostructures which can be harnessed for gene delivery.

Initially, we confirmed that the previously studied amphiphilic H3gT peptide was able to self-assemble into multi-compartment micelles and condense 22mer single-stranded DNA (ssDNA) [3]. In order to improve entrapment efficiency of ssDNA and investigate double strand DNA (dsDNA) entrapment, we designed a new amphiphilic peptide on the basis of the H3gT sequence. Our ultimate goal is to incorporate protein coding sequences in peptide nanoparticles for efficient gene-based therapy.

For this purpose, we increased the charge of the hydrophilic domain by including three arginine (R) residues that follow each histidine (H) at the N-terminus of the H3gT sequence. Additionally to increasing hydrophobicity, three D-leucine–L-tryptophan [$_D$L-$_L$W] sequence of truncated gramicidin A (gT) were added to the hydrophobic C-terminus of the H3gT (Fig. 1).

Fig. 1 Schematic representation of amphiphilic (HR)3gT peptide and the incorporation of DNA mediated by electrostatic interactions during self-assembly into multicompartment micelles.

In this reaction, the hydrophobic domain supports the self-assembly of such amphiphilic peptides into supramolecular assemblies, whilst the hydrophilic domain facilitates DNA entrapment. Comparing the hydrophobic to hydrophilic domain's weight ratio of the H3gT and (HR)3gT, it was increased from 38.4% to 44.5% respectively.

Material and methods

H3gT and (HR)3gT comprising 10 and 19 amino acids, respectively, were synthesised on a rink amide resin using standard fluorenyl-methoxycarbonyl (Fmoc) solid phase peptide synthesizer chemistry and DIC/OXYMA coupling methods. Peptide cleavage from the resin and removal of the protective groups were performed using a mixture of trifluoroacetic acid (TFA), triisopropylsilane and H_2O. The crude peptides were filtered, solubilized with acetonitrile and aqueous TFA (0.05%, v/v), and lyophilized. Peptides were purified by reverse phase high performance liquid chromatography (HPLC) and analysed by liquid chromatography mass spectrometry (LC-MS).

Self-assembly of H3gT and (HR)3gT was carried out by solvent exchan, dialysing the organic solvent (ethanol 35%) against milli-Q H_2O. Self-assembly of H3gT and (HR)3gT was studied with pure peptides and in the presence of 22- and 100-nucleotide ssDNA and corresponding dsDNA.

Supramolecular nanostructures resulting from the self-assembly of the peptides in the presence of DNA were characterized by dynamic light scattering (DLS), zeta potential measurements, transmission electron microscopy (TEM) and fluorescence correlation spectroscopy (FCS). Cytotoxicity analysis was performed using CellTiter 96 AQueous One Solution Cell Proliferation Assay (MTS). The cellular uptake of nanoparticles by HeLa-GFP-H2B cells was examined by confocal laser scanning microscopy (CLSM).

Results

TEM analysis of self-assembled nanostructures revealed that the newly designed (HR)3gT peptide is able to form spherical, multi-compartment micellar assembly in the presence of ssDNA and dsDNA, each comprising 22 or 100 nucleotides (nt) or base pairs (bp). In contrast, H3gT nanoparticles were observed only in the presence of 22mer ssDNA but not with the other DNAs. DLS measurements revealed the size distribution of DNA-loaded H3gT and (HR)3gT nanoparticles (NPs) (Fig. 3).

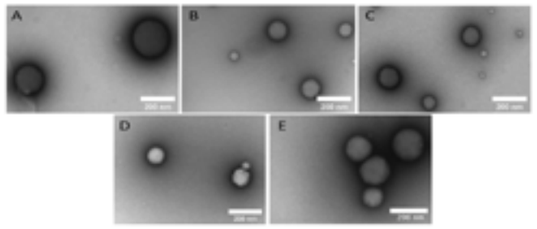

Fig. 2 TEM analysis of 22mer loaded-H3gT (A), 22mer loaded-(HR)3gT (B), 22bp loaded-(HR)3gT (C), 100mer loaded-(HR)3gT (D), 100bp loaded-(HR)3gT (E).

With a hydrodynamic diameter of ~120 nm, DNA-loaded (HR)3gT NPs were smaller than H3gT NPs entrapping 22mer ssDNA (~200 nm) which could enhance their gene delivery potential. FCS analysis of NPs hydrodynamic diameters revealed consistent with those from DLS measurements. DLS and TEM demonstrated that (HR)3gT NPs with and without DNA do not tend to aggregate whereas H3gT peptide nanoparticles tend to aggregate in the absence of DNA.

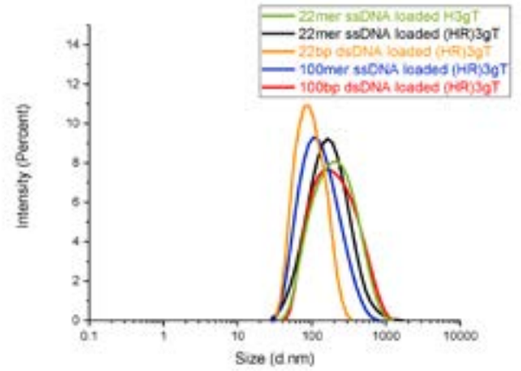

Fig. 3 DLS of DNA-loaded H3gT and (HR)3gT peptide nanoparticles

The entrapment of DNA in H3gT and (HR)3gT NPs was studied by FCS (Fig. 4). FCS autocorrelation curves revealed a 4-fold increase of 22mer ssDNA entrapment by (HR)3gT in comparison to H3gT NPs (20 versus 5 ssDNA/particle).

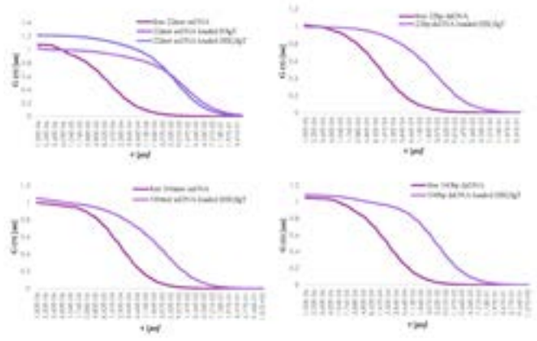

Fig. 4 Fit of correlation function of free DNA and DNA-loaded H3gT and (HR)3gT peptide nanoparticles.

Cell proliferation assays with different concentrations of DNA-loaded and DNA-free NPs indicated that (HR)3gT NPs had no toxic effects on HeLa cells after 24 h of incubation (Fig. 5). Cellular uptake of peptide NPs loaded with fluorescently labelled Atto550-DNA fragments in H2B-GFP expressing HeLa cells was examined by CLSM (Fig. 6). Uptake efficiency of 22mer ssDNA was significantly higher for (HR)3gT than for H3gT NPs. The increased cellular uptake of NPs assembled from the newly designed peptide could be related to the cell penetrating properties of arginine-histidine repeats that are exposed on the hydrophilic surface of the multicompartment micelles. Furthermore, (HR)3gT NPs are loaded with higher amounts of 22mer ssDNA.

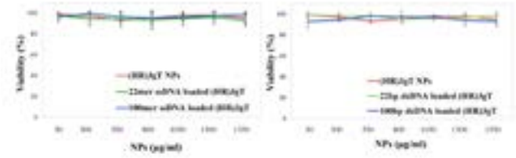

Fig. 5 Effect of control and DNA-loaded (HR)3gT peptide nanoparticles on cell proliferation.

Consistent with the notion that only (HR)3gT is able to entrap 22mer dsDNA and longer (100 nt) DNA fragments, CLSM data showed no uptake of corresponding H3gT NPs.

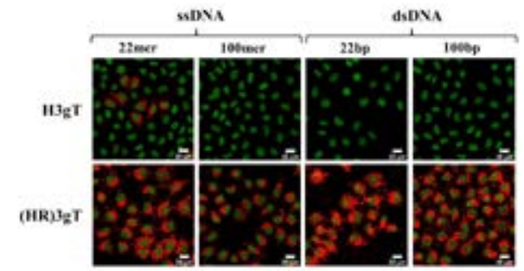

Fig. 6 CLSM merged images (GFP and atto550) of H2B-GFP expressing HeLa cells treated with DNA-loaded H3gT and (HR)3gT peptide nanoparticles for 24 hours.

Conclusion and outlook

After direct modification of the original H3gT peptide sequence, the new peptide (HR)3gT was shown to self-assemble into multi-compartment micelles. More importantly, (HR)3gT is able to condense 22- and 100-nucleotide ssDNA and dsDNA and resulting NPs function as a vehicle for DNA transfer into cells. Furthermore, (HR)3gT shares several features with amphipathic cell penetrating peptides, e.g. length, polar and non-polar regions, an abundance of positively charged arginine residues, and evenly distributed tryptophan residues, that are known to mediate translocation through membranes and increase cellular internalization [4]. Our future efforts are directed towards further modifying the physical and chemical properties of self-assembling peptide-carriers to obtain non-viral nanoparticles that efficiently entrap and release protein encoding DNAs in cells and tissues.

References

[1] L. W. Seymour, A. J. Thrasher, *Gene therapy matures in the clinic*, Nat. Biotechnol. **30(7)**, 588-593 (2012)

[2] H. Yin, R. L Kanasty, A. A Eltoukhy, A. J. Vegas, J. R. Dorkin, D. G. Anderson, *Non-viral vectors for gene-based therapy*, Nat. Rev. Gen., **15(8)**, 541-555 (2014)

[3] S. J. Sigg, V. Postupalenko, J. T. Duskey, C. G. Palivan, W. Meier, *Stimuli-Responsive Codelivery of Oligonucleotides and Drugs by Self-Assembled Peptide Nanoparticles*, Biomacromolecules, **17(3)**, 935-945 (2016)

[4] A. Borrelli, A. Tornesello, M. Tornesello, F. Buonaguro, *Cell penetrating peptides as molecular carriers for anti-cancer agents*, Molecules, **23(2)**, 295 (2018)

Understanding phonon propagation in nano-devices

Project P1607: Understanding and engineering of phonon propagation in nanodevices by employing energy resolved phonon emission and adsorption spectroscopy
Project Leader: I. Zardo and C. Schönenberger
Collaborators: L. Gubser (SNI PhD Student), G. Fülop, M. Nielsson, A. Baumgartner, L. Sorba, and V. Zannier

Introduction
During the last few decades research has improved our knowledge and control over electrons and photons, enabling impressing advances for electronic and optoelectronic applications. The same degree of control is still lacking for phonons. The ability to manipulate phonons and phonon transport on a quantum level would lead to full control over heat flow in nanodevices. This could be used in the form of phonon transistors [1] or is also proposed as a building block for logic gates [2].

The goal of the project is twofold. First, efficient phonon emitters and detectors have to be developed. Second, the developed devices can then be used to investigate and engineer phonon band structures. To realise the former, inelastic tunnelling through the states of a double quantum dot shall be used as phonon emitter and detector.

DQD phonon emitter/detector
The group of Jason Petta has demonstrated a maser driven by single-electron tunnelling through a double quantum dot (DQD) in a semiconducting nanowire (NW) [3]. Such a device is based on inelastic tunnelling through the energy states of the two QDs, when the system is driven by an applied bias voltage.

A schematic of the proposed DQD structure is presented in figure 1. Under an applied bias, an electron undergoes three subsequent tunnel transitions: i) from source to eigenstate ε_1 of QD1; ii) from ε_1 to ε_2 in QD_2; iii) from ε_2 to drain.

Inelastic tunnelling takes place if the energy levels are detuned ($\varepsilon_1 \neq \varepsilon_2$). The electron will then tunnel through the DQD emitting/absorbing a particle (a photon or a phonon) able to account for the energy difference. When $\varepsilon_1 > \varepsilon_2$, tunnelling can only take place if such a particle is emitted. Hence, the device acts as a photon or phonon emitter. Analogously, when $\varepsilon_2 > \varepsilon_1$, tunnelling can only take place if a particle is simultaneously absorbed. The device now acts as a detector. In the work of Petta et al. the DQD system was coupled to a microwave cavity, as their interest was focused on photon emission and absorption. In absence of such a cavity emission/absorption of phonons is expected to be dominate. This makes the DQD system an excellent choice to emit and detect monochromatic phonons.

Two barrier NW measurements
While QDs are often defined by narrow gate lines, this approach does not allow for a strong confinement with QD eigenstates that are separated by > 1 meV. We use instead QDs that are defined by InAs/InP nanowire heterostructure (Fig. 2). This approach allows for very small QDs with a large level spacing [4] (Fig. 2).

Low temperature (20 mK) electrical transport measurements on a single QD (Fig. 2 left) were performed using three contacts. The idea is to place the contacts in such a way that a QD is localized between two neighboring contacts. Since there is only one QD grown in a single nanowire, the other contact pair should then measure a pure InAs segment. Due to the largely different conductance values for a pure InAs segment and one with a QD, this approach allows to unambiguously localize the QD.

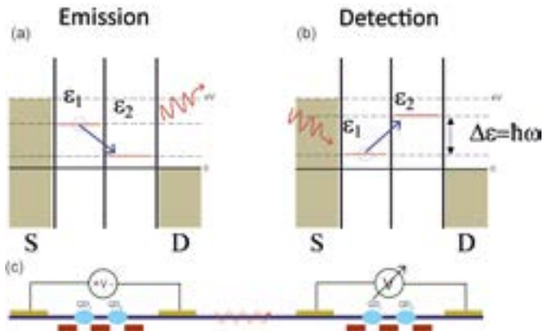

Fig. 1 Illustration of (a) a phonon emitter and (b) detector using a double quantum dot (DQD). Driven by an applied bias, inelastic tunnelling is used to either emit or detect phonons. (c) Schematic of an envisaged device. Inside the semiconducting nanowire two double quantum dots (light blue) are defined by local bottom gates (red). Phonons are then generated by an applied bias through source (S)-drain (D) contacts in the left DQD system and detected by measuring the voltage in the right DQD.

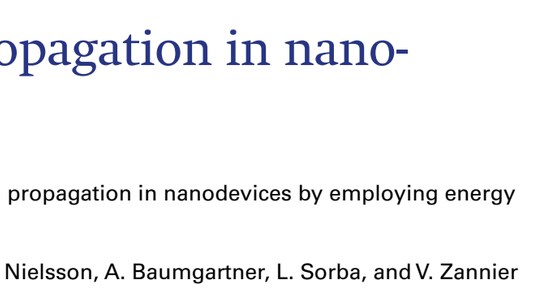

Fig. 2 Transmission electron microscope image of the InAs wires with symmetric InP barriers. Due to the difference in bandgap of the materials (InAs: 0.354 eV; InP: 1.344 eV) tunnel barriers are formed. Two barriers define a single quantum dot (a), whereas three barriers form a double quantum dot (b).

An example of the measured bias- and gate-dependent differential conductance for the two segments of a single nanowire is shown in figure 3. Figure 3a and b correspond to a segment with QD and figure 3c without. The observation of well defined and regularly spaced Coulomb-blockade diamonds confirm that a single QD is localized in between the contact pairs in the measurements of figure 3a and b.

Further analysis with the goal of obtaining the tunnel coupling parameters Γ_1 and Γ_2 is being performed in collaboration with Frederick Thomas.

Three barrier NW measurements
To be able to fully characterize the three barrier NWs (Fig. 2 right), the design of the devices was adapted to a two terminal structure with two side gates, where these side gates should

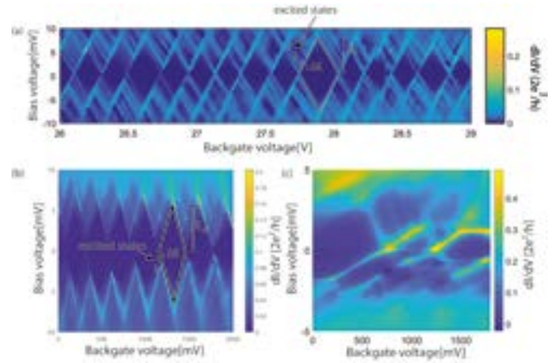

Fig. 3 a, b Measured differential conductance as a function of bias and gate voltage in a segment containing a QD. Addition energies of 6-8 meV were observed with a QD level spacing of 400-700 μeV. The extracted values are consistent over multiple wires. (c) Differential conductance measured on a pure InAs segment. Though the pattern resembles a QD, the observed structure is irregular and caused by "soft" potential well.

tune the eigenstate in the left and right QD. By measuring the differential conductance while sweeping the electrical potential of the two side gates, a honeycomb pattern, characteristic of a DQD system should be obtained.

Unfortunately, electrical transport measurements performed on the three barrier NWs at 270 mK so far have only shown signatures of a single QD.

In order to elucidate the origin of the single QD behaviour and to extract some characteristic energy values, charge stability measurements were performed (Fig. 4). From the difference in energy level spacing from 4a to 4b (~5 meV to 500 μeV), it is likely that the QD measured for 4b is much larger than the QD shown in 4a. The difference in measured values suggests that one QD is not defined by the InP barriers. A likely explanation could be over etching at the source-drain contacts during fabrication.

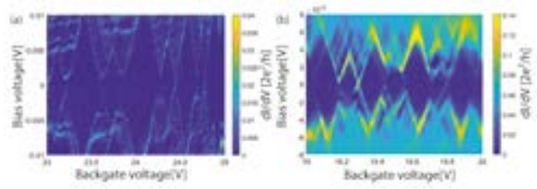

Fig. 4 a Charge stability diagram measured on a three barrier NW. A clear single dot structure is observed. A charging energy of 4-5 meV and an energy level spacing of 4-5 meV could be extracted. (b) The same measurement on a different wire shows a similar structure. The extracted values for the charging energy are still 4-5 meV, the energy level spacing although is only 500 μeV. This discrepancy is likely due to one dot not being defined by the InP barriers.

Outlook
Further measurements on the three barrier NWs are necessary to understand why only 2 barriers can be seen in electron transport measurements. Possible explanations include overgrowth of the barriers with InAs and band bending at the heterostructure interface, with the latter one being the most likely option. Furthermore the fabrication recipe has to be improved to reduce over etching at the contacts. Once the electrical properties of the DQD are known first experiments probing phonon interaction will be performed. Then one DQD will be used as a phonon detector, while the phonon emission will still be provided by other means, e.g. heating and/or optical excitation.

References

[1] B. Li, L. Wang, G. Casati, *Negative differential thermal resistance and thermal transistor*, Appl. Phys. Lett. **88**, 143501 (2006)

[2] L. Wang and B. Li, *Thermal Logic Gates: Computation with Phonons*, Phys. Rev. Lett. **99**, 177208 (2007)

[3] Y.-Y. Liu, J. Stehlik, C. Eichler, M. J. Gullans, J. M. Taylor, J. R. Petta, *Semiconductor double quantum dot micromaser*, Science **347(6219)**, 285-287 (2015)

[4] S. Roddaro, A. Pescaglini, d. Ercolani, L. Sorba, F. Beltram, *Manipulation of Electron Orbitals in Hard-Wall InAs/InP Nanowire Quantum Dots*, Nano Lett., **11(4)**, 1695-1699 (2011)

Few layer semiconducting MoS_2 with superconducting contacts

Project P1701: Van der Waals 2D semiconductor nanostructures with superconducting contacts
Project Leader: A. Baumgartner and C. Schönenberger
Collaborator: M. Ramezani (SNI PhD Student), K. Watanabe, and T. Taniguchi

Introduction

The goal of this project is to identify a layered two-dimensional semiconductor, ideally with a large spin-orbit interaction, suitable for electronic device fabrication, and to develop superconducting contacts for this material. Such a new semiconductor platform might form the basis for many fundamental experiments, replacing the well-established semiconducting nanowires to facilitate more complex device architectures, or replacing MBE grown heterostructures, for which superconducting contacts are extremely challenging. Recently, superconducting contacts to graphene have been established and intensively studied [1, 2], and also results on layered semiconductors have been reported [3-5]. In the first year of this project we aim to adapt similar methods to electrically contact molybdenum di-sulfide (MoS_2) with a superconductor and maintain a similar material quality.

Methods and normal metal contacts

The fabrication of high-quality electronic devices based on atomically thin material layers typically requires extra considerations to suppress oxidation of the material and to reduce contamination. To achieve this goal we established a recipe and procedure to stack materials inside a new glovebox with a N2-atmosphere (partial pressures of H_2O and O_2 < 0.1 ppm). Figure 1 shows a photograph of the glovebox installed in spring 2018, featuring a state of the arts optical microscope and a commercially available transfer stage for stacking layered materials.

First, we established normal metal electrical gold contacts to a few-layer MoS_2 flake in a geometry with bottom contacts, where 30 nm thick and 200 nm wide metallic leads are fabricated on top of a Si/SiO_2 wafer using electron beam lithography and thermal metal deposition, which is then cleaned using an atomic force microscope. A pre-fabricated stack of few layers of MoS_2 (~4-5 atomic layers) and of hexagonal boron nitride (hBN) is then deposited on top of the contacts, which established a partially encapsulated active MoS_2 layer. In an additional electron beam lithography step a top gate (TG) is fabricated to tune the electron density (the Si-wafer is rather ineffective as a gate because it is shielded by the bottom contacts).

The devices are then characterized first at room temperature and then at 4.2 K. For these devices we find a field effect mobility of up to 800 cm^2/Vs at an electron density of 3 x 10^{12} cm^{-2}, similar [5, 6] or slightly smaller [7] than in the most recent published results.

MoRe/Pt superconducting contacts

In a second step we used the same device fabrication scheme to fabricate superconducting bottom contacts. For this we replaced the Au leads by MoRe with a Pt capping layer using the sputtering technique in a UHV system. An optical microscopy image of such a device is shown in the inset of figure 1.

MoRe is a superconductor with a critical temperature on the order of 10 K and a second critical field on the order of 8 T [2], which allows us to perform first electrical characterizations of such a device at a temperature of 1.5 K in a variable temperature insert. The inset of figure 2 shows the two-terminal differential conductance as a function of the top gate voltage. At low gate voltages, the current is zero and increases at fairly large positive gate voltages, suggesting a population of the conduction band and an increase in the electron density. However, the top gate also tunes the relatively large contact resistance, possibly due to the formation of a Schottky barrier. The device characteristics show a roughly linear dependence on the gate voltage in the interval $6<V_{TG}<8$ V, expected for a dominating channel resistance, which gives a lower bound for the electron mobility.

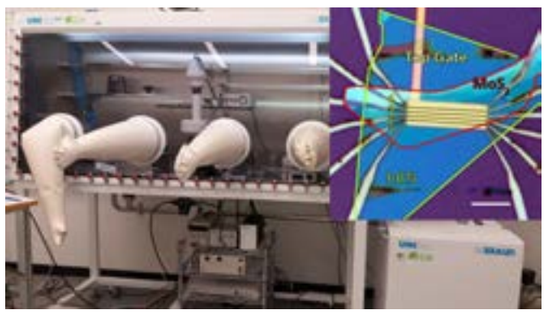

Fig. 1 Photograph of the glovebox and transfer system. Inset: optical microscopy image of a typical MoS_2 device. The scale bar is 5 µm.

We speculate that at $V_{TG}>8$ V the channel resistance is strongly reduced and the total resistance dominated by the contact resistance. In four terminal measurements (not shown) we find a minimum contact resistance of ~3 kΩ.

A typical experiment to demonstrate superconducting contacts is to perform bias spectroscopy measurements at different magnetic fields. A set of preliminary data is shown in figure 2, where we plot the differential conductance, G, as a function of the applied bias voltage, V, at a top gate voltage of +9V, for a series of magnetic fields B applied perpendicular to the device plane. At B=0, we find a pronounced suppression in the differential conductance. We speculate that this suppression might be due to the superconducting gap Δ in the contacts. In this case, the apparent gap in the transport, $4\Delta/e \sim 6$ mV, would be slightly larger than observed in devices based on carbon nanotubes, possibly due to the large series resistance of the Schottky barrier. At higher magnetic fields, the depth of this gap decreases and the shape of the curves become rather non-ideal. These effects require further investigation, but might already be taken as first indications of superconducting contacts to MoS_2.

Outlook

Our current devices establish contacting schemes and material properties, as well as the fact that we can already fabricate devices of a complexity larger than possible in semiconducting nanowires, e.g. multi-terminal lateral devices (not shown here). We expect that it will be straight forward to use the same techniques to fabricate fully hBN encapsulated active semiconductor layers to increase the carrier mobility. In parallel, we will also work on cleaner bottom contact surfaces by improving the sputter deposition process, which should lower the contact resistance considerably. As a major next step we will use the more established superconductor Aluminium with the now established Pt top layer, which should allow us to unambiguously proof superconducting effects in our devices.

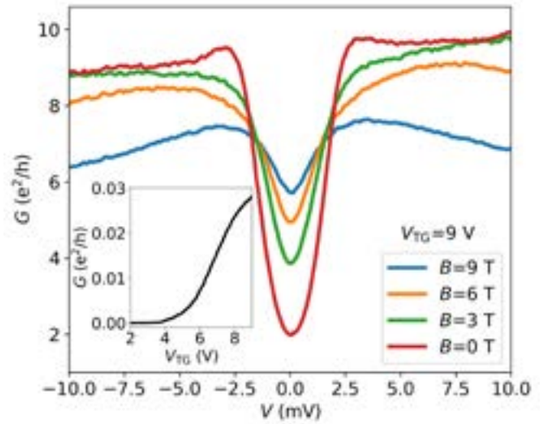

Fig. 2 Differential conductance G as a function of the applied bias voltage V, for the indicated magnetic fields B, applied perpendicular to the device plane and a top gate voltage of 9 V. The inset shows G as a function of top gate voltage V_{TG} at zero bias.

References

[1] I. V. Borzenets, et al., *Ballistic graphene Josephson junctions from the short to the long junction regimes*, PRL **117**, 237002 (2016)

[2] D. I. Indolese, R. Delagrange, P. Makk, J. R. Wallbank, K. Wanatabe, T. Taniguchi, C. Schönenberger, *Signatures of van Hove singularities probed by the supercurrent in a graphene-hBN superlattice*, arXiv:1805.10184 (2018)

[3] D. A. Bandurin et al., *High electron mobility, quantum Hall effect and anomalous optical response in atomically thin InSe*, Nature Nanotechnol. **12**, 223 (2017)

[4] X. Cui et al., *Multi-terminal transport measurements of MoS2 using a van der Waals heterostructure device platform*, Nature Nanotech. **10**, 534 (2015)

[5] R. Pisoni, Z. Lei, P. Back, M. Eich, H. Overweg, Y. Lee, K. Wanatabe, T. Ihn, K. Ensslin, *Gate-Tunable Quantum Dot in a High Quality Single Layer MoS2 Van der Waals Heterostructure*, arXiv:1801.00452 (2018)

[6] K. Marinov, A. Avsar, K. Watanabe, T. Taniguchi, & A. Kis, *Resolving the spin splitting in the conduction band of monolayer MoS2*, Nature Comm. **8**, 1938 (2017)

[7] R. Pisoni et al., *Interactions and magnetotransport through spinvalley coupled landau levels in monolayer MoS2*, arXiv:1806.06402 (2018)

Grayscale lithography for nanofluidic device fabrication in the context of neurogenerative diseases

Project P1702: Single organelle size sorting by a nanofluidic device
Project Leader: Y. Ekinci and H. Stahlberg
Collaborator: T. Mortelmans (SNI PhD Student), X.-D. Li, and T. Braun

Research context
Currently, despite the substantial progress made towards the unraveling the multi-faceted disease pathology of Parkinson's disease, the exact cause of the disease still has to be confirmed [1]. Moreover, in a clinical setting, it is not always possible to diagnose the disease at an early stage of development. This causes a delay between disease onset and treatment. Also, it should be pointed out that there is no curative therapy available [2]. Therefore, it is of great importance to further ameliorate our understanding of the disease progression and pinpoint its origin.

The role of mitochondrial dysfunction in the onset of Parkinson's' disease has been well-established [3–5]. In addition, it is suggested that there is a shift in their size and density distribution attributed to mitochondrial alterations [6]. As such, a device that enables to quantify these changes would provide researches with valuable insights to understand the underlying bio-mechanisms.

In this context, nanofluidic devices have gained increasing interest in the field of biomedical research because of their rapid sample processing, low sample volume required and precise fluid control [7–9]. To this extent, the focus of this PhD-work is to develop a nanofluidic device which allows for accurate manipulation, particle trapping or monitoring of single organelles.

At present, the fabrication of nanofluidic devices largely depends on the employment of templating procedures. Herein, the master structure is synthesized via 3D-lithography, such as two-photon polymerization and e-beam lithography and transferred into a polymer substrate [10–12]. However, each adjustment in device design requires a novel master to be made, which is a time-consuming process. Grayscale lithography via direct laser writing is an alternative and very promising patterning technique, which enables quick changes to the device layout while retaining a high writing speed and adequate resolution.

In this annual report, the first steps which were taken towards the synthesis of such a device are presented. More specifically, the versatility of the fabrication procedure was explored by patterning a high-dynamic range photoresist with a variety of 3D-features. The obtained protocol paves the way for further device fabrication and possible elucidation of neurodegenerative disease profiles.

Results and discussion
A key difference between standard binary lithography and grayscale lithography is the behavior of the resist material. In binary lithography, a high-contrast is wanted, however, in grayscale lithography, a linear relationship between exposure dose and development rate is of importance [13]. Moreover, to allow for the synthesis of 3D-structures, such as the nanofluidic sorter, there must be a spatial difference in delivered dose. The MicroWriter ML3 Baby, which is a tabletop Laser Pattern Generator (LPG) provided by Durham Magneto Optics allows doing so by correlating the blue intensity of each pixel in an RGB-image. The higher the blue intensity (0-255), the higher the dose.

The versatility of this fabrication procedure was explored by patterning complex 3D-features as shown in figure 1. Pyramids, spheres, and whirlpools with a width of 100 µm were easily obtained. The smallest achieved width with a reasonable resolution was 25 µm (not shown). The optimization of the various parameters achieved in this process will enable to pattern the envisioned device structure with the highest precision allowed by equipment constraints. However, it should be noted that the stitching errors were found to be rather significant, with an average of 1.2 µm lines.

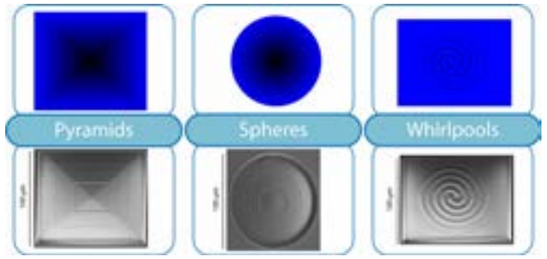

Fig. 1 Complex 3D-Patterns (pyramids, spheres, and whirlpools) designs for grayscale laser lithography and respective SEM-images.

Eventually, once the proof-of-principle is obtained with respect to the size sorting abilities of the device, a bridging stage is required to bridge the gap between 'nano' and 'bio' as can be seen in figure 2. To this extent, liposomes will be used. These are spherical molecules consisting of a lipid bilayer and they therefore approximate the elasticity of biological components while retaining a less complex shape. Moreover, because of their hydrophilic core and hydrophobic intramembrane space, it is possible to encapsulate a wide range of hydrophilic as well as hydrophobic fluorophores, allowing to accurately monitor their position in the device via confocal microscopy. The information obtained with respect to the elastic behavior of these liposomes will allow to modify the device in such a manner that biological components, such as mitochondria, can be more easily sorted.

Once the gap is bridged, a suitable cell-line has to be chosen. Therefore, as a primary cell culture of dopaminergic neurons has a limited scale, it is of interest to use a different cell-type as model to monitor the mitochondrial size and density distribution. To this extent, lund human mesencephalic (LUHMES) cells, which can be easily differentiated to have a similar properties as a primary cell-line, will be used. Furthermore, by incubating them with α-synuclein particles, a cellular Parkinson's disease model is obtained [14].

To summarize, the presented laser lithography method allows for rapid 3D structures to be synthesized and permits for rapid nanofluidic device prototyping. Nevertheless, present machine errors (such as the stage-stitching) place certain limitations on the accuracy of the fabrication procedure. Therefore, for future work, it is of interest to resolve the present shortcomings by postprocessing procedures the resist material by chemical or thermally reflow to smoothen out the stitching errors. Additionally, alternate methods of nanofabrication will be explored to achieve the desired profile with low roughness and high reproducibility.

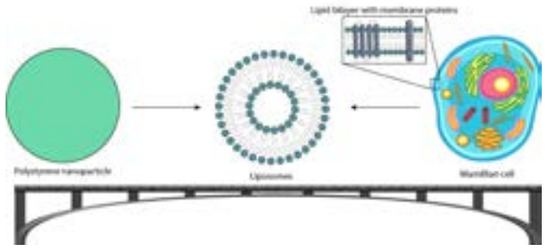

Fig. 2 Strategy to bridge the gap between the 'nano' and 'bio'. Fluorescent polystyrene particles will be used for the proof-of-principle of the device to prove its size sorting capabilities.

References

[1] S. Przedborski, *The two-century journey of Parkinson disease research*, Nat. Rev. Neurosci. **18**, 251–259 (2017)

[2] W. Poewe, et al., *Parkinson disease*, Nat. Rev. Dis. Prim. **3**, 1–21 (2017)

[3] J.-S. Park, R. L. Davis, C. M. Sue, *Mitochondrial Dysfunction in Parkinson's Disease: New Mechanistic Insights and Therapeutic Perspectives*, Curr. Neurol. Neurosci. Rep. **18**, 21 (2018)

[4] S. H. Shahmoradian, et al., *Lewy pathology in Parkinson's disease consists of a crowded organellar membranous medley*, bioRxiv 137976 (2017) doi:10.1101/137976

[5] E. M. Simcox, A. Reeve, D. Turnbull, *Monitoring mitochondrial dynamics and complex I dysfunction in neurons: implications for Parkinson's disease*, Biochem. Soc. Trans. **41**, 1618–1624 (2013)

[6] A. Bose, M. F. Beal, *Mitochondrial dysfunction in Parkinson's disease*, J. Neurochem. **139**, 216–231 (2016)

[7] T. S. Santra, F. G. Tseng, *Micro/nanofluidic devices for single cell analysis*, Micromachines **5**, 154–157 (2014)

[8] K. Zand, T. Pham, A. Davila, D. C. Wallace, P. J. Burke, *Nanofluidic platform for single mitochondria analysis using fluorescence microscopy*, Anal. Chem. ***85***, 6018–6025 (2013)

[9] M. A. Gerspach, N. Mojarad, T. Pfohl, Y. Ekinci, *Glass-based geometry-induced electrostatic trapping devices for improved scattering contrast imaging of nano-objects*, Microelectron. Eng. **145**, 43–48 (2015)

[10] A. A. Yazdi, et al., *3D printing: an emerging tool for novel microfluidics and lab-on-a-chip applications*, Microfluid. Nanofluidics **20**, 1–18 (2016)

[11] M. C. Moolman, Z. Huang, S. T. Krishnan, J. W. J. Kerssemakers, N. H. Dekker, *Electron beam fabrication of a microfluidic device for studying submicron-scale bacteria*, J. Nanobiotechnology **11**, 12 (2013)

[12] J. Friend, L. Yeo, *Fabrication of microfluidic devices using polydimethylsiloxane*, Biomicrofluidics **4**, (2010)

[13] M. Guillorn, M. Guillorn, *Laser Direct Write Grayscale Photolithography*, Sci. York 46–47 (2005)

[14] X. M. Zhang, M. Yin, M. H. Zhang, *Cell-based assays for Parkinson's disease using differentiated human LUHMES cells*, Acta Pharmacol. Sin. **35**, 945–956 (2014)

Directed evolution of affinity proteins for biomedical applications

Project P1704: Evolving Protease Enzymes with New Sequence Specificity using Peptide-Hydrogel Cell Encapsulation
Project Leader: M. Nash and S. Reddy
Collaborator: J. López Morales (SNI PhD Student)

Evolution of new affinity scaffolds

During biological evolution, iterated mutation and natural selection provide solutions for challenges that organisms face in the natural world. However, the traits that result from natural selection only occasionally overlap with features of biomolecules that are sought by humans for engineering applications and/or therapeutic purposes. In order to guide molecular evolution and access useful artificial properties more frequently, directed evolution in the laboratory has been used to mimic natural evolution. Here, a diverse library of genes is translated into a corresponding library of proteins and screened/selected for functional variants in a manner that maintains the correspondence between genotype (genes) and a desired phenotype (proteins and their functions). These functional mutant genes are replicated and serve as starting points for subsequent rounds of diversification and screening. Over many generations, these beneficial mutations accumulate, resulting in a successively improved phenotype for specific biological events. Here, we aim to enhance protein receptor-ligand interactions using directed evolution for biomedical applications.

First, a protein-engineering approach was used to increase the possibilities of enhancing the desired properties of a cohesion (Coh) domain. This domain has been reported to form a complex with its corresponding ligand with outstanding stability, and is also highly resistant to unfolding under mechanical tension. The biophysical properties of this domain can therefore be considered ideal.

We are undertaking various bioinformatic analyses for efficient library design, focused on effective residue site-saturation and while keeping WT bias. Here, structural motifs of crystallized homologous protein domains are maintained, such that the inner core formed by highly hydrophobic residues and surrounded by an outer core of mostly aliphatic maintain a strong cluster of hydrogen bonding interactions that prevent the newly designed mutant molecules from unfolding. In addition, a mechanical clamp motif, an Ig-like fold, topology with a reinforced third β-sheet, a ligand-binding site and suitable exposed loops are all features that were identified and maintained during mutagenesis for function or structural conservation. Further analysis included solvent-accessible surface area (SASA) of amino acids located in flexible loop regions to determine what positions are prone to mutations and which should be conserved as WT bias. Moreover, an extensive phylogenetic analysis by a multiple alignment of related molecules from different species included the conservation and sequence identity percentage, strand propensity, hydrophobicity and the buried index to identify mutagenesis-allowing or -forbidding secondary structure and motifs. A more detailed phylogenetic analysis was performed on the residues of the selected loops to observe key residues to preserve the stability of the protein while having permissive positions for evolution efforts. Finally, loop length variability analysis among several homologous domains was performed to verify the influence of the number of residues in each loop and their role in stability. All these data were integrated (Fig. 1), and a focused-library design was obtained.

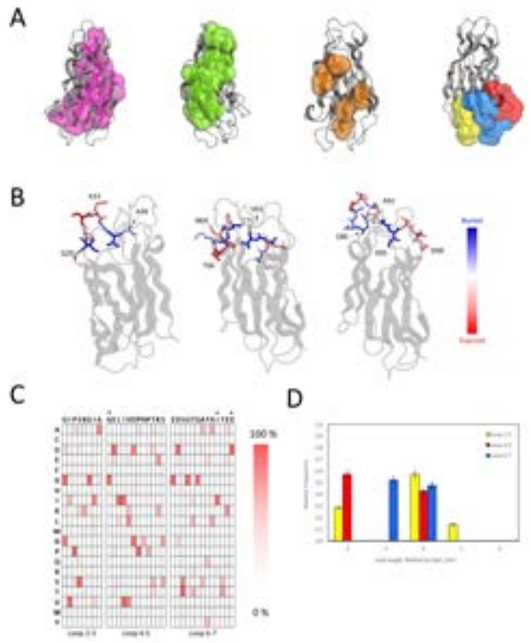

Fig. 1 Bioinformatic analysis of mechanically strong proteins. A. Structural motif recognition in crystallized Cohesin (Coh) domains. B. Identification of residues prone to mutations in exposed loops by solvent-accessible surface area (SASA) analysis. C. Phylogenetic alignment of position variability and frequency of residues in exposed loops of Coh. D. Length variability of exposed loops of Coh.

Once the focused library was designed, diversity generation of Coh took place by means of molecular cloning and wide site-saturation mutagenesis on residues of the selected loops using oligo-based in vitro gene assembly and overlap extension polymerase chain reactions (PCRs). Briefly, short single stranded DNA fragments of the Coh gene with complementary sequences were annealed to form larger double-stranded DNA fragments. The desired mutations were introduced in desired multiple positions using degenerate codon sequences to maximize the variability while reducing undesired products. Complementary flanking regions in the fragments allowed the assembly of even larger fragments in repetitive PCR reactions to ultimately yield complete synthetic Coh gene constructs. The constructs were finally cloned into the desired plasmid of interest by Gibson isothermal assembly to generate randomized Coh libraries, confirmed by sequencing purified plasmids of selected bacterial clones.

As part of the screening method of Coh libraries, yeast surface display was employed as the carrier organism of full length and correctly folded Coh mutants due to the high efficiency of homologous recombination exploited for in vivo library cloning, its widespread use for directed evolution, and its easy manipulation during force analysis and measurements. The display system consists of genetically encoded mutant library plasmids thermo-chemically introduced into yeast cells. The plasmid contains a signal peptide and an AGA2P domain that translocates from the cell membrane to the cell wall and forms a complex with the anchored AGA1P via disulfide bridges, exposing therefore the C-terminal part of AGA2 and the mutant construct to the medium. The displayed Coh mutant contains different peptide sequences that can be labelled with fluorescent antibodies for imaging and flow cytometric analysis. Optimal expression conditions of constructs of interest were assessed by immunolabelling and cytometry, where 48 h of expression at 20 °C were found to be the best conditions for Coh display on yeast cells (Fig. 2).

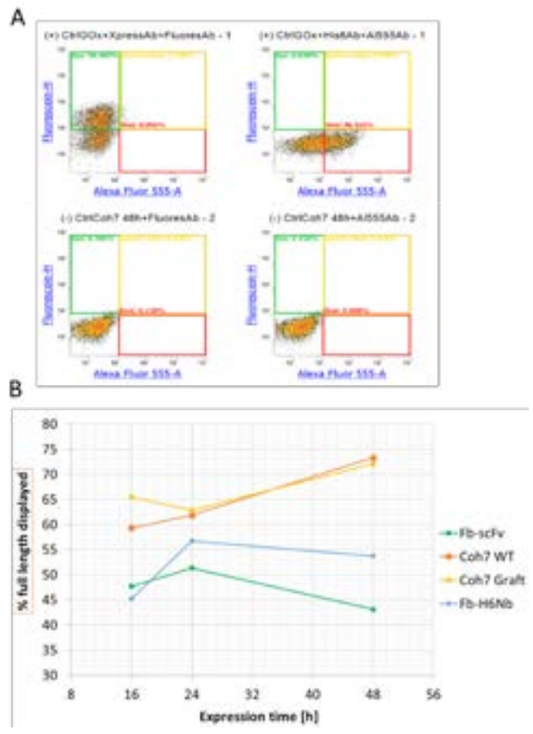

Fig. 2 Display analysis by immunolabelling/cytometry (A) and expression conditions (B) of Coh mutants.

The screening for enhanced variants of Coh will be done by means of a new high throughput screening (HTS) method (patent application anticipated) developed in the Nash lab for screening protein variants with resistance to hydrodynamic shear stress, which can be applied directly to yeast cells.

Mutant proteins that pass the screen will be individually characterized by DNA sequencing and by assessing their recombinant expression and purification yields. Furthermore, selected variants will be analyzed by atomic force microscopy-single molecule force spectroscopy (AFM-SMFS). In these experiments, ligands of interest will be functionalized on a surface and the mutant Coh will be functionalized onto a cantilever. The protein complex with the highest mechanical strength can be further analyzed with different pulling geometries and finally coupled to different biomedical applications, given that any ligand of interest can be used as a target where mechanical forces play a role during biological processes have high importance in disease developments and their treatments.

We envision that the outcome of this project will offer a molecule with biomedical impact in diseases that currently lack treatments or diagnosis tools; and an efficient platform for directed evolution of proteins within the rising field of mechanobiology.

References

[1] W. Ott, M. A. Jobst, C. Schoeler, H. E. Gaub, M. A. Nash, *Single-molecule force spectroscopy on polyproteins and receptor-ligand complexes: The current toolbox*, Journal of Structural Biology **197**, 3-12 (2017)

[2] M. Otten, W. Ott, M. A Jobst, L. F Milles, T. Verdorfer, D. A. Pippig, M. A. Nash, H. E. Gaub, *From genes to protein mechanics on a chip*, Nature Methods **11**, 1127–1130 (2014)

[3] T. Verdorfer, R. C. Bernardi, A. Meinhold, W. Ott, Z. Luthey-Schulten, M. A. Nash, H. E. Gaub, *Combining in Vitro and in Silico Single-Molecule Force Spectroscopy to Characterize and Tune Cellulosomal Scaffoldin Mechanics*, Journal of the American Chemical Society **139 (49)**, 17841–17852 (2017)

[4] E. T. Boder and K. D. Wittrup. *Yeast surface display for screening combinatorial polypeptide libraries*, Nature Biotechnology **15**, 553–557 (1997)

Towards label-free HTS in enzyme engineering

Project P1705: Genetic selection of nanocatalysts
Project Leader: S. Panke, P. S. Dittrich, and T. R. Ward
Collaborator: E. Rousounelou (SNI PhD Student)

Introduction

Natural enzymes are highly versatile and their diverse characteristics offer unique advantages for many applications. Nonetheless, in order for a natural enzyme to meet the criteria for a specific application, it needs to undergo alterations and improvements [1]. Although enzymes can be engineered via rational design, there are cases where evaluating large numbers of variants is of great interest, especially when there is limited biochemical and/or structural data available. In that context, protein engineering often mimics natural evolution and creates large variant libraries which are then screened to identify those with desired properties [2]. Consequently, there is a need for genotype-to-phenotype linkage which is often respected by compartmentalization to spatially separate the library members, while miniaturizing the compartments and accelerating the screening [3]. Moreover, screening efforts require an assay where the enzymatic activity of the variants is coupled to a readout, which is often a change in optical properties (e.g., fluorescence or absorbance), usually via either substrate depletion or product formation [4]. Hence, it is typically required to either label the analyte or use an indicator reaction. However, an indicator reaction is usually of no industrial importance, as few biotechnologically relevant substrates carry fluorophores or chromophores, while, an optical readout is not always or easily related to a chemical reaction, thus making quantification of the reaction challenging [3]. This problem could be tackled by using label-free analysis methods, such as mass spectrometry (MS). MS reports the mass of the molecule and can observe each of the species present in a reaction, including the enzyme's substrate, the intended products and the unintended side-products. That leads to a more complete assessment of an enzyme's activity. However, its throughput is currently low when compared to label-dependent methods. Furthermore, owing to the destructive process of mass determination, it is associated with loss of the genetic information [5].

Considering the limitations of current analytical methodologies, this PhD works on the development of a novel label-free high throughput screening (HTS) method by coupling droplet-based microfluidics to MS. In this method, the genotype-phenotype connection will be retained via the novel strategy of peptide barcoding; thus, overcoming the genetic information loss during MS analysis. In figure 1, a simplified overview is illustrated. The first step is to generate a library of unique DNA and peptide barcode combinations, which are then identified via next generation sequencing (NGS). The second step is the generation of the enzyme variant library (e.g. via error prone PCR), followed by its subsequent cloning into the plasmid that carries the DNA and peptide barcodes (plasmid library). Therefore, at this step, each variant library will be associated with a unique combination of DNA and peptide barcodes. After the transformation of E. coli cells, the latter are individually encapsulated into droplets, followed by the transcription/translation of the peptide barcodes and the enzyme variants. Subsequently, the cells are lysed and the samples are incubated with one (or more) candidate substrate(s) and cofactor(s) for the the reaction to take place. The MS analysis of the sample delivers not only information about the product amount or distribution, but also its unique identity via the peptide barcode. Thus, after designing DNA primers specific to the DNA barcode that is uniquely associated with the peptide barcode of the variant, we can genetically retrieve the desired variant by PCR, from a pool of myriads of variants.

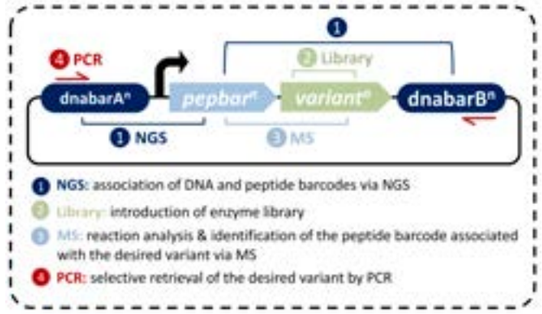

Fig. 1 Simplified overview of the proposed HTS method. For further information, refer to text.

Co-expression of peptide barcode & enzyme

The proposed method rests on the concomitant detection of a peptide barcode and the product in the MS-signal and the subsequent retrieval of the desired variant via PCR, using primers specific for the associated DNA barcode. Consequently, we need to ensure that a suitable peptide barcode is expressed at sufficiently high level in the cell that also expresses the enzyme variant of interest.

Although recombinant protein synthesis in E. coli is a standard method of genetic engineering, the synthesis of short peptides is not. One of the central reasons for that might be that short peptides are an important nutrient source in E. coli and therefore might be difficult to accumulate in the cytoplasm. This problem will be tackled from two ends: On the one hand, we will ensure that recombinant peptide production is as efficient as possible, and on the other hand we will, if required, attempt to delete the most important peptidases form the cytoplasm. Furthermore, the enzyme variant needs to be synthesized to a suitable level, so the reaction in question is sufficiently rapidly catalyzed for subsequent detection in the MS.

To ensure efficient peptide and protein synthesis, we will first investigate how the relative position of the peptide gene to the gene of the enzyme variant influences the expression of both genes. Four modular constructs were designed with the gene for an easily detected model protein (green fluorescent protein, GFP) and for the gene template of a peptide whose sequence was chosen randomly, implementing different possibilities to co-produced peptide and protein: protein fusion via protease hydrolysis site or separate expression and the gene for the peptide is positioned either upstream or downstream of the gfp gene. Finally, a fifth modular construct was designed in which the gene templates for GFP and the peptide sequence have opposite directions. A flag tag is fused to both peptide and GFP templates in order to facilitate their analysis via Western blotting. The modular design of the constructs will facilitate the investigation of different variants of this basic design, including variations of regulatory elements, positional details and gene orientations. Each design was inserted into a suitable plasmid and will be be investigated against different conditions.

DNA barcode library

While the peptide barcode identified from the MS-signal is supposed to uniquely identify the clone that is analyzed, the sample and with it the improved enzyme variant is still destroyed in the process. To retrieve the sequence of the enzyme, we need to map the peptide barcode information back to the specific plasmid from which it originated, and which is still available from a duplicate of the plasmid library. This mapping is achieved via linkage between a unique peptide barcode sequence and a unique DNA barcode sequence on the same plasmid. The unique DNA barcode can then be used to design PCR primers and selectively retrieve the gene in question from the duplicate library.

To implement the unique linkage between peptide and DNA barcode, each peptide barcode will be associated with two unique DNA sequences that flank the region for recombinant gene expression. Each of these flaking sequences is a random 40bp nucleotide sequence, ensuring a sufficiently large number of different sequences. The GC content of each of these random sequences is kept constant as part of the design and together with the sufficiently long nucleotide sequence of 40bp enable the design of primers with different melting temperatures, so that two primers with similar melting temperature can be designed for each plasmid.

As a proof-of-principle for the DNA barcode strategy, we will confirm our ability to retrieve specific genes from a sequence pool by retrieving the gene for yellow fluorescent protein (yfp) from a background of constructs carrying gfp. The two genes differ only in 5 point mutations, but the gene products can be easily told apart due to their different fluorescence properties. This way, we can create a realistic test scenario in which the outcome is not overly influenced by different sequences that need to be amplified. Furthermore, the success of the retrieval can be quantified; the PCR product will be cloned and expressed and the obtained plasmids can be rapidly investigated whether they contain the target gene or the background via fluorescence. Finally, the yfp template will be mixed by different ratios into the gfp background and we will determine the minimum ratio from which it can be robustly retrieved. This ratio might also determine the maximum library size.

Peptide barcode library

The peptide barcodes are the unique identifiers of the variant they are associated with. For that reason, it should be possible to link their mass profile unambiguously to a specific amino acid (aa) sequence and through that to a unique DNA barcode. Consequently, each peptide barcode should have a unique molecular mass. In cases where accurate mass determination is not sufficient to identify the peptide barcode, tandem fragmentation will provide detailed information of its sequence. Moreover, the theoretical and experimental diversity of the peptide barcode library should exceed vastly the total number of variants present in the library. This is going to be tackled by designing barcode sequences of medium-length (30-40 aa long) and/or by combining two or more peptides that together compose one peptide barcode.

The final design of the peptide barcode sequences will be devoid of methionines and cysteins, as they could cause oxidation and cross-linking, but will carry at least one proline residue to facilitate collision-induced fragmentation (CID)6. Finally, it will position one basic amino acid (K or r) at the C-terminal and/or at the N-terminal, but not at central positions, to increase gas-phase basicity and consequently, peptide ionization.

References

[1] M. Baweja, P. K. Singh, P. Shukla, in Frontier Discoveries and Innovations in Interdisciplinary Microbiology 207–212 (2015)

[2] A. K. Patel, R. R. Singhania, A. Pandey, in Biotechnology of Microbial Enzymes 13–41 (2017)

[3] M. Wójcik, A. Telzerow, W. J. Quax, Y. L. Boersma, *High-throughput screening in protein engineering: Recent advances and future perspectives*, Int. J. Mol. Sci. **16**, 24918–24945 (2015)

[4] J. D. Bloom, M. M. Meyer, P. Meinhold, C. R. Otey, D. MacMillan, F. H. Arnold, *Evolving strategies for enzyme engineering*, Curr. Op. Struct. Biol.**15(4)**, 447 (2005)

[5] M. Wleklinski, B. P. Loren, C. R. Ferreira, Z. Jaman, L. Avramova, T. J. P. Sobreira, D. H. Thompson, R. G. Cooks, *High throughput reaction screening using desorption electrospray ionization mass spectrometry*. Chem. Sci. **9**, 1647 (2018)

[6] P. Egloff, et al. *Engineered Peptide Barcodes for In-Depth Analyses of Binding Protein Ensembles* bioRxiv (2018)

Fiber-based cavity optomechanics

Project P1706: Ultrasensitive Force Microscopy and Cavity Optomechanics using Nanowire Cantilevers
Project Leader: M. Poggio and F. Braakman
Collaborator: D. Jäger (SNI PhD Student)

Introduction
Nanoscale mechanical resonators such as thin membranes or nanowire crystals have the potential to uniquely enrich the capabilities of force microscopy. Currently, force microscopy techniques rely heavily on micron-sized cantilevers as force transducing elements, such as silicon beams or quartz tuning forks. In recent years, a new direction has emerged that replaces these conventional cantilevers with bottom-up grown nanoscale structures, such as carbon nanotubes or nanowires. Their small size and nearly defect-free crystal structures leads to potentially record force sensitivities, low mechanical losses and high operation frequencies. Several experiments have recently demonstrated the potential and versatility of this approach. In our own lab, we have demonstrated a new type of force microscopy using nanowires, in which we have shown sensitivity not only to the magnitude of forces, but also their direction [1].

Furthermore, nanomechanical resonators enable fundamental studies into the hybridization of different physical quantities, such as light and mechanical motion. Such hybrid systems form a promising platform to implement measurements operating at the limits imposed by quantum uncertainty and quantum non-demolition measurements. They may also allow investigation of quantum decoherence mechanisms, entanglement, and ultimately the transition from quantum to classical physics. Nanowire heterostructures are particularly interesting hybrid systems, as they can combine excellent mechanical properties with bright optically active qubits in the form of embedded quantum dots. These qubits themselves already form interesting objects of study, as they are potentially very sensitive meters of localized electric and strain fields [2]. Moreover, when coupled to a mechanical degree of freedom, qubits can through their nonlinear character generate very large enhancement of the radiation pressure interaction between light and matter, as well as boost optical cooling of the mechanical resonator [3].

Preliminary experiments have laid bare several fundamental obstacles that currently limit the measurement sensitivity of nanowire mechanical oscillators and embedded optical emitters such as quantum dots. The collected signal in the form of photons reflected of the nanowires, or emitted by quantum dots, is very weak for the structures that hold the most promise (small nanowires, long-lived quantum dot excitations). Furthermore, studies of the quantum dots used in our experiments have thus far been limited due to the use of non-resonant excitation. Their broad emission linewidth (>25 μeV) severely limits quantum dot spectroscopy.

Our aim is to enable operation of nanowire mechanical resonators in regimes dominated by quantum effects, by improving optical excitation and detection of the nanowire and embedded quantum dots. To reach this goal, we will:

1: Integrate nanowire cantilevers into high-finesse optical cavities. Read-out of both the mechanical motion of the nanowires and of the photons emitted by embedded quantum dots can be much improved by placing the nanowire inside an optical cavity. Moreover, such a cavity allows to strongly couple the nanowire motion as well as quantum dots to the cavity light field. In particular, in the case of nanowires with embedded quantum dots this provides a straightforward path to the realization of a tri-partite hybrid system [3]. Such a hybrid system allows to significantly enhance optical cooling and will allow the observation and utilization of quantum states of motion.

2: Implement resonant excitation of quantum dots in a force microscopy setup. This will significantly reduce the optical linewidth of the dots and should allow for mechanical displacement sensitivity reaching the Heisenberg uncertainty limit.

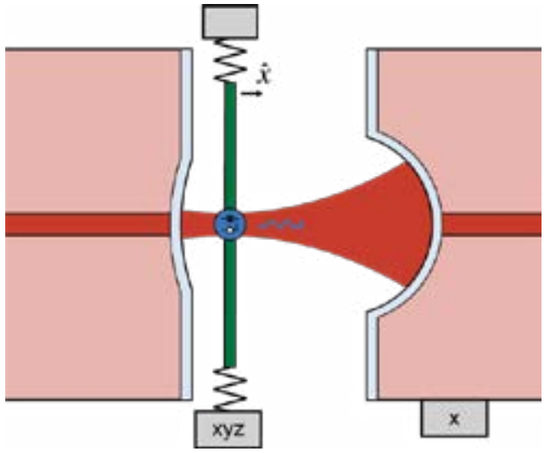

Fig. 1 Schematic drawing of a nanomechanical resonator and quantum emitter coupled to a high-finesse fiber-based optical cavity.

Optical Setup
In this first year, we have constructed an optical setup that serves as the basic platform for our experiments. The main elements of the setup are a highly tunable laser, two double-pass acousto-optic modulator units, and two low-noise photodiodes. The setup allows to insert two beams of light into an optical cavity with tunable frequency difference between the beams. The cavity can be measured through reflection or transmission. This will enable basic optomechanical experiments, such as optical cooling of a mechanical oscillator, as well as basic cavity QED experiments, allowing the measurement of a tri-partite hybrid system.

In addition to this setup, we have built a smaller optical setup that serves to test fiber cavities and to characterize single fibers with ablated concave mirrors. This allowed us to construct a first optical cavity, made with a fiber-based mirror on one side and a planar mirror on the other side (Fig. 2).

Ablation
We have made a set of 200 fibers with concave mirrors ablated on their cleaved facets. The concave dimples were produced with a laser ablation setup constructed earlier in collaboration with Prof. Richard Warburton. The set covers a large range of geometrical dimple parameters, which should allow the use

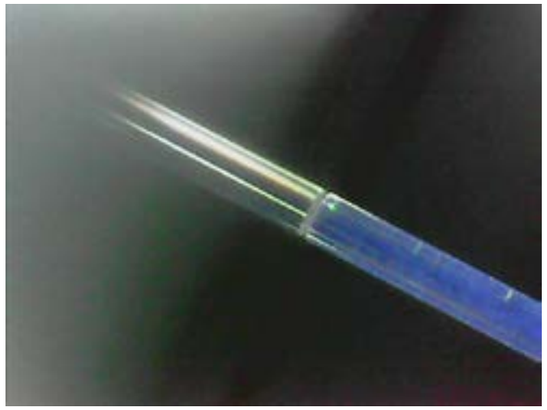

Fig. 2 A photograph of an fiber-based ablated concave mirror closely approached to a planar mirror. The resulting cavity allows us to measure the optical properties of our custom-made fiber-based mirrors.

of these fibers for various kinds of optical cavities. The fibers were coated with a highly reflective layer through ion beam sputtering by a commercial company (LASEROPTIK). In addition, we have developed a fabrication protocol to coat fibers with gold through thermal evaporation in-house. We have begun the characterization of these fibers with integrated concave mirrors in the test setup mentioned above.

Finally, we have submitted a manuscript on the optimization of single-shot laser ablation to produce mirror templates on fiber tips with geometrical parameters especially suitable for experiments in quantum electrodynamics and optomechanics [4].

Membranes
As first step towards creating a tri-partite hybrid system, we have started working with membranes made from flakes of two-dimensional materials. In particular, we focus on membranes of two-dimensional transition-metal dichalcogenides (TMDCs) and hexagonal boron nitride (hBN). Several TMDCs, including WSe_2, MoS_2, and $MoSe_2$ have been reported to contain optical emitters. These emitters have been shown to be single-photon sources. Such emitters can also be found in hBN, where lattice defects play this role.

We have made first steps towards integration of membranes of TMDC or hBN flakes with our fiber-based optical cavities. We follow two strategies: we either place the membrane directly onto the fiber surface, using a micromanipulator setup, or we use a separate holder to insert the membranes freely into the cavity. First trials have shown that it is feasible to place a flake directly on top of the fiber surface (Fig. 3).

hBN appears to be particularly promising. Optical emitters have been reported show single-photon emission at room temperature. Furthermore, hBN membranes are mechanical oscillators with favorable frequencies (MHz regime), low mass, and high quality factors. Finally, hBN can be etched directly by electron beams, allowing for straightforward patterning of flakes. This would for instance allow the fabrication of photonic crystals, trampoline resonators, or venting holes on the membranes.

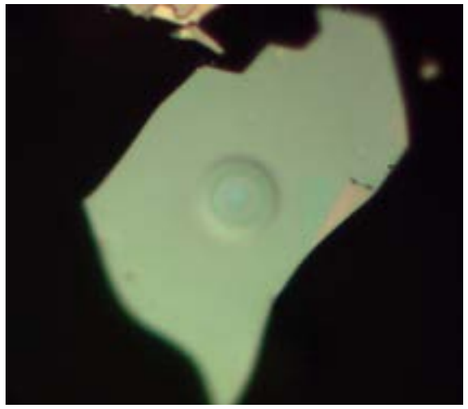

Fig. 3 Optical micrograph of a hBN flake which has been directly placed on top of a fiber-based ablated concave mirror.

References

[1] N. Rossi, F. R. Braakman, D. Cadeddu, D. Vasyukov, G. Tütüncüoglu, A. Fontcuberta i Morral, M. Poggio, *Vectorial scanning force microscopy using a nanowire sensor*, Nat. Nanotechnol. **12**, 150 (2017)

[2] M. Montinaro, G. Wüst, M. Munsch, Y. Fontana, E. Russo-Averchi, M. Heiss, A. Fontcuberta i Morral, R. J. Warburton, M. Poggio, *Quantum dot opto-mechanics in a fully self-assembled nanowire*, Nano Lett. **14**, 4454 (2014)

[3] J. Restrepo, C. Ciuti, I. Favero, *Single-Polariton Optomechanics*, Phys. Rev. Lett. **112**, 013601 (2014)

[4] T. Ruelle, M. Poggio, F. R. Braakman, *Optimized single-shot laser ablation of concave mirror templates on optical fibers*, arXiv:1811.11532 (2018)

Interlayer excitons in a $WSe_2/MoSe_2$ heterobilayer van der Waals heterostructure

Project P1707: Nano-photonics with van der Waals heterostructures
Project Leader: R. J. Warburton and I. Zardo
Collaborator: L. Sponfeldner (SNI PhD Student)

III-V semiconductor heterostructures are very often used for electrooptics applications as their properties can be engineered over a wide range. However, GaAs for instance does not form a native oxide. The dangling bonds at the surface pin the Fermi energy in the energy gap, resulting typically in a large electric field at the surface. This means that the active elements in an electrooptic device must be positioned relatively far from the surface. This in turn limits the feature size that can be created by an on-surface pattern: high spatial frequencies are lost at the buried active layer. A new class of semiconductor has emerged for which this problem does not arise. In a van der Waals heterostructure, a device is constructed from individual layers, for instance graphene, hexagonal-BN, $MoSe_2$, and so on. Due to their truly two-dimensional nature each constituent performs perfectly well in its monolayer form: there are no dangling bonds.

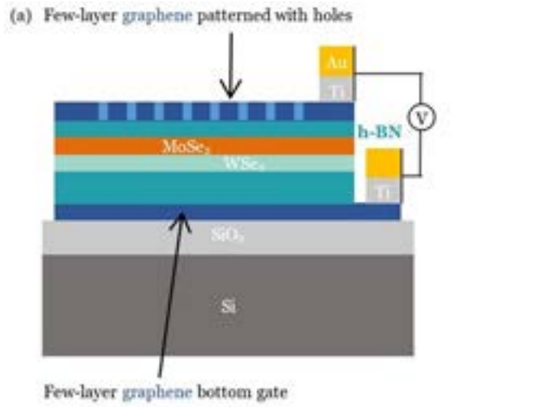

Fig. 1 (a) Schematic of the proposed van der Waals heterostructure with the aim of creating optically-active quantum dots. (b) Optical microscope image of the heterostructure.

In this project, semiconducting transition-metal dichalcogenide (TMD) heterobilayers consisting of $MoSe_2$ and WSe_2 are studied. These heterobilayers form a type-II band alignment which leads to an electron potential well in the $MoSe_2$ layer and a hole potential well in the WSe_2. The possibility arises of forming so-called interlayer excitons (IX) with a permanent dipole-moment and enhanced radiative-lifetime with respect to excitons in single monolayers [1]. By embedding encapsulated heterobilayers in a gated van der Waals heterostructure, where the top electrode is patterned by electron-beam lithography and plasma etching, we hope to create optically-active quantum dots utilizing the so-called quantum confined Stark effect. Figure 1a illustrates a schematic and figure 1 (b) shows an optical microscope image of an example heterostructure.

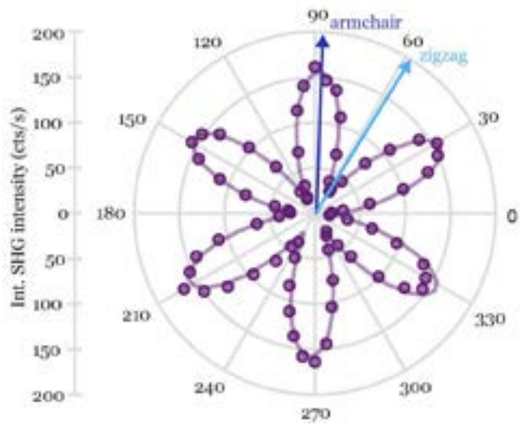

Fig. 2 Angle-resolved second-harmonic generation (SHG) intensity measured on a monolayer of encapsulated InSe. The underlying 6-fold crystal symmetry and its exact orientation is directly visible enabling the determination of the armchair and zigzag crystal-axes [2].

The interlayer coupling in the bilayer depends on the relative orientation of the crystal axes of the constituent monolayers. If the crystal axes of each monolayer are aligned along the same direction, the coupling is maximized. We determine the crystal orientation of the TMD monolayers with the help of angle-resolved second-harmonic generation (SHG). Figure 2 shows the angle-resolved SHG intensity measured on a monolayer of encapsulated InSe [2]. The SHG signal shows a strongly varying, 6-fold symmetry which correlates to the underlying crystal-symmetry of the monolayer InSe-flake. This experiment demonstrates that angle-resolved SHG is a fast, non-invasive tool to determine the crystal axes, not only for InSe, but also for other TMD monolayers [2]. With this method, we determine the crystal axis orientation of the $MoSe_2$ and WSe_2 monolayers and align them on fabricating the bilayer in order to achieve a good interlayer coupling.

Figure 3 shows the photoluminescence (PL) spectrum recorded from the area of the sample shown in figure 1b at a temperature of 4 K. At high energies, one can see the emission peaks from intralayer excitons in the two monolayers. The red-shifted peak, 200 meV below the $MoSe_2$ intralayer exciton peak, is identified as emission from the interlayer exciton (IX). Compared to the monolayer region, the emission from the intralayer excitons is quenched which indicates an efficient charge transfer between the layers.

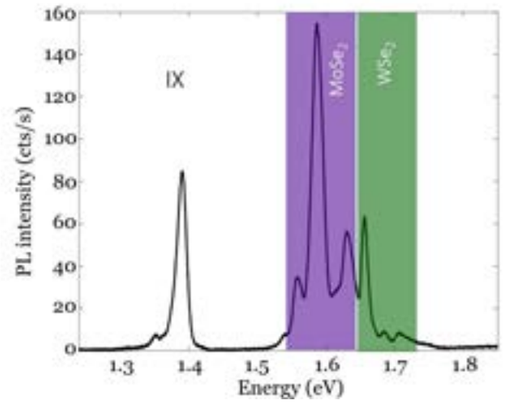

Fig. 3 Photoluminescence (PL) spectrum from the specific area of the heterostructure at a temperature of 4 K. The interlayer exciton (IX) emission energy is lower than the intralayer excitons in both $MoSe_2$ and WSe_2.

The advantage of this heterobilayer over individual monolayers lies in the response to a vertical electric field.

In an external electric field perpendicular to the two-dimensional layers, neutral and charged excitons experience an energy shift given by $\Delta E = -\mu z F z - \beta z F z^2$, where Fz is the applied electric field, μz is the excitonic dipole moment and βz is the excitonic polarizability. This effect is called the quantum-confined Stark effect (QCSE) [3].

This quantum-confined Stark shift has been measured for an encapsulated MoS_2 monolayer [4]. The neutral exciton PL emission energy as a function of the applied electric field for constant electron density is shown in figure 4a. Due to symmetry reasons, the dipole moment μz is zero, such that the QCSE scales quadratically with the electric field. Stark shifts of about half the homogeneous linewidth were achieved, which demonstrates that excitons can be polarized [4]. However, these energy shifts are quite small. Electrical control of excitons based on the QCSE requires much larger polarizabilities or a non-zero dipole moment.

In type-II TMD heterobilayers, the interlayer excitons exhibit a non-zero dipole moment. These dipole moments are also perfectly aligned perpendicular to the monolayers. Figure 4b shows the IX PL peak energy as a function of applied gate voltage. Here, the Stark shift is linear as the polarizability term is much smaller compared to the dipole moment term. The total energy shift is around 40 meV, which is much larger than the shift measured for monolayer MoS_2.

This large tuning range of the IX emission energy should allow us to trap an IX by creating a lateral variation of the vertical electric field. Our approach is to create nano-holes in the top few-layer graphene electrode. In a next step, we shall fabricate a heterobilayer heterostructure where each monolayer is electrically contacted allowing us to control the charge carrier concentration in each layer. By keeping the charge carrier density low, we hope to achieve an even larger QCSE shift.

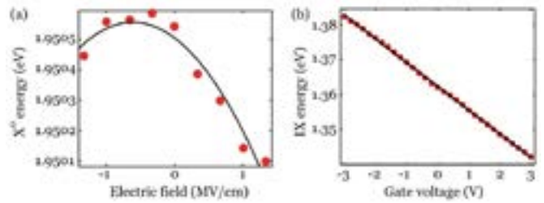

Fig. 4 (a) Neutral exciton energy (peak position) as a function of the applied electric field in a MoS_2 monolayer. The black line is a parabolic fit to the data [4]. (b) IX energy (peak position) as a function of applied gate voltage measured on the heterostructure region shown in figure 1 (b). The black line is a linear fit to the data.

References

[1] P. Rivera, et al. *Observation of long-lived interlayer excitons in monolayer MoSe2–WSe2 heterostructures*. Nat. Commun. **6**, 6242 (2015)

[2] N. Leisgang, J. G. Roch, G. Froehlicher, M. Hamer, D. Terry, R. Gorbachev, R. J. Warburton, *Optical second harmonic generation in encapsulated single-layer InSe*. AIP Advances **8**, 105120 (2018)

[3] D. A. B. Miller, D. S. Chemla, T. C. Damen, A.C. Gossard, W. Wiegmann, T. H. Wood, C. A. Burrus, *Band-Edge Electro-absorption in Quantum Well Structures: The Quantum-Confined Stark Effect*. Phys. Rev. Lett. **53**, 2173 (1984)

[4] J. G. Roch, N. Leisgang, G. Froehlicher, P. Makk, K. Watanabe, T. Taniguchi, C. Schönenberger, R. J. Warburton, *Quantum-Confined Stark Effect in a MoS2 Monolayer van der Waals Heterostructure*. Nano Lett. **18**, 1070-1074 (2018)

Freeform optics for LED lighting

Project P1708: Non-visual effects of LED lighting on humans
Project Leader: E. Meyer and R. Ferrini
Collaborator: T. Aderneuer (Associate SNI PhD Student)

Non-visual effects of LED lighting on humans
Nowadays most people spend the majority of their day inside, where they are exposed to artificial lighting. Professional lighting solutions are mainly provided by LED luminaires and their implementation will even increase. Noteworthy, the recently discovered non-visual photoreceptors, the so called intrinsically photosensitive retinal ganglion cells (ipRGCs), make light the most important Zeitgeber for circadian rhythms of our inner clock according to chronobiology experts [1]. Light is a powerful tool to trigger effects such as alertness, cognitive performance, mood and sleep-wake cycle. These non-visual effects are much less understood in contrast to visual effects of lighting on humans (e.g. glare and visual acuity). This shows the need to identify and optimize professional lighting conditions with respect to non-visual effects. Research focuses to resemble daylight spectrum and intensity. Investigation of the spatial variance of light though is very poorly covered scientifically.

The project aims to produce optimized illumination patterns for non-visual effects using freeform optical lenses or microlens arrays.

Analysis of metameric lighting
Before investigating the effect of spatial variation of lighting, the first step was to analyze the possibilities and limitations of spectral variations of light. State of the Art is to have an impact on the circadian rhythm by changing the color of lighting. Modification of the spectrum is of interest because the sensitivity of the ipRGCs is blue shifted compared to the visual photoreceptors. Our aim was to have a new approach by changing the spectrum but keeping the CCT (correlated color temperature) constant. Same white tone of 4000K but different composition of colors. This means using the concept of metamers: optical stimuli that are spectrally different but chromatically equivalent (i.e. perceived as same color). In order to develop a lighting solution which is accepted and implemented, it is important to consider good visual properties for sufficient color rendering.

Different spectral power distributions (SPDs) were generated by mixing the spectra of 5 colored LEDs. They were optimized for non-visual effects and restricted to have a sufficient color rendering quality. We applied the theoretical model suggested by Rea et al.: the circadian stimulus (CS) [2]. Circadian stimulus is a theoretical measure how much melatonin can be suppressed, the hormone which regulates our sleep-wake cycle. The resulting four SPDs are displayed in figure 1. We computed two scenarios: one only optimizing for circadian effect (SPD 1 & 2) and one optimizing for circadian effect as well as restricting to have a sufficient optical performance, namely a color rendering index above 80 (SPD 3 & 4).

A significant difference of the circadian stimulus can be achieved which is shown in figure 2.

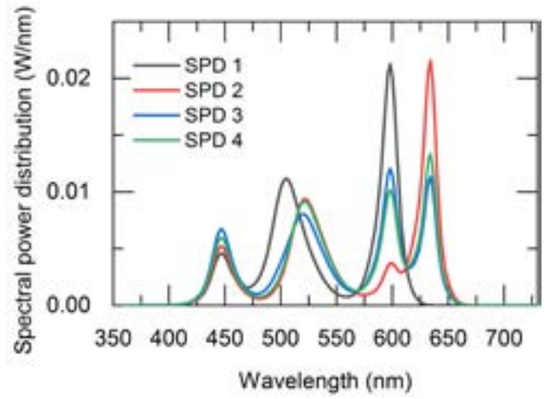

Fig. 1 Metamer LED combinations. The SPD are generated as a combination of 5 LEDs (red, yellow, green, verde, blue). SPD 1 & 2 are optimized for a non-visual effect only. SPD 1 has a min. CS (circadian stimulus), SPD 2 a max. CS, SPD 3 & 4 are optimized for a non-visual effect in addition to a restriction for good optical performance. SPD 3 has a min. CS, SPD 4 a max. CS while both have a CRI (color rendering index) above 80.

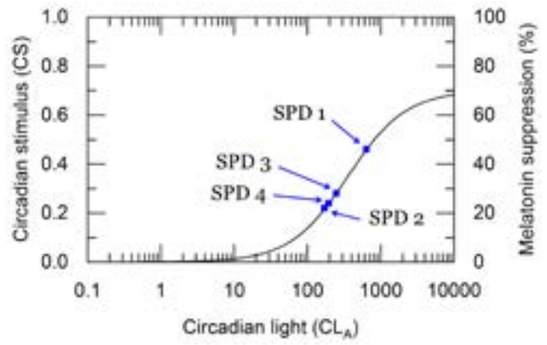

Fig. 2 The relative melatonin suppression as a function of circadian light. The difference of CS between SPD 1 and 2 is more than 0.2 while the difference between SPD 3 and 4 is below 0.05.

The effect is only achieved though in the expense of color rendering properties. As a consequence it can be assumed that it is not possible to create a metameric lighting solution that has a circadian effect and good visual quality at the same time. Thus a combination of spectral and spatial distribution of light is suggested.

Freeform optics for LEDs
To develop an innovative lighting solution and go beyond spectral light distribution it is promising to change the spatial distribution. Therefore our goal is to develop an optical structure that enables nonsymmetrical distribution of light, a so called freeform structure.

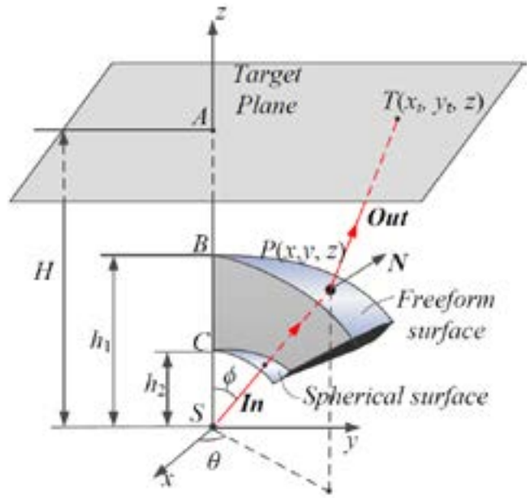

Fig. 3 Geometrical layout of freeform lens design [3]. A light source is placed at the origin S. A target illumination at a distance H is defined. Then point by point the shape of a surface in between is calculated which guides the light rays to the defined area.

The geometrical layout of such a beam shaping lens is shown in figure 3. Ray mapping methodology is used to compute the lens [3]. The idea is to have a defined target illumination and a light source at a specific working distance. It is then calculated how the optical structure in front of the light source has to be shaped. Figure 4 shows an example of a computed freeform lens, figure 5a and b show the respective target illumination and resulting illumination when testing the lens with a raytracing software.

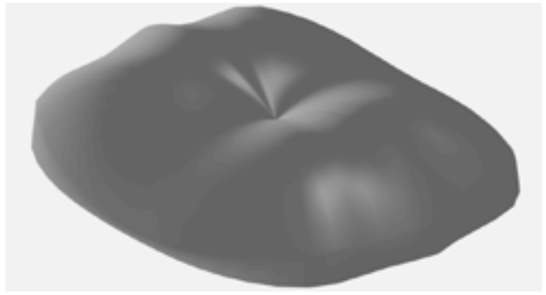

Fig. 4 Top view of computed freeform lens for the target illumination shown in figure 3a.

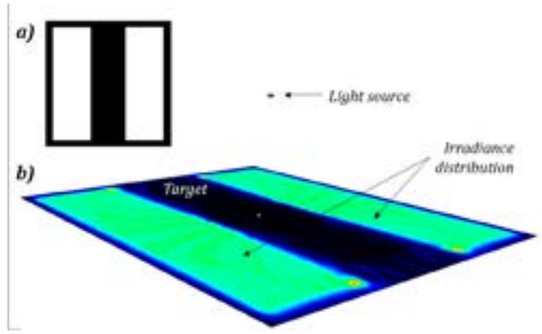

Fig. 5 a) Target illumination. b) Illumination resulting from freeform lens when tested with raytracing software.

The design of freeform lenses for LED light sources raises several challenges. For example to take account of extended light sources (in contrast to point sources), different intensity distributions (e.g. Lambertian, cosine, …), fabrication restrictions (e.g. no negative contact angles, thickness reduction),… Also computational challenges raise as the design needs to be processed with optical softwares for the proceeding fabrication steps.

Outlook
Future steps will include the fabrication and replication of the designed structures. At the end of the day our aim is to design a large scale lighting solution together with chronobiology experts. It is then to be tested in a laboratory study to investigate non-visual effects of spatial light distribution.

References

[1] C. Cajochen, S. L. Chellappa, Ch. Schmidt, *Circadian and light effects on human sleepiness–alertness*. Chapter 2 in Sleepiness and Human Impact Assessment, Springer, (2014)

[2] M. S. Rea, M. G. Figueiro, A. Bierman, R. Hamner, *Modelling the spectral sensitivity of the human circadian system*, Lighting Research & Technology **44**, 386–396 (2012)

[3] D. Ma, *Exploration of ray mapping methodology in freeform optics design for non-imaging applications*, The University of Arizona (2015)

Applicability of 3D electron diffraction in the pharmaceutical industry

Project A12.01: A3EDPI (PSI, University of Basel C-CINA, DECTRIS Ltd. Baden-Dättwil, Crystallise! AG Schlieren)
Project Leader: T. Grüne
Collaborators: S. De Carlo, H. Stahlberg, N. Blanc, and G. Steinfeld

Electron Crystallography as powerful extension to X-ray crystallography

3D electron crystallography has been developed in the past 1-2 decades by several research groups across the world. The technique determines the 3D atomic structure of chemical and biochemical molecules. It is very similar to X – ray crystallography but exchanges X-ray radiation with electron radiation. As a main consequence, the crystal size can be several orders of magnitude smaller. X-ray crystallography is widely used in many fields of chemistry. Many compounds are available as powder, but cannot be turned into crystals large enough for X-ray crystallography. With electron crystallography, crystal structures can be determined directly from the powder and even from heterogenous blends. Yet, before the nanoArgovia project A3EDPI, 3D electron crystallography was hardly known to chemists and appeared to be a niche technology. Hence, the main goal of A3EDPI was to evaluate whether electron crystallography can be productively used in the chemistry and pharmaceutical lab. The results show that electron crystallography is matured and complements X-ray crystallography. It is the technique of choice for all unsolved cases where crystal size is the limiting factor. The main results of A3EDPI were published in Angewandte Chemie Intl. Ed. [1]. These results caused an overwhelming reaction in the scientific community.

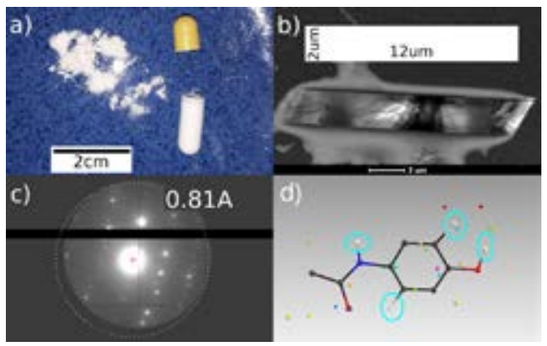

Fig.1 Structure of paracetamol from a blend of microcrystalline and non-crystalline compounds.

The prestigious journal Science selected the results as one of ten candidates for the break-through research results of the year 2018, and A3EDPI ranked fifth in the public voting. The success was amplified with a publication from UCLA [2] only a few weeks after with the same results – a head-to-head race led by A3EDPI.

Key to the A3EDPI project was the installation of an EIGER X 1M detector (DECTRIS Ltd.) [3] to transmission electron microscopes (TEM), kindly provided both by C-CINA (Uni Basel) and ScopeM (ETH Zurich). The unique specifications of this detector avoid several sources of errors: data can be collected under continuous rotation of the crystal. The detector is radiation hard so that the direct electron beam does not need to be shielded. The installation of the EIGER X 1M created an electron diffractometer that enabled productive structure determination. The performance of the diffractometer was demonstrated by two different results. Figure 1 shows a capsule of the commercial cold medicine Grippostad®. The powder is composed of several crystalline and non-crystalline compounds. The microcrystals (Fig. 1b) appear large in the electron microscope, but they are too small for conventional X-ray crystallography. With electron radiation, the tiny crystal diffracts to atomic resolution (Fig. 1c), and identifies the compund as paracetamol (Fig. 1d). As second result, the structure of a new methylene blue compound was determined from a thin crystalline needle less than 1 µm wide (Fig. 2). Not only is this a very complex structure ever solved with electron crystallography - the structure was determined within only 4 hours. Such a speed is expected from modern X-ray facilities. Hence A3EDPI proved the applicability of electron diffraction and places this method on par with X-ray crystallography.

In addition to these two published results, A3EDPI also determined a third important structure from the energy sector in collaboration with Crystallise! AG, with a patent pending.

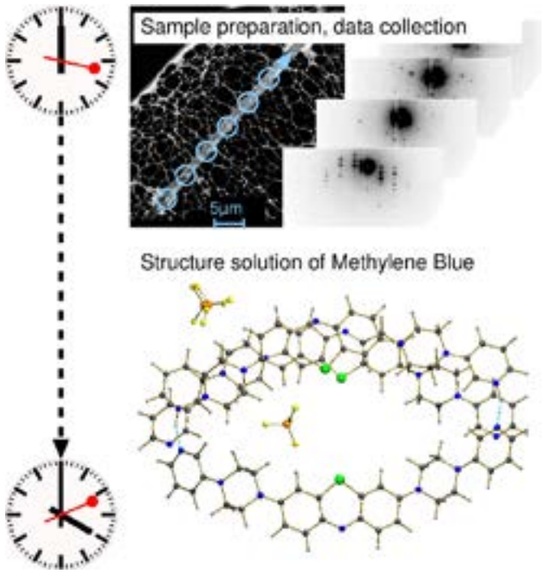

Fig. 2 Structure solution of a new methylene blue derivative proves electron crystallography a powerful extension for every X-ray facility.

Nanotechnology for a 3D view

A complete crystallographic data set requires the crystal to be rotated by 180°. This is not possible with electron diffraction, because the sample holder inevitably shades the electron beam from the sample in certain orientations. For complete data, data sets from several crystals would have to be merged. However, as many crystals have a flat appearance, such data sets only repeat the same region of the reciprocal (“crystal”) space.

A3EDPI presents two solutions for this problem. One is based on ultra-thin nylon fibres that create a disruptive “jungle” for the crystals. The other one curls the carbon layer of the sample holder. In both cases, a very small number of crystal was sufficient to create complete data sets (Fig. 3). Both solutions are easy to realise and future structure solutions have no more excuse for incomplete data, and A3EDPI increases the reliability of electron diffraction studies.

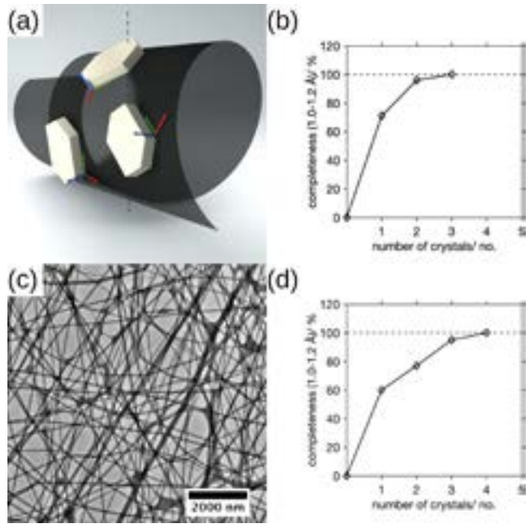

Fig. 3 A3EDPI solutions to the missing wedge problem: Coiled carbon provides a selection of different orientations. Nano-nylonfibres disrupt the surface of the sample holder.

Nanoprecision for the next generation diffractometers:

A3EDPI created a prototype electron diffractometer and proved its maturity for structural chemistry. While several structures were determined with high accuracy, the project also located limitations of current instrumentation. The success of the experiments not only required mounting the EIGER X 1M to the electron microscope, but also neat solutions to control the data collection process and access to the parameters required for data collection. These solutions are described in a separate manuscript. They also locate the next bottleneck to address: a sample goniometer with nanometer precision. Mechanically such solutions already exist [4] and only need to be adapted to electron microscropes – maybe the next nanoArgovia project.

References

[1] T. Gruene et al., *Rapid Structure Determination of Microcrystalline Molecular Compounds Using Electron Diffraction*, Angew. Chemie Intl. Ed., **57**, 16313-16317 (2018)

[2] C. G. Jones, M. W. Martynowycz, J. Hattne, T. J. Fulton, B. M. Stoltz, J. A. Rodriguez, H. M. Nelson, T. Gonen, *The CryoEM Method MicroED as a Powerful Tool for Small Molecule Structure Determination*, ACS Cent. Sci., **4**, 1587–1592 (2018)

[3] G. Tinti, E. Fröjdh, E. van Genderen, T. Gruene, B. Schmitt, D. A. Matthijs de Winter, B. M. Weckhuysen, J. P. Abrahams, *Electron crystallography with the EIGER detector*, IUCrJ, **5**, 190-199 (2018)

[4] S. Waltersperger et al., PRIGo: a new multi-axis goniometer for macromolecular crystallography, J. Synchrotron Radiat., **22**, 895-900 (2015)

The atomic structure of a large protein complex from less than 1 µl cell lysate

Project A12.10: MiPIS (University of Basel C-CINA. FHNW Muttenz, leadXpro AG Villigen)
Project Leader: T. Braun
Collaborators: M. Hürzeler, M. Chami, M. Hennig, M. Botte, C. Schmidli, L. Rima, and T. Stohler

Introduction
Direct electron detection cameras for electron microscopes (EM) introduced a fast and lasting change to structural biology and are now regarded as a standard method for the structural analysis of protein-complexes to atomic resolution. However, protein isolation techniques and sample preparation methods for cryo-EM remain a bottleneck.

For a high-resolution analysis of proteins by the cryogenic EM (cryo-EM) single-particle approach, only 10'000 to a few million individual protein particles must be imaged. Therefore, microfluidic technologies can provide enough protein complexes for the structural investigation of proteins by cryo-EM [1].

Here we present a method for (i) the microfluidic isolation of an untagged protein from less than 1 µL of lysate from eukaryotic cells [2], (ii) the direct and blotting-free preparation of the cryo-EM grid [3, 4], (iii) the collection of high-resolution data using cryo-EM, (iv) the reconstruction of a 3D mass-density map of the protein complex with a resolution below 4 Å, and (v) the modelling of the 3D structure with an atomic model.

Protein isolation and cryo-EM grid preparation
Figure 1 shows the principles of the microfluidic protein isolation and cryo-EM grid preparation. We use 'fragment antigen binders' (Fab) to recognize and extract untagged target proteins from the raw cell lysate. We covalently modified the Fab fragments with a photo-cleavable cross-linker ending with a biotin moiety, which strongly binds to the streptavidin functionalization of the magnetic bead (Fig. 1A). Figure 1B shows the principles of the microfluidic protein isolation: First, the cell lysate is incubated with Fab fragments. Then paramagnetic, streptavidin coated particles are added to bind the biotinylated Fab fragments. From this solution, a volume of approx. 900 nL is aspirated in the microcapillary. The paramagnetic particles are immobilized by a magnetic field gradient generated with two electromagnets (Fig. 2). Therefore, only the Fab target-proteins are trapped while other proteins can be washed away. The photo-cleavable crosslinker, connecting the Fab to the magnetic bead, is cracked by UV light, resulting in a 20 nL eluate. The isolated protein is directly used to prime two cryo-EM grids, while the magnetic particles are retrained in the microcapillary. For cryo-EM grid preparation, the integrated cryoWriter set-up was used, allowing a virtually lossless grid preparation without paper blotting [2, 3].

Incubation of the cell lysate with Fab fragments and the magnetic beads is the time limiting step. Therefore, we do not incubate in the micro-capillary, but in small containments allowing the multiplexing of the isolation process. After the incubation of the cell lysate, all processing steps are performed in the same microcapillary tip, minimizing sample transport and avoiding unspecific binding of the isolated protein to the containment. Figure 2 shows the embodiment of the magnetic trap and the integration of the protein isolation module in the cryoWriter set-up.

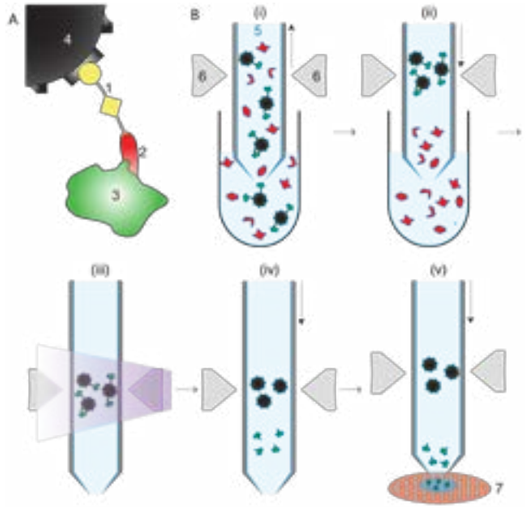

Fig. 1 Principles of microfluidic protein isolation and cryo-EM grid preparation. A) Composite material for 'protein fishing.' A photo-cleavable biotin linker (1) is covalently attached to a Fab (2) capturing the target protein (3). The biotin moiety of the linker binds to streptavidin-coated magnetic particles (4). B) Protein isolation work-flow. (i) The magnetic beads are incubated with biotinylated Fab fragments and cell lysate to capture the target structures (green). An approx. 0.9 µL volume of sample is aspirated into the microcapillary (5). (ii) The magnetic beads are immobilized in the magnetic trap (6). Non-bound lysate components (red) are flushed away. (iii) Illumination with UV light breaks the cross-linker. (iv) Separation of the capturing magnetic bead and the eluted proteins. (v) The isolated target proteins are directly deposited on a cryo-EM grid (7) for vitrification. Vertical arrows indicate the pump direction.

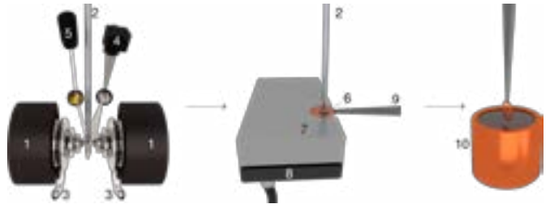

Fig. 2 Integration of protein isolation module in the cryoWriter set-up. The electromagnetic trap consists of two magnets (1) aligned with opposite poles to each other. A water-cooling system (3) controls the temperature of the electromagnets. A camera (4) allows the monitoring of the capillary and the magnetic-bead trapping. A UV-light emitting diode (LED, 5) enables photo-cleavage of the linker (see Fig. 1). After protein isolation, the capillary nozzle is moved above a cryo-EM grid (6). The 'dew point stage' (7) tightly controls the cryo-EM grid temperature with the connected Peltier element (8). The microcapillary primes the cryo-EM grid, leaving a thin layer of the isolated protein eluate on the grid. In the end, the cryo-EM grid is removed by the tweezers (9), flipped by 90°, and vitrified by plunging the sample into a container filled with liquid ethane (10).

The human 20S Proteasome
We isolated the untagged human 20S Proteasome form less than one µL cell lysate and prepared two cryo-EM grids from the 20 nL eluate. The 3D map of the protein complex has overall a resolution of less than 4 Å. However, the resolution of the attached Fabs is significantly lower than the resolution of the target protein-complex. The 3D mass density map allowed the modeling of all 14 subunits of the protein-complex as shown in figure 3.

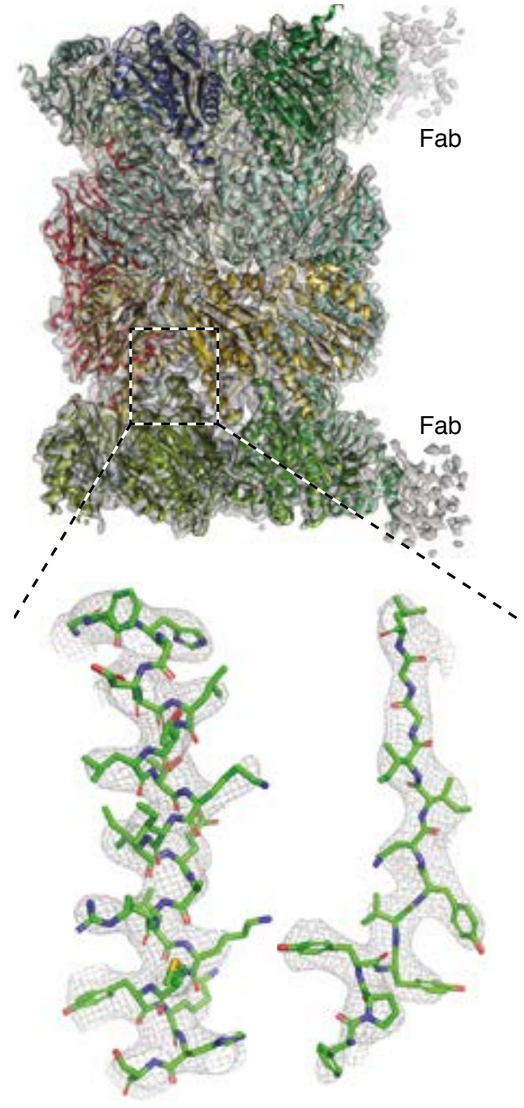

Fig. 3 Side view of the 3D mass-density of the human 20S Proteasome. For all 14 subunits, an atomic model is shown with different color. Two exemplary helices are depicted below. Note that the human 20S proteasome only exhibits a C2 symmetry. (Figure courtesy of C. Schmidli (C-CINA)).

We added TMV particles to the elution buffer as a positive control for the cryo-EM grid quality and solved the TMV structure at a resolution of 2.5 Å resolution. Our results show shows that the cryoWriter set-up can provide cryo-EM grids suitable for generating high-resolution structures (Fig. 4).

Fig. 4 Mass density volume of the Tabak mosaic virus (TMV) at a resolution of 2.5 Å. The virus particles were added to the elution buffer as positive control for the grid preparation.

Conclusions
The results demonstrate that the cryoWriter system allows (i) the isolation and preparation of target proteins from a tiny amount of starting material in a brief time, and (ii) to gain high-resolution cryo-EM data allowing the building of atomic models of the target protein.

References
[1] S. A. Arnold, S. A. Müller, C. Schmidli, A. Syntychaki, L. Rima, M. Chami, H. Stahlberg, K. N. Goldie and T. Braun, *Miniaturizing EM sample preparation: Opportunities, challenges and "visual proteomics"*, Proteomics **18**, 1700176 (2018)

[2] D. Giss, S. Kemmerling, V. Dandey, S. Stahlberg, T. Braun, *Exploring the inter-actome: microfluidic isolation of proteins and interacting partners for quantitative analysis by electron microscopy*, Anal. Chem., **86**, 4680–4687 (2014)

[3] S. A. Arnold, S. Albiez, A. Bieri, A. Syntychaki, R. Adaixo, R. A. McLeod, K. N. Goldie, H. Stahlberg, and T. Braun, *Blotting-free and lossless cryo-electron microscopy grid preparation from nanoliter-sized protein samples and single-cell extracts*, JSB **197**, 3 (2017)

[4] C. Schmidli, L. Rima, S. A. Arnold, T. Stohler, A. Syntychaki, A. Bieri, S. Albiez, K. N. Goldie, M. Chami, H. Stahlberg, T. Braun, *Miniaturized Sample Preparation for Transmission Electron Microscopy*, JoVE **137**, e57310 (2018)

Plasmonic nanoscale retarder controlled with liquid crystals

Project A12.13: PlasmoRetarder (CSEM Muttenz, PSI, Rolic Technologies Ltd. Allschwil)
Project Leader: B. Gallinet
Collaborators: L. Driencourt, R. Ferrini, D. Kazazis, Y. Ekinci, F. Federspiel, and R. Frantz

Surface plasmon resonances in metallic nano-structures enable the confinement and manipulation of the electromagnetic field well below the diffraction limit, thus opening new paradigm for optical devices. This project aims for developing an active filter whose transmitted color can be electrically tuned. This is achieved by design and fabrication of plasmonic nanostructures showing a strong and spectrally narrow birefringence effect. The color transmitted through the plasmonic retarder can be actively controlled by liquid crystals.

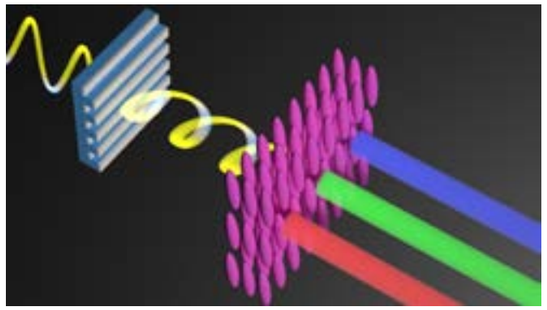

Fig. 1 Plasmonic retarder between in a polarizer and a liquid crystal based polarization analyzer, allowing to generate a variety of colors as a function of the voltage applied to the liquid crystal cell.

The basic working principle of the device developed in the project is shown in figure 1. A plasmonic phase retarder between crossed polarizers can generate different colors in transmission when it is placed between crossed polarizers, where the output polarizer (the analyzer) is mechanically rotated in order to generate these different colors [1]. The plasmonic phase retarder consists of a period array of deep-subwavelength metallic nanowires, in order to have a stable optical response as a function of the incidence angle. The light polarized across the nanowires (TM) excites a plasmonic resonance, while the other polarization (TE) does not induce a resonance. Here, a first entrance polarizer prepares the incident light in a polarization state oriented at 45° from the nanowires orientation. A phase retardation between TM and TE polarization yields an elliptically polarized light in transmission. A polarization analyzer based on liquid crystal cells allows to project the transmitted light onto a polarization state whose orientation depends on the applied voltage. Interferences between the different birefringent contributions lead to a color effect. As a result, the transmitted light has different colors depending on the applied voltage.

A periodic grating master over an area of 30x30 mm² has been fabricated. In order to avoid diffraction effects, the grating must have a sub-wavelength period of 160 nm with a duty cycle of ~0.3, which gives a linewidth of ~50 nm. Moreover, the grating needs to have low line edge roughness, be mechanically stable, and its height should be on the order of 120 nm, which are requirements for the nanoimprint process. We chose electron beam lithography (EBL) as the patterning technique, as it can easily fulfill all the above requirements. In addition, the EBL tool that was used, had a low field stitching error of ~20-30 nm for fields of 320 µm. A 100 mm Si wafer was

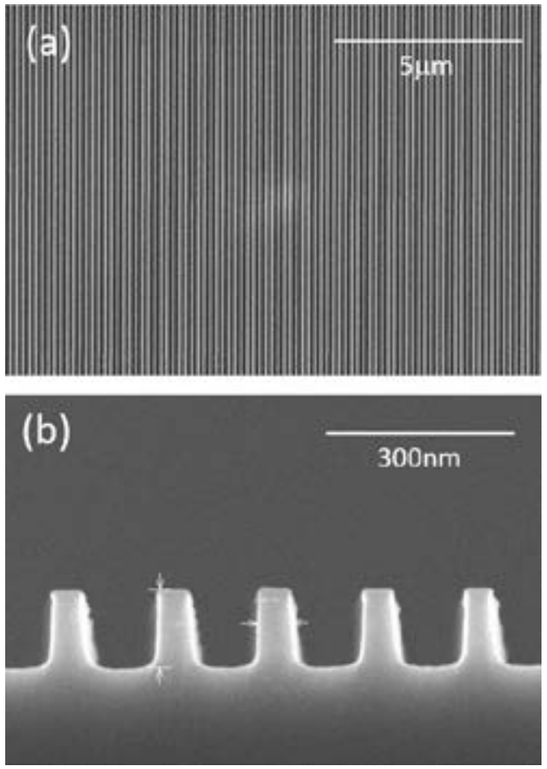

Fig. 2 Scanning electron micrographs of the grating master. (a) Large area view. (b) Cross section.

initially covered with 20 nm of Cr in a blanket deposition by electron beam evaporation. A thin ~100 nm PMMA layer was subsequently spin-coated onto the Cr layer and exposed by EBL. The wafer was developed in an MIBK:IPA 1:3 solution and the pattern was then transferred from the PMMA layer onto the Cr layer by plasma etching of the Cr (Cl-based plasma). The PMMA layer was subsequently stripped in an acetone bath and the grating pattern was transferred into the Si wafer by inductively coupled plasma reactive ion etching (ICP-RIE) at a very low pressure of 8 mTorr and a temperature of 5oC. A mixture of C4F8 and SF6 was used in a 3:1 ratio, which resulted in a well-controlled and anisotropic etch. Finally the Cr mask was removed by Cl-based plasma etching. A top view scanning electron micrograph (SEM) of the final Si master is shown in figure 2a showing the uniformity of the lines over a large area. Figure 2b shows a cross section of the 120 nm high grating etched into the Si wafer.

A plasmonic phase retarder has been fabricated by UV-nanoimprint of the grating master and evaporation of a silver thin film, followed by an encapsulation. The resulting structure is sketched in figure 3a. Ellipsometric measurements have been performed by ROLIC to measure the phase retardation between the transmitted TM and TE fields (Fig. 3b). A strong

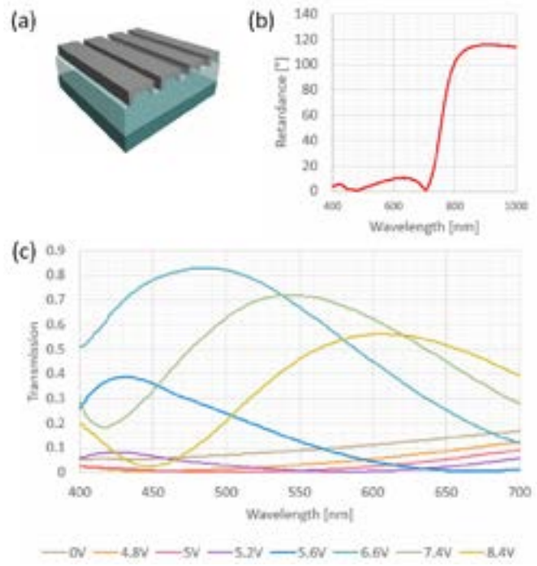

Fig. 3 (a) Plasmonic phase retarder made of a deep subwavelength array of silver nanowires. (b) Measured phase retardance between polarization along and across the wires. (c) Transmittance spectrum in the visible range in combination of a liquid crystal cell as a function of the applied voltage.

phase variation is observed at the plasmon resonance at 750 nm. This phase behavior for a thickness below 100 nm cannot be obtained from phase retarders based on form birefringence. Placed between a polarizer oriented at 45° from the nanowires orientation and a liquid crystal cell, the transmission spectrum of the plasmonic phase retarder can be tuned with the voltage applied to the liquid crystal cells (Fig. 3c). For a low voltage, up to 4 V, the polarization transmitted through the liquid crystal cell is oriented along the gratings lines. For a voltage of 6 V, the light transmitted through the liquid crystal cell is oriented across the grating lines and the resulting spectrum has a dip in transmission, which is the signature of a plasmon resonance at 725 nm. The resulting transmission peak at 450 nm is at the origin of the blue color and is further enhanced by a Michel-Lévy color. At a voltage of 8 V, a full rotation of the polarization by 180° has been spanned but the resulting spectrum has an additional peak at 600 nm compared to the spectrum at 4 V, which takes its origin from another Michel-Levy interference.

The corresponding colors are shown in the CIE plot of figure 4a. A large range of colors can be spanned using this approach. Compared to a system where the analyzing polarization is rotated mechanically, the colors are similar for a low voltage up to 5.5 V and diverge for higher voltages. The different originates from the appearing of Michel-Lévy colors in the birefringent liquid crystal cells. Therefore, only a voltage of 8 V is enough to scan a large number of different colors. In figure 4b, different colors have been selected at particular voltages, showing in particular that orange, magenta, purple, blue, turquoise, green and yellow can be obtained. Further colors ranging from orange to more saturated purple and blue can be obtained for higher voltages (from 9 V to 20 V), corresponding to a larger contribution of the Michel-Lévy interference colors.

They are similar to the ones obtained in the range from 5 V to 5.5 V. However, these colors require more time to be generated which reduces their applicability to a display device with high frequency.

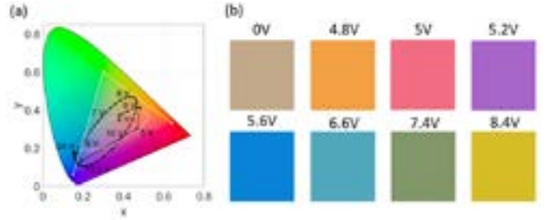

Fig. 4 (a) CIE plot of color range spanned by the system. White: colors obtained by mechanical rotation of an analyzing polarizer. Black: colors obtained by increasing the voltage applied to the liquid crystal cell from 0 V to 20 V. (b) Colors at particular voltages.

In summary, we performed the design, fabrication and characterization of plasmonic phase retarders with spectrally narrow phase variations. Starting with the fabrication of a high resolution master using electron beam lithography, an upscalable nanoimprint and thin film coating process flow has been used to fabricate the plasmonic retarders. We have shown the tunability of their transmitted colors using liquid crystal cells, which paves the way towards their implementation in displays [2]. In particular, a range of 8 V is enough to span already a large gamut of transmitted colors.

References

[1] L. Dümpelmann, A. Luu-Dinh, B. Gallinet, L. Novotny, *Four-fold color filter based on plasmonic phase retarder*, ACS Phot. **3(2)**, 190 (2016)

[2] L. Shao, X. L. Zhuo, J. Wang, *Advanced Plasmonic Materials for Dynamic Color Display*, Adv. Mater. **30(16)**, 1704338 (2018)

3D printable nanoporous Cellophil® membranes for tissue regeneration applications

Project A12.17: 3D Cellophil® membrane (FHNW Muttenz, University of Basel HFZ, CIS Pharma AG Bubendorf)
Project Leader: U. Pieles and F. Koch
Collaborators: S. Stübinger and Ch. Geraths

Introduction
The project aims for the development of a 3D printable membrane composed of the new biocompatible polymer family "Cellophil®" and gradients of hydroxyapatite to be utilized in a 3 D printing process on a RegenHu Bioprinter. The functional membranes are crosslinked during the printing process to achieve a polymer network, with a barrier function on one side and a porous structure on the other side of the membrane allowing cells to grow and the tissue to regenerate. Furthermore the membrane will be functionalized by e.g. growth factors to assist the regeneration process. The immobilization of the selected factors will be accomplished by non-covalent interactions by so called coiled-coil peptides, where one coil is attached to the membrane and the other coil to the factor. These peptides interact with each other by building up a super-coiled conformation. The super-coiled conformation shows strong ionic and hydrophobic affinities (K_d up to 10^{-10}). The peptides will be produced by genetic engineering and expressed in E. Coli. After purification further chemically functionalized allowing the immobilization of growth factor and to the membrane respectively. Because the binding is based on non-covalent interaction the immobilization of the growth factors will take place under very mild conditions and is universally applicable. Furthermore the number of bound molecules can be controlled very precisely.

Synthesis of pre-polymer hydrogels
In the first part of the project a suitable set of different pre-polymers was synthetized utilizing RAFT polymerization and a bifunctional RAFT linker which was designed and synthesized in course of the project. In order to make use of the immobilization strategy based on coiled-coil peptides the pre-polymers where chemically modified allowing the immobilization process via click-chemistry.

In a subsequent step of the project, CIS Pharma has successfully established a protocol for the generation of pre-polymeric hydrogels (membranes) with variable mechanical properties. Although the formed membranes were stable during extended washing procedures, they tend to dissolve slowly under cell culture conditions (DMEM, 37°C). This dissolution process was reduced by increasing of crosslinker concentrations and decreasing Cellopohil® content. However, the reduced Cellophil® content resulted in lower biocompatibility. Moreover, the integration of hydroxyapatite nanoparticles failed due to too strong absorbance/reflection of UV light.

Therefore, an alternative crosslinking strategy based on direct polymerization of Cellophil® monomers, conventional co-monomers & bifunctional crosslinker was established. Into this new type of membrane, hydroxyapatite nanoparticles have been successfully integrated without interference of the polymerization process.

The resulting three-layered membrane was stable under cell culture conditions. Since reaction solution had a too low viscosity for a 3D printing process without extremely high concentration of supporting polymers, the production process was changed to a molding process. The molding process was optimized in regard to different crosslinking degrees in the three-layered setup. For this purpose, three different crosslinker densities were used (Fig. 1).

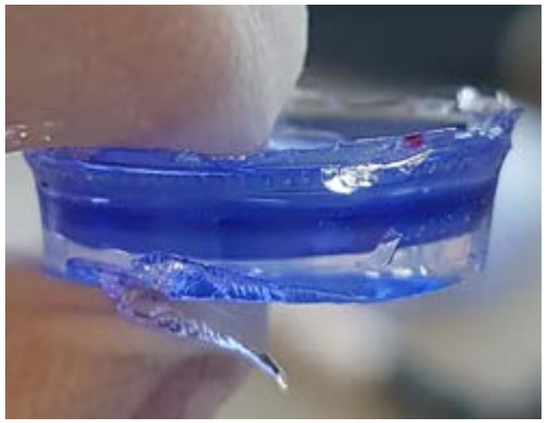

Fig.1. Blue colored layers with variable crosslinking degree.

Expression of ACID and BASE coiled-coil peptides
The expression "coiled-coil" designates a protein structure motif. Proteins and their functions are determined by their three-dimensional structure, which occurs by folding processes performed by many natural proteins. The first and simplest form of protein folding is the α-helical coiled coil. Therefore, those interactions are among the best-understood motifs, so such structures are often main objects for protein studies [1, 2]. In the context of the project, coiled-coil peptides are used to stimulate cell growth in an indirect way. Thereby, one coil is bound to a scaffold surface and one coil is connected to a growth factor, such as BMP. The two coils will form a supercoil (coiled-coil) by non-covalent interaction. As the sequences of the coiled-coil peptides contain also a MMP-2 cleavage site, a controlled release of the growth factor from the surface of the scaffold will be ensured.

The plasmid coding for the coiled-coil peptide (ACID) was obtained from CIS Pharma AG. Coil peptide BASE was created by cloning reaction between the synthetically ordered sequence for the coil BASE (Geneart, Thermo Fisher Scientific) and the backbone of the plasmid coding for ACID using the same restriction enzymes EcoR1 and Nde1 for both reactions. Ligation was performed over night with T4 DNA Ligase for increased efficiency and maximum yield.

Transformation reactions were conducted using heat shock treatment of NEB5α competent E.coli to obtain high amount of plasmid DNA. Due to an ampicillin resistance marker on the plasmid, selection of successfully transformed bacteria was possible on ampicillin LB agar plates. The sequence of the plasmids (ACID and BASE) was confirmed by sequencing (Synergene Biotech), the peptide sequence (ACID and BASE) and His-Tag (for protein purification) as well as the enzymatic cleavage sites in the fusion protein is necessary, as solely expression of the coiled-coil peptides is, due to small size, not possible.

Finally, plasmids were transformed into BL21 E.coli strains for expression. After culture reached suitable cells density protein expression was induced with Isopropyl-β-D-thiogalactopyranoside (IPTG). The bacteria in the culture were lysed with detergents in combination with ultrasound. After high speed centrifugation, the supernatant, containing the soluble protein fraction, was collected and purified with Ni-NTA-based chromatography package material on Profinia Affinity Chromatography Protein Purification System by Bio-Rad. In course of the project the peptide production process will be further optimized and utilized in the non-covalent modification process of the 3 D printed Cellophil® membranes.

The transformation protocol of plasmids, designed in a previous step, was further optimized to achieve higher protein yields. Purification was optimized on an Ekta Express FPLC system. Subsequently SDS PAGE was performed, confirming high purity of proteins (Fig. 2).

The expression enhancer protein was subsequently cleaved by protease digestion. Analysis of cleaved coiled-coil peptides was performed by SEC and LC-MS analysis and correct mass was verified.

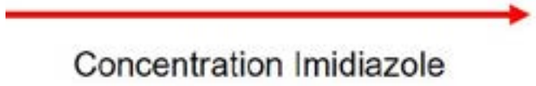

Fig. 2 Purification of coiled coil peptides by Ekta Express FPLC system. Fractions were further analyzed by SDS page. Red circle indicate the expressed protein construct.

Proof of Concept Coiled-coil interaction
In order to demonstrate coiled-coil interaction, coiled-coil BASE was immobilized on a gold QCM-D sensor by its n-terminal thiol group. Subsequently interaction was proven by a shift in frequency in QCMD by incubation with coiled-coil ACID (Fig. 3).

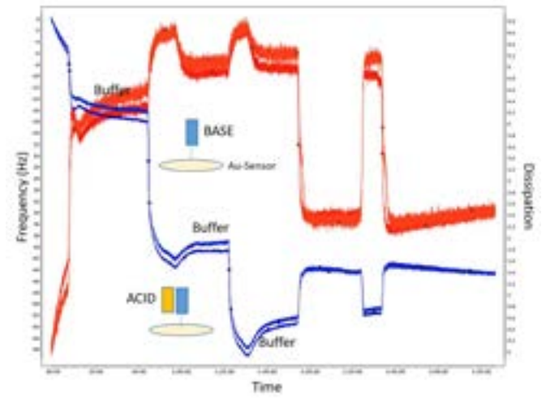

Fig. 3 Study of coiled coil interaction by QCM-D.Blue correspond to frequency shift (mass on the sensor), red represent shift in dissipation (visco-elastic properties).

Outlook
In the last year we hope to establish a functional prototype membrane, which is suitable for preclinical testing. In this regard extensive characterization of the material under cell culture conditions will be performed. Due to the change of the polymerization setup viscoelastic properties have to be assessed in more detail.

References

[1] A. L. Boyle and D. N. Woolfson, *De novo designed peptides for biological applications*, Chem. Soc. Rev., **40**, 4295–4306 (2011)

[2] D. N. Woolfson, *The design of coiled-coil structures and assemblies*, Adv. Protein Chem., **70**, 79–112 (2005)

NANOCREATE: a new enabling technology for microfabrication

Project A13.01: NANOCREATE (PSI, FHNW Windisch, GratXray AG Villigen)
Project Leader: K. Jefimovs
Collaborators: L. Romano, R. Holtz, B. Resan, M. Stauber, and Z. Wang

X-ray grating based Interferometry needs unconventional microfabrication

Grating interferometry enables significant improvements in the X-ray examination of soft tissues. Until now, different soft tissue types were difficult to separate in a classical X-ray examination. The advantage of grating interferometry over classical X-ray imaging is that not only the X-ray absorption but also its refraction and scattering are used to create the image. Grating interferometry in combination with CT scanner produces three-dimensional images with improved contrast and therefore offers decisive advantages in the examination of breast tissue and the diagnosis of malignant tumors [1]. Grating interferometry for medical diagnostics has been extensively developed over the last decade, but the production of specialized gratings and their high cost is still a limiting factor for the technique's broad application.

In the Nano-Argovia project "NANOCREATE", we developed a cost-effective fabrication method for optical X-ray gratings at the Paul Scherrer Institute (PSI), in collaboration with the University of Applied Sciences FHNW and GratXray AG (Villigen, AG). The gratings are used in a computed tomography (CT) scanner developed by GratXray, that allows for high-resolution, high-contrast imaging of the female breast. A concept picture of the proposed CT scanner by GratXray is shown in figure 1.

Fig. 1 3D concept image of the Grating Interferometry Breast CT system developed by GratXray AG (http://www.gratxray.com).

The NANOCREATE research plan consisted of three main tasks: 1) to produce high aspect ratio silicon gratings based on Metal Assisted Chemical Etching (MacEtch)[2]; 2) to fill silicon MacEtch gratings, which have low X-ray absorbance, with gold [3], which strongly absorbs X-rays, by using electroplating; 3) to explore laser ablation as an alternative method to directly make the gratings from a tungsten foil [4].

Metal Assisted Chemical Etching of Silicon

MacEtch is a local electrochemical method to etch silicon in a liquid solution containing HF and H_2O_2 [2]. The metal (Au, Ag, Pd or Pt) serves as a catalyst for H_2O_2 reduction with a consequent holes injection deep into the valence band of the silicon. This creates a hole rich region of silicon surrounding the metal catalyst that is readily oxidized by HF to form silicon fluoride compounds with the reaction continuing as the catalyst is pulled into the substrate. MacEtch has been mainly used as nanofabrication technique, being the etching quality strongly dominated by the catalyst stability [2]. We recently discovered that the catalyst nanostructuring is able to control the etching direction in patterned microstructures [2], opening the possibility of a new microfabrication technology. The catalyst nanostructuring is realized by a self assembly thermal dewetting of metal thin films on oxygen terminated silicon substrate [2]. Figure 2 shows a Scanning Electron Microscopy (SEM) image of a representative metal film dewetting.

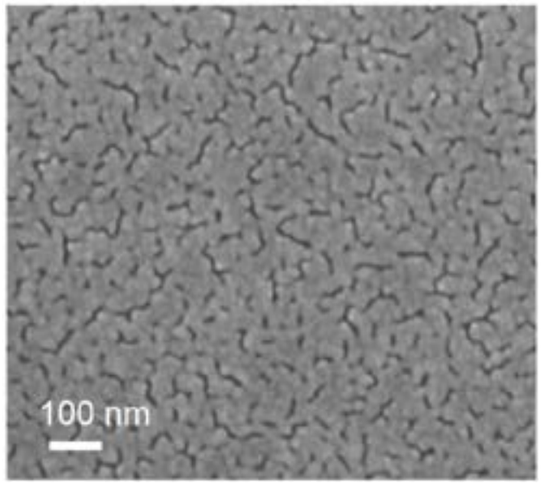

Fig. 2 SEM plan view of metal thin film on Si after thermal dewetting, the film fractures (dark contrast) are exposing the Si substrate

.

The size and the distribution of the random holes in the thin film are mainly determined by the film thickness and the annealing temperature. The presence of holes helps the diffusion of etchant and reactants during MacEtch, favoring a uniform etching. One of the main requirements for the realization on the Grating Interferometry Breast CT system is the use of hard X-ray. This means that a deep silicon etching is required. The main issue of MacEtch is the catalyst stability. A special catalyst pattern design has been implemented, which links the neighboring catalyst lines in a large area interconnected pattern. MacEtch is performed in liquid. Si lamellas can collapse by capillary effects during the drying process, therefore some Si stabilizing lines were added to improve the system stability. An example of the metal pattern is reported in figure 3.

An example of Si grating with period of 4.8 µm and duty cycle of 0.5 is reported in figure 4, the etching depth is 125 µm and the aspect ratio is 52:1.

The etching required high concentration of water diluted HF (25 wt%). The operator safety required implementation of a new large volume etching tank for the LMN clean room of PSI. We demonstrated the fabrication feasibility on 4 inch wafers.

Gold Electroplating

Au electroplating is performed in a cyanide based bath, an example of the Au filled grating is reported in figure 5.

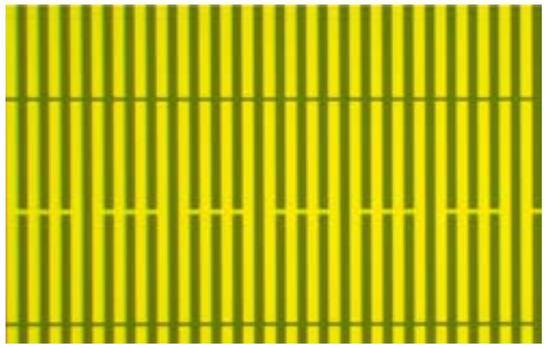

Fig. 3 Optical microscopy image of grating mask with interconnected lines (MacEtch catalyst will be the grey).

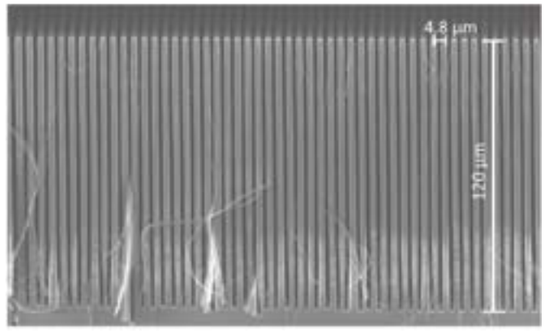

Fig. 4 SEM in cross section of Si grating with pitch of 4.8 µm and depth of 125 µm realized by MacEtch. The nanofilaments are due to the nanostructuring of the catalyst metal layer, their X-ray absorption is negligible.

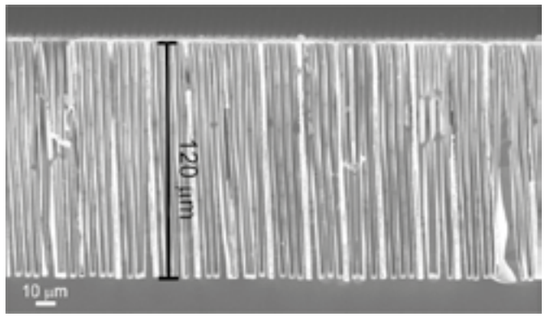

Fig. 5 SEM in cross section, pitch 4.8 µm and depth 120 µm realized by MacEtch and filled with Au (bright) by electroplating.

Laser Ablation of Tungsten foil

The laser ablation technique has also been tested in order to produce the gratings. The used laser emits 10 ps pulses, with up to 5 W of average power, at wavelength of 355 nm. Two approaches were tested.

In the first approach, an Axicon lens provides a quasi-Bessel beam with the spot diameter in the order of one µm and the focus depth in the order of one cm. The grid is then machined by movement of the translation axes. The second approach uses a standard type lens with 32 mm focal length combined with a scanner to guide the beam. The spot size achieved is about five microns.

The use of the Axicon lens allows production of better and sharper walls of the trenches. The second method is much faster, but it produces worse edges of the walls (conical entrance). The pitch of 10 µm is achieved with both approaches. The main challenge is the high aspect ratio (> 10:1), which creates a problem for the evacuation of the removed particles during the ablation process. The ablated particles block the slit preventing the laser beam from continuing deeper ablation. Nevertheless, it was possible to produce 14 µm wide slits in a 200 µm thick tungsten sheet with the standard lens (Fig. 6).

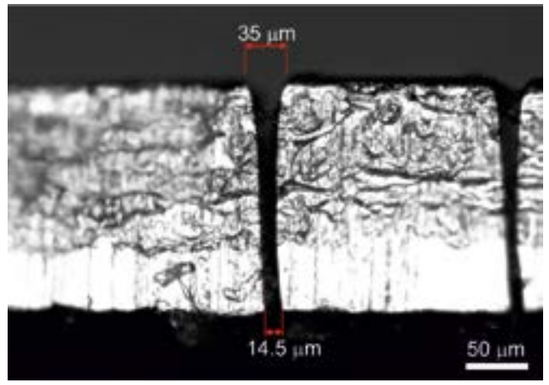

Fig. 6 Image from a light microscope. Side view of a 200 µm thick tungsten plate.

Conclusions

Hard X-ray absorbing gratings with feature size in the µm range and aspect ratio in the range of 50:1 are feasible by using MacEtch and Au electroplating, while laser ablation still requires deeper investigations.

References

[1] M. Stampanoni, Z. Wang, T. Thüring, C. David, E. Roessl, M. Trippel, R. A. Kubik-Huch, G. Singer, M. K. Hohl, N. Hauser, *The First Analysis and Clinical Evaluation of Native Breast Tissue Using Differential Phase-Contrast Mammography*, Invest. Radiol., **46(12)**, 801-6, (2011)

[2] L. Romano, M. Kagias, K. Jefimovs, M. Stampanoni, *Self-assembly nanostructured gold for high aspect ratio silicon microstructures by metal assisted chemical etching*. RSC Advances, **6(19)**, 16025-16029, (2016)

[3] M. Kagias, Z. Wang, V. A. Guzenko, C. David, M. Stampanoni, K. Jefimovs, *Fabrication of Au gratings by seedless electroplating for X-ray grating interferometry*. Mater. Sci. Semicond. Process. (2019)

[4] J. Lungershausen, A. Stumpp, A. Ferrari, D. Poulikakos, V. Kurtcuoglu, *Advanced laser ablation for the surface microstructuring of cardiovascular implants*. European Cells and Materials, **26** Suppl.1: 3, (2013)

Efficient capturing of mRNA for single-cell-transcriptomics

Project A13.04: ecamist (FHNW Muttenz, D-BSSE ETH Basel, Memo Therapeutics AG Basel)
Project Leader: G. Lipps
Collaborators: R. Dreier, M. Napiorkowska, S. Raman, S. Schmitt, and M. Held

Introduction

Single cell transcriptomics (SST) is of crucial interest for science and industry. It delivers essential clues for the development of new precision cancer therapies, the discovery of new drug targets and finds application in the fast growing field of medicinal antibodies development [1-3]. By looking at events on single-cell level, phenomena may be observed, which would be usually averaged out if the experiment were conducted in bulk [4].

A major role in SST plays messenger RNA (mRNA), which acts as an intermediate between DNA and protein synthesis. One of the first steps of SST is to capture as much of the approximately 100'000 mRNA molecules present in a single cell. The currently used method to capture mRNA involves the lysis of single cells in droplets in the presence of oligo dT-microbeads. The capturing happens via an interaction of the poly adenine-tail of the mRNA and the poly thymine-tail of the bead. One of the major drawbacks is that this interaction (hybridization) between bead and mRNA is of relatively weak non-covalent nature and therefore the captured mRNA can de-hybridize and is then lost for sequence analysis.

The intention of ecamist is to develop an efficient method to bind mRNA from single cells covalently to microbeads by help of an enzyme. This approach should increase the yield of adsorption as well as the quality of the analysis in comparison to the currently used method. A critical point is the choice of the enzyme, which is catalyzing the binding-reaction; it should remain active in the lysis buffer used, which possesses a high salt concentration and contains denaturing agents.

Challenge

The projects consists of three major challenges; 1) the covalent binding of a catcher oligonucleotide to microbeads 2) the optimization of the lysis conditions and 3) the stabilization of the RNA-DNA hybrid by a lysis buffer-stable enzyme.

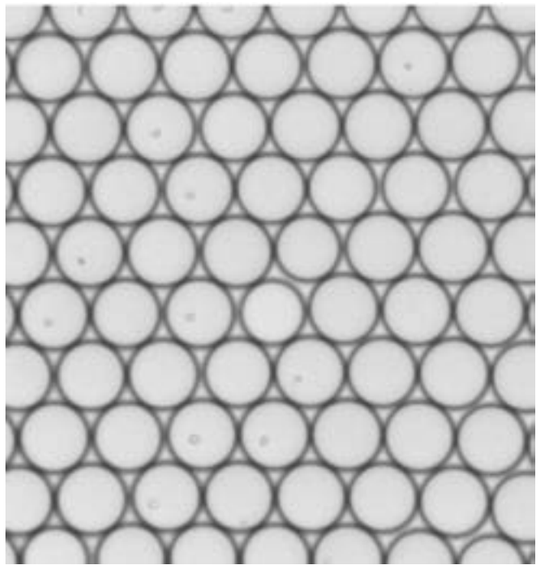

Fig. 2 Single-cells are separated in droplets of a water-in-oil emulsion followed by lysis and capturing of mRNA.

Results

Literature research showed that there are multiple synthetic routes for binding the catcher oligonucleotide covalently [6]. First trials were conducted according to Lönne et al. [7] involving tosyl-modified microbeads and amine modified oligonucleotides. This approach was not successful as no reaction took place. Changing to "click-chemistry" using azide-modified magnetic beads and DBCO-modified oligonucleotides it was possible to form a covalent bond between bead and catcher oligonucleotide (see Fig. 3, first step). The number of oligonucleotides on the surface was determined to be 36000 molecules /bead (equivalent to an approximate complete coverage of the bead surface with catcher oligonucleotides).

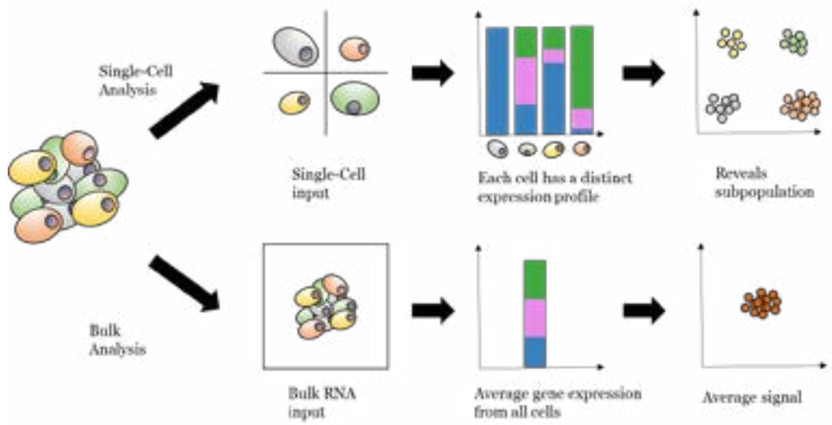

Fig. 1 Graphical representation of the difference between single-cell analysis and bulk analysis, adapted from Ye et al. [5].

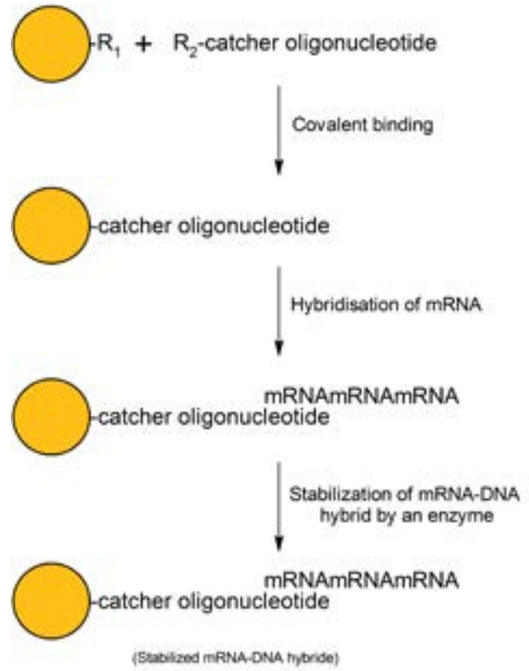

Fig. 3 Graphical representation of the approach of ecamist; the yellow circles represent microbeads.

An optimized lysis protocol was developed in order to achieve compatibility with the enzymatic reaction used for stabilization of the mRNA-DNA hybrid. The salt concentration remained high, as it has an influence on the hybridization properties of the mRNA to the catcher oligonucleotide.

Finally, an enzyme, which increases the stability of the RNA-DNA hybrid, was expressed in E. coli and tested. It kept its activity under the high salt concentrations as well as under the optimized conditions (data not shown).

References

[1] H. Mendes, L. Jinzhou, P. Sims, *Single-Cell Transcriptomic Analysis of Tumor Heterogeneity*, Trends Cancer **4(4)**, 264-268 (2018)

[2] J. M. Spaethling and J. H. Eberwine, *Single-cell transcriptomic for drug target discovery*, Curr. Opin. Pharm. **13(5)**, 786-90, (2013)

[3] Y. F. Seah, H. Hu, Ch. A. Merten, *Microfluidic single-cell technology in immunology and antibody screening*, Mol. aspects Med. **59**, 47 - 61 (2018)

[4] V. Chokalingam, J. Tel, F. Wimmers, X. Liu, S. Semenov, J. Thiele, C. G. Figdor, W. T. Huck., *Probing cellular heterogeneity in cytokine-secreting immune cells using droplet-based microfluidics*, Lab on a Chip **13(24)**, 4740-4, (2013)

[5] F. Ye, W. Huang, G. Guo, *Studying hematopoiesis using single-cell technologies*, J Hematol. and Oncol. **10 (27)**, (2017)

[6] M. Lönne, S. Bolten, A. Lavrentieva, F. Stahl, T. Scheper, J. G. Walter, *Development of an aptamer-based affinity purification method for vascular endothelial growth factor*, Biotechnol. Rep. **28(8)**,16-23, (2015)

[7] M. Malone, V. Cavett, B. Paegel, *Chemoselective Coupling Preserves the Substrate Integrity of Surface-Immobilized Oligonucleotides for Emulsion PCR-Based Gene Library Construction*, ACS Combinatorial Science **19(1)**, 9-14,(2017)

Disruptive power storage technology applying electrolyte nano dispersions

Project A13.08: MEGAnanoPower (FHNW Muttenz, CSEM Muttenz, Aigys AG Rheinfelden)
Project Leader: U. Pieles
Collaborators: S. Fricke, J. Schleuniger, M. Zinggeler, G. Álvarez, M. Waser, and A. Schimanksi

Background
The Aigys power storage technology is based on so-called redox-flow principle. The patented Aigys Power-Cell® technology uses solid dispersions instead of solved chemical compounds as charge carriers. Currently micro-particulate dispersions are used with the disadvantage of limited stability and insufficient charge density. To overcome these limitations, this project aims to develop stable nano-dispersions as high capacity energy storage media and to apply surface enlarged nano/micro structured electrodes as efficient current collectors.

Introduction
In redox-flow batteries the energy is stored in solved chemical compounds (electrolytes) which is highly interesting for large scale energy storage (decoupling of storage capacity and power). Mainly vanadium compounds are used in today's commercially available redox-flow batteries. However, due to the limited solubility of these chemicals the achievable energy density of such systems is still low.

The goal of this project is to test novel particle based electrolyte dispersion as energy storage media (Fig. 1) and use surface enlarged nano/micro structured electrodes as efficient current collectors. In a first phase of the project electrolyte dispersion made of well-known lithium-based compounds are used to test the working principle und to understand the basic behavior of particle based electrolyte dispersion. However, in a later stage we will also investigate alternative materials with better availability, lower price and strongly reduced hazardous potential.

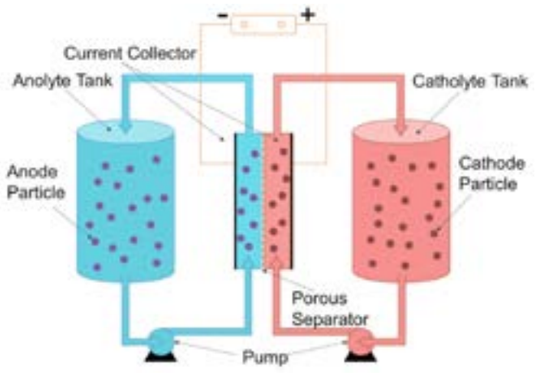

Fig. 1 General working principle of a redox-flow battery with solid electrolyte dispersions (source: ref. [1]).

Li-ion dispersion battery based on nano-particulate lithium cobalt oxide (LCO)
Nano-particulate LCO was successfully synthesized using a hydrothermal approach. The obtained plate-like particles have a size of 50-100 nm (Fig. 2). These particles were added to an electrolyte/solvent mixture to obtain a nano-particulate dispersion.

This dispersion was used for first electrochemical measurements. Two setups have been built for the characterization of the electrolytes, current collector and membranes. A small setup without pumps for the circulation is built for fast screening of potential electrolyte materials. The developed PE-half-cells were assembled and equipped with electrodes and membranes to a full test cell setup. The developed setup is very versatile due to a high flexibility in terms of adapting to the needs of the experiment e.g. half-cell experiments with reference electrodes, changing the membranes or the electrodes. Instead of circulation, the electrolyte dispersions are stirred with a magnetic stirrer. The active membrane area is 7 cm^2 and the minimum amount of electrolyte solution is less than 20 ml (Fig. 3).

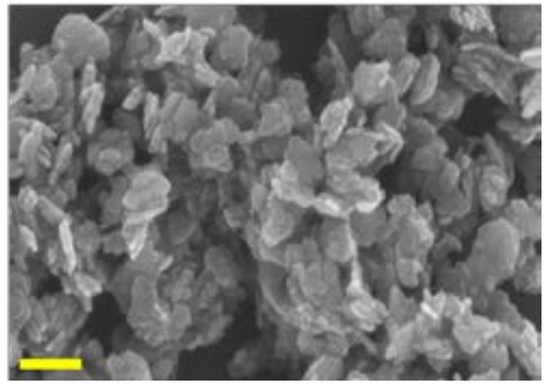

Fig. 2 SEM image of LCO nanoparticles (scale bar 200 nm)

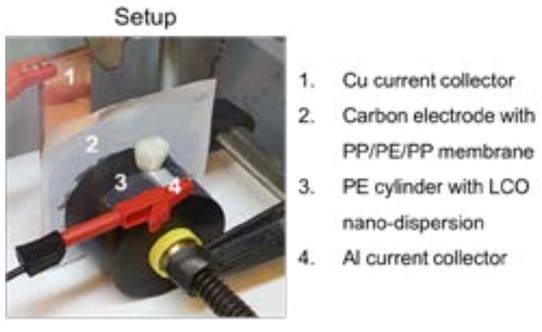

Fig. 3 Small setup with graphite electrode as negative electrolyte

A second setup was built to test all processes for redox flow batteries including the pumping of electrolytes. Similar to the small cell, the setup is very versatile. Electrodes and membrane can be easily adapted and replaced to the need of the experiment. The active area is 27.5 cm^2 and the minimum volume of electrolyte for each cell is around 80 ml. The setup was successfully tested with Vanadium solution as electrolyte, Nafion-membrane and Graphite bipolar-plates as electrodes (Fig. 4).

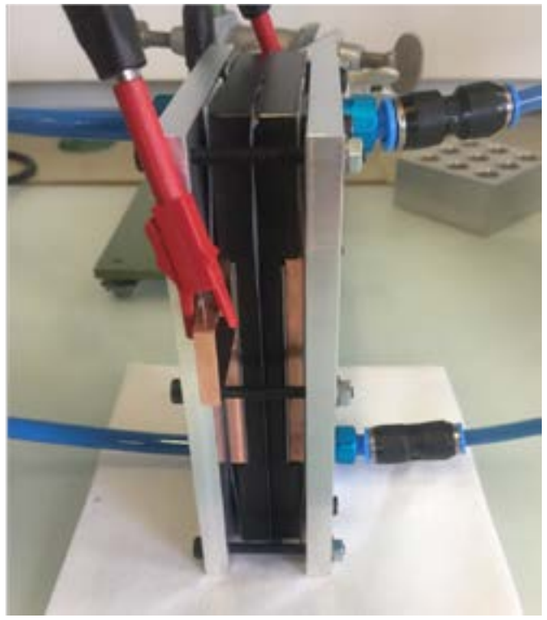

Fig. 4 Assembled cell of the big setup

Cyclic voltammetry results confirm that reversible redox reactions can be performed with LCO nano-particles at expected potentials. Further, four charge-discharge cycles were successfully conducted and showed a stable coulombic efficiency at around 84%. Due to the low mass transport in the system (weak magnetic stirring) the battery was not completely charged/discharged. This explains the low capacities in the shown charge/discharge measurements (Fig. 5).

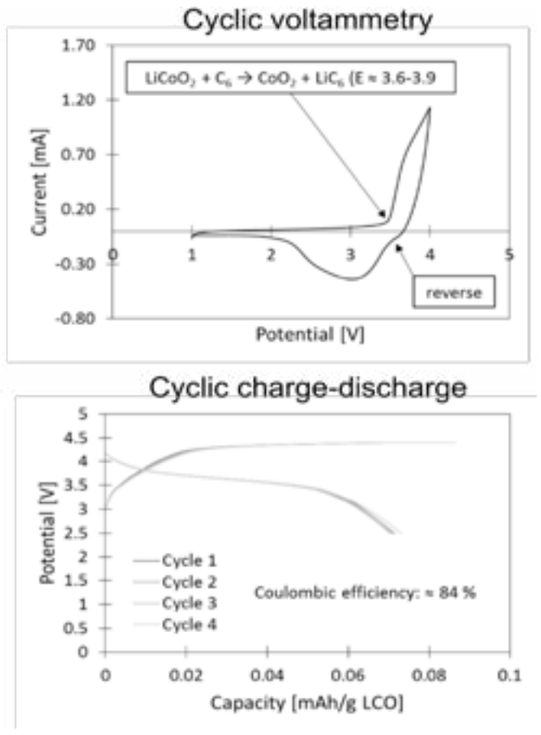

Fig. 5 Electrochemical measurements

Structuring of electrodes – surface enlargement by hot-embossing
The structuring of the current collector surface aims to enlarge the interacting surface area in general and to adapt specific surface topographies which enable rapid charge transfer processes. In a first approach, a graphite/polymer current collector plate was structured by hot embossing with a nickel shim. In this case, the topography of the shim could be perfectly copied to the graphite/polymer plate (Fig. 6).

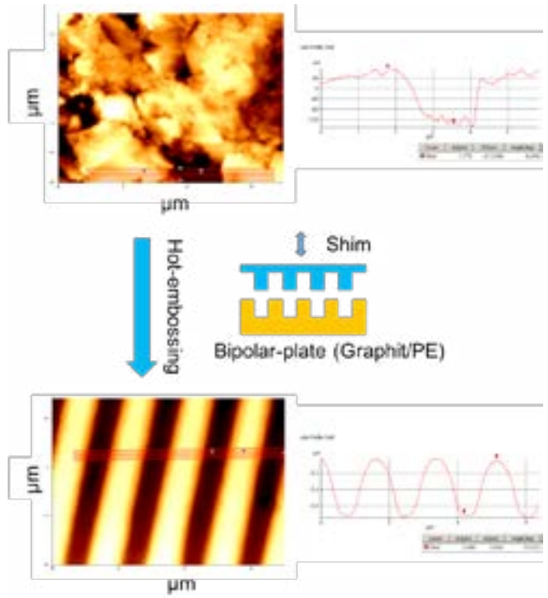

Fig. 6 Atomic force microscope (AFM) picture of non-structured and structured graphite/polyethylene current-collector.

Initially the shim depth and period was 600 nm respectively 1760 nm. The depth of the hot embossed plate is 663 nm. This is in good agreement with the shim since during the embossing process compression and expanding can lead to bigger depth than the original depth. The chosen topography (period and depth) was an adoption to the potential particle size of the dispersion. These values can be easily adapted to the final particle size.

References

[1] Z. Qi and G. M. Koenig, *Review Article: Flow battery systems with solid electroactive materials,* Journal of Vacuum Science & Technology B **35**, 040801 (2017)

Biomimetic growth of calcium phosphate ceramics on Ti implants

Project A13.09: NanoCoat (PSI, FHNW Muttenz, Medicoat AG Mägenwil, Atesos Medical AG Aarau, Hager & Meisinger GmbH Neuss, Deutschland)
Project Leader: A. Testino
Collaborators: M. de Wild, E. Mueller, A. Carino, F. Dalcanale, P. Gruner, and W. Moser

Summary of the project progress

Parallel to the development of economy and technology, the number of aged people demanding compromised tissue replacement is rapidly increasing. Moreover, there is an expanding requirement for hard tissue replacement because of sports-related and degenerative injuries. It is estimated that >70% of biomedical implants are made of metallic materials. Among them, titanium (Ti) and its alloys are widely used in dental, craniomaxillofacial, spinal, and orthopaedic surgery because of their excellent mechanical properties that are required for load-bearing applications. These Ti implants are often coated with calcium phosphate (CaP) to enhance bone bonding and accelerate osseointegration. Currently, hydroxyapatite (HA) is deposited by plasma-spraying technique onto Ti substrate. Plasma-spray, although clinically established, has specific drawbacks such as the extremely high processing temperatures and difficulties to coat complex-shaped parts. The biomimetic route is nowadays very promising to modify the implant surface with CaP. In this project, an innovative and extremely competitive protocol for Ti surface modification with CaP is developed. Implant prototypes were produced and characterized.

During the first year of the project, we optimised the process for the implant surface modification. Initial trials were done on Ti grade-4 discs of 10 mm diameter and a thickness 1 mm. The discs surface was prepared according to three different treatments, which are consistent with the existing implant surfaces: polished (PO), sandblasted (SB), and sandblasted and acid etched (BA) (Fig. 1). The BA surface corresponds to the state-of-the-art treatment used for dental implants.

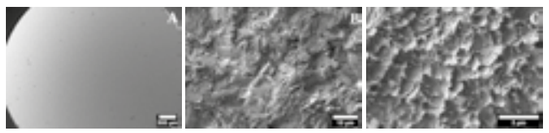

Fig. 1 Ti (grade 4) surface treatments. A: polished (PO, 22 x); B: sandblasted (SB, 1530 x); C: sandblasted and acid etched (BA, 4900 x).

The novel surface modification process consists of two steps. In the first step, a highly porous structure, the so-called grafting layer, is promoted on the Ti surface. The grafting layer is obtained in a way similar to the well-known Kokubo method [1]. Ti parts undergo a chemical treatment (soaking into an alkaline solution) followed by a thermal treatment. The obtained surface consists of a porous layer (~1 µm) of hydrogen and sodium titanate ceramics. It has been demonstrated – both in-vitro and by long-term clinical trials – that the grafting layer provides a bioactive surface and accelerates osseointegration. In the second step, the synthetic bone (CaP) is grown under biomimetic conditions within the porosity of the grafting layer. The synthetic bone formation is carried out under strictly controlled physiological conditions by monitoring and tuning pH, ionic strength, temperature, and saturation level of the system with respect to the solid phase objective of the deposition. This goal can be achieved thanks to the thermodynamic-kinetic model [2] developed for calcium phosphate formation. As a result, the thickness, morphology, deposition rate, and chemical phase of CaP can be accurately controlled. Figure 2 shows the BA surface after the first and second step of the process.

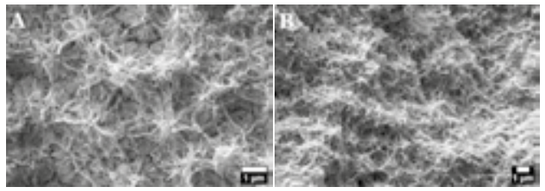

Fig. 2 Modified surfaces after (A) step 1 and (B) step 2.

Due to the small thichenes of the modified layer, the initial Ti roughness induced by the blasting treatment is preserved. Figure 3 shows the optical roughness measurement (LEXT OLS3000, Olympus, Japan) of the BA surface at each step of the process. The figure reports on three series of samples subjected to different grafting layer and synthetic bone deposition treatments produced during the surface optimization studies (such as tuning the soaking conditions or the thermal treatment profile of the first step).

Once optimized on Ti discs, the process was applied to medical implants, such as dental screws. They are made of Ti grade-4 with a BA surface (commercially known as SLA surface). Figure 4 shows a cross-section (FIB/SEM ZEISS NVision40) of the first microns of a dental screw after optimized surface modification; the porosity of grafting layer is clearly visible. Moreover, the EDX analysis confirms that CaP grows within the grafting layer.

A fundamental prerequisite of the modified surface is that, upon implantation, the surface and its characteristics are preserved. To demonstrate that, mechanical tests were carried out on dental screws prototypes by tightly screwing them into standard synthetic sawbones material (polyurethane, 30 pcf). After implantation, both screws surface and sawbones material were analysed by FIB/SEM. No evidence of delamination was detected, and both CaP and the grafting layer were preserved.

It is well-known from in-vivo tests and clinical applications, that after implantation osseointegration of Ti implants occur. Nevertheless, the formation of the new bone tissue requires time, between six weeks and six months. The cells adhesion, migration and proliferation on the implant are regulated by different proteins. Their interactions with the implants are facilitated when they can be easily absorbed on the implant surface. High porosity, hydrophilicity, and bioactivity are fundamental surface characteristics for an implant. In addition, topography and chemical ion release have a dramatic effect in the process effectiveness. These properties contribute to a shorter healing time and a better implant stability.

The presence of the grafting layer already improves several aspects. However, a soluble CaP phase predeposited in the grafting layer add additional features. In fact, the formation of a new phase on a substrate (such as by heterogeneous nucleation) is an activated process that needs a certain induction

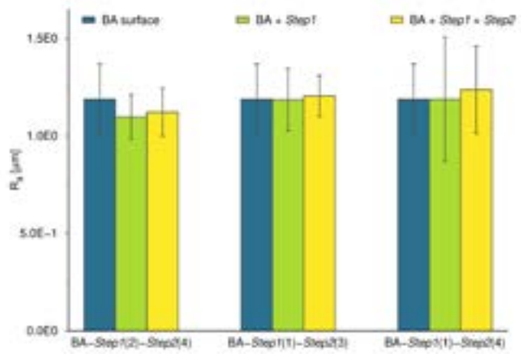

Fig. 3 Optical roughness measurement comparison among different process steps. Three series of samples are reported produced with minor differences in the first and second step of the surface modification. Blasted and acid-etched (BA) surface roughness (blue); after step 1 (green); after step 2 (yellow).

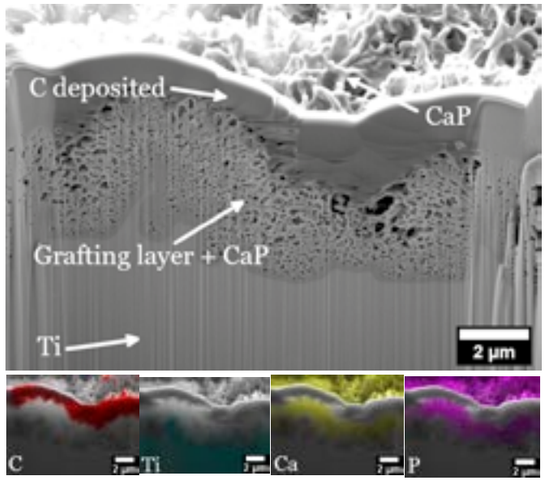

Fig. 4 Cross section obtained by FIB of a dental implant where the CaP was grown inside the porous grafting layer. The carbon layer was deposited for technical reasons. The chemical mapping (EDX) denotes the composition within the grafting layer.

time. In the case discussed here, this initial slow step of calcifying the implant surface is carried out before the implantation, during the second step of the surface modification. As a result, upon implantation, new bone may immediately grow without the need of an activated process (such as heterogeneous nucleation), which initially slows down the osseointegration. In addition, the solubility of the deposited CaP can be tailored by modifying the phase (hydroxyapatite, HA, or octacalcium phosphate, OCP) and its nanostructure. Our previous studies demonstrated that the deposited layer has a higher solubility with respect to mature HA [2]. Moreover, OCP is considered the most active CaP phase, being the precursor of natural bone during osteogenesis.

While the hydrophilicity can be easily demonstrated, as shown in figure 5 where implant prototypes are put into contact with pure water, a shorter healing time can be evaluated only in-vivo. Nevertheless, preliminary in-vitro test on the apatite-forming ability according to the ISO/FDIS 23317 were carried out on samples with or without the CaP deposition. Preliminary results indicate that, in a time frame of two weeks, a larger amount of HA was grown on the surface modified with steps 1 & 2 compared to the surface with grafting layer only. As a comparison, of the BA surface, no HA deposition was detected after the same timeframe.

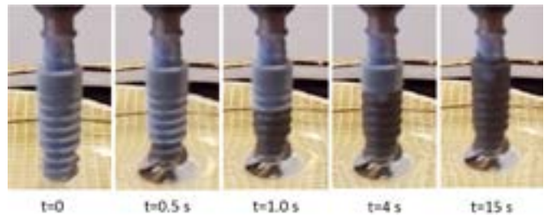

Fig. 5 Hydrophilicity of the modified surface due to the nanostructured CaP surface. The capillary force in action.

Today, the surface modification protocol is carried out at lab scale using small reactors. The objectives of the second year of the project are devoted to the process scaleup, the verification of the protocol reproducibility to the larger scale, to evaluate bioactivity and cytocompatibility of the modified implant surface by in-vitro tests, to carry out additional mechanical tests, to plan in-vivo tests, and to validate the entire processes in view of the legal steps toward the notification of the implants as medical devices.

References

[1] T. Kokubo and S. Yamaguchi, *Bioactive Ti Metal and its Alloys Prepared by Chemical Treatments: State-of-the-Art and Future Trends*, Advanced Biomaterials **12(11)**, B597 (2010)

[2] A. Carino, C. Ludwig, A. Cervellino, E. Muller, A. Testino, *Formation and transformation of calcium phosphate phases under biologically relevant conditions: Experiments and modelling*, Acta Biomaterialia **74**, 478 (2018)

Embedding of GPCR–arrestin nano-machineries in synthetic nanocompartments

Project A13.12: NanoGhip (InterAx Biotech AG, University of Basel Dept. of Chemistry and Biozentrum, PSI)
Project Leader: M. K. Ostermaier
Collaborators: S. Yorulmaz Avsar, J. Mühle, E. Lesca, L. E. Kapinos-Schneider, C.-A. Schoenenberger, R. Y. H. Lim, G. F. X. Schertler, and C. G. Palivan

Introduction

G protein-coupled receptors (GPCRs) are the largest family of membrane proteins. As the master regulators of cells, they are involved in a multitude of sensory and vital functions and are thus pharmacologically highly important. With more than 40% of all prescribed drugs targeting GPCRs, they are in fact the single most important class of drug targets. However, for more than 70% of all pharmacologically relevant GPCRs the therapeutic potential remains so far untapped because suitable technologies are lacking.

GPCRs are challenging targets due to their inherent instability outside of their native environment. Thus, many of the currently established drug screening and characterization assays are not applicable. Besides the eponymous G proteins, arrestins are the most prominent intracellular binding partners for GPCRs. Arrestins play an essential role in signal-termination: By binding to the core region of the receptor, they sterically hinder the agonist-activated GPCR to further propagate G protein-dependent signaling; this then leads to receptor internalization. Biologically active compounds that may be further developed into drugs are usually characterized with respect to their direct interaction with the receptor and their ability to alter signaling processes, in particular G protein signaling and desensitization by arrestins.

Synthetic nanoassemblies for stabilization of GPCRs

Membrane proteins are usually embedded in a lipid bilayer, which is sensitive to mechanical disruption and oxidation processes. Artificial membranes assembled from amphiphilic block copolymers have been shown to allow functional insertion of membrane proteins [1, 2] while providing a more robust framework. Therefore, the use of synthetic assemblies is expected to improve the stability of integrated membrane proteins, such as a GPCR and extend the lifetime of corresponding assays. Within the scope of this project we aim at developing novel GPCR screening assays that monitor the interaction of arrestins with a target GPCR. As GPCRs are known to be much more sensitive to their lipid environment compared to bacterial membrane proteins, including bacterial retinal proteins, we have taken a two-pronged approach using synthetic membranes as well as lipid polymer membranes for protein insertion (Fig. 1).

Production and characterization of the photo-activate-able GPCR JSR1 and arrestin-3

We have chosen the light-activated, bistable opsin Jumping Spider Rhodopsin 1 (JSR1) as GPCR sample as it is i) recombinantly expressed and purified in its native form, ii) biochemically stable, iii) activated by light, and iv) attractive for bioengineering approaches.

Recombinant JSR1, expressed in a stably transfected mammalian cell line, was harvested after two to three months of suspension culture. Yields were typically 2.3 mg of purified JSR1 from 15g of dry cell pellets. After reconstitution with 9-cis-retinal in the dark, JSR1 was solubilized with dodecyl maltoside (DDM). 1D4-antibodies are used for a first affinity chromatography, followed by size-exclusion chromatography (SEC) as final purification step. Within the first year of this project, about 2.5 mg of total JSR1 have been produced. Attempts to adapt the purification procedure to detergent with high aggregation number, such as octyl-glucoside (OG) to facilitate integration into synthetic membranes, were hampered by a significant loss of protein during individual purification steps. The quality of purified JSR1 was assessed by SEC (monodispersity), SDS-PAGE (purity) and UV-vis spectroscopy (purity, concentration and functionality) (Fig. 1).

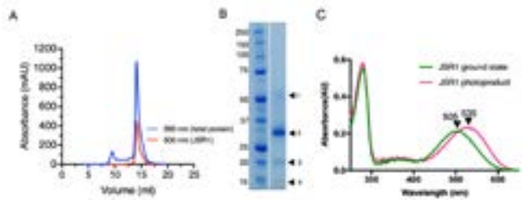

Fig. 1 A) Size-exclusion chromatography shows JSR1 as a monodisperse sample. 280 nm absorbance (blue line) refers to the total protein amount, while 500 nm (red line) indicates the protonated Schiff base signal. B) SDS-PAGE of JSR1 after size-exclusion chromatography with DDM. The left lane shows protein markers and the right lane JSR1. Protein bands have been analyzed by mass spectrometry (MALDI/MS/MS): 1, JSR1 dimer or protein disulfide-isomerase A3; 2, monomeric JSR1; 3, degraded JSR1 or mitochondrial ATP synthase subunit D; 4, degraded JSR1. C) JSR1 reconstituted with 9-cis-retinal (isorhodopsin) has absorbance maxima at 505 nm and the photoproduct at 535 nm.

Human His_6-arrestin-3 WT and its mutants were produced in E. coli at 20°C for 24 h [3]. Upon sonification of the cell pellet, the protein was isolated from the crude extract by ultracentrifugation followed by Ni-NTA affinity chromatography and anion exchange (Q Sepharose) chromatography. Final purification was achieved by size exclusion chromatography. Typically, 1 L culture yielded 0.3 to 0.5 mg of pure His_6-arrestin-3.

Synthesis and characterization of synthetic nanoassemblies

We selected to synthesize amphiphilic copolymers poly(2-methyl-2-oxazoline)-block polydimethyl-siloxane-block-poly(2-methyl-2-oxazoline) (PMOXA-b- PDMS-b-PMOXA) because they already served for successful insertion of membrane proteins [1, 2]. We synthesized two different PMOXA-b-PDMS-b-PMOXA copolymers by cationic ring-opening polymerization of 2-methyl-2-oxazoline on PDMS macroinitiators. Nuclear magnetic resonance (NMR) and gel permeation chromatography were used to characterize the resulting triblock copolymers (Fig. 2A, B). Self-assembly of these copolymers using solvent exchange and film rehydration methods induced formation of nanoassemblies, such as micelles and polymersomes (Fig. 2C). In addition, closely-packed two-dimensional mono-layers were assembled at the air-water interface in order to create a soft membrane on a solid support (Fig. 2D). The latter represents a stepping-stone towards the design of the chip using polymer membranes.

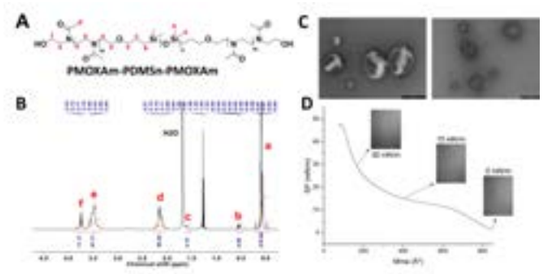

Fig. 2 A) Chemical structure of PMOXA-PDMS-PMOXA triblock copolymers. B) Representative 1H NMR spectra of PMOXA6-PDMS36-PMOXA6. C) Transmission electron microscopy (TEM) micrographs of nanoassemblies formed by PMOXA6-PDMS24-PMOXA6 in aqueous solution. D) Langmuir isotherm of PMOXA6-PDMS36-PMOXA6 and Brewster angle images at 0, 15, and 30 mN/m. Breaking point of Langmuir monolayer is 47 mN/m.

GPCR-arrestin-3 interaction measured by QCM-D

To develop a polymer membrane-based GPCR binding assay, we first tested the interactions of purified GPCR with immobilized His_6-arrestin-3. We used a supported lipid bilayer (SLB) deposited on a silicon oxide sensor to immobilize different His_6-arrestin-3 proteins and analyzed their interaction with light-activated JSR1 in DDM micelles by quartz crystal microbalance with dissipation monitoring (QCM-D) (Fig. 3). Addition of JSR1-DDM micelles to His_6-arrestin-3 immobilized on SLBs caused significant changes in frequency and dissipation signals, while in the absence of surface-bound arrestin-3 or in case of DDM micelles lacking JSR1 only small changes were observed. Thus, QCM-D results demonstrate in situ interactions of the light-activated JSR1 in DDM micelles with His_6-arrestin-3 immobilized on SLB platform in real time.

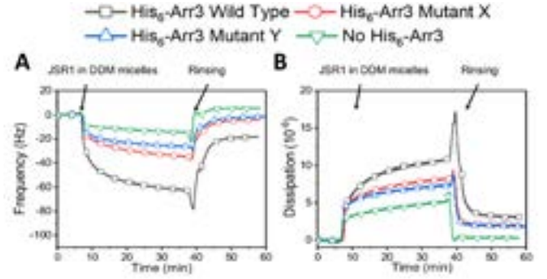

Fig. 3 Interaction of immobilized arrestin-3 with light activated JSR1 in DDM micelles measured by QCM-D. After the SLB formation, arrestin-3 WT (black square), MX mutant (red circle), and MY mutant (blue triangle) were immobilized on SLB with 5% DGS-NTA(Ni^{2+}), followed by the addition of JSR1 in micelles. Changes in (A) frequency and (B) dissipation were recorded upon addition of JSR1 in DDM micelles to immobilized arrestin-3 proteins on the SLB platform.

GPCR-arrestin-3 interaction test in BLI and SPR

Finally, an interaction of GPCR, e.g. JSR1, with the surface-immobilized His_6-arrestin-3 and mutants was also validated by surface plasmon resonance (SPR) and biolayer interferometry (BLI). His_6-arrestin-3 (or its mutants) was successfully immobilized on the Ni^{2+}-NTA sensor chip, or on the HPA sensor chip functionalized with a Ni^{2+}-NTA-lipid mono-layer (SLM). Alternatively, they were also immobilized on the Ni^{2+}-NTA tips used in the BLI measurements. Activity of the immobilized arrestin-3 was verified with heparin using BLI method. Light-activated JSR1 (solubilized in DDM micelles) was titrated to His_6-arrestin-3 and the resulting sensograms were fitted assuming a 1:1 binding model to obtain the equilibrium and kinetic dissociation and association constants (K_D, k_d and k_a) (Fig. 4). In our assays we have demonstrated that the recombinantly expressed biosensors (e.g. arrestin-3 WT and its mutants) and the GPCR JSR1 are still functional in such setup and their interaction can be successfully measured on the biochip.

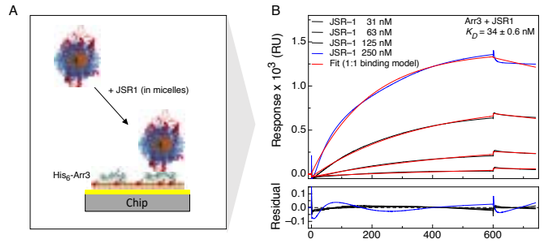

Fig. 4 A) Interaction of immobilized arrestin-3 with light-activated JSR1 in DDM micelles measured by SPR. B) After the SLM formation, arrestin-3 WT (black lines), MX mutant and MY mutant (not shown) were immobilized on SLM with 5% DGS-NTA(Ni^{2+}), followed by the addition of JSR1 in DDM micelles. Representative binding curves together with the fit are shown.

Summary

We have produced functionally active JSR1 and arrestin-3 in quantities sufficient for SPR- and QCM-D-based interaction studies. Immobilized WT and mutant arrestin-3 was used to demonstrate that JSR1-arrestin binding parameters can be successfully assessed in such a setting. Preliminary data using immobilized arrestin-3 indicate an interaction with JSR1. These promising results will be fully explored in the second period of the grant.

References

[1] S. Yorulmaz Avsar, M. Kyropoulou, S. Di Leone, C.-A. Schoenenberger, W. P. Meier, C. G. Palivan, *Biomolecules turn self-assembling amphiphilic block co-polymer platforms into biomimetic interfaces*, Front. Chem. **6**, (2019)

[2] M. Garni, R. Wehr, S. Yorulmaz Avsar, C. John, C. G. Palivan, W. Meier, *Polymer membranes as templates for bio-applications ranging from artificial cells to active surfaces*, Eur. Polym. J. **112**, 346-64, (2018)

[3] R. S. Haider, F. Wilhelm, A. Rizk, E. Mutt, X. Deupi, C. Peterhans, J. Mühle, P. Berger, G. F. X. Schertler, J. Standfuss, M. K. Ostermaier, *Arrestin-1 engineering facilitates complex stabilization with native rhodopsin*, Sci. Rep. **9**, 439, (2019)

Self-assembled block copolymers for nanoscale toughening of epoxy matrices

Project A13.13: NanoTough (FHNW Windisch, University of Basel Dept. of Chemistry, Huntsman Basel)
Project Leader: C. Dransfeld
Collaborators: C. Dransfeld, E. Rehmann, D. Widner, M. Wink, C. Fodor, J. Gaitzsch, C. John, W. Meier, L. Dumas, A. Napoli, and K. Scobbie

Introduction

Fiber-reinforced composites combine high stiffness and strength with very low weight and are increasingly used in automotive and aerospace industries. However, the relatively low toughness of epoxies, the most common composite matrix systems, limits their damage tolerance. One way to toughen epoxy matrices is through the addition of block-copolymers (BCP), where at least one block is epoxy-philic and one is epoxy-phobic. These BCPs self-assemble into nano- or microstructures in the epoxy matrix. Here, we investigate how the obtained morphology influences the composite's properties with the aim to deliberately design BCPs for optimal toughening without impairing glass transition temperature (Tg) or processing viscosity. To this end, we explore commercially available BCPs as well as tailor-made BCPs with narrow polydispersity and well-defined block length.

Synthesis of well-defined BCPs

We have analysed the commercially available polymers of the Fortegra, Pluronics and MNAM family using 1H-NMR spectroscopy, gel permeation chromatography (GPC) and differential scanning calorimetry (DSC). Combined, we have shown that these were broadly distributed PEO-b-PBO (Fortegra) and PEO-b-PPO-b-PEO (Pluronics) BCPs.

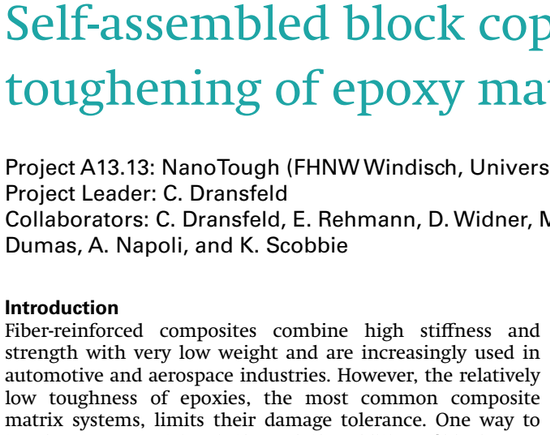

Fig. 1 Synthesis of well-defined BCPs using conventional and microwave-assisted synthesis. The resulting polymers were narrowly dispersed and contained no starting PEO-block (GPC traces shown).

In order to broaden the available BCPs, we have introduced commercially available PEO-b-PBO BCPs. We also synthesised PEO-b-PBO BCPs with various molecular weights in order form the desired vesicles or worm-like micelles in epoxy matrices.

We have decided to use a conventional synthetic approach, which yielded over 10 grams of various BCPs after 72h of synthesis. Switching to a microwave (µW)-assisted approach cut the synthesis time to 1-2 hours. However, upscaling using µW was only possible using a number-up approach, e.g. synthesising several batches of the same polymer. In sum, the time gained during the synthesis is slightly diminished by this factor. Both methods yielded narrowly dispersed BCPs (Đ>1.05). An extensive combined purification cut out any remaining starting block and side-products of the reaction (Fig. 1).

Cure kinetics

The cure kinetics of neat and toughened matrices were determined with dynamic measurements in differential scanning calorimetry (DSC). Using model free kinetics (MFK) and applying the isoconversional principle, the degree of cure (α) was calculated for isothermal or variothermal cure cycles. It was found that the addition of toughners led to slightly slower curing but did not affect the maximum degree of cure (Fig. 2).

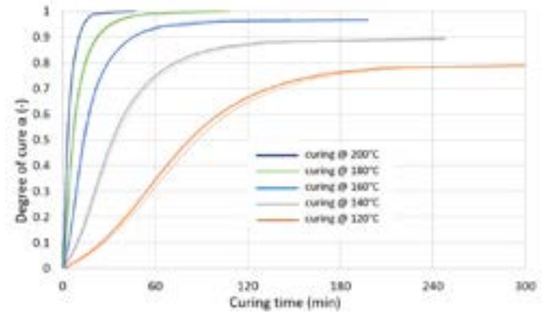

Fig. 2 Degree of cure as a function of curing time for isothermally cured samples (determined by DSC). Comparison of neat matrix (continuous lines) and matrix with 5% of toughener C1 (dotted lines).

Fracture surfaces of toughened matrices

Having established a suitable processing and curing protocol for the high temperature epoxy matrix, samples with a fixed amount of added commercial toughners were prepared. Fracture surfaces were investigated with scanning electron microscopy (SEM) in order to determine the morphology and size of self-assembled BCP structures (Fig. 3).

Mechanical and thermal properties of toughened epoxies

Critical energy release rate GIc was determined as a measure of fracture toughness by single edge notched bending (SENB) and Young's moduli were assessed by tensile testing (Fig. 4). Addition of BCPs led to substantial toughening, however, the targeted toughness (> 350 J/m2) was only reached with C1. Young's moduli decreased in toughened systems, whereby the most substantial drop was observed for the best toughener C1. The commercial variant of the PEO-b-PBO BCP C1 showed a better toughening performance than the very similar custom-synthesized variant S. In contrast, the drop in Young's modulus was much less severe for S than for C1.

The properties of toughened matrices are summarized in Table 1. The synthesized BCP S has a lower polydispersity than commercial products C1 C4, but this did not translate into a better toughening performance. The Tg of dry specimens was unaffected by the addition of BCPs.

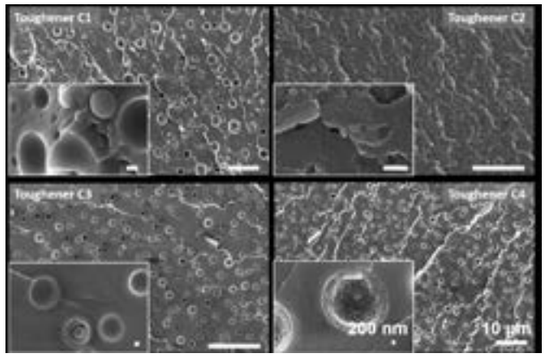

Fig. 3 SEM images of fracture surfaces. Commercial toughners self-assemble into spherical structures of different sizes when cured in a high temperature epoxy resin. The toughners vary in type and number of blocks as well as in molecular weight.

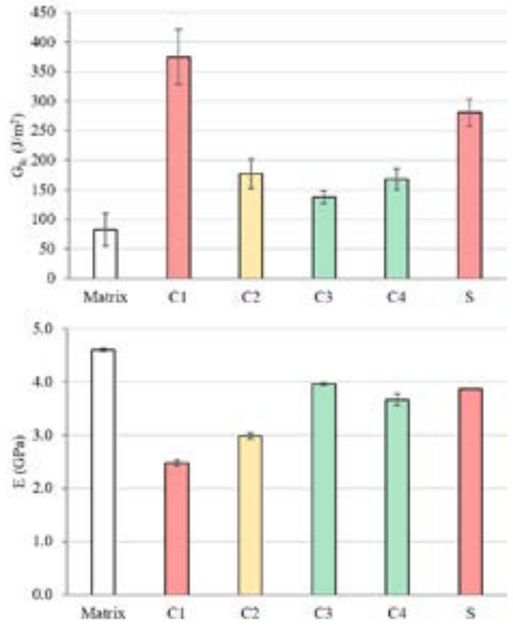

Fig. 4 Toughness GIc (upper panel) and Young's modulus (lower panel) of the epoxy matrix and systems toughened with PEO-b-PBO diblock copolymers (C1 and S), an acrylate based triblock copolymer (C2) and Pluronic-type triblock copolymers (C3 and C4). BCPs denoted with C are commercial products, BCP S was custom-synthesized at Uni Basel.

	M_n (g/mol)	D (-)	T_g dry (°C)	G_{Ic} (J/m²)	E (GPa)
C1	1'200	1.17	185	375	2.48
C2	41'000	1.71	187	177	2.99
C3	3'000	1.13	186	138	3.95
C4	5'800	2.32	188	168	3.67
S	5'690	1.09	178	281	3.87

Table 1: Molecular weight (Mn), Đ (Mw/Mn), T_g of dry specimens as determined from dynamic mechanical analysis (DMA) and mechanical properties of epoxy matrices toughened with commercial (C) and synthesized (S) BCPs.

Conclusion and Outlook

We successfully synthesised narrowly dispersed PEO-b-PBO BCPs to enhance the range of available materials. Conventional and microwave-assisted synthesis proved to be potent methods.

The investigated commercial block copolymers all self-assembled into spherical structures of various sizes when added to a high temperature epoxy system. These structures led to an increase in toughness and a decrease in elastic modulus, while the glass transition temperature and cure kinetics remained similar to those of the neat epoxy. No clear correlation between the obtained nano- or micro-structure and the mechanical performance of the toughened epoxy could be established apart from crack pinning effects observed for the spherical block copolymer structures. Designer block copolymers of the type PEO-b-PBO tailored towards specific self-assembled structures with low polydispersity yielded good toughening performance and a comparably low decrease in Young's modulus. However, Tg was substantially lower than for the commercial variant.

In a next step, we plan to combine various toughening strategies in order to avoid detrimental effects on Young's modulus while maintaining good toughening performance and good processability.

References

[1] M.A. Hillmeyer, P. M. Lipic, A. Hajduk, K. Almdal, F. S. Bates, *Self-assembly and polymerization of epoxy resin amphiphilic block copolymer nanocomposites*", J. Am. Chem. Soc. **119 (11)**, 2749 (1997)

[2] M. Larranaga, N. Gabilondo, G. Kortaberria, E. Serrano, P. Remiro, C. C. Riccardi, I. Mondragon, *Micro- or nanoseparated phases in thermoset blends of an epoxy resin and PEO-PPO-PEO triblock copolymer*, Polymer **46 (18)**, 7082 (2005)

[3] J.M. Dean, P. M. Lipic, R. B. Grubbs, R. F. Cook, F. S. Bates, *Micellar structure and mechanical properties of block copolymer-modified epoxies*, B: Polym Phys, **39 (23)**, 2996 (2001)

Nanophotonics for quantum sensing technology

Project A13.15: NQsense (University of Basel Dept. of Physics, PSI, Qnami Basel)
Project Leader: P. Maletinsky
Collaborators: F. Favaro de Oliveira, M. Munsch, G. Seniutinas, and C. David

Introduction
Magnetic field imaging has been widely used across different fields, ranging from basic material science to biology. Notwithstanding, classical sensing technologies fail to address the nano-scale due to physically-imposed limitations in resolution and sensitivity. Such nano-scale magnetic field imaging is, however, exactly what is needed to investigate systems of great interest for researchers and industries such as transistors and magnetic memory bits, as well as proteins and molecules.

Quantum sensing using spin defects in diamond offers a disruptive approach to address such systems at the nano-scale. In particular, the nitrogen-vacancy (NV) center in diamond – an optically addressable spin, with excellent properties for such nanoscale quantum sensing - has already been successfully employed in several breakthrough applications[1]. The Quantum Sensing Group led by Prof. P. Maletinsky is implementing such spins in diamond in a imaging modality called scanning probe microscopy (SPM), which they originally developed[2]. This successful research history has triggered the creation of QNAMI, a spin-off company that commercializes quantum sensors made of diamond.

During the first year of the Nano-Argovia project NQsense, activities were developed in the frame of establishing a strong collaboration between the partners from the public and private sectors in the region of Northwestern Switzerland. The main project outcomes were the theoretical modeling of the photon collection efficiencies of diamond quantum sensors and the concomitant optimized fabrication design of a new generation of sensors, as well as the transfer of Qnami's nano-fabrication activities to the industry-standard cleanroom at the PSI (see details below).

Theoretical investigation of the photon collection efficiency for improved sensitivity
The single-spin quantum sensors pursued within the NQsense project consist of an all-diamond cantilever with a sub-micrometer sharp tip containing a single NV center spin at its apex. The signal from the embedded NV center sensor is read out optically using its spin-dependent fluorescence. Typically, only a very small fraction (few percent) of the emitted photons can be collected due to challenges in nano-photonics related to the high refractive index of diamond. As the corresponding sensitivity to magnetic fields is inversely proportional to the square-root of the number of collected photons[1], a lower number of collected photons translates directly into a poor device sensitivity.

The sharp tip containing the NV center not only acts as a contact point to the sample of interest, but also as a wave-guide to the emitted photons. Thus, a careful design of the tip shape can increase the number of photons guided towards the detection optics. To this end, Finite Difference Time Domain (FDTD) simulations were used in order to find the parameter space for an optimum guiding of photons and thus a better sensitivity.

The effect of tapering, that is, a cone-like shaping (see inset of Fig. 1), was investigated by FDTD taking as a benchmark the routinely-fabricated cylindrical wave-guides of the first generation of sensors (200 nm cylindrical wave-guides). The top graph in figure 1 shows the dependence of the photon collection efficiency on the top diameter of the wave-guide. Two values of numerical aperture (NA) of 0.7 and 0.8 were considered, which are typical for sensor implementation.

As shown in the figure, the collection efficiency increases by tapering the structure and reaches a maximum of ~70% (into NA=0.7) at a top pillar diameter of 1000 nm. Moreover, losses occurring due to internal reflection in diamond are minimized by introducing a ~110 nm thin SiO_2 anti-reflection coating into simulations, which increased the predicted collection efficiency to around 76% for NA = 0.7 – a two times enhancement compared to the cylindrical geometry.

To further understand the effect of tapering, far-field intensity distribution profiles of the emission towards the detection optics were also investigated for wave-guides of various geometries, as presented in figure 1 (lower). One can clearly see that the tapering reduces the aperture of the emission, approaching a Gaussian-like beam shape.

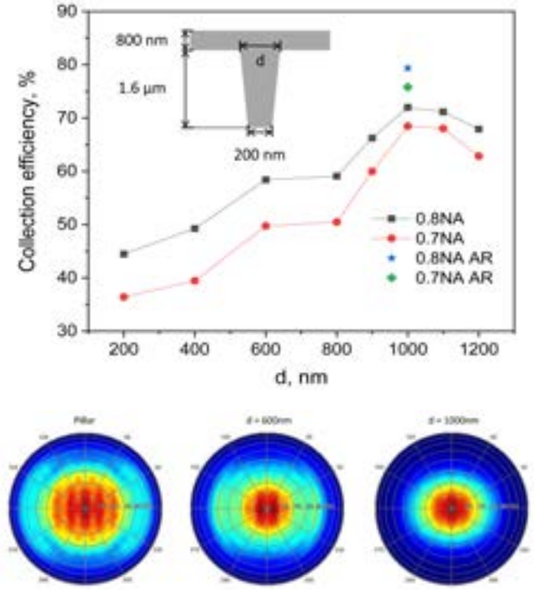

Fig. 1 Finite Difference Time Domain (FDTD) simulation results of wave-guiding properties of nanoscale quantum sensors. The upper figure presents the photon collection efficiency vs different top diameters (d) of the wave-guide, starting from a cylindrical shape and keeping the bottom-diameter constant. Black and red curves represent a collection efficiency utilizing lenses with numerical apertures (NA) of 0.8 and 0.7, respectively. Blue and green dots represent the addition of an anti-reflection coating (see text). The lower figures represent the far-field profiles of 200 nm cylindrical (left), 200 nm lower and 600 nm upper diameter (middle) and 200 nm lower and 1000 nm upper diameter (right) wave-guides.

Nano-fabrication of quantum sensors with enhanced properties.
Following the designs theoretically investigated, the next generation of quantum sensors was then fabricated with a tapered wave-guide, aiming at a half-taper wall angle between 5° to 10°.

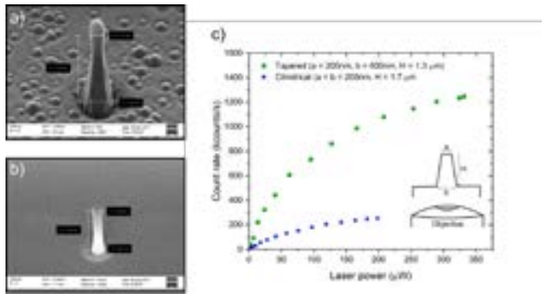

Fig. 2 a) and b): SEM images of the wave-guide shapes from the new tapered 200 nm lower and 600 nm upper diameter and the previous cylindrical, 200 nm diameter sensor generations, respectively. c) Total photon count rate of wave-guides containing single NV centers. Blue and green correspond to the cylindrical and tapered wave-guide geometries.

Figure 2 a) and b) presents scanning electron microscopy (SEM) images of the new generation, tapered-shaped and the previous generation, cylindrical-shaped wave-guides, repectively. With the development of a novel nano-fabrication routine and extensive refinement of the diamond dry-etching process, a half-taper wall angle of 6o has been achieved, which agrees well with the targeted value from simulations.

As seen in figure 2 c), the total number of photons emitted by single individual NV centers embedded into wave-guides with the two described geometries is increased by a factor of six using the tapered walls. This, in turn, represents an improvement of more than two times in the device sensitivity to magnetic fields.

Summary
The results from the first year of the NQsense project have led to significant improvements in sensor performance for magnetic field imaging at the nano-scale. This represents not only advances in the technology capabilities, but also positions Qnami as a leader in the commercialization of highly sensitive quantum sensors made of diamond. The new generation of sensors commercialized by Qnami is already in use in several countries world-wide, which represents significant traction for the young start-up and provides the needed feedback to further establish and advance the technology.

Several challenges are to be addressed within the next project year. The fine-tuning related to the transfer of the nano-fabrication capabilities of Qnami to the PSI cleanroom have to be realized, as well as the development of novel designs to improve the device sensitivity even further, with a target two-fold enhancement from the current wave-guide geometry.

References

[1] L. Rondin, J.-P. Tetienne, T. Hingant, J.-F. Roch, P. Maletinsky, V. Jacques, *Magnetometry with nitrogen-vacancy defects in diamond*, Rep. Prog. Phys. 77, 056503 (2014)

[2] P. Maletinsky, S. Hong, M. S. Grinolds, B. Hausmann, M. D. Lukin, R. L. Walsworth, M. Loncar, A. Yacoby, *A robust scanning diamond sensor for nanoscale imaging with single nitrogen-vacancy centres* , Nature Nanotechnology 7, 320–324 (2012)

Publication list (peer-reviewed)

Abreu-Villela R, Schonenberger M, Caraballo I, Kuentz M. *Early stages of drug crystallization from amorphous solid dispersion via fractal analysis based on chemical imaging*. Eur J Pharm Biopharm. **133**, 122-30, https://doi.org/10.1016/j.ejpb.2018.10.007 (2018)

Aleandri S, Schonenberger M, Niederquell A, Kuentz M. *Temperature-Induced Surface Effects on Drug Nanosuspensions*. Pharm Res-Dordr. **35(3)**, https://doi.org/10.1007/s11095-017-2300-6 (2018)

Arnold SA, Muller SA, Schmidli C, Syntychaki A, Rima L, Chami M, et al. *Miniaturizing EM Sample Preparation: Opportunities, Challenges, and "Visual Proteomics"*. Proteomics. **18**(5-6), https://doi.org/ 10.1002/pmic.201700176 (2018)

Barfuss A, Kolbl J, Thiel L, Teissier J, Kasperczyk M, Maletinsky P. *Phase-controlled coherent dynamics of a single spin under closed-contour interaction*. Nat Phys. **14(11)**, 1087-91, https://doi.org/10.1038/s41567-018-0231-8 (2018)

Braakman FR, Rossi N, Tutuncuoglu G, Morral AFI, Poggio M. *Coherent Two-Mode Dynamics of a Nanowire Force Sensor*. Phys Rev Appl. **9(5)**, https://doi.org/10.1103/PhysRevApplied.9.054045 (2018)

Camenzind LC, Yu LQ, Stano P, Zimmerman JD, Gossard AC, Loss D, et al. *Hyperfine-phonon spin relaxation in a single-electron GaAs quantum dot*. Nat Commun. **9**, https://doi.org/10.1038/s41467-018-05879-x (2018)

Castellanos S, Wu LJ, Baljozovic M, Portale G, Kazazis D, Vockenhuber M, et al. *Ti, Zr, and Hf-based molecular hybrid materials as EUV photoresists*. Proc Spie. 10583, https://doi.org/10.1117/12.2297167 (2018)

Challier M, Sonusen S, Barfuss A, Rohner D, Riedel D, Koelbl J, et al. *Advanced Fabrication of Single-Crystal Diamond Membranes for Quantum Technologies*. Micromachines-Basel. **9(4)**, https://arxiv.org/abs/1802.08971 (2018)

Clabbers MTB, Abrahams JP. *Electron diffraction and three-dimensional crystallography for structural biology*. Crystallogr Rev. **24(3)**, 176-204, https://doi.org/10.1080/0889311X.2018.1446427 (2018)

Clabbers MTB, Gruene T, Parkhurst JM, Abrahams JP, Waterman DG. *Electron diffraction data processing with DIALS*. Acta Crystallogr D. **74**, 506-18, https://doi.org/10.1107/S2059798318007726 (2018)

De Bardi M, Muller R, Grunzweig C, Mannes D, Boillat P, Rigollet M, et al. *On the needle clogging of staked-in-needle pre-filled syringes: Mechanism of liquid entering the needle and solidification process*. Eur J Pharm Biopharm. **128**, 272-81, https://doi.org/10.1016/j.ejpb.2018.05.006 (2018)

Debiossac M, Schatti J, Kriegleder M, Geyer P, Shayeghi A, Mayor M, et al. *Tailored photocleavable peptides: fragmentation and neutralization pathways in high vacuum*. Phys Chem Chem Phys. **20(16)**, 11412-7, https://doi.org/10.1039/C8CP01058G (2018)

Eftekharzadeh B, Daigle JG, Kapinos LE, Coyne A, Schiantarelli J, Carlomagno Y, et al. *Tau Protein Disrupts Nucleocytoplasmic Transport in Alzheimer's Disease*. Neuron. **99(5)**,925-+, https://doi.org/10.1016/j.neuron.2018.07.039 (2018)

Einfalt T, Witzigmann D, Edlinger C, Sieber S, Goers R, Najer A, et al. *Biomimetic artificial organelles with in vitro and in vivo activity triggered by reduction in microenvironment*. Nat Commun. **9**, https://doi.org/10.1038/s41467-018-03560-x (2018)

Emilsson G, Sakiyama Y, Malekian B, Xiong KL, Adali-Kaya Z, Lim RYH, et al. *Gating Protein Transport in Solid State Nanopores by Single Molecule Recognition*. Acs Central Sci. **4(8)**, 1007-14, https://doi.org/10.1021/acscentsci.8b00268 (2018)

Emilsson G, Xiong KL, Sakiyama Y, Malekian B, Gagner VA, Schoch RL, et al. *Polymer brushes in solid-state nanopores form an impenetrable entropic barrier for proteins*. Nanoscale. **10(10)**, 4663-9, https://doi.org/10.1016/j.ejpb.2018.05.006 (2018)

Finizio S, Wintz S, Bracher D, Kirk E, Semisalova AS, Forster J, et al. *Thick permalloy films for the imaging of spin texture dynamics in perpendicularly magnetized systems*. Phys Rev B. **98(10)**, https://doi.org/10.1103/PhysRevB.98.104415 (2018)

Freund S, Pawlak R, Moser L, Hinaut A, Steiner R, Marinakis N, Constable EC, Meyer E, Housecroft CE, Glatzel T. *Transoid-to-Cisoid Conformation Changes of Single Molecules on Surfaces Triggered by Metal Coordination*. ACS Omega **3(10)**, 12851, https://doi.org/10.1021/acsomega.8b01792 (2018)

Frey L, Hiller S, Riek R, Bibow S. *Lipid- and Cholesterol-Mediated Time-Scale-Specific Modulation of the Outer Membrane Protein X Dynamics in Lipid Bilayers*. J Am Chem Soc. **140(45)**, 15402-11, https://doi.org/10.1088/1367-2630/aaf8f5 (2018)

Friedl M, Cerveny K, Weigele P, Tutuncuoglu G, Marti-Sanchez S, Huang CY, et al. *Template-Assisted Scalable Nanowire Networks*. Nano Lett. **18(4)**, 2666-71, https://doi.org/10.1021/acs.nanoleF.8b00554 (2018)

Froning FNM, Rehmann MK, Ridderbos J, Brauns M, Zwanenburg FA, Li A, et al. *Single, double, and triple quantum dots in Ge/Si nanowires*. Appl Phys Lett. **113(7)**, https://doi.org/10.1063/1.5042501 (2018)

Ganier O, Schnerch D, Oertle P, Lim RYH, Plodinec M, Nigg EA. *Structural centrosome aberrations promote non-cell-autonomous invasiveness*. Embo J. **37(9)**, https://doi.org/10.15252/embj.201798576 (2018)

Garni M, Einfalt T, Goers R, Palivan CG, Meier W. *Live Follow-Up of Enzymatic Reactions Inside the Cavities of Synthetic Giant Unilamellar Vesicles Equipped with Membrane Proteins Mimicking Cell Architecture*. ACS Synth. Biol. 7(9), 2116, https://doi.org/10.1021/acssynbio.8b00104 (2018)

Garcia-Suarez VM, Garcia-Fuente A, Carrascal DJ, Burzuri E, Koole M, van der Zant HSJ, et al. *Spin signatures in the electrical response of graphene nanogaps*. Nanoscale. **10(38)**, 18169-77, https://doi.org/10.1039/c8nr06123h (2018)

Gerspach MA, Mojarad N, Sharma D, Ekinci Y, Pfohl T. *Pneumatically Controlled Nanofluidic Devices for Contact-Free Trapping and Manipulation of Nanoparticles*. Part. Part. Syst. Charact. **35(12)**, 1800161, https://doi.org/10.1002/ppsc.201800161 (2018)

Goers R, Thoma J, Ritzmann N, Di Silvestro A, Alter C, Gunkel-Grabole G, Fotiadis D, Müller DJ, Meier W. *Optimized reconstitution of membrane proteins into synthetic membranes*. Comm. Chem. **1(1)**, 35 https://doi.org/10.1038/s42004-018-0037-8 (2018)

Gruene T, Wennmacher JTC, Zaubitzer C, Holstein JJ, Heidler J, Fecteau-Lefebvre A, et al. *Rapid Structure Determination of Microcrystalline Molecular Compounds Using Electron Diffraction*. Angew Chem Int Edit. **57(50)**, 16313-7, https://doi.org/10.1002/anie.201811318 (2018)

Gurram M, Omar S, Zihlmann S, Makk P, Li QC, Zhang YF, et al. *Spin transport in two-layer-CVD-hBN/graphene/hBN heterostructures*. Phys Rev B. **97(4)**, http://dx.doi.org/10.1103/PhysRevB.97.045411 (2018)

Hartmann JB, Zahn M, Burmann IM, Bibow S, Hiller S. *Sequence-Specific Solution NMR Assignments of the beta-Barrel Insertase BamA to Monitor Its Conformational Ensemble at the Atomic Level*. J Am Chem Soc. **140(36)**, 11252-60, https://doi.org/10.1021/jacs.8b03220 (2018)

Indolese DI, Delagrange R, Makk P, Wallbank JR, Wanatabe K, Taniguchi T, et al. *Signatures of van Hove Singularities Probed by the Supercurrent in a Graphene-hBN Superlattice*. Phys Rev Lett. **121(13)**, http://dx.doi.org/10.1103/PhysRevLett.121.137701 (2018)

Keller SG, Probst B, Heinisch T, Alberto R, Ward TR. *Photo-Driven Hydrogen Evolution by an Artificial Hydrogenase Utilizing the Biotin-Streptavidin Technology*. Helv Chim Acta. **101(4)**, http://dx.doi.org/10.1103/PhysRevApplied.10.044053 (2018)

Kisiel M, Brovko OO, Yildiz D, Pawlak R, Gysin U, Tosatti E, et al. *Mechanical dissipation from charge and spin transitions in oxygen-deficient SrTiO3 surfaces*. Nat Commun. **9**, https://doi.org/10.1002/hlca.201800036 (2018)

Kuhlmann AV, Deshpande V, Camenzind LC, Zumbuhl DM, Fuhrer A. *Ambipolar quantum dots in undoped silicon fin field-effect transistors*. Appl Phys Lett. **113(12)**, https://doi.org/10.1063/1.5048097 (2018)

Leisgang N, Roch JG, Froehlicher G, Hamer M, Terry D, Gorbachev R, et al. *Optical second harmonic generation in encapsulated single-layer InSe*. Aip Adv. **8(10)**, https://doi.org/10.1063/1.5052417 (2018)

Makk P, Handschin C, Tovari E, Watanabe K, Taniguchi T, Richter K, et al. *Coexistence of classical snake states and Aharonov-Bohm oscillations along graphene p-n junctions*. Phys Rev B. **98(3)**, http://dx.doi.org/10.1103/PhysRevB.98.035413 (2018)

Malekian B, Schoch RL, Robson T, del Castillo GFD, Xiong KL, Emilsson G, et al. *Detecting Selective Protein Binding Inside Plasmonic Nanopores: Toward a Mimic of the Nuclear Pore Complex*. Front Chem. **6**, https://doi.org/10.3389/fchem.2018.00637 (2018)

Mehlin A, Gross B, Wyss M, Schefer T, Tutuncuoglu G, Heimbach F, et al. *Observation of end-vortex nucleation in individual ferromagnetic nanotubes*. Phys Rev B. **97(13)**, https://doi.org/10.1103/PhysRevB.97.134422 (2018)

Muller V, Hinaut A, Moradi M, Baljozovic M, Jung TA, Shahgaldian P, et al. *A Two-Dimensional Polymer Synthesized at the Air/Water Interface*. Angew Chem Int Edit. **57(33)**, 10584-8, https://doi.org/10.1002/anie.201804937 (2018)

Nijs T, Klein YM, Mousavi SF, Ahsan A, Nowakowska S, Constable EC, et al. *The Different Faces of 4'-Pyrimidinyl-Functionalized 4,2':6',4"-Terpyridin es: Metal-Organic Assemblies from Solution and on Au(111) and Cu(111) Surface Platforms*. J Am Chem Soc. **140(8)**, 2933-9, https://doi.org/10.1021/jacs.7b12624 (2018)

Nirmalraj PN, Thodkar K, Guerin S, Calame M, Thompson D. *Graphene wrinkle effects on molecular resonance states*. Npj 2d Mater Appl. **2**, https://doi.org/10.1038/s41699-018-0053-7 (2018)

Nultsch K, Bast LK, Naf M, El Yakhlifi S, Bruns N, Germershaus O. *Effects of Silk Degumming Process on Physicochemical, Tensile, and Optical Properties of Regenerated Silk Fibroin*. Macromol Mater Eng. **303(12)**, https://doi.org/10.1002/mame.201800408 (2018)

Opara NL, Mohacsi I, Makita M, Castano-Diez D, Diaz A, Juranic P, et al. *Demonstration of femtosecond X-ray pump X-ray probe diffraction on protein crystals*. Struct Dynam-Us. **5(5)**, https://doi.org/10.1063/1.5050618 (2018)

Patlatiuk T, Scheller CP, Hill D, Tserkovnyak Y, Barak G, Yacoby A, et al. *Evolution of the quantum Hall bulk spectrum into chiral edge states*. Nat Commun. **9**, https://doi.org/10.1038/s41467-018-06025-3 (2018)

Roch JG, Leisgang N, Froehlicher G, Makk P, Watanabe K, Taniguchi T, et al. *Quantum-Confined Stark Effect in a MoS2 Monolayer van der Waals Heterostructure*. Nano Lett. **18(2)**, 1070-4, https://doi.org/10.1021/acs.nanolett.7b04553 (2018)

Rohner D, Thiel L, Muller B, Kasperczyk M, Kleiner R, Koelle D, et al. *Real-Space Probing of the Local Magnetic Response of Thin-Film Superconductors Using Single Spin Magnetometry*. Sensors-Basel. **8(11)**, https://arxiv.org/abs/1807.07584v1 (2018)

Rouse I, Willitsch S. *Energy distributions of an ion in a radio-frequency trap immersed in a buffer gas under the influence of additional external forces*. Phys Rev A. **97(4)**, https://doi.org/10.1103/PhysRevA.97.042712 (2018)

Saxena N, Keilhofer J, Maurya AK, Fortunato G, Overbeck J, Müller-Buschbaum P. *Facile Optimization of Thermoelectric Properties in PEDOT:PSS Thin Films through Acido-Base and Redox Dedoping Using Readily Available Salts*. ACS Applied Energy Materials. **1(2)**, 336-42, https://doi.org/10.1021/acsaem.7b00334 (2018)

Schätti J, Rieser P, Sezer U, Richter G, Geyer P, Rondina GG, et al. *Pushing the mass limit for intact launch and photoionization of large neutral biopolymers*. Communications Chemistry. **1(1)**, 93, https://doi.org/10.1038/s42004-018-0095-y (2018)

Schmidli C, Rima L, Arnold SA, Stohler T, Syntychaki A, Bieri A, et al. *Miniaturized Sample Preparation for Transmission Electron Microscopy*. Jove-J Vis Exp. **(137)**, https://doi.org/10.3791/57310 (2018)

Thoma J, Manioglu S, Kalbermatter D, Bosshart PD, Fotiadis D, Müller DJ. *Protein-enriched outer membrane vesicles as a native platform for outer membrane protein studies*. Communications Biology. **1(1)**, 23, https://doi.org/10.1038/s42003-018-0027-5 (2018)

Thoma J, Sapra KT, Müller DJ. *Single-Molecule Force Spectroscopy of Transmembrane β-Barrel Proteins*. Annual Review of Analytical Chemistry. **11(1)**, 375-95, https://doi.org/10.1146/annurev-anchem-061417-010055 (2018)

Thoma J, Sun Y, Ritzmann N, Muller DJ. *POTRA Domains, Extracellular Lid, and Membrane Composition Modulate the Conformational Stability of the beta Barrel Assembly Factor BamA*. Structure. **26(7)**, 987-+, https://doi.org/ 10.1016/j.str.2018.04.017 (2018)

Tinti G, Frojdh E, van Genderen E, Gruene T, Schmitt B, de Winter DAM, et al. *Electron crystallography with the EIGER detector*. Iucrj. **5**, 190-9, http://doi.org/10.1107/S2052252518000945 (2018)

Vasyukov D, Ceccarelli L, Wyss M, Gross B, Schwarb A, Mehlin A, et al. *Imaging Stray Magnetic Field of Individual Ferromagnetic Nanotubes*. Nano Lett. **18(2)**, 964-70, http://doi.org/10.1021/acs.nanolett.7b04386 (2018)

Viero Y, Guerin D, Vladyka A, Alibart F, Lenfant S, Calame M, et al. *Light-Stimulatable Molecules/Nanoparticles Networks for Switchable Logical Functions and Reservoir Computing*. Adv Funct Mater. **28(39)**, https://doi.org/10.1002/adfm.201801506 (2018)

Zanetti-Dallenbach R, Plodinec M, Oertle P, Redling K, Obermann EC, Lim RYH, et al. *Length Scale Matters: Real-Time Elastography versus Nanomechanical Profiling by Atomic Force Microscopy for the Diagnosis of Breast Lesions*. Biomed Res Int., https://doi.org/10.1155/2018/3840597 (2018)

Zeissler K, Finizio S, Shahbazi K, Massey J, Al Ma'Mari F, Bracher DM, et al. *Discrete Hall resistivity contribution from Neel skyrmions in multilayer nanodiscs*. Nat Nanotechnol. **13(12)**, 1161-+, https://doi.org/10.1038/s41565-018-0268-y (2018)

Zhang Y, Haitjema J, Baljozovic M, Vockenhuber M, Kazazis D, Jung TA, et al. *Dual-tone Application of a Tin-Oxo Cage Photoresist Under E-beam and EUV Exposure*. J Photopolym Sci Tec. **31(2)**, 249-55, https://doi.org/10.2494/photopolymer.31.249 (2018)

Zihlmann S, Cummings AW, Garcia JH, Kedves M, Watanabe K, Taniguchi T, et al. *Large spin relaxation anisotropy and valley-Zeeman spin-orbit coupling in WSe2/Gr/hBN heterostructures*. Phys Rev B. **97(7)**, 075434, http://dx.doi.org/10.1103/PhysRevB.97.075434 (2018)

Swiss Nanoscience Institute – A research initiative of the University of Basel and the Canton of Aargau

Educating
Talents
since 1460.

Universität Basel
Petersplatz 1
Postfach 2148
4001 Basel
Schweiz

www.unibas.ch

Swiss Nanoscience Institute
Universität Basel
Klingelbergstrasse 82
4056 Basel
Schweiz

www.nanoscience.ch